



universität
wien

MASTERARBEIT / MASTER'S THESIS

Titel der Masterarbeit / Title of the Master's Thesis

„Detection of surface changes using terrestrial laser
scanning:
A field study on rock instabilities in the Ybbs Valley, Lower
Austria“

verfasst von / submitted by

Anna Iglseder, BSc

angestrebter akademischer Grad / in partial fulfilment of the requirements for the degree of

Master of Science (MSc)

Wien, 2018 / Vienna 2018

Studienkennzahl lt. Studienblatt /
degree programme code as it appears on the
student record sheet:

A 066 856

Studienrichtung lt. Studienblatt /
degree programme as it appears on the student
record sheet:

Masterstudium Kartographie und Geoinformation

Betreut von / Supervisor:

Univ.-Prof. Dipl.-Geogr. Dr. Thomas Glade

Author's declaration

Herewith I confirm, that the presented master's thesis is written by me. Neither did I use other resources than the cited references nor made I use of any other illegitimate means of help. Furthermore, the master's thesis was not submitted as an examination paper neither in Austria nor abroad. This thesis is identical with the version evaluated by the supervisor.

Vienna, May 2018

(Anna Iglseder)

Acknowledgements

A lot of people accompanied me on my long way through the process of this thesis. At this point I would like to take the chance to express some explicit thank. First, I would like to thank my supervisor Thomas Glade for guiding me through the process with a comprehensive scientific perspective and giving me the possibility to contribute to the NoeSLIDE Project. Thanks to Eki for introducing me to the field of terrestrial laser scanning, encouraging me to focus on this method in my thesis and giving me start-up support. Following, I would like to thank Berndl, Gregor, Margeritha and Marco for a lot of helping hands in the field. Thanks to Agnes for enriching discussions - although working on completely different topics, knowing that the coworker sitting on the table next to you is going through the same makes it a lot easier. Thanks to Stefan for not only joining me in the field but also always having an open ear for all kinds of problems and need for discussion and moreover for the extensive feedback on the work. Thanks to Doro for being my constant psychological support through all ups and downs of the process. Biggest thanks to Sarah for proof reading more than hundred pages outside of her field. And special thanks to my mum for always supporting my decisions.

Abstract

Rock fall is a prominent gravitative process in mountainous regions. Due to road cuts and steep slopes with bare rock faces, the Ybbs Valley in Lower Austria is a rock fall endangered area. This master's thesis deals with the detection of small scale rock events by means of terrestrial laser scanning. Furthermore, it aims at the evaluation of the registration and change detection steps of the processing workflow. The study area is the Amtmann, a 40 m high rock monolite in the Ybbs Valley between Opponitz and Waidhofen an der Ybbs. The used data consists of high density 3-D point clouds acquired from up to three different positions in a total of four scanning campaigns between July 2014 and October 2017. For method evaluation, small scale artificial manipulation of the surface is performed prior to the last scanning campaign. The data processing workflow includes registration, filtering and change detection. Different registration methods (MSA, ICP) and different point to point change detection approaches are tested. The results are evaluated statistically by comparing descriptive parameters and analysed by rank scale test. Moreover, the output is cross-checked visually. The optimal derived workflow for the thesis includes automated tie point registration, the ICP algorithm for fine alignment and the M3C2 algorithm for change detection. The results show that small scale changes from ~ 0.025 m local surface change are detectable. Limiting impacts are the accessible scan positions which do not allow all around scanning of the Amtmann and shadowing effects of local vegetation lead which lead to incomplete surface data.

Kurzfassung

Steinschlag ist ein weit verbreiteter Prozess in gebirgigen Regionen. Aufgrund von Hanganschnitten durch Straßenbau und frei stehenden Felsstrukturen zählt das Ybbstal in Niederösterreich zu steinschlaggefährdeten Gebieten. Diese Masterarbeit widmet sich der Erfassung von kleinmaßstäbigen Steinschlagevents unter Einsatz von terrestrischem Laserscanning. Das Ziel der Arbeit ist eine Methodenevaluierung verschiedener Ansätze für Punktwolkenregistrierung und Nachweis von Oberflächenveränderungen. Das Untersuchungsobjekt ist der Amtmann, ein 40 m hoher Felsturm im Ybbstal zwischen Opponitz und Waidhofen an der Ybbs. Für die vorliegende Arbeit wurden hochaufgelöste 3-D Punktwolken von vier Feldkampagnen verwendet, die bis zu drei verschiedene Scanpositionen beinhalten. Die Datenaufnahme wurde zwischen Juli 2014 und Oktober 2017 durchgeführt. Für die Evaluierung der Methodik wurden vor der letzten Scankampagne kleinmaßstäbige Styroporobjekte auf der gescannten Felsoberfläche installiert. Der Datenverarbeitungsprozess besteht aus Registrierung und Filtern der Punktwolken sowie Detektierung von Oberflächenveränderungen. Verschiedene methodische Ansätze zur Punktwolkenregistrierung (MSA, ICP) und verschiedene punktwolkenbasierte Ansätze zum Erkennen von Oberflächenveränderungen wurden getestet. Die Ergebnisse wurden durch deskriptive Statistik evaluiert sowie durch nicht-parametrische Testverfahren überprüft. Darüber hinaus wurden die Ergebnisse visuell interpretiert. Die ausgewählten Methoden für die Punktwolkenverarbeitung in dieser Masterarbeit beinhalten automatisierte Grobregistrierung mit hochreflektierenden Passpunkten, ICP-Algorithmen für Feinregistrierung sowie verschiedene punktdatenbasierte Algorithmen (C2C und M3C2) für die Erfassung von Oberflächenveränderungen. Die Ergebnisse zeigen eine minimal messbare Veränderung von ~ 0.025 m. Limitierende Faktoren sind die Einschränkung der möglichen Scanpositionen durch die lokale Topographie sowie Abschattungseffekte lokaler Vegetation, welche zu unvollständiger Oberflächenrepräsentation führen.

Content

| | |
|---|----|
| List of figures | V |
| List of tables | IX |
| List of abbreviations | XI |
| | |
| 1. Introduction | 1 |
| 1.1 Background and problem statement | 1 |
| 1.2 Objectives and research questions | 2 |
| 1.3 Thesis outline | 4 |
| | |
| 2. Change detection using terrestrial laser scanning | 5 |
| 2.1 Physical basics of electromagnetic waves and laser | 5 |
| 2.2 Concepts of distance measurement using a laser | 9 |
| 2.2.1 Pulse based measurement | 10 |
| 2.2.2 Continuous wave modulation | 11 |
| 2.2.3 Other distance measuring techniques | 13 |
| 2.3 Development and concept of terrestrial laser scanning | 14 |
| 2.3.1 The concept of scanning profiles and surfaces | 15 |
| 2.3.2 Specifications of a terrestrial laser scanner – the RIEGL VZ 6000 | 17 |
| 2.4 Processing of terrestrial laser scanning data | 19 |
| 2.4.1 Registration of multiple scan positions | 19 |
| 2.4.2 Filtering of point clouds | 23 |
| 2.4.3 Concepts of change detection | 23 |
| 2.5 Applications of TLS change detection | 26 |

| | | |
|-----------|---|-----------|
| 2.5.1 | Monitoring of artificial objects..... | 26 |
| 2.5.2 | Monitoring of natural structures..... | 27 |
| 2.5.3 | Monitoring of rock structures..... | 30 |
| 2.6 | Uncertainties and challenges..... | 32 |
| 3. | Data and Methods | 37 |
| 3.1 | Field work..... | 37 |
| 3.1.1 | The scanning process..... | 38 |
| 3.1.2 | Manipulation of the surface | 38 |
| 3.2 | Data | 39 |
| 3.3 | Registration | 41 |
| 3.3.1 | Target-based registration | 41 |
| 3.3.2 | Iterative closest point (ICP) registration in CloudCompare | 42 |
| 3.3.3 | Multi station adjustment (MSA) registration in RiSCAN PRO | 44 |
| 3.3.4 | Registration tests and final fine registration..... | 45 |
| 3.4 | Co-registration and extraction..... | 46 |
| 3.5 | Filtering | 47 |
| 3.5.1 | Removing the vegetation | 47 |
| 3.5.2 | Further filtering methods | 50 |
| 3.6 | Change detection | 51 |
| 3.6.1 | Cloud to cloud distance C2C..... | 52 |
| 3.6.2 | Cloud to cloud distance M3C2 | 53 |
| 3.6.3 | Application and evaluation of chosen change detection approaches..... | 55 |
| 4. | Research Area | 57 |
| 4.1 | Location and infrastructure | 58 |
| 4.2 | Environmental characteristics of the research area | 59 |
| 4.3 | Rock falls and related investigations..... | 60 |

| | |
|--|---------|
| 5. Results | 63 |
| 5.1 Field work | 63 |
| 5.2 Initial check of the raw data | 64 |
| 5.3 Registration | 65 |
| 5.3.1 Initial coarse registration: point pair picking and tie points | 65 |
| 5.3.2 Fine registration: testing different options | 66 |
| 5.3.3 Fine registration: final registration | 77 |
| 5.4 Extraction and co-registration | 79 |
| 5.5 Filtering | 81 |
| 5.5.1 Removing the vegetation | 82 |
| 5.5.2 Further filtering | 84 |
| 5.6 Change detection | 87 |
| 5.6.1 Change detection comparing different epochs | 87 |
| 5.6.2 Evaluation of change detection approaches | 93 |
| 5.6.3 Detailed change detection evaluation for test areas | 98 |
| 6. Discussion | 105 |
| 6.1 Data | 105 |
| 6.2 Registration | 106 |
| 6.3 Filtering | 109 |
| 6.4 Change detection | 110 |
| 6.5 Research questions | 114 |
| 7. Conclusion | 119 |
| 8. Outlook | 121 |
| Bibliography | 123 |
| Appendix | 143 |

List of figures

| | | |
|-------------------|---|----|
| Figure 1: | Model of an electromagnetic wave | 6 |
| Figure 2: | The range of the electromagnetic spectrum (after HERITAGE AND LARGE 2009b: 22)..... | 7 |
| Figure 3: | Surface reflection types: (a) specular, (b) diffuse, (c) mixed. (after HERITAGE AND LARGE 2009b: 23)..... | 7 |
| Figure 4: | Comparison of the radiation of natural light (a) and a laser (b) (after HERITAGE AND LARGE 2009b: 25)..... | 8 |
| Figure 5: | Pulse characteristics of emitted pulse (a) and received echoes (b) measurement (after BERLADIN ET AL 2010: 4) | 10 |
| Figure 6: | Amplitude modulation of an electromagnetic wave (after PRICE AND UREN 1989: 167) | 12 |
| Figure 7: | Measuring phase differences of an electromagnetic wave for distance measurement (after PRICE AND UREN 1989: 165)..... | 13 |
| Figure 8: | The principle of a terrestrial laser scanner (Riegl) (after KRAUS 2004: 472)..... | 16 |
| Figure 9: | Classical scanning setup: The Riegl VZ 6000 laser scanner on a tripod connected to a laptop and a differential GNSS. | 17 |
| Figure 10: | The principle of registration of point clouds: the Helmert Transformation..... | 21 |
| Figure 11: | Workflow of point cloud data processing | 37 |
| Figure 12: | Preparing and performing surface manipulation. A: Polystyrene objects – original and adapted forms. B/C: Measuring the volume of the adapted objects by water displacement. D: Fixing the manipulation objects to the Amtmann. E/F: Manipulated surface. | 39 |
| Figure 13: | Data overview of the different used scans from all four scanning campaigns..... | 40 |
| Figure 14: | Vegetation filtering process: Combination of filtering based on geometrical information, intensity and manual editing | 49 |

| | | |
|-------------------|---|----|
| Figure 15: | Spatial concept of the octree-structure (after CHÁVET AND KARSTOFT 2012)..... | 50 |
| Figure 16: | Hausdorff distance vs. "true" distance (after CLOUDCOMPARE COMMUNITY 2018)..... | 52 |
| Figure 17: | Concepts of local surface modelling for C2C. A: least square plane, B: Delaunay triangulation, C: quadric modelling | 53 |
| Figure 18: | Illustration of the M3C2 change detection concept (after Lague et al 2013)..... | 54 |
| Figure 19: | Upper part of the Amtmann, a free-standing rock structure in the Ybbs Valley | 57 |
| Figure 20: | Location of the Amtmann in the Ybbs Valley, Lower Austria..... | 58 |
| Figure 21: | Climate diagramm Waidhofen an der Ybbs, 1971-2000 (data: ZAMG 2017) | 59 |
| Figure 22: | Car hit during a rock fall event in 2010 (photo: Freiwillige Feuerwehr Opponitz 2010) | 60 |
| Figure 23: | Selected views of the initial data check. A/B/C: Zooming in 2016 SP01 data. D. Close-up of the 2014 data. E/F: Same part of the 2017a (E) and 2017b (F) data – added structures visible on F within the red indications. | 64 |
| Figure 24: | Distribution of the polydata extracted by plane patch filter, exemplarily for SP01 of 2016 data | 67 |
| Figure 25: | Output of MSA and ICP using different settings (test data: 2016, SP01 with 6,002,675 points and SP02 with 11,765,226 points)..... | 73 |
| Figure 26: | Output of MSA and ICP using different settings (test data: 2016, SP01 segmented using 314,536 points and SP02 segmented using 275,534 points) | 74 |
| Figure 27: | Comparing MSA and ICP - Error and numbers of observations used for registration. A: using all data, B: using cropped data..... | 76 |
| Figure 28: | Visual presentation of the final registration for all four epochs | 78 |
| Figure 29: | Screenshot: Coarse co-registration using manual point pair picking in CloudCompare | 79 |
| Figure 30: | Cross-sections of the four co-registered point clouds revealing the co-registration quality | 81 |
| Figure 31: | Training of the CANUPO classification using the 2016 point cloud data..... | 82 |

| | | |
|-------------------|---|-----|
| Figure 32: | Workflow of vegetation filtering by the example of the 2014 data. A: Point cloud cut to 9 sections for filtering. B: Derivates from the filtering process. C: Merged combination of the selected derivates. D: Final result of the filtering after manually filtering. E: Close-up from the upper part of the vegetation-filtered Amtmann. F: Cross-section of the point cloud. D: Close-up of a lower part of the point cloud. | 83 |
| Figure 33: | Examples of detailed results of the vegetation filtering. A: Original top part of the 2016 point cloud. B: Classified as "rock": detail section shown in A after applying the CANUPO filter. C: Close-up of 2017a data: points classified as rock and filling of the gaps using intensity filtered low confidence vegetation data. D: Results after the final manual vegetation filtering of the 2017b data with four cross-sections..... | 84 |
| Figure 34: | Close-up of the point clouds showing the different filtering steps (unit of the scale bar in m)..... | 85 |
| Figure 35: | Final point clouds of the different epochs (colored by grey-scaled intensity values) | 86 |
| Figure 36: | Results of the 2014-2017a change detection | 88 |
| Figure 37: | Results of the 2016-2017a change detection | 91 |
| Figure 38: | Results of the 2017a-2017b change detection | 95 |
| Figure 39: | Histograms showing the results of the 2017a-2017b change detection | 96 |
| Figure 40: | Boxplots and chosen quantiles from the analysis of the 2017a-2017b change detection results..... | 97 |
| Figure 41: | Test areas for the detailed change detection evaluation (unfiltered point cloud) | 99 |
| Figure 42: | Area of changed surface (left) and area of no surface change (right) within test area 1 | 99 |
| Figure 43: | Results of the detailed change detection evaluation 2017a-2017b of the manipulated surface for the different processing steps of the point cloud, 0.01 m threshold for change..... | 101 |
| Figure 44: | Results of the detailed change detection evaluation 2017a-2017b of the manipulated surface for the different processing steps of the point cloud, 0.02 m threshold for change..... | 103 |
| Figure 45: | Small scale surface changes between 2016 and 2017 referring to the analyses in Figure 37. A/C: different views of the point cloud section. B: cross section revealing the different surfaces | 112 |

List of tables

| | | |
|-----------------|--|----|
| Table 1: | Range measurement performance of the Riegl VZ 6000 (Riegl 2017) | 18 |
| Table 2: | Dimensions of the objects for surface manipulation | 39 |
| Table 3: | Settings of the different plane patch filters used for MSA tests | 45 |
| Table 4: | Resulting errors of the initial coarse registration | 66 |
| Table 5: | Number of data points resulting from the plane patch filter | 66 |
| Table 6: | Example of the MSA registration test: test data 2016, SP01 as model point cloud, SP02 and SP03 as data point clouds, histograms of the residues added in Appendix D | 68 |
| Table 7: | Output of the final registration realized using ICP (CloudCompare). Settings: minimum change of RMS per iteration of 10^{-5} m, final overlap 25%, random sampling limit $5 \cdot 10^6$ points | 77 |
| Table 8: | Co-registration of the point clouds from the different scanning campaigns | 80 |

List of abbreviations

| | | | |
|--------|--|-----------|--|
| ALS | airborne laser scanning | M3C2 | multiscale model to model cloud comparison |
| AM | amplitude modulation | MSA | multi station adjustment |
| C2C | cloud to cloud | PAM | piecewise alignment method |
| C2M | cloud to mesh | PCA | principal component analysis |
| CAD | computer-aided design | PPF1 - 4 | plane patch filter 1 to 4 |
| CANUPO | caractérisation de nuages de points (point cloud characterization) | PRCS | project coordinate system |
| CHM | cropped height model | rad | radian |
| CSM | cropped surface model | RGB | red green blue |
| DEM | digital elevation model | RMSD | root-minimum-square distance |
| DOD | digital terrain model of difference | SC2014 | scanning campaign 2014 |
| DTM | digital terrain model | SC2016 | scanning campaign 2016 |
| EDM | electronic distance measuring | SC2017a | scanning campaign 2017a |
| FDR | Fisher Discrimination Ratio | SC2017b | scanning campaign 2017b |
| FM | frequency modulation | SNR | signal-to-noise ratio |
| GCP | ground control points | SOCS | scanner's own coordinate system |
| GNSS | global navigation satellite system | SOR | statistical outlier removal |
| ICP | iterative closest point | SP01 - 03 | scan position 1 to 3 |
| LDA | linear discriminant analysis | TIN | triangular irregular network |
| LOD | level of detection | TLS | terrestrial laser scanning |
| LS3D | least squares 3D surface | TOF | time of flight |
| M2M | mesh to mesh | TPL | tie point list |

1. Introduction

Referring to BURTON ET AL, a “*hazard results from the interaction of a natural and a social system*” (BURTON ET AL 1978: 19). Natural hazards can therefore be defined as “*all atmospheric, hydrologic, geologic [...], and wildfire phenomena that, because of their location, severity, and frequency, have the potential to affect humans, their structure, or their activities adversely*” (DEPARTMENT OF REGIONAL DEVELOPMENT AND ENVIRONMENT, EXECUTIVE SECRETARIAT FOR ECONOMIC AND SOCIAL AFFAIRS ORGANIZATION OF AMERICAN STATES 1990: 24). According to the the World Disaster Report 2016, more than 108 million people were affected by such events in 2015, and summing up the annual reports, more than 1.9 billion people in the decade from 2006 to 2015 (SANDERSON AND SHARMA 2016).

1.1 Background and problem statement

In mountainous regions, gravitative processes like landslides, mudslides, rock falls, rock slides or snow avalanches are decisive hazardous events (GRACHEVA AND GOLYEVA 2009). For damage prevention, it is important to be aware of the occurrence of these processes and include them to spatial planning and development (GLADE AND RUDOLF-MIKLAU 2015, PROMPER AND RUDOLF-MIKLAU 2015). Especially rock falls, occurring not only in natural mountainous regions but also in artificial excavations and along road cuts (CROSTA ET AL 2015) and are widespread phenomena in Austria with a strong impact on infrastructure even claiming lives (ORF 2017a-h, ORF 2018a-f). In general, rock fall is understood as an extremely rapid type of landslide: a mass of rock is detached along rock discontinuities and free-falls and bounces or roles down a steep slope (VARNES 1976, WHITTOW 2000, BOURRIER ET AL 2012, HUNGR ET AL 2014). To reduce the risk that comes with rock fall events, sectoral planning based on hazard analysis and risk management provide useful approaches (CLOUET ET AL 2012, GLADE AND RUDOLF-MIKLAU 2015). For the estimation of risk and for a substantial base for monitoring and taking protective measures like installing rock fall nets nets or building rock fall galleries to minimize the effect rock falls, a documentation of occurred events

is essential (BMLFUW IV/5 2016). While big events, especially with damage to infrastructure or harm to persons, are usually well-documented (e.g. HÜBL ET AL 2002), also small events with no direct influence on humans or infrastructure are of interest for monitoring, risk estimation and rock fall modelling. Moreover, with detection of small scale rock falls in centimeter range, active areas can be identified. Therefore, it is essential for comprehensive studies to find possibilities to detect rock falls of all scales.

Technical development during the last decades provides various methods for detection of surface changes which comes along with rock fall or other gravitational movements (ABELLÁN ET AL 2016). One method that offers a possibility of rapid and highly accurate surface recording and, when retaken, detection of surface changes, is the use of terrestrial laser scanning (TLS). Laser scanning or LiDAR (Light Detection and Ranging) is defined as an active photogrammetric procedure using laser ranging for distance measurement. In regular vertical and horizontal resolution, an object of interest is scanned and geometric information is derivated (ENGSTRÖM AND JOHANSSON 2009). From close range 3D object recording to large scale topographic mapping, laser scanning has revolutionized the acquisition of 3D data since the 1990s. A basic distinction between airborne laser scanning (ALS) and terrestrial laser scanning (TLS) is made (KRAUS 2004). Within the last years, TLS, next to other remote sensing techniques, developed into an important instrument of all kind of natural hazard risk management approaches (METTERNICHT ET AL 2005, JABOYEDOFF ET AL 2012, COROMINAS ET AL 2014, KROMER ET AL 2017). Facing recent developments of TLS, the technique is constantly getting more rapid and more efficient: scanning frequencies and range capabilities are rising, additional information like multiple or full-wave echoes or intensity values are included in the scanning data and high-resolution images allow coloring of the point cloud which gives the opportunity to various data analyses (BARBARELLA AND FIANI 2013a, PIROTTI ET AL 2013).

TLS appears as an ideal approach for detection of surface changes. Hence, a detailed evaluation of the method for small scale change detection in rockfall endangered is necessary to give a profounded statement concerning its application in this field.

1.2 Objectives and research questions

This thesis is embedded in the NoeSLIDE project managed by the ENGAGE working group of the Institute of Geography and Regional Research, University of Vienna, in cooperation with the Provincial Government of Lower Austria and the Geological

Survey of Austria. The main objective of this overall project is a detailed long-term landslide monitoring of six locations in the districts Waidhofen and der Ybbs, Amstetten and Scheibbs in the southwest of Lower Austria.

Within this project, the following thesis is dedicated to the evaluation of the application of TLS for detection of small scale rock fall events focusing on a sub-decimeter range of rock surface changes. Therefore, the Amtmann, a 40 m high freestanding rock formation in the village Kreilhof in the municipal district of Waidhofen an der Ybbs, one of the six locations within the NoeSILDE project, is chosen exemplarily as area of interest. Using the data of four different scanning campaigns performed within four years, the process from acquisition, preparation and analysis of TLS data is examined. The focus of the thesis lies on the evaluation of different point cloud registration methods and change detection approaches. Achievable accuracies, usability and limitations of propriatory and open source software as well as challenges in data processing are examined. Considering these aims, the following main research questions are postulated for guiding further steps:

RQ1 What point cloud registration methods provide the most accurate and efficient approach (regarding usability and processing) for the research area?

The first research question refers to the necessity of relating different point clouds within one scanning campaign and between several scanning campaigns for further data processing and data analyses. Depending on the study site and the scanning process, there are different possibilities of point cloud registration. Also, different software packages offer various approaches.

RQ2 What methods of surface change detection using TLS data serve the requirements of the research area best?

Such as in point cloud registration, also various methods of change detection using point cloud data are available. The approach to answer the second research question pursues the research of available change detection methods, evaluation of different methods considering recent scientific publications and testing chosen approaches on the collected point cloud data.

RQ 3 What magnitudes of change are detectable using the TLS under the given environmental conditions in the study area?

As numerous parameters influence the capabilities of TLS systems, it is not possible to specify general change detection accuracies. The third research question applies to estimation of magnitudes of change for the research area in order to give references for similar regions and TLS settings.

RQ4 Which recommendations can be given for future scanning campaigns with regard to data analyses for the study site and comparable areas?

As the thesis in general is addressed to a methodological evaluation of the TLS process, a detailed report on the various methods and the workflow is one major output. The fourth research question outlines the gathering of the experience gained within the whole data collection and data processing procedure.

1.3 Thesis outline

This master's thesis is based on physical principles of laser ranging, the development of TLS, a presentation of registration and change detection methods and an overview of recent applications of TLS, which are presented in Chapter 2. After this general introduction, Chapter 3 includes a description of the data used within the thesis and a presentation of the methodology: the data process workflow is summarized and a detailed description of the chosen methods is given. In Chapter 4, the research area is presented briefly with a short introduction on the characteristics of the physical environment as well as an overview of surrounding infrastructure, documented rock fall events and related investigations. The results of the research are stated in Chapter 5 followed by a detailed discussion of the results and the postulated research questions in Chapter 6. In Chapter 7, conclusions from the results and the research process are drawn and the findings are integrated into a broader context. In the final Chapter 8, an outlook on future perspectives and possibilities of TLS in small scale rock fall detection is given.

2. Change detection using terrestrial laser scanning

When speaking about detection of change, the methodology is based on the very fundamental principle of measuring distances. Measuring in general is one basic principle of empirical science. When thinking about measuring in natural sciences and engineering, one of the most important disciplines is physical metrology, which includes measuring devices based on physical principles used within clocks, thermometers or scales (MESCHEDE 2015). An important sub-discipline of physical metrology is optical metrology. By exploring the microcosmos using microscopes or the macrocosm using telescopes, optical metrology makes a key contribution to the science from the 16th and 17th century (DONGES AND NOLL 2015) until present. In the following Chapter, the concepts of optical metrology for measuring distances using the wave characteristics of a laser beam are presented. Further, the development of TLS is introduced, followed by a review of point cloud processing methods and recent applications of change detection using TLS.

2.1 Physical basics of electromagnetic waves and laser

An electromagnetic wave is defined as a transversal wave and characterized by its wavelength (which is indirect proportional to its frequency) and its amplitude (MESCHEDE 2015). It is made up of photons of no mass and the energy is proportional to the wavelength (HERITAGE AND LARGE 2009b). Graphic representations of electromagnetic waves are shown in a coordinate system with time on the x-axis and the amplitude on the y-axis as seen in Figure 1. The wavelength λ is determined by a whole cycle of the wave, which can further be divided in different phases (angles) measured in radian (rad) with 2π as a full wave cycle (MESCHEDE 2015). Physically, electromagnetic radiation shows behavior of both, waves and particles (HERITAGE AND LARGE 2009b), but in the following chapter, the model of waves for electromagnetic

radiation is used. For more information on theory of light, the interested reader is referred to Chapter 14 in MESCHEDE (2015).

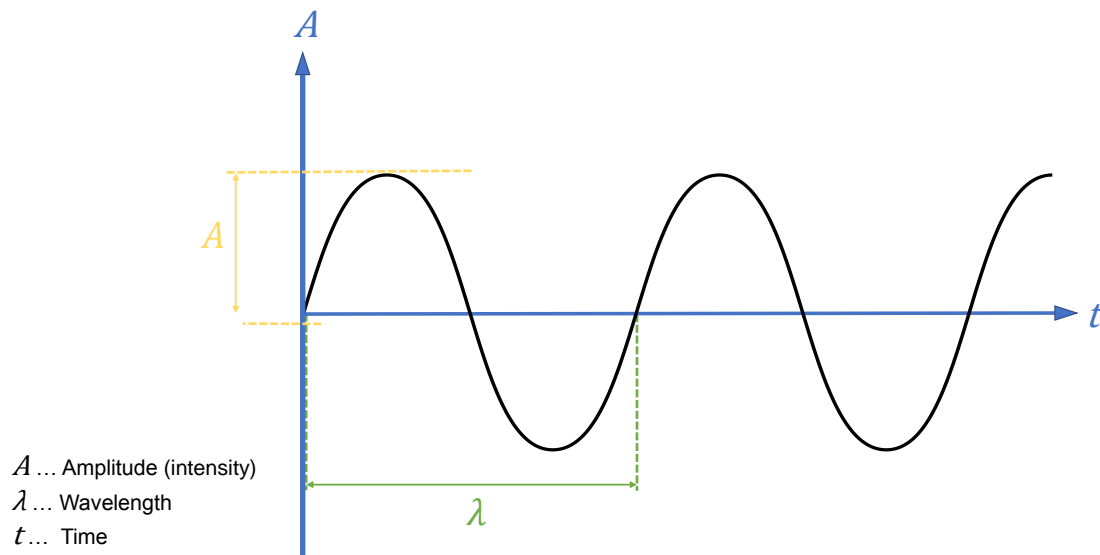


Figure 1: Model of an electromagnetic wave

Originating from Maxwell's equations on electric and magnetic fields (MAXWELL 1864), the existence of electromagnetic waves which propagate with the speed of light was theoretically predicted and later empirically detected by Heinrich Hertz in the 1880s (MESCHEDE 2015). Visible light was recognized as a special case of an electromagnetic wave in the small range from 0.4 μm to 0.8 μm wavelength (DONGES AND NOLL 2015). The general spectrum of electromagnetic waves is shown in Figure 2. Natural light is a mix of electromagnetic waves with a variety of wavelengths and is emitted along random trajectories. When the light strikes an object, the radiation is, depending on the surface characteristics, partly absorbed, transmitted and reflected. What wavelengths are absorbed and what are reflected within the visible spectrum defines the color of the object. The reflected part of the radiation is of interest for all kinds of optical metrology. Depending on the surface, there are different kinds of reflections which are shown in Figure 3: specular reflectance is the reflectance of radiation in a single direction, which happens when the roughness of the surface is smaller than the wavelength of the radiation. In this case, no radiation returns in the direction of the source. When the roughness of the surface is greater than the wavelength of the incident radiation, the reflection is diffuse and depends on the angle of incident and the arrangement of roughness on the surface. For most natural

environments, a combination of both reflectance types (mixed) is found. (HERITAGE AND LARGE 2009b)

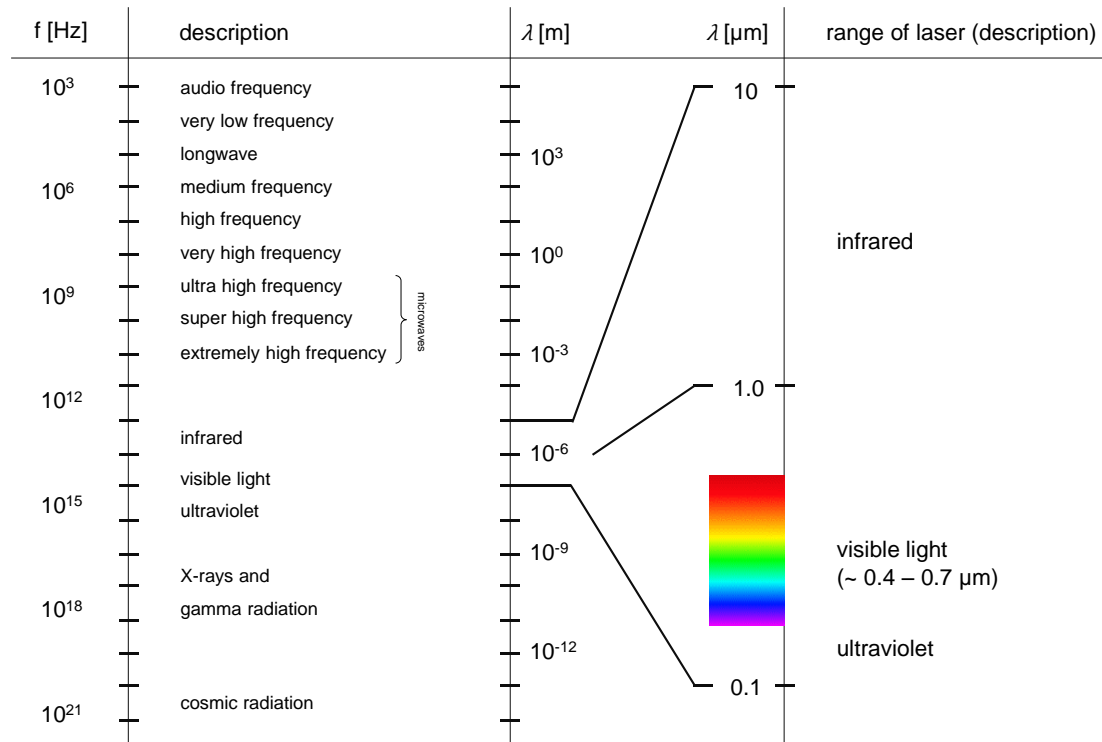


Figure 2: The range of the electromagnetic spectrum (after HERITAGE AND LARGE 2009b: 22)

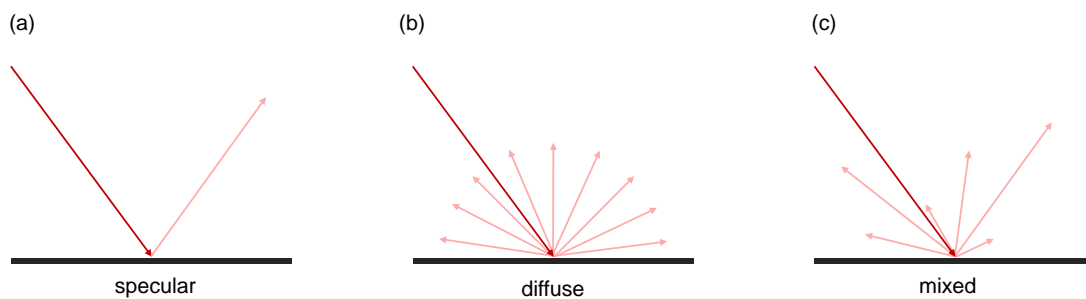


Figure 3: Surface reflection types: (a) specular, (b) diffuse, (c) mixed. (after HERITAGE AND LARGE 2009b: 23)

Based on Einstein's approaches of quantum theory of radiation (EINSTEIN 1916) and the theoretical framework on infrared and optical masers of Schawlow and Townes (SCHAWLOW AND TOWNES 1958), in 1960, Maiman created a monochromatic radiation

2. CHANGE DETECTION USING TERRESTRIAL LASER SCANNING

with a wavelength of 6943 \AA ($0.6943 \text{ }\mu\text{m}$) by optical pumping using a ruby as the active material (MAIMAN 1960). This is known as the first realization of a laser (DONGES AND NOLL 2015).

To generate laser light, a light source is used to excite electrons of the laser source into a higher energetic state. The excited atomic structure is unstable and therefore emits energy as a photon as the electron returns to its original state. When the emitted photon strikes another excited atom, another photon of the same wavelength and direction is emitted. The photons are reflected within the laser source where the emission of more photons of the same wavelength and direction continues, while the so generated radiation of same wavelength and direction is only allowed to exit the laser source through one end as highly coherent and low divergence **Light Amplified by Stimulated Emission of Radiation** – as a **LASER**. Besides the use of a ruby as a solid-state laser material, the variety nowadays includes gas lasers, dye lasers or semiconductor diode lasers. (HERITAGE AND LARGE 2009b)

Laser radiation is characterized by a wavelength from $0.1 \text{ }\mu\text{m}$ to $1.0 \text{ }\mu\text{m}$ and is represented by a plane harmonic wave. A plane harmonic wave is described by five independent parameters: intensity, phase angle, direction of propagation, wavelength and direction of polarization. (DONGES AND NOLL 2015)

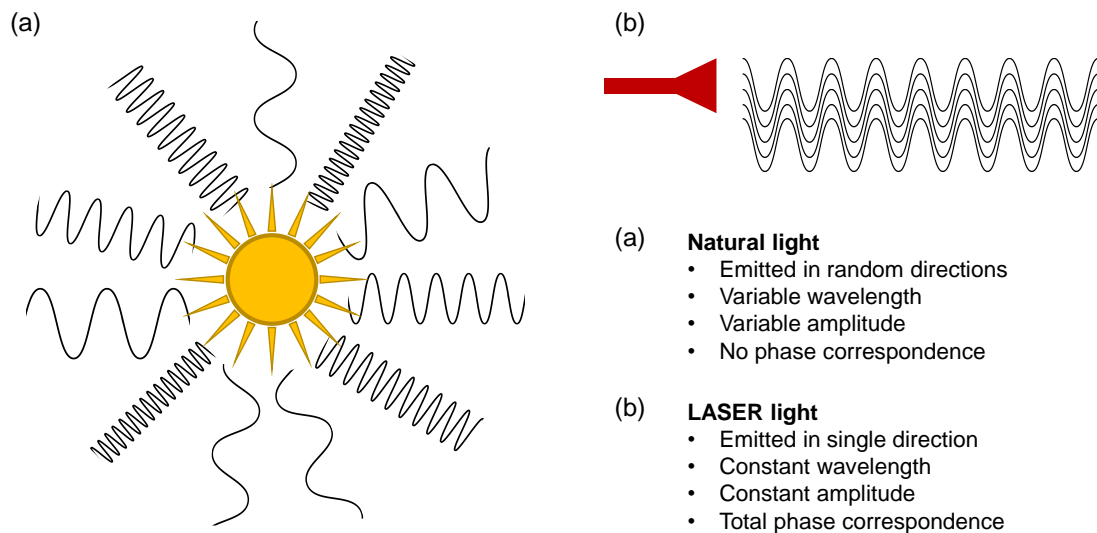


Figure 4: Comparison of the radiation of natural light (a) and a laser (b) (after HERITAGE AND LARGE 2009b: 25)

Comparing a laser beam with natural light (white light), the light beam emitted by a laser is coherent, in phase, emitted in one single direction and practically monochromatic with a well-defined energy and frequency and wavelength, whereas white light is broadband over many wavelengths and amplitudes with no phase correspondence and emitted in a spatially isotropic way. (HERITAGE AND LARGE 2009b, DONGES AND NOLL 2015) Figure 4 illustrates these differences.

Lasers are broadly used, for example in communication technology, material processing, medicine, data storage, environmental monitoring, laser ablation or laser additive manufacturing. Due to special characteristics, lasers are also versatile measurement tools. Selected applications are routine testing in manufacturing processes, quality assurance, recycling technology, biotechnology or medical technology. Laser measurement technology is characterized by its high flexibility, the high measuring speed, high precision and the possibility of non-contact measurement. (DONGES AND NOLL 2015) Following, different concepts of distance measurement using laser beams are presented.

2.2 Concepts of distance measurement using a laser

As a fundamental property, light waves travel with a finite and constant velocity depending on the given medium. Measuring the time delay of light travelling from a source to a reflective surface and back to the source gives a very convenient way to calculate the distance between the source of light and the reflecting surface. Laser ranging is therefore based on the relation of velocity, time and distance which is displayed in the following formula:

$$l = \frac{\Delta t \cdot c_n}{2}$$

l ... measured distance

Δt ... transit time

c_n ... speed of light in the propagation medium

(Equation 1)

The speed of light in a vacuum is currently defined as $c = 299\,798\,458$ m/s. Depending on the propagation medium, the velocity must be adapted by dividing c by the correct refractive index n . The refractive index of atmospheric air depends on temperature, pressure and humidity and is about $n \approx 1.00025$. (BERLADIN ET AL 2010, DONGES AND NOLL 2015)

There are different approaches to measure or calculate the transit time or the distance which are presented in the following subchapters.

2.2.1 Pulse based measurement

One way to measure the transit time is the emission of one laser pulse and measuring the time until the echo of a fraction of the pulse returns to the laser scanner. This is also referred to the time-of-flight principle. Therefore, the transit time is directly measured. For the exact determination of the time of flight, a laser pulse is emitted and the detector generates a time-tagged trigger pulse when detecting the echo depending on the implemented criterion. Different detection methods are peak detection, where a trigger pulse is set at the maximum amplitude of the echo, threshold detection, where the trigger pulse is generated when the echo exceeds a predefined threshold or constant fraction detection, where the trigger pulse is produced at a preset fraction (typically 50%) of its maximum amplitude. (BERALDIN ET AL 2010, DONGES AND NOLL 2015)

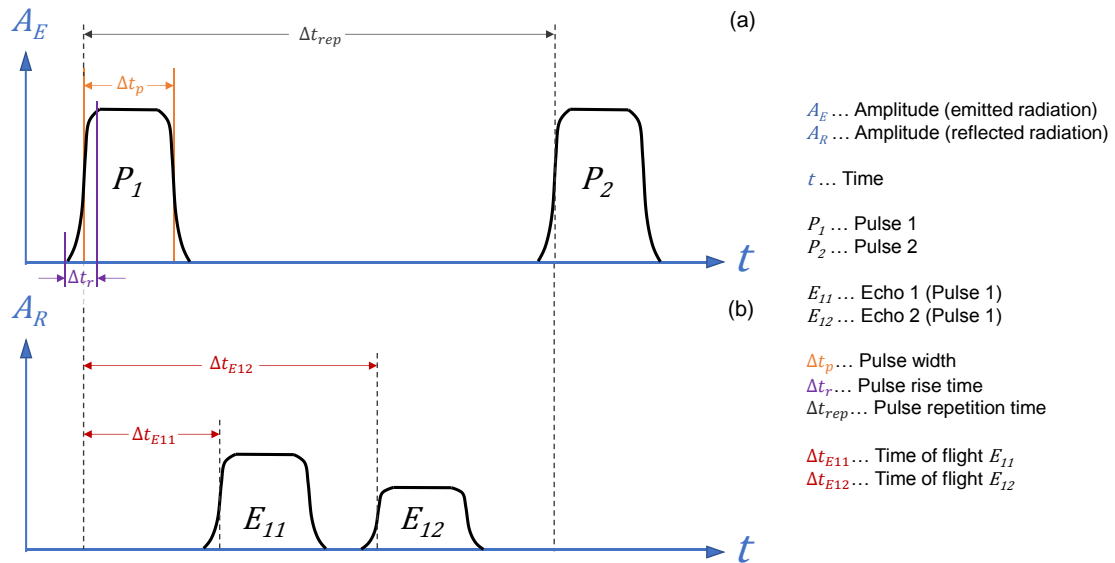


Figure 5: Pulse characteristics of emitted pulse (a) and received echoes (b) measurement (after BERLADIN ET AL 2010: 4)

Due to site characteristic (e.g. vegetation), one pulse can lead to multiple echoes. Depending on the distance, multiple echoes can be captured. The minimum distance for two different echoes E_1 and E_2 to be detected is calculated by using the pulse width Δt_p . For discrimination of different surfaces covered by one pulse, it is

necessary that the echoes do not overlap, which means that $\Delta t_2 > \Delta t_1 + \Delta t_p$ (Δt_1 and Δt_2 being two different measured transit times from the two different echoes resulting from one pulse). Transforming the relation and using Equation 1, two echoes can only be discriminated if their distance is larger than half of the pulse length l_p . A pulse width of $\Delta t_p = 5$ ns therefore corresponds with an echo discrimination distance of 0.75 m. In Figure 5, the principle is visualized. (BERALDIN ET AL 2010)

Due to white noise, a measuring distance using single pulse includes uncertainty. This uncertainty can be estimated with the following equation:

$$\delta_{r-p} \approx \frac{c_n \cdot t_r}{2\sqrt{SNR}}$$

δ_{r-p} ... range uncertainty for a single pulse
 c_n ... speed of light in the propagation medium
 t_r ... rise time of the laser pulse (see **Figure 5**)
 SNR ... signal – to – noise ratio

(Equation 2)

The signal-to-noise ratio is the dimensionless relation of power of the signal to the power of the noise. (BERALDIN ET AL 2010)

2.2.2 Continuous wave modulation

Next to the use of short laser pulses, also a modulation of a continuous wave is used for distance measurement. The modulation can be applied to several wave characteristics, e.g. amplitude modulation (AM) or frequency modulation (FM). (BERALDIN ET AL 2010)

For amplitude modulation, the amplitude of a laser beam is affected by modulating the intensity. Therefore, a carrier wave is modulated by a measuring wave as seen in Figure 6 (PRICE AND UREN 1989). The transit time is measured indirectly in this concept. By measuring the phase difference $\Delta\varphi$ between the emitted and the collected laser light, the phase difference as fraction of one wavelength can be calculated:

$$\Delta\lambda_m = \frac{\Delta\varphi}{2\pi} \cdot \lambda_m$$

$\Delta\lambda_m$... distance resulted from the phase difference
 $\Delta\varphi$... phase difference in radian
 λ_m ... wave length of the modulated wave

(Equation 3)

2. CHANGE DETECTION USING TERRESTRIAL LASER SCANNING

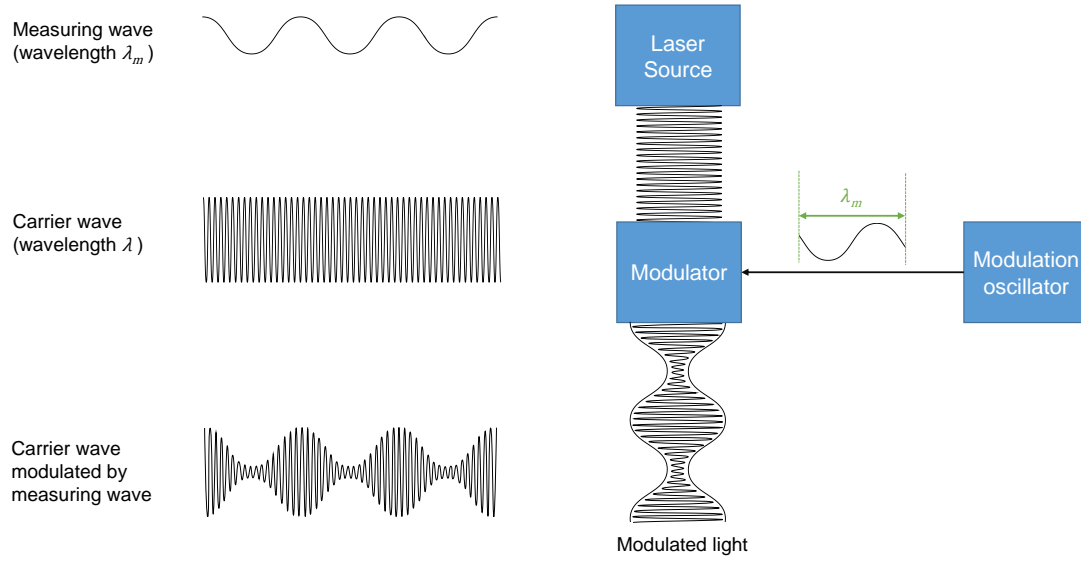


Figure 6: Amplitude modulation of an electromagnetic wave (after PRICE AND UREN 1989: 167)

The range uncertainty can approximately be calculated by

$$\delta_{r-AM} \approx \frac{1}{4\pi} \cdot \frac{\lambda_m}{\sqrt{SNR}}$$

λ_m ... wave length of the modulated wave
 SNR ... signal – to – noise ratio

(Equation 4)

shown by BERALDIN ET AL 2010. Figure 7 shows the principle of measuring phase differences and where the phase angle is found in the continuous wave.

Translating the graphic representation in a formula, the wanted distance is calculated directly without extraction of the transit time Δt :

$$= \frac{1}{2}(n \cdot \lambda_m + \Delta\lambda_m)$$

l ... measured distance
 n ... integer number of full wavelengths
 λ_m ... wave length of the modulated wave
 $\Delta\lambda_m$... distance resulted from the phase difference

(Equation 5)

By phase comparison, λ_m is known and only $\Delta\lambda_m$ can be measured. For the calculation of the distance, the quantity of full wavelengths n is also required. Coping with this problem is known as resolving the ambiguity. Different methods such as

increasing the measuring wavelength in multiples of ten (PRICE AND UREN 1989) or using multiple frequency waveforms (BERALDIN ET AL 2010) are used.

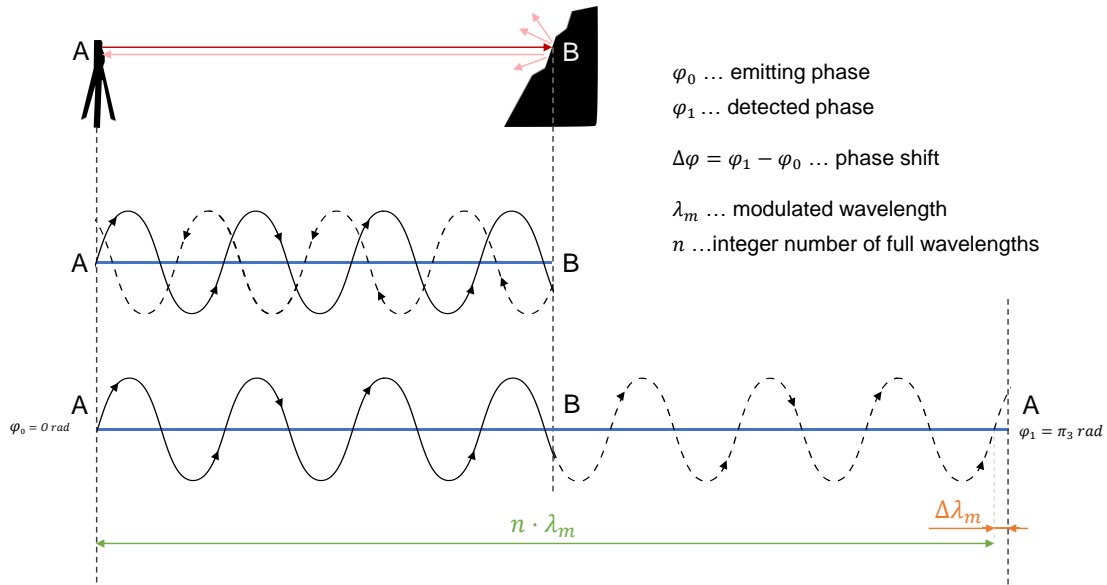


Figure 7: Measuring phase differences of an electromagnetic wave for distance measurement (after PRICE AND UREN 1989: 165)

Comparing pulse based measurement and measurement based on phase modulation, the advantage of pulse based measurement is a larger range capacity while phase-measurement based systems are more accurate and faster in scanning. Therefore, pulse based measurement dominates due to its larger range airborne laser scanning systems (BERALDIN ET AL 2010, WALTON ET AL 2014). When comparing different terrestrial laser scanner, listed in LARGE AND HERITAGE (2009b), there is also a domination of pulse based systems, but with a clear deficiency relating to data collection rate (up to 50,000 points per second in contrast to 500,000 points per second with phase-measurement systems). Including recent product releases of market leaders such as Leica Geosystems or Riegl, the technical development allows data collection rates in the range of several 100,000 points per second (RIEGL 2017) up to 1,000,000 points per second (LEICA 2017) using pulse based measurement.

2.2.3 Other distance measuring techniques

Besides pulse based measurements and continuous wave modulation, there are other techniques for distance measuring using a laser.

Other forms of continuous wave modulations are frequency modulation where beat frequencies are exploited (BERALDIN ET AL 2010) or the use of laser interferometry: Interferometry in general uses the behavior of superimposed waves. (MEINERS-HAGEN ET AL 2009). The basic principle of all laser interferometers works similar: an incident laser beam is split into two (or more) coherent sub-beams. After the sub-beams have traveled along different long optical paths, they are superimposed again and the occurring interference pattern is analyzed to figure out the integer and fractional order of interference to calculate the asked distance. (DONGES AND NOLL 2015)

For short distance measuring (up to 5 m), triangulation-based measurements are often used. Therefore, a laser beam is emitted and the scattered light is collected at a distinct vantage point. Due to a position-sensitive emitter and detector, the projection and the detection angle are known. As the known distance between the emitter and the detector represents the base line of a triangle with two known adjoining angles, the other dimensions of the triangle which represent the distance of interest can be derived using the cosine law. (BERALDIN ET AL 2010)

Besides the indirect measurement of the distance to the object via the transit time, also the amount of power scattered back can be calculated. Of that, detailed information on material can be extracted due to different absorption or scattering characteristics. (DONGES AND NOLL 2015)

2.3 Development and concept of terrestrial laser scanning

After the realization of the first solid state ruby laser in 1960 as described in Chapter 2.1, the period from 1962 to 1968 brought basic development of the technology followed by a period of improvement of the reliability of the technique in the 1970s (LARGE AND HERITAGE 2009b). Geoscience related use of laser technology started with SMULLIN AND FIOCCO in 1962 using laser-generated light with a ruby as a laser source for atmospheric research by emitting a laser beam and detecting the backscatter. First applications for terrestrial use started with recognizing the potential of a laser as an alignment instrument by giving a reference direction with a narrow, straight beam. For distance measurement, the theodolite was the most extensively used and versatile instrument before the development of measuring instruments using electromagnetic radiation (LARGE AND HERITAGE 2009b). By measuring angles in horizontal and vertical planes alignments are made and distances are calculated by spatial intersection or resection (KAHMEN 2006). The benefits of using a laser for

distance measurement – so-called electronic distance measuring (EDM) – are discovered soon. In early instruments of EDM, reflectors are necessary to perform measurement. Therefore, only selected distinct points are measured (SHAN AND TOTH 2009). Further on, EDM is proved as an efficient and reliable way of data collection for the creation of a digital elevation model (DEM) (LARGE AND HERITAGE 2009b). After the development of reflectorless distance measurements in the mid-1990s, devices for not only surveying distinct points but for profiling and scanning of are built (SHAN AND TOTH 2009).

First terrestrial laser scanners are built in the early 1990s for robot navigation to detect obstacles in the vehicle's path and to locate the robot on a map. This is referred to as laser radar (ladar) (SINGH AND WEST 1991, HANCOCK ET AL 1998). Also, the possibilities of terrestrial laser scanning for 3D modelling of real world structures such as sculptures (BERALDIN ET AL 2000) or industrial applications such as plant design verifications (SEQUEIRA AND GONÇALVES 2003) are discovered soon after. After the rapid development of the terrestrial laser scanning technology including improvement of the maximum distance in the late 1990s and early 2000s, the applications of TLS increased including the creation of 3D models of large surfaces in field like architecture, archaeology and topography (ABELLÁN ET AL 2006) and TLS is also implemented in monitoring of natural hazards like volcanoes (HUNTER ET AL 2003) and landslides (ROWLANDS ET AL 2003, BITELLI ET AL 2004).

2.3.1 The concept of scanning profiles and surfaces

To create a profile using EDM, a series of closely spaced points located adjacent to one another along a line on the terrain is measured. For a two-dimensional profile, distances from the laser ranger to the points and the angles between the points are measured. The profile (the elevation differences) can be derived from this data by using simple trigonometry. The principle of laser profiling is especially used in airborne or spaceborne applications. (SHAN AND TOTH 2009)

Adding a second direction of motion provides a laser profiler with the ability to not only determine elevation values along a line but to scan an area of the terrain. This expands the functionality of a laser profiler to a laser scanner. The vertical motion, which is given by a rotating mirror or prism is extended by a controlled motion in the azimuth direction, usually by implementing a motor drive. From this, position and elevation data for the creation of 3D models of the scanned terrain are provided. (SHAN AND TOTH 2009)

2. CHANGE DETECTION USING TERRESTRIAL LASER SCANNING

The concept of a terrestrial laser scanner is, as already discussed, based on a fixed scanning platform and deflection mechanisms which allow the scanner to adapt the horizontal and vertical angles of the beam emission. Addressing the model shown in Figure 8, the laser beam is generated in the range finder electronics unit (1) and emitted towards the polygonal mirror element (3) which is rotating at relatively high speed. On the surface of the mirror, the laser beam (2) is deflected by the changing vertical angle ζ . Using the concepts of distance measurement described in 2.2, the distance l between the scanner and the scanned surface is measured for each point. After the scanning of a vertical profile line, the whole upper part (4) of the device rotates through a small angle α to record the neighboring ζ -profile. The results of the process are point-based spatial data provided in polar coordinates α , ζ and the measured distance l . The exportable data is usually provided in three-dimensional cartesian coordinates with xyz-coordinates for each point. (KRAUS 2004)

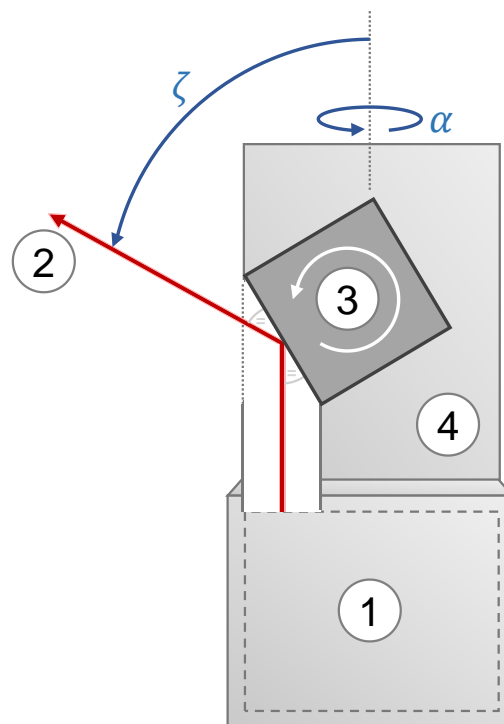


Figure 8: The principle of a terrestrial laser scanner (Riegl) (after KRAUS 2004: 472)

For creating a 3-D model, an object is usually scanned from different measurement positions with an overlap of the point clouds. Connecting the point clouds from several

scan positions to one cloud in one coordinate system is called registration of the scans. Different methods including tie points or registration algorithms like ICP (iterative closest point) are discussed in Chapter 2.4.1. In a further step, the point cloud can be transferred from the local coordinate system to a global coordinate system by georeferencing. (KRAUS 2004)

2.3.2 Specifications of a terrestrial laser scanner – the RIEGL VZ 6000

To get an idea about the technical specifications of a scanner, the RIEGL VZ 6000 (shown in Figure 9), the terrestrial laser scanner used for the surveying of thesis, is presented. All the following information are presented in the Riegl VZ 6000 data sheet (RIEGL 2017).



Figure 9: Classical scanning setup: The Riegl VZ 6000 laser scanner on a tripod connected to a laptop and a differential GNSS.

2. CHANGE DETECTION USING TERRESTRIAL LASER SCANNING

The Riegl VZ 6000 is classified as a Class 3B Laser Product according to IEC 60825-1:2014. Class 3B laser radiation is “*hazardous to the eyes and in special cases also for the skin. Diffuse scattered light is safe usually*” (DONGES AND NOLL 2015: 39). The measuring principle is pulse based measurement (described in Chapter 2.2.1) with single pulse ranging mode of operation. The laser scanner operates with near infrared radiation. Scans can be performed within a field of view of 60° vertical and 360° horizontal.

Depending on the pulse frequency, the range of the laser scanner is up to 6000 m and can reach performances shown in Table 1.

Table 1: Range measurement performance of the Riegl VZ 6000 (RIEGL 2017)

| | | | | |
|--|---|---------|---------|---------|
| Laser pulse repetition rate | 30 kHz | 50 kHz | 150 kHz | 300 kHz |
| Effective measurement range (meas./s) | 23,000 | 37,000 | 113,000 | 222,000 |
| Max. measurement range (average conditions, ambiguity to be resolved by post processing) | | | | |
| Natural targets with reflectivity > 90% | 6,000 m | 6,000 m | 4,200 m | 3,300 m |
| Natural targets with reflectivity > 10% | 3,600 m | 3,600 m | 2,400 m | 1,800 m |
| Max. number of targets per pulse | Practically unlimited (laser power is split according to the targets) | | | |

Under test conditions of 150 m distance from the scanner to the object of interest, the accuracy, which is in this context defined as the degree of conformity of a measured quantity and its true value, is 15 mm and the precision (the reproducibility) is 10 mm. The laser beam has a diameter of 15 mm at the exit and a divergence of 12 mrad with the result of 12 mm beam diameter increasing per 100 m distance. The angle measurement resolution is defined by the selection of the angular step width $\Delta\alpha$ horizontal and $\Delta\zeta$ vertical (see Figure 8) of $0.002^\circ \leq \Delta\alpha \leq 0.28^\circ$ and $0.002^\circ \leq \Delta\zeta \leq 3^\circ$.

Besides the creation of 3D-data, also images with a resolution of 5 megapixels can be taken during a scan which can be used to color the point cloud by assigning RGB-values to every single point. The Riegl VZ 6000 can also digitize the echo signals to create full waveform data for echo waveform analysis. For scanning campaigns, the laser scanner is fixed and positioned on a tripod and can either perform the scans as a stand-alone device or connected to a laptop.

To give a glimpse of the speed of progress in the development of terrestrial laser scanners, pioneer TLS surveys took place at the end of the 1990s / beginning of the 2000s with a device designed by Riegler which is able to scan 4 points per second on a 10 m range and one point per second on a 2 km range with an accuracy of ± 25 mm. (PAAR ET AL 2000, SCHEIKL ET AL 2000, HUNTER ET AL 2003)

2.4 Processing of terrestrial laser scanning data

To promote the use of point cloud data for change detection, appropriate data analysis techniques and workflows are necessary (WALTON ET AL 2014). After data acquisition using a terrestrial laser scanner, the data must be processed for further use. Depending on the field of application, the scale, the possibilities on the scanning sight and accuracy requirements, different processing approaches are suitable. In the following chapter, different ways of registration of point clouds, filtering of point cloud data and change detection using TLS data are presented.

2.4.1 Registration of multiple scan positions

The survey of an object of interest often needs several scans from different positions to get comprehensive data. For each scan, a new local coordinate system is generated. For further processing, the scans need to be combined using one common coordinate system. This process is called registration of the scan positions (GRUEN AND AKCA 2005, CHARLTON ET AL 2009, LICHTI AND SKALLOUD 2010). The aim is to transfer point clouds from the scanner's own coordinate system (SOCS), which is individual for each scan position, to the project coordinate system (PRCS). The SOCS defines coordinates with respect to the scanner's center of rotation mechanism. The PRCS is defined arbitrarily (RIVEIRO ET AL 2011). Usually, one of the SOCS is determined as the PRCS. Besides the registration of different scan positions to compose one point cloud for an object of interest, it's also necessary to co-register scans of different epochs for multitemporal point cloud analysis. The point clouds from different epochs are not merged to a single cloud but must be in the same coordinate system. Besides co-registration, also the position and the orientation of the scanner can be fixed to compare scans from different epochs (LINDENBERG AND PFEIFFER 2005).

To transform coordinates from one coordinate system to another in 3D space, the Helmert transformation, which belongs to the group of similarity transformations, is used. The transformation is based on seven transformation parameters:

- Three translations T_X , T_Y and T_Z in direction of the coordinate axes
- Three rotations ω_X , ω_Y and ω_Z
- A scale factor q

With these parameters, whose geometrical application is shown in Figure 10, the transformation can be performed (KAHMEN 2006). Theoretically, for the registration of two point clouds, it's only necessary to identify three identical non-collinear points in both point clouds but in practice there is a need of at least an extra fourth or fifth point to find a unique solution and even more points for an acceptable precision (HASHEMI ET AL 2013, MUKUPA ET AL 2017). The most commonly used quality control factor is the root-mean-square difference (RMSD) (CHARLTON ET AL 2009). There are different approaches for determination of the registration parameters which are presented following the differentiation of LICHTI AND SKALOUD (2010) in target-based registration, iterative closest point methods and feature based registration. MUKUPA ET AL (2017) present a good overview in a recent review paper.

One possibility to register different scan position is to look for distinct points which can be clearly identified in different scans, so-called target points. The points can either be artificial or natural. As artificial points, reflective targets can be installed in the scanning area. Due to the characteristic reflection, it is possible to clearly identify the targets in the scans. Usually, they are scanned in a high resolution for accurate positioning. Examples for targets are round or square patches of reflective material or solid reflective geometrical objects like cylinders (CHARLTON ET AL 2009, MUKUPA ET AL 2017). This procedure is often only one part of the registration process. The coarse target-based registration is usually followed by a fine statistical alignment (LIM ET AL 2005, ROSSER ET AL 2005).

Fine alignment methods are based on algorithms. The first landmark registration method, which is also used in concepts of change detection, is the Iterative Closest Point (ICP) algorithm and was developed by BESL AND MCKAY (1992) and similarly applied by CHEN AND MEDIONI (1991) and ZHANG (1994). The ICP searches pairs of nearest points in two point clouds and estimates parameters for a transformation which aligns them. The transformation is then applied on one point cloud and the procedure is iterated until convergence. The aim is to minimize the sum of the quadratic distance between all corresponding points. The mathematical assumption behind the algorithm is that one point cloud is a subset of the other point cloud. The ICP requires a coarse registration of the data before the algorithm is used (GRUEN AND AKCA 2005, MUKUPA 2017).

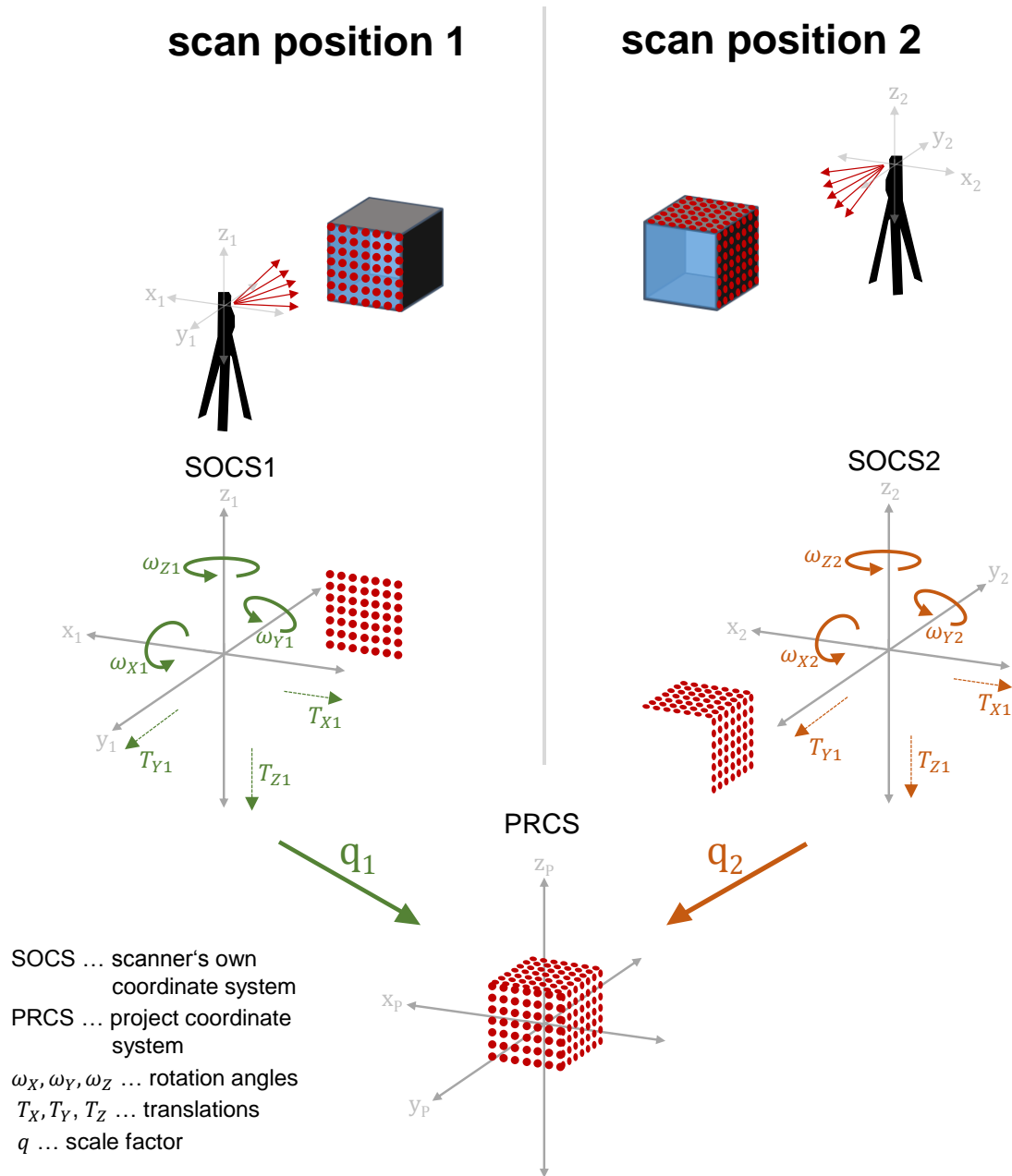


Figure 10: The principle of registration of point clouds: the Helmert Transformation

Based on the ICP, several improvements and adjustments are created (RUSINKIEWICZ AND LEVOY 2001). GRUEN AND AKCA (2005) give a broad review of the research and development on registration algorithms. Recent notable algorithms are the Least Squares 3D surface matching (LS3D) by GRUEN AND AKCA (2005) which was further on used by MONSERRAT AND CROSETTO (2008), the PointReg algorithm by OLSEN ET

AL (2011) or the point-to-plane registration developed by GRANT ET AL (2012). The algorithms are often also used in the process of change detection.

There are also multiple approaches of registration methods using algorithms specialized on distinct geometric primitives found in the scans. Local search algorithms are looking for surface normal vectors, curvature and change of curvature as information for corresponding items. Such approaches are for example presented by DOLD AND BRENNER (2006) using corresponding planar patches, AL-DURGHAM ET AL (2013) using 3D linear features, YANG AND ZANG (2014) using curves as matching primitives, BAE AND LICHTI (2004) using geometric primitives in general or HAN (2010) using hybrid geometric features involving points, lines, planes and groups of points. Besides geometric features, there are also approaches considering image-based (IBR) like presented by AL-MANASIR AND FRASER (2006) or intensity-based tested by the intensity AKCA (2007).

There are several possibilities to perform registration as an end user. Commercial software products like RiSCAN PRO provide different options such as target-based registration or multi station adjustment (MSA) which is based on the ICP algorithm. Also, the open source project CloudCompare, started by Girardeau-Montaut in 2003, gives several opportunities on registration. Another notable open source project for point cloud processing including approaches for point cloud registration is the Point Cloud Library (pcl) with the implemented FLANN registration tool.

Next to transferring several scans into one coordinate system, for some applications, especially concerning geosciences, it is necessary to transfer the data of the registered point cloud to a global coordinate system. This can also be applied on single scans. Georeferencing can be performed directly by a known position of the scanner (using differential GNSS or place the scanner on a known fixed survey point) or based on known ground control points (GCPs) which is equal to the point based registration (ALBA ET AL 2007). As georeferencing is not performed in the following thesis it will not be discussed further, the interested reader may find further information in ALBA ET AL (2007).

After the registration (and georeferencing if necessary), points are attributed with x, y and z data for determination of the location in space in a suitable coordinate system. Optional, additional attributes such as amplitude or echo count are added and furthermore, the data is called a registered point cloud. (BERALDIN ET AL 2010, VOSSelman AND KLEIN 2010).

2.4.2 Filtering of point clouds

According to ABELLÁN ET AL (2014), filtering serves different purposes: removal of extraneous points, isolation of the surface of interest and optimization of the data for further analysis.

For removal of unwanted points (e.g. vegetation), algorithms using geometrical characteristics of the point cloud for classifications are often used. JABOYEDOFF ET AL (2007) use local changes of orientation and inclination of surface normal for distinguishing between several classes. BRODU AND LAGUE (2012) present an approach where the local organization of the point cloud geometry is analyzed at different scales. The classification can be fully automated or customized using training areas within the CANUPO plug-in (CAractérisation de NUages de Points – point cloud characterization) in CloudCompare. Besides geometry, also other point data attributes like intensity and echo number (GOEPFERT ET AL 2008), spectral information from high resolution images (LAU ET AL 2015) or the full waveform analysis of the returning signal (DI SALVO AND LO BRUTTO 2014) are helpful attributes for filtering. In addition to the presented approaches, manual editing is often inevitable (ABELLÁN ET AL 2014).

Besides the extraction of the surface of interest by removing unwanted points, scattering and instrumental error effects on the point cloud are issues that shall be considered. LINDENBERGH AND PFEIFFER (2004) use a maximum root mean square distance (RMSD, see 3.3.2) and a maximum change of the estimated normal vector of neighboring points as exclusion criteria. ABELLÁN ET AL (2009) use a nearest neighbor averaging technique to reduce errors in raw data comparison. Also, octree structures (see Chapter 2.4.3) are used for homogenization point clouds and adapting the density, especially when working with large data sets (CLOUDCOMPARE COMMUNITY 2018, ELSEBERG ET AL 2011, ELSEBERG ET AL 2013).

2.4.3 Concepts of change detection

After the preparatory work of registration and filtering of point clouds, multitemporal change analysis is performed to identify surface changes on an object of interest. LINDENBERGH AND PIETRZYK (2015) give definitions for the terms change detection and deformation analysis: change detection is looking for the binary answer whether the geometric state of a scene has changed or not. If changes are detected, quantification of these changes can be another aim of research. These is described as deformation analysis (LINDENBERGH AND PIETRZYK 2015). Both concepts are of interest in this thesis, but the focus lies on a general binary identification of change – the term change detection is henceforth used for detection of surface changes and

implies the quantification. Also, the term monitoring is often used (TELLING ET AL 2017) which also implies comparing data from different epochs looking for differences.

Traditionally, changes are monitored with point-wise surveying techniques using high precision levelling, total stations or GNSS (global navigation satellite system). Recently, the benefits of TLS which provides high spatial resolution 3D data have gained attention (LOVAS ET AL 2008, MUKUPA ET AL 2017). The technical realization of change detection using TLS point cloud data is based on comparison and computing distances of point clouds acquired at different dates. There are different approaches including direct use of the point cloud data or creating an intermediary model using the point cloud (GIRARDEAU-MONTAUT ET AL 2005, MUKUPA ET AL 2017). The intermediary models can be 3D models like a surface meshed by triangles (e.g. a triangular irregular network – TIN) or a 2.5D model like a digital terrain model (DTM), where the elevation dimension z is referred to a regular xy -grid and visualized as different grey values (TEZA ET AL 2007). In literature, there are different classification of change detection methods: MUKUPA ET AL (2017) and MILL (2016) distinguish three methods: point to point, point to surface and surface to surface change detection. OHLMANN-LAUBER AND SCHÄFER (2011) present a differentiation into five categories: point based strategies, point cloud based models, surface based approaches, geometry based methods and parameter based procedures (WUNDERLICH ET AL 2016). Besides different methods, there are also several output possibilities: volume differences, displacement distances or displacement matrices can be specified (OPPIKOFER ET AL 2008). Several chosen approaches of change detection are presented following.

A common method for change detection, especially on large planar investigation sites in earth sciences, is the calculation of DTMs of difference (DOD). This approach is based on gridding the point cloud data to generate a DTM where the information on surface elevation is stored pixelwise. The height value for one pixel can either be the mean or median of the height of all points within a pixel (binning), the height of the point nearest to the center of the pixel or the height using a previously defined triangular irregular network (TIN). Two DTMs can further be compared pixel by pixel by simply subtracting the elevation values to get distance values for each pixel in the two DTMs (VOSSELMAN AND KLEIN 2010, WHEATON ET AL 2010, LAGUE ET AL 2013). A quite related approach is gridding of a TIN by interpolation. Here, the data is still stored as vector data with the elevation information attributed to the nodes (SCHÄFER ET AL 2004).

GIRARDEAU-MONTAUT ET AL (2005) present the strategy of direct comparison of two point clouds (C2C) by calculation of the Hausdorff distance, which computes for each point in one cloud the distance to its nearest point in the other cloud. The comparison of the point clouds results in a colored visualization of the distances. As already presented in Chapter 2.4.1, Girardeau-Montaut initially developed the open source software CloudCompare and implemented this point cloud based change detection method. Further improvements of the approach include local surface modelling strategies. (GIRARDEAU-MONTAUT ET AL 2005, CLOUDCOMPARE COMMUNITY 2018)

Because of issues finding the real corresponding points using the direct cloud-to-cloud comparison with the closest point technique on surfaces with high roughness, LAGUE ET AL developed the Multiscale Model to Model Cloud Comparison (M3C2) presented in LAGUE ET AL (2013): normal vectors are calculated for core points using a defined neighborhood and point cloud distances are estimated using the mean point position of a defined neighborhood on the surface normals. This distance represents the local change of surface including a local roughness indicator using the standard deviation of the projected points for each cloud. (LAGUE ET AL 2013)

Besides the creation of a DOD or the direct comparison of two point clouds, also a point cloud and a reference 3D mesh created by triangulation of the reference point cloud (or a theoretical model) can be compared. Originating from this approach, also two 3D meshes can be compared (M2M). Such as in C2C, these approaches also use the Hausdorff distance, but calculating the distance of a point to a triangle (CIGNONI ET AL 1998, ASPERT ET AL 2002). This is also applied in point-to-surface difference (C2M) calculation presented by CIGNONI ET AL (1998) and ASPERT ET AL (2002).

For high-precision change detection on a small scale, TSAKIRI ET AL (2006) add artificial targets as control points to the moving area of interest. The points are recognized by the scanning software and so the traditional tacheometric method of surveying distinct points is implemented in the comprehensive modelling of the structure of interest. (SCHÄFER ET AL 2004, ALBA ET AL 2006, TSAKIRI ET AL 2006).

The methods discussed above can be assigned to point based, point cloud based and surface based approaches according to the classification of OHLMANN-LAUBER AND SCHÄFER (2011) and are the preferred approaches point cloud change detection of geoscientific objects with a roughly unstructured surface (NEUNER ET AL 2016). As geometry and parameter based models are not considered in this thesis, they are not discussed further. The interested reader may find further information in OHLMANN-LAUBER AND SCHÄFER (2011), WUNDERLICH ET AL (2016) or NEUNER ET AL (2016).

Another concept of change detection which will not be covered following is the description of the movement of distinct structures using roto-translational parameters as released in MONSERRAT AND CROSETTO (2008).

2.5 Applications of TLS change detection

Change detection using TLS data is currently a quite active field of research. The approaches presented in Chapter 2.4.3 have been directly or modified implemented in many projects. Outdoor applications, which are of interest for this thesis, can be differentiated in monitoring of artificial objects like buildings, dams or tunnels and natural structures (NEUNER ET AL 2016) like slopes, landslides, rock faces or cliffs. As the thesis is committed to the monitoring of a rock structure, the focus is on chosen publications on this topic. For giving an impression on the variety of application of TLS in change detection, also usage in monitoring of artificial structures and other natural surfaces will be discussed. The main interest is on data processing methods of change detection in the different publications.

2.5.1 Monitoring of artificial objects

The monitoring of artificial structures, especially in construction and civil engineering, is traditionally high-precise point-wise surveying as already mentioned in Chapter 2.4.3. Recently, also the use of TLS is gaining interest in change detection of artificial structures.

An early use of TLS data on beam loading is presented by GORDON ET AL (2004): two stationary laser scanners are used to detect the deflection of loaded and unloaded beams. As the scanners are not moved during the experiment, there is no need for referencing. The change detection is performed using control points. Besides direct use of the point cloud, the beams are also modelled geometrically. In another pioneer work SCHÄFER ET AL (2004) use TLS for change detection on the hydropower station of Gabčíkovo on the Danube in Slovakia. The point cloud data is gridded to compare scans of two different epochs. VAN GOSLINGA ET AL (2006) also use interpolation and gridding of the point cloud data for change detection of a bored tunnel, but apply cylindric coordinates for gridding as it fits better to the tunnel surface. BARBARELLA ET AL (2017a) use the creation of DTMs from point clouds and extraction of profile lines from the DTMs for monitoring of airport pavements.

ALBA ET AL (2006) monitor change detection of the dam of Lake Cancano in Italy using multiple approaches. From the point clouds of different epochs, meshes and polynomial surface models are created and compared with each other which can be

described as different kinds of C2M and M2M comparing methods. HAUPT ET AL (2016) also test different change detection method on a gabion wall. Geometric approximation, the M3C2 algorithm for C2C comparing and a block gridding method proposed by ELDING (2009) are used.

LINDENBERG AND PFEIFFER (2005) use pointwise change detection along defined normal vectors and parameterization for planar patches for change detection of a lock. LI ET AL (2012) present an algorithm for point cloud segmentation based on normal vectors to select suitable points for change detection in a subway tunnel. LIEBIG ET AL (2011) use classification of point segments and pointwise change detection for surveying of a motorway bridge.

Monitoring of artificial structures often implies geometrical modelling like fitting structures to geometric primitives like polynomial curves or more complex parametric modelling like adjusting Bézier curves to structures (BUREICK ET AL 2016). GONZÁLES-AGUILERA ET AL (2008) implement this approach in structural monitoring of the large Las Corgotas Dam in Avila, Spain, using radial basis functions. CHMELINA ET AL (2012) use cylindric modelling for tunnel change detection, WALTON ET AL (2014) developed an algorithm to find the best fitting ellipse for monitoring of tunnel cross sections which is also used by WENIGHOFER ET AL (2016). VEZOČNIK ET AL (2009) use quadrics for changes of pillars' axes of underground pipelines. SARTI ET AL (2009) and HOLST ET AL (2014) also use quadrics for parameterizing of the main reflectors of radio telescopes.

For a more detailed overview of recent publications see NEUNER ET AL (2016) and MUKUPA ET AL (2017).

2.5.2 Monitoring of natural structures

The use of terrestrial laser scanning as a primary tool for data acquisition in earth sciences has strongly increased in the last ten years. There are many recent publications using TLS data for monitoring of various applications. The following chapter presents a selection of publications.

An early application of TLS in monitoring of natural structures is presented by HUNTER ET AL (2003) at the Mount Etna, Sicily, Italy: scanning campaigns took place in October 2000. Using a 3-D CAD software package, DTMs are derived from the point cloud. From that, detailed contour maps and cross sections are created. There was no change detection in this study.

A long-term study was published by AVIAN ET AL (2009): Between 2000 and 2008, a rock glacier at Hinteres Langtalkar, Hohe Tauern, Austria, was monitored using TLS in one or two scanning campaigns per year. For registration, stable targets are used. DTMs are generated from the point clouds and further georeferenced. Following, simple difference calculations between the DTMs – DODs – are used for change detection.

A large field of research using TLS is the monitoring of landslides. First uses of TLS for surveying landslides are presented by ROWLANDS ET AL (2003): a shallow landslide in the Cotswolds, England, is scanned. BITELLI ET AL (2004) publish a study in which photogrammetry and TLS are compared on the Cà di Malta landslide near Bologna, Italy. Two scanning campaigns were conducted, one in 2001 including three scan positions and one in 2004 including four scan positions. For registration of the scan positions, reflective targets are used. For co-registration of the point clouds from the different epochs, manual coarse registration and ICP fine registration implemented in PolyWorks software are applied. After filtering, DTMs are created and compared, resulting in a DOD as the final output of change detection. TEZA ET AL (2007) release a modified approach of the ICP for landslide monitoring: the piecewise alignment method (PAM). PAM addresses the problem that the calculation of a global minimum for co-registration using the ICP is problematic when the morphological modifications that have affected the landslide are relatively small. Using PAM, a first landslide model is defined as a reference, and point clouds of following scanning campaigns are divided into sub-areas with a side of a few meters and individually aligned to the reference model using the ICP algorithm. The change detection is later calculated by combining translational and rotational movements. The algorithm is first tested in numerical experimentations and later applied on two test sites located in the North-Eastern Italian Alps affected by high-risk slump type landslides. A recent study is presented by KROMER ET AL (2017): automated terrestrial laser scanning with near-real-time change detection is implemented in monitoring of the Séchilienne landslide close to Grenoble, France. Data was collected in a 30 min interval for a six week period. The whole cloud processing workflow is designed to work automatically to fulfill the near-real time processing aim of the study. After an automatic filtering, the registration is performed by initial alignment using the scan position and fine alignment by iteratively finding repeatable keypoints using the PCL registration application. For change detection, the method described in KROMER ET AL (2015a) is used which is C2C-based and similar to the M3C2 algorithm.

LAGUE ET AL (2013) use the specially developed M3C2 algorithm for TLS-monitoring of the rapidly eroding bedrock of the meandering Rangitikei River canyon, New

Zealand. Five scanning campaigns took place between February 2009 and December 2012. For the registrations, targets mounted on tripods and targets bolted to the bedrock are used. Registration of the single scan positions and co-registration of the different epochs was performed at once. For change detection between the different epochs, the M3C2 algorithm presented in Chapter 2.4.3 is first applied. The algorithm is used in other recent projects: BARNHARD AND CROSBY (2013) compare the M3C2 algorithm and the C2M approach applying the methods to 58 scans of the Selawik retrogressive thaw slump, Alaska. WESTOBY ET AL (2016) survey the interannual surface evolution of an Antarctic blue-ice moraine, Patriot Hills, Antarctica using TLS besides structure from motion using an UAV. Two field campaigns took place within 12 months from December 2012 to January 2014. Registration and co-registration is performed using manual point-matching coarse registration and ICP-based fine alignment. For change detection, the M3C2 algorithm is used. LEYLAND ET AL (2016) use the M3C2 algorithm for monitoring extreme flood-driven fluvial bank erosion using a mobile laser scanner along a 2 km study site on the Mekong River 60 km from Kratie, Cambodia. For co-registration, FLANN mentioned in Chapter 2.4.1 is implemented. MARX ET AL (2017) use TLS for quantifying small-scale vertical movements of the ground surface in Arctic permafrost regions in an area located within the continuous permafrost zone close to Inuvik, Northwest Territories, Canada. Three scanning campaigns with seven scan positions each were performed from June 2015 to August 2016. The scans were registered and co-registered using stable subsidence stations and rods. For the vertical deformation analysis, raster-based approaches with DTMs and point-based approaches using M3C2 are tested.

A different field of research is the use of TLS detecting the growth of plants: MARX ET AL (2016) present a study where TLS data is used as reference data for monitoring the growth of a maize field in Heidelberg, Germany, for management of crop production. The georeferenced crop surface model (CSM) is subtracted from a DEM to calculate a crop height model (CHM). CROMMELINCK AND HÖFLE (2016) created an automatic approach for this aim, tested also on a maize field in Heidelberg, Germany. The registration is automated using the scanner's position and two point reflectors and the ICP implemented in RiSCAN Pro Multistation Adjustment. Like in MARX ET AL (2016), a georeferenced CHM with a resolution of 0.25 m was created.

For further information, a review by TELLING ET AL (2017) gives a summary of the use of TLS in Earth Sciences. JABOYEDOFF ET AL (2012) present especially studies on landslide monitoring using TLS, EITEL ET AL (2016) present studies on natural surfaces with a focus on multitemporal change detection.

2.5.3 Monitoring of rock structures

The earliest found reference of the use of TLS on rock structures is a study by HOBBS ET AL (2002) on coastal recessing at twelve different investigation sites in the UK. Different scans are combined to create a not more specified topographic model of the cliffs. One of the first more detailly described applications of TLS in monitoring rock faces is a comparison of different data bases for creation of a high accurate DTM in the Vall the Núria, a rock fall endangered valley in the Eastern Pyrenees, Spain, by JANERAS ET AL (2004). DTMs are created using airborne and terrestrial laser scanning and compared with a photogrammetricly created DTM. The TLS-created DTM provides the finest resolution (2 m) comparing to ALS (8 m) and photogrammetry from aerial photographs (15 m). Also, ABELLÁN ET AL (2006) present an early study from this study area. In this study, there is also no comparison of different epochs but an investigation on rock fall source areas and creation of a high accuracy DTM for rock fall simulations. For the creation of the DTM, Delauney triangulation and kriging interpolation are used.

ROSSER ET AL (2005) use TLS for measurement of cliff erosion on a cliff in Whitby, North Yorkshire, UK. After co-registration of scans of different epochs using control points, the scanner's position and a minimum square best fit between the coordinate sets proposed BY LIM ET AL (2005), a TIN created from the first scan is defined as the reference surface. The change detection to the point clouds of the following scanning campaigns is performed by comparing the point clouds to the reference surface along a defined normal vector. The study continued and more results are shown in ROSSER ET AL (2007): Monthly scanning campaigns over a period of 32 month are taken, changes are calculated using the M2M approach and visualized on a 0.1 m grid. The aim of the study is the observation of precursory pattern of small rock falls leading to larger failure.

ABELLÁN ET AL (2009) ask if TLS is suitable for detection of millimetric deformation and perform an experiment: a plane, a hemisphere and an irregular form are fixed on a vertical plane and displaced in ranges between 5 mm to 25 mm between different scans from 50 m distance. Change detection is performed by the procedure proposed in ROSSER ET AL (2005). Besides the raw data, also interpolated data created by nearest neighbor averaging is tested. The comparison of the raw data shows significant results from a displacement up from 15 mm, the interpolated data even show good results at 5 mm displacement. The approach is applied to a rock fall event at the basalt cliff at Castellfolit de la Roca, Catalonia, Spain, from September 2006 to April 2007 which shows deformation of the cliff prior to a great failure in April 2007. In ABELLÁN ET AL (2011), the study on the Castellfolit de la Roca was continued.

In another study by ABELLÁN ET AL (2010), a rock face, which is the scar of landslide in Puigcercos, Catalonia, Spain, from 1881 is monitored. The scans from different epochs are co-registered using visual identification of homologous points for a coarse registration and ICP algorithm for fine alignment. For change detection, the approach from ROSSER ET AL (2005) was used again. Furthermore, volumetric calculations are performed using the surface to plane command in Polyworks software. The study site is under ongoing investigation, TONINI AND ABELLÁN (2014) perform a statistical cluster analysis on more than 600 rock fall events on the rock face evolving the change detection method which is based on a k nearest neighbors algorithm with the possibility to remove clutters.

OPPIKOFER ET AL (2008) use TLS for monitoring a large rock fall: the collapse at the eastern Eiger flank in the Swiss alps, where the main event occurred on July 13th, 2006. The distance of slope movements, the volume of the collapse and displacement vectors are derived. The co-registration is performed using manual coarse registration by point pair matching and the surface-to-surface ICP for fine registration. The basic change detection and volumetric calculations are realized by surface interpolation (meshing) and comparison (M2M). The displacement vectors of different rockslide parts are derived by manual identification of corresponding points. Another large rock fall, the Åknes rockslide in Western Norway, is investigated using TLS and presented by OPPIKOFER ET AL (2009). For the co-registration, the same procedure as in OPPIKOFER ET AL (2008) is used. Instead of creating 3D models by meshing, the point clouds are compared directly looking for the nearest neighbor in the reference point cloud. As in the previous study, also displacement vectors and roto-translation matrices are derived to describe the movement behavior.

CORSINI ET AL (2013) present a study on long-range TLS at the Piagneto rock slide in the northern Apennines, Italy. For the reference data set from April 2010, ALS and TLS data is integrated to create a high resolution digital terrain model. The ALS and TLS point clouds are registered using homologous points for coarse registration and the ICP algorithm for fine registration. Also, the co-registration of the two additional point clouds from scanning campaigns in November 2010 and April 2011 is performed this way using reflecting targets installed in stable zones as homologous points and furthermore stable areas for performing the ICP algorithm. For change detection, the point clouds are meshed using the Delaunay triangulation and the distances are computed along local normal vector (M2M).

In a study presented by KROMER ET AL (2015b), the White Canyon of the Thompson River valley, British Columbia, Canada, is surveyed before a 2600 m³ rock slide

occured in June 2013. The aim of the study is to identify rock slope failure precursors. The registration and change detection is implemented using PolyWorks Software: registration by rough manual alignment followed by ICP algorithm, change detection by comparison of average surface meshes along the shortest distance vector. The volumes are calculated using a reference plane.

In more recent studies, the focus from simple change detection using TLS to more complex problems. CARREA ET AL (2015) create a methodology for automatic rock fall volume estimation computing concave volumes for every rock fall event of a lateral scarp which is the supply area of a landslide in La Cornalle, Vaude, Switzerland. The rock fall positions are detected using the approach presented by TONINI AND ABELLÁN (2014). OLSEN ET AL (2015) extend this approach by evaluation of hole filling on point cloud surface modelling with TLS data from study sites in Alaska, acquired in three surveys in summer 2012, 2013 and 2014.

STRUNDEN ET AL (2015) detect 122 rock falls in a study including nine fields campaigns over a period of 18 months in Lauterbrunnen Valley, Switzerland. The software Joint Research Center 3-D Reconstructor 2 is used for registration and co-registration of the point clouds. For further M2M processing, meshes are created. Locations and volumes of the rock falls are detected using the proposed cut and fill algorithm on previously by comparison of photographs identified rock fall regions on interest. The results are correlated with environmental factors like temperature, precipitation and seismicity.

TOMÁS ET AL (2017) combine different geomorphological, geotechnical and geophysical approaches for investigation of rock spreading on an urban slope in Finestrat, Spain. TLS is used for extracting rock discontinuities and evaluating the activity. Over five years from 2011 to 2016, four TLS field surveys are performed. Changes are detected using the M3C2 algorithm on different scales from large changes in a range of 5 m up to small scale change detection in a range of 30 cm.

For a more detailed overview, there are review papers on the topic: besides the already mentioned review of Earth science research using terrestrial laser scanning by TELLING ET AL (2017), ABELLÁN ET AL (2014) present a review paper on TLS of rock slope instabilities.

2.6 Uncertainties and challenges

No physical measurement, howsoever carefully made, is completely free of uncertainties. In scientific measurements, the term error is used for uncertainties that

attend measurements (TAYLOR 1997). To deal with these circumstances, it is necessary to understand where errors originate, minimize errors where possible and quantify the effects of errors on the end results (SCHÜRCH ET AL 2011).

For change detection, the quantification of uncertainties and resulting errors based on assessment of the instrumentation and data processing are essential. The determination of the minimum change that can be detected is based on these errors (OPPIKOFER ET AL 2009). Especially when calculating volumes, the consideration of errors is important, as very small uncertainties in elevation can lead to large uncertainties in volume (SCHÜRCH ET AL 2011). For evaluating uncertainties in point clouds, LAGUE ET AL (2013) identify three main sources:

- Uncertainty of point clouds: position uncertainties are characteristics of the scanning instrument. As discussed in 2.3.2, the range accuracy of the Riegler VZ 6000 is 15 mm and the precision is 10 mm at a range of 150 m under test conditions. Besides the range, there are also uncertainties in vertical and horizontal angular measurement. Also, increased laser footprint size at low incidence angles, variation in surface reflectance, variable point density and multiple reflections cause faulty points in the raw data. Additionally, the point density is lower at the boundaries of the surveyed area because of the distance from the instrument – and it is not trivial to define where the density is sufficiently high to get reliable data. Furthermore, multiple reflections from a single beam and climatic conditions like rain can cause erroneous points which must be filtered.
- Registration uncertainty between point clouds: for registration of point clouds, the two general approaches as discussed in 2.4.1 are using ground control points (GCPs) that are fixed between surveys and cloud matching algorithms. Errors occurring within registration are a complex function of the registration method, the number of scan positions and the scanning instrument characteristics. At overlapping areas with imperfect matching, the registered point cloud separates into distinct layers with each layer belonging to one scan position. The quality of the registration can be assessed by independent control points which are not used for the registration process. In natural environments, the registration errors are typical within a few cm.
- Surface roughness related errors: These errors are results of the difficulty of recondition the same scan position between surveys for scanning the same surface points and shadowing effects due to rough surfaces. Therefore, spatial sampling of rough surfaces is never identical between surveys and even if the

surface did not change, small difference will be systematically measured. These errors can be handled by defining a confidence interval which correctly identifies non-statistically significant distances.

(LAGUE ET AL 2013, SCHÜRCH ET AL 2011, WALTON ET AL 2014, HOLST AND KUHLMANN 2016, BARBARELLA ET AL 2017b)

Also, environmental conditions such as humidity, light conditions or temperature can affect the data quality within the data acquisition process (CHARLTON ET AL 2009). Especially with larger measurement range, environmental parameters are of interest. As the measurement distance within the field survey of the thesis is comparatively small within a range of about 20 m to 100 m, these factors are not taken in account.

Further uncertainties arise from editing the point cloud or the creation of models based on the point clouds. For example, edits like filtering to remove vegetation or other non-surface objects from the data can lead to further uncertainties (BARBARELLA ET AL 2017b). Also, when gridding the point cloud by creating a DTM where one grid cell may contain tens to hundreds of points, finding the optimal elevation for each grid cell is not trivial and results in increasing of uncertainties (SCHÜRCH ET AL 2011).

Evaluations of the accuracy of the points can be performed based on footprint size and resolution. These evaluations are helpful but do not include further processing steps as registration, editing or modelling. It must be considered that the instrument accuracy specification provided by the manufacturers is more a theoretical value, but the precision of the survey and the output product are of other uncertainties. The final accuracy of the point cloud is basically unknown. (BARBARELLA ET AL 2017b)

Besides uncertainties, there are other limits in the use of TLS: there is, although quite large for terrestrial monitoring, a maximum range – recent instrument can perform scans over max. 6 km under optimal circumstances. Furthermore, even after merging scans from several positions, there can still be shadowed areas (occlusions) (ABELLÁN ET AL 2014). Moreover, single measurements cannot be exactly repeated as no explicit points are aimed and publications like TSAKIRI ET AL (2006) use this fact to justify that exact deformation extraction can't be performed using TLS point clouds. There are also limits when considering details: the actual spatial resolution, which governs the level of identifiable detail within a scanned point cloud, is also limited and depends on sampling steps and laser beamwidth (BARBARELLA ET AL 2017b).

Another issue in TLS data processing is the presence of vegetation. Dense vegetation, especially grass, makes distinguishing the true ground surface difficult

(BARBARELLA AND FIANI 2012b). Especially in long range applications, the influence of atmospheric conditions must be considered (HEJBUDZKA ET AL 2010).

Summarizing all the considerations made, there are different error sources which must be considered when performing change detection using TLS and it is necessary for any measurement to know the involving uncertainties. The measured physical quantity of change must be larger than the estimated error (SIMENOI AND ZANEI 2008).

3. Data and Methods

In the following Chapter, the different methods used within the thesis and the provided and collected data are presented. The methods are chosen after a comprehensive review of the methodological approaches used within recent scientific publications (see Chapter 2.4). The workflow, from field work to final data processing, is shown in Figure 11. Within the thesis, for point cloud processing, the proprietary software RiSCAN PRO and the open source software CloudCompare are used. When referring to the software further on, RiSCAN PRO refers to the software version 2.1.1 and CloudCompare to the software version 2.9.1.

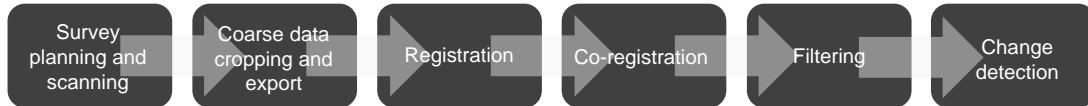


Figure 11: Workflow of point cloud data processing

While in literature (LIM ET AL 2009, ABELLÁN ET AL 2014), filtering is recommended before the registration process (registration and co-registraion), due to software requirements these two steps are changed within the workflow of this thesis. Automatic tie point registration is a useful registration tool provided by the scanner's own software RiSCAN PRO. There is no possibility found to use this tool on point clouds which are preprocessed (filtering) using other software packages. In addition, filtering after registration leads to a homogenous density of the point cloud. Therefore, these two processing steps are switched.

3.1 Field work

Within this thesis, three scanning campaigns are performed. For the scanning, the Riegl VZ 6000 (see Chapter 2.3.2) is used. The campaigns took place on October 24th, 2016 (SC2016) and October 5th, 2017 (SC2017a and SC2017b).

3.1.1 The scanning process

Before starting the scanning campaigns, different scan positions are discussed to allow the best coverage of the area of interest. For the data acquisition, the scanner is fixed on a tripod on a stable underground and adjusted to face the area of interest. The scanning jobs can either be created directly on the GUI (graphical user interface) of the scanner, or the scanner is connected to a laptop and the scanning is performed using the RiSCAN PRO environment. RiSCAN PRO is the accompanying software package for the Riegl VZ 6000 for acquisition, visualization and manipulation of laser scanning data. The program structure is project oriented – all data including scan data, calibrated photographs, information on registration etc. is stored within a single directory structure (RIEGL 2015). For the SC2016 and SC2017a, the scanner is connected to the laptop using RiSCAN PRO infrastructure for the scanning process. The SC2017b was performed using only the scanner and the internal memory. The data is exported later and a project file is created separately.

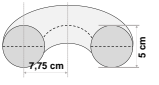
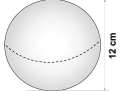

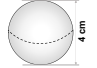
The scanning process starts with a 360° overview scan with low resolution which is shown on the scanner's display. The area of interest is chosen by manual selection in the overview scan and a fine scan is performed. The resolution of the fine scan is chosen in consideration of preventing overlapping footprints but gaining a fine resolution doing a rough estimation of the scanning distance and the therefore expected footprint size. In 2016, 25 reflector patches (tie points) are installed: the flat circular retroreflectors with a diameter of 5 cm were fixed directly onto the upper part of the Amtmann using industrial adhesive. Therefore, after the fine scan, an automated reflector search and reflector fine scan is performed in order to simplify the registration process later on. During SC2014 and SC2016, also images are produced using the scanner integrated camera.

3.1.2 Manipulation of the surface

As no visual changes between 2016 and 2017 are detected, in order to validate the change detection, the surface is manipulated between SC2017a and SC2017b. Inspired by ABELLÁN ET AL (2009), for the manipulation, eight different shapes are prepared. Therefore, polystyrene objects are used. Three different sizes of spheres and one semi-torus are adapted: The objects are cut in half, one half is used in the original geometric form, and the other half is manipulated to get closer to representing a natural surface. The volume of the geometrically original objects is calculated using the diameters, the volume of the manipulated objects is measured by measurement of water displacement, where an accuracy of $\pm 5 \text{ cm}^3$ is reached.

The objects are shown in Figure 12 A, the volume measurement is visualized in Figure 12 B/C. The results of the volume calculation and measurement are shown in Table 2.

Table 2: Dimensions of the objects for surface manipulation

| Object | | Volume [cm ³] | |
|---|------------|---------------------------|------------------|
| | | geometrical half | manipulated half |
|  | semi-torus | 193.6 | 155 |
|  | sphere 1 | 452.4 | 200 |
|  | sphere 2 | 134 | 60 |
|  | sphere 3 | 16.8 | 8 |

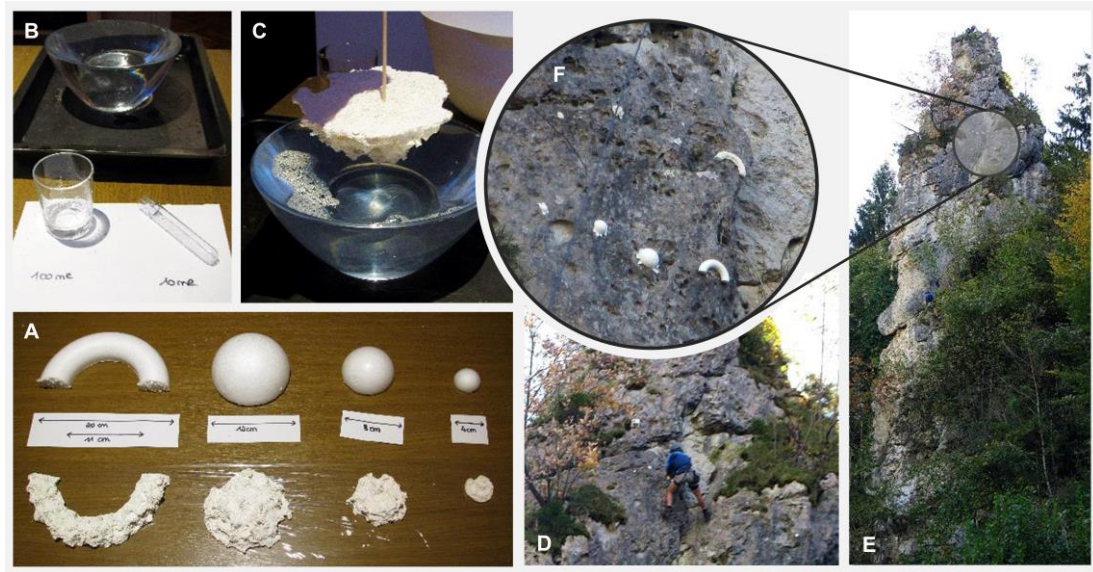


Figure 12: Preparing and performing surface manipulation. A: Polystyrene objects – original and adapted forms. B/C: Measuring the volume of the adapted objects by water displacement. D: Fixing the manipulation objects to the Amtmann. E/F: Manipulated surface.

3.2 Data

The data used in the thesis covers four different scanning campaigns which are performed between June 2014 and October 2017. The data from the first scanning

3. DATA AND METHODS

campaign in 2014 is provided by the ENGAGE working group, Institute for Geography and Regional Research, University of Vienna. The SC2016, SC2017a and SC2017b are performed within the thesis.

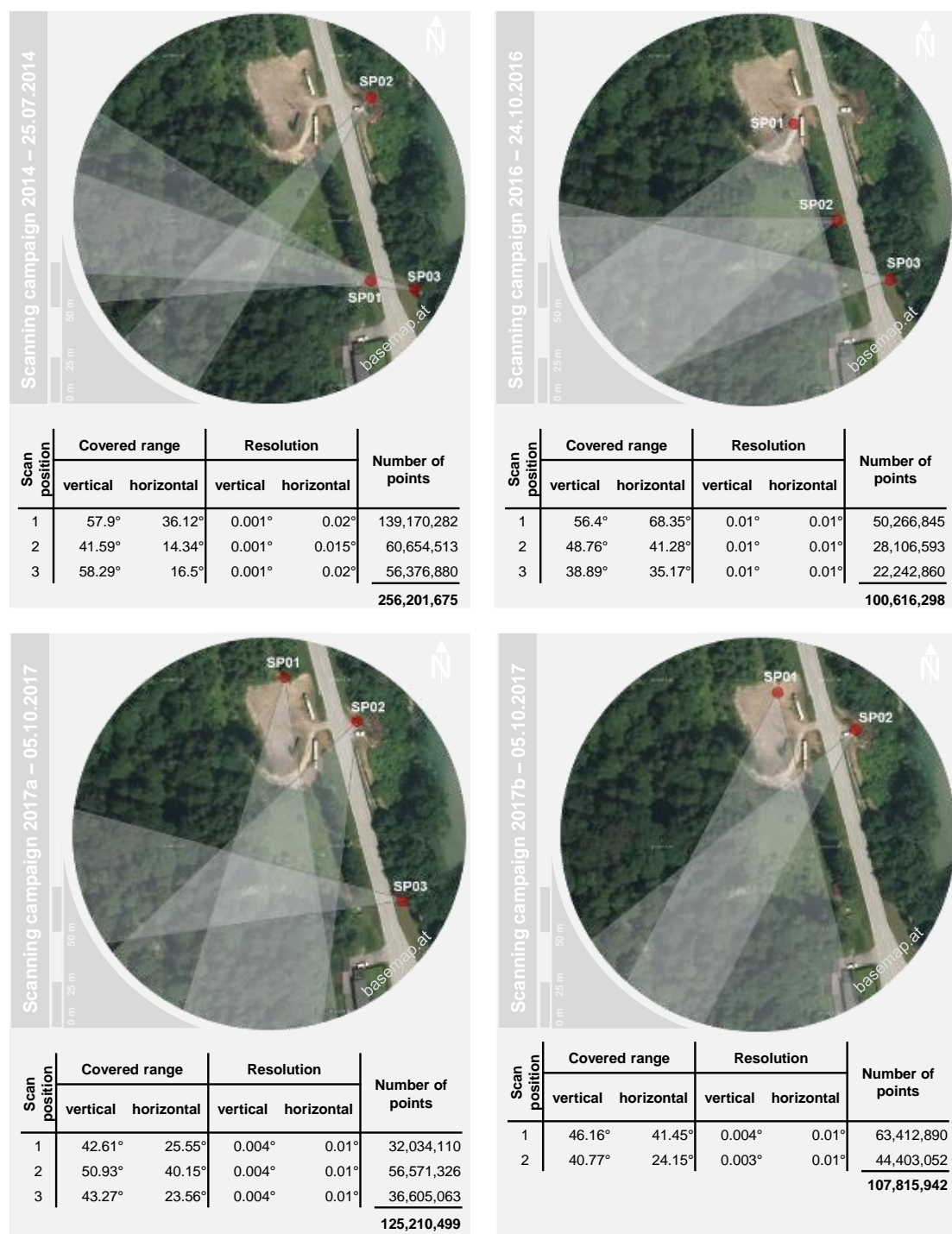


Figure 13: Data overview of the different used scans from all four scanning campaigns

From several overview and detail scans, 11 scans (three from SC2014, SC2016 and SC2017a and two from SC2017b) are chosen for further processing. Figure 13 shows an overview of the data, more detailed information concerning the single scans in each scanning campaign is presented in Appendix A. The SC2017a and SC2017b are performed on the same day before and after installing features for the evaluation of change detection. Within SC2014 and SC2016, also images are taken and RGB-information is added to the data points. As reflectors are installed during the scanning campaign in 2016, for the scans from 2016, 2017a and 2017b, high-resolution tie point scans are available. Besides the geometric information, also the echo number and the amplitude of the reflected beam are gathered. Also, the full waveform of the received pulse is stored, but this data will not be considered in this thesis.

For further data processing and analysis, the single scans are coarsely cropped to get rid of artefacts and points clearly out of area of interest. Also, the scans are exported from RiSCAN PRO to the commonly usable data format .las.

3.3 Registration

The first step of data processing within this thesis is the registration of different scan positions. First, the parameters for the transformation are estimated followed by a transformation of the data from individual SOCS to one PRCS using a 3D rigid body transformation, as there are no differences in scale between the single scan positions (LICHTI AND SKALLOUD 2010). For this thesis, target-based and ICP-based approaches using RiSCAN PRO and CloudCompare are used and combined for the tests and processing steps. This methodological choice includes the common methods used in recent scientific publications. Following the differentiation of LICHTI AND SKALLOUD (2010) presented in Chapter 2.4.1, only feature based registration due to a lack of suitable objects within the scanning area is not considered.

3.3.1 Target-based registration

The most basic approach is to find corresponding points in all different scan positions. For the data of 2014, the so-called “point pair picking” is used for the coarse registration of the scans. Scan position 1 is set as the master position and therefore defines the PRCS. The possibility of “point pair picking”-registration is implemented in RiSCAN PRO as well as in CloudCompare. For the estimation of the transformation parameters, four corresponding point pairs for each master position and the to-be registered scan positions 2 and 3 are manually identified. The results are validated visually and numerically by combining the point clouds and by providing the

registration error which is the standard deviation of the distances between corresponding points in meters in RiSCAN and the root-mean-square deviation in meters in CloudCompare.

The second used point-based approach is the registration using tie points. The tie points in the scanning campaign are white retro-reflective flat circular patches (reflectors) with a diameter of 5 cm. During the overview scanning process, the reflectors are automatically identified due to the high reflectance values. In addition to the scan of the whole area of interest, a detailed scan of the reflectors with higher resolution is performed during the scanning campaign and a tie point list (TPL) is created. RiSCAN PRO provides a module for registration via tie points. The “find corresponding points” function uses the tie point list to define point pairs. The minimize error mode is used for the point pair definition; alternatively, point pairs can also be found by name. The default settings for tolerance (the maximum distance between two corresponding points) and the minimum number of point pairs of 0.1 m tolerance and a minimum of 3 corresponding points are used. Within the tie point registration, it is possible to define more than one fixed position to improve the accuracy of the results. The quality of the registration is evaluated by the given registration error, which is defined by the standard deviation of the distances between the point pairs in meters. As the reflectors are installed within the SC2016, this approach is used as point-based coarse registration on the 2016 and 2017 data.

3.3.2 Iterative closest point (ICP) registration in CloudCompare

For more exact and more resilient registration results, the use of more points is expedient. The methods for fine registration used in this thesis are all based on the ICP algorithm. As already described in 2.4.1, the ICP algorithm is based on an iterative process of minimizing the distances between two point clouds. The following steps are extracted from the original consideration made by BESL AND MCKAY (1992).

For the application of the ICP algorithm, it is necessary that the point clouds are roughly registered to ensure a useful starting point. The point clouds are defined as “data” (to be registered) and “model” (reference). Following, these designations are hereinafter used within this thesis. The algorithm then runs through the following steps:

- Computation of the closest point of the model point cloud for each point in the data point cloud
- Computation of the transformation matrix which leads to the minimum root-mean-square difference (RMSD) for the distance between all point pairs

- Applying the registration on the data point cloud
- Iteration until the change of the RMSD is lower than a preset threshold

The RMSD in context of point cloud registration is described as the quadratic root of the squared sum of all distances divided by the number of associated point pairs (nearest neighbors).

$$RMSD = \sqrt{\frac{\sum_{i=1}^n (d_i)^2}{n}}$$

RMSD ... root – mean – square difference
d_i ... distance between p_{1i} and p_{2i} (see Equation 7)
n ... number of associated point pairs (nearest neighbour)
(CLOUD COMPARE COMMUNITY 2018) (Equation 6)

To find the closest point in the model point cloud for each point in the data point cloud (further referred to as a point pair), the calculations are vector-based and the distance between two points is defined using the Euclidean metric:

$$p_1 = \begin{pmatrix} x_{1i} \\ y_{1i} \\ z_{1i} \end{pmatrix}, \quad p_2 = \begin{pmatrix} x_{2i} \\ y_{2i} \\ z_{2i} \end{pmatrix}$$

$$d_i = d(p_{1i}, p_{2i}) = \|p_{1i} - p_{2i}\|_2 = \sqrt{(x_{1i} - x_{2i})^2 + (y_{1i} - y_{2i})^2 + (z_{1i} - z_{2i})^2}$$

p_{1i} ... coordinates of point in the model point cloud
p_{2i} ... coordinates point in the data point cloud
d_i = d(p_{1i}, p_{2i}) ... Euclidean distance (metric) between p_{1i} and p_{2i} (Equation 7)

After the definition of the point pairs, in the next step, a transformation is wanted that brings the point pairs together in the best possible way. The best fitting transformation matrix (combination of rotation and translation) is defined looking for the minimum RMSD of all point pairs. The transformation matrix consists of a 3x3 rotation matrix and a translation vector. The function to be minimized by differentiation in order to get the parameters is

$$f(p) = \frac{1}{n} \sum_{i=1}^n \|p_{1i} - R p_{2i} - q_T\|_2$$

n ... number of associated point pairs
R ... 3x3 rotation matrix
q_T ... 3x1 translation vector. (Equation 8)

The transformation matrix is then applied on the to-be-registered point cloud, and the process starts over until the optimization by another iteration (the change of the

RMSD) is lower than a given threshold. For more detailed explanation, the interested reader is referred to BESL AND MCKAY (1992).

The fine registration in CloudCompare is using the described ICP algorithm. Either the number of iterations or the minimal change in RMSD between two iterations can be chosen as varying parameters. Furthermore, the final overlap of the point clouds can be defined. The registration is performed on a randomly chosen sample of the data point cloud, where the number of chosen points can be defined. If point clouds should only be rotated or translated, specific axis rotations or translations can be locked. Also weights and farthest points removal can be activated.

The minimal change of RMSD is set to 10^{-5} m. The fine registration of the point cloud is applied to the coarsely by target-based registration aligned point clouds using different combination of the settings. The random sampling limit is set to 50,000, 500,000 and 5,000,000 points, the final overlap changed between 25%, 50%, 75% and 100%. Within the performed registration process, all rotations and translations are enabled but the scale adjustment is disabled. Also, options on the use of weights and farthest points removal are omitted. The accuracy of the registration in CloudCompare is described using the final RMSD.

3.3.3 Multi station adjustment (MSA) registration in RiSCAN PRO

The fine registration in RiSCAN PRO is performed using the multi station adjustment (MSA). Different input data such as tie points, tie object, polydata objects (derivates from the original point cloud such as filtered or segmented data) or measured scan positions are used to perform an ICP-based registration. Individual weights can be assigned to the input data.

To derive polydata which can be used for the MSA, a plane patch filter (PPF) is applied. This is the only form of filtered polydata which is accepted by the MSA. The plane patch filter algorithm looks for planar areas in the point cloud. Therefore, the point cloud is segmented to equal size cubes. For each cube, the best fitting plane (estimated using the least-square method) is identified. If the standard deviation of all normal distances between the points in the cube and the plane is smaller than the preset maximum plane error, the center of gravity of the points and the normal vector are saved. Otherwise, the cube is divided into eight even sub-cubes. The plane estimation is repeated until all points fulfil the condition of the minimum plane error or a predefined minimum number of points per plane or minimum search cube size is reached (RIEGL 2015). The adjustable parameters are therefore the maximum plane error, the minimum number of points per plane, and the minimum and maximum

search cube size in an interval of 0.016 m to 262.144 m. The different adjustments presented in Table 3 are used.

Table 3: Settings of the different plane patch filters used for MSA tests

| Name | Maximum plane error [m] | Minimum number of points per plane | Minimum search cube size [m] | Maximum search cube size [m] |
|------|-------------------------|------------------------------------|------------------------------|------------------------------|
| PPF1 | 0.05 | 50 | 0.512 | 32.768 |
| PPF2 | 0.03 | 10 | 0.256 | 1.024 |
| PPF3 | 0.02 | 8 | 0.064 | 1.024 |
| PPF4 | 0.005 | 3 | 0.016 | 1.024 |

For the MSA, input data can be chosen and various parameters can be set. The MSA is performed using the recommended all nearest points mode. The search radius defines the distance within the algorithm searches for corresponding plane patch gravity points. The maximum tilt angle is another sorting criteria: if the angle between the normal vectors (which are stored with the gravity points of the plane patch filter) is larger than the maximum tilt angle, the point pair is also dismissed. These two parameters are varied within the MSA adjustments. Fixed parameters are the minimum change of error 1 and 2. The minimum change of error 1 represents the minimum improvement of the error between two iterations before the corresponding planes are again newly defined. The minimum change of error 2 defines the minimum change of error before the final alignment. These two parameters are set to the default values of 0.1 m (min. change of error 1) and 0.01 m (min. change of error 2), as variations of these values do not show notable changes in results. Furthermore, outliers beyond 2 sigma (standard deviation) are eliminated. The recommended least square fitting calculation mode, which is more sensible to outliers than the robust fitting, is used.

3.3.4 Registration tests and final fine registration

Two different registration tests are done. First, all scan positions per epoch are registered at once always using scan position 1 as the reference point cloud. The registration parameters are constantly refined using search radii of 0.5 m, 0.2 m, 0.1 m, 0.05 m and 0.02 m (the smallest one only for PPF3 and 4) and maximum tilt angles from 15° to 10° and 5°. All the settings are used with the four different plane patch filter options, which leads to 56 different MSA adjustments per epoch.

The second registration test is performed to obtain results that can be compared with the CloudCompare registration. Therefore, one model and one data point cloud of one epoch are used and after each change of settings, the registration is set back to the target-based registration output. The search radius values are extended to 3 m, 5 m and 10 m and maximum tilt angles of 45°, 90° and 180° are considered. Only PPF3 and PPF4 are used for this test.

The output of the MSA is the error (the standard deviation of the differences of all the point pairs) in meters as well as a histogram of all the residues. Also, the number of used data (tie points and polydata) and the running time is available. The standard deviation is used as measure for the accuracy of the registration and is defined by

$$s = \sqrt{\frac{\sum_{i=1}^n (D_i - \bar{D})^2}{n}}$$

s ... standard deviation of the point pair distances
D_i ... difference between the points of an associated point pair
 \bar{D} ... mean point pair difference
n ... number of associated point pairs. (Equation 9)

The difference between an associated point pair is not equal to the distance shown in Equation 7. While the distance is per definition a positive value, the point pair difference includes the relative positions of the points. The values can therefore be positive or negative, depending on whether the data point is closer to (the amount of the vector is smaller) or further away from (the amount of the vector is larger) the coordinate origin than the associated model point.

The tests aim to point out if there are differences in fine registration quality between the MSA and the ICP. If showing comparable or better results, the decision is made in favor of ICP in CloudCompare, as the thesis aims to prefer open source software over proprietary software. After the testing of the different registration approaches and the different settings, the ICP registration implemented in CloudCompare is applied using 25% theoretical overlapping and 5,000,000 points of random sample limit. Besides the description of the registration quality using the RMSD, the registration quality is checked by visual interpretation.

3.4 Co-registration and extraction

For comparing clouds of different epochs, the next step after the registration and merging of the several scan positions within one scanning campaign is the co-registration of the produced point clouds. Therefore, the same procedure as for the

registration is used: initially, the point clouds are coarsely co-registered by target-based approaches. Therefore, the 2016 point cloud is used as model point cloud for all registrations. The 2014 point cloud is coarsely co-registered by point pair picking, the 2017 point clouds are co-registered using tie point registration (see 3.3.1).

Before the fine registration, the area of interest is chosen and the data is cropped to a smaller all overlapping area.

The fine co-registration is also performed using the ICP algorithm implemented in CloudCompare with the same settings as used for the fine registration described in 3.3.4. Also, the co-registration is visually evaluated.

3.5 Filtering

The filtering process is, as proposed in Chapter 2.4.2, separated in filtering of the vegetation and homogenization of the point cloud. The vegetation extraction is applied first, so that the final change detection can be tested on the raw data as well as on the homogenized data. For the vegetation filtering, the implementation of the approach presented by BRODU AND LAGUE (2012) is chosen. As the method is designed for distinction of different natural surfaces (differentiation of riparian vegetation and ground surfaces in fluvial environments or classification of surfaces in rockfall endangered cliff environments), acceptable results are expected for the point cloud data used within this thesis. Further, the fact that the algorithm is implemented in CloudCompare and therefore easily available and applicable, including the aspect of general usability, is an argument in favor for this approach. Within the process, also the intensity values (AKCA 2007, PESCI ET AL 2008) are integrated in the vegetation filtering process. The homogenization is performed using the statistical standard tools provided in CloudCompare.

3.5.1 Removing the vegetation

For filtering of vegetation, an approach combining geometrically based filtering and filtering on intensity values is used.

The geometrical filtering approach is based on the CANUPO-algorithm developed by BRODU and LAGUE and is initially presented in their 2012 published paper about classifications of complex natural scenes used in a case study about point cloud classification in fluvial environment. As already mentioned in Chapter 2.4.2, within this paper, it is pointed out that distinctive properties of natural surfaces are defined at different scales. Therefore, the algorithm considers local dimensionality of

neighboring points at different scales – it is classified if the point cloud is locally rather linear (f.e. small branches at a medium scale), planar (f.e. rock surface at small scales) or distributed in the whole volume (f.e. bushes on medium to large scale) of the considered sphere.

The classification is trained using manually chosen data samples for the different classes. The data on different dimensionalities at different scales is projected in a plane of maximal separability between the classes using an adapted form of the principal component analysis (PCA): instead of maximizing the projected variance between the classes, a criterion for optimizing the class separability – the linear discriminant analysis (LDA) - is used for deriving the projection parameters. Furthermore, a line which can be manually adapted separates the classes. For classification quality, a validation using 50,000 test points per class is performed. Furthermore, the Fisher Discriminant Ratio (FDR) is used as a quality parameter: The mean of the distances of each point of a class to the class separating line is calculated for both classes and the distance of both means is derived. This distance is divided by the product of the two squared standard deviations to include inner class scattering. Therefore, higher FDR-values indicate a better class discrimination. The trained classifier is then applied on the to-be-classified point clouds. (BRODU AND LAGUE 2012)

The interested reader is referred to the original paper. For the classification, 50 different scales from 0.01 m to 0.5 m with steps of 0.01 m are used with a consideration of two dimensions per scale. Furthermore, all the points of the selected point cloud are used as core points for the vegetation and no further advanced settings are chosen. Results of the CANUPO Classification tool are two additional attributes for each point of the point cloud: the class and a confidence value for each point.

Besides the geometrically based filtering, also intensity is used for optimization of the vegetation filtering process. The intensity values show the amplitude ratio of the emitted and received signal during the scanning process (RIEGL 2015). The measuring unit is decibel (dB), which reflects the ratio in a logarithmic scale (MESCHÉDE 2015).

Within the filtering, the CANUPO-algorithm, which is implemented in CloudCompare, is trained by two manually extracted training areas “rock” and “vegetation”. The point clouds from the four different scanning campaigns are then split in three to nine sections (each between $4 \cdot 10^6$ to $7 \cdot 10^6$ points) segmented along the z-axis to provide crashing of the plug-in. Then, the classification is applied to the different sections.

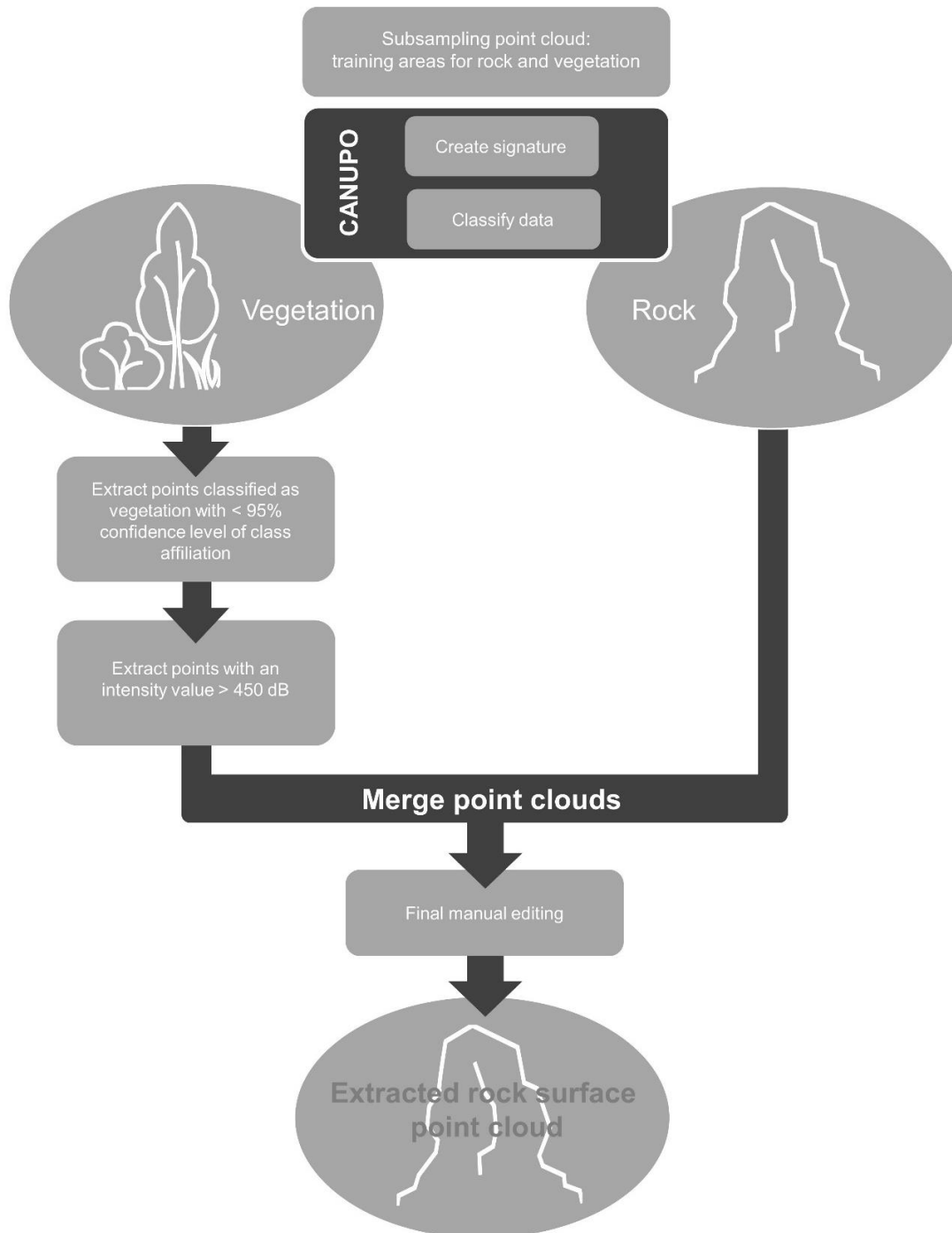


Figure 14: Vegetation filtering process: Combination of filtering based on geometrical information, intensity and manual editing

As the algorithm shows general classification problems on borders and within the classification on the Amtmann case-related false classifications in cleavages, the

vegetation-classified values with lower than 95% confidence are extracted. As higher intensity values (a lower receiving amplitude) are reached within cleavages, the extracted point cloud is then split by intensity of 24 dB, which is chosen from visual interpretation.

Larger gaps are expected between the different segments. Therefore, layers of 5 cm along the borders of the sections are extracted from the vegetation-classified point cloud. Finally, the point cloud classified as rock within the CANUPO-classification, the intensity-classified point cloud with a lower CANUPO-classification certainty than 95% and the extracted point cloud along the borders of the sections are merged and manually cleaned by visual final distinguishing. The workflow of the vegetation filtering is illustrated in Figure 14.

3.5.2 Further filtering methods

For change detection, a homogenous point cloud is preferable. Therefore, filter with a smoothing and balancing effect are applied after the vegetation filtering. For these processing steps, the possibilities offered by CloudCompare are used.

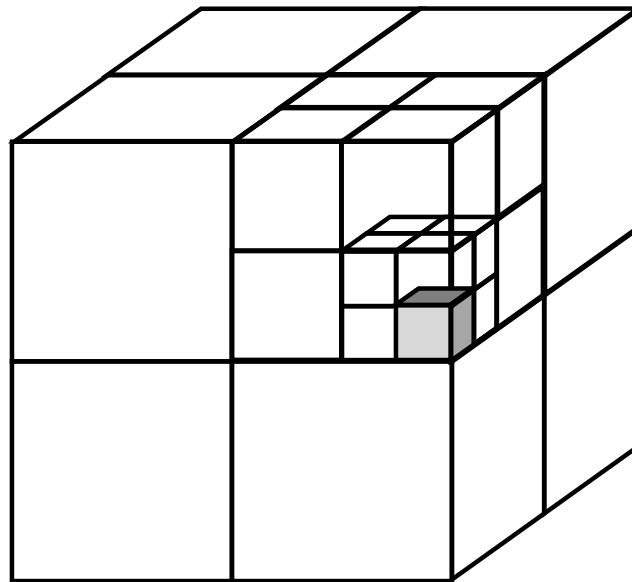


Figure 15: Spatial concept of the octree-structure (after CHÁVET AND KARSTOFT 2012)

The base of all filter tools and a lot of other point cloud manipulations in CloudCompare is structuring the point cloud using an octree. The structure is already

mentioned in Chapter 2.4.3 and further described more in detail. Octrees are three-dimensional hierarchical data structures using spatial subdivision of 3D data (CHÁVEZ AND KARSTOFT 2012). Therefore, the starting point is a bounding box which encloses the entire data. The box is constantly subdivided into a maximum of eight non-empty even sub-cubes (voxels) until a given level of subdivision or until a cube only contains one data point (VOSSELMANN AND KLEIN 2010). This data structure allows efficient storing and reasonable processing time even on point clouds of several million points (GIRARDEAU-MONTAUT ET AL 2005). Figure 15 visualizes the concept of octree structuring.

The statistical outlier removal (SOR) filter tool calculates the average distance of each points to its k neighbors. Following, the points showing an average distance larger than the overall average distance plus n times the standard deviation are rejected. For the filtering, the number k of nearest neighbors for the calculation and the n times of standard deviation are the adjustable parameters. Therefore, the filter removes scattered single points (CLOUDCOMPARE COMMUNITY 2018). For the SOR-filtering of the point clouds, $k = 15$ neighbor points and $n = 2$ standard deviations are chosen.

To harmonize the density of all point clouds, subsampling of the point cloud is used. The subsamples can be random, spatial or octree-based. Within random subsampling, a specified number of points is picked in a random manner. Spatial subsampling is defined by a minimum distance between two points. Further on, points from the original point cloud are picked on condition that the minimum distance between all points of the output point cloud is the chosen value. Octree subsampling divides the point cloud to a defined level of subdivisions and exports for each octree voxel the point which is nearest to the center. On the contrary, the resample octree tool exports the gravity point of each octree voxel to the new point cloud (CLOUDCOMPARE COMMUNITY 2018). For the point cloud processing of this thesis, the minimum distance condition with a value of 0.01 m is chosen.

3.6 Change detection

As described in Chapter 2.4.3, there are numerous different approaches of change detection using point cloud data. While raster based approaches (DODs) are suitable for rather large scale and plane structures, mesh or point-based methods are applicable for three dimensional structures. As the focus of the thesis is on small scale change detection on a three-dimensional object, using point cloud data instead of derivatives like meshes or TINs is preferred. Therefore, the two point to point (MUKUPA ET AL 2017, MILL 2016) or point and point cloud based (OHLMANN-LABER AND SCHÄFER

2011) approaches C2C and M3C2, which are used in several scientific publications (see Chapter 2.4.3) and easily accessible as implemented tools in CloudCompare, are chosen. As for the registration, the roles of the two point clouds are defined. One point cloud is set as reference or model point cloud and one as data or comparing point cloud. The results of the approaches are displacement distances.

3.6.1 Cloud to cloud distance C2C

The Cloud to Cloud distance tool (C2C) is based on a nearest neighbor distance measurement. Therefore, for each point of the point cloud S , the Euclidean distance (see Equation 7) to the nearest neighbor in the point cloud S' is calculated. This distance is called the Hausdorff distance and defined as shown below in Equation 10.

$$d(p, S') = \min_{p' \in S'} \|p - p'\|_2$$

p ... point of point cloud S
 S' ... point cloud S'
 p' ... point of point cloud S'

(Girardeau – Montaut 2005)

(Equation 10)

As shown in Figure 16, the Hausdorff distance does not necessarily map the “real” distance of the data and the reference surface. Therefore, also local surface modelling of the model point cloud can be performed. Further on, this is referred to as C2C with local modelling. It differs slightly from C2M, as the model surface and the surface normal is computed for each point individually by using a defined neighborhood.

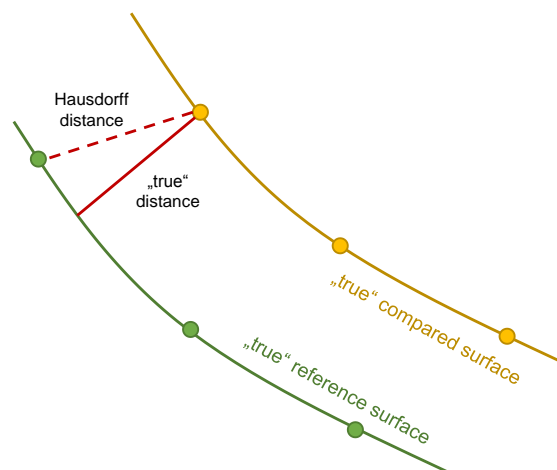


Figure 16: Hausdorff distance vs. “true” distance (after CLOUDCOMPARE COMMUNITY 2018)

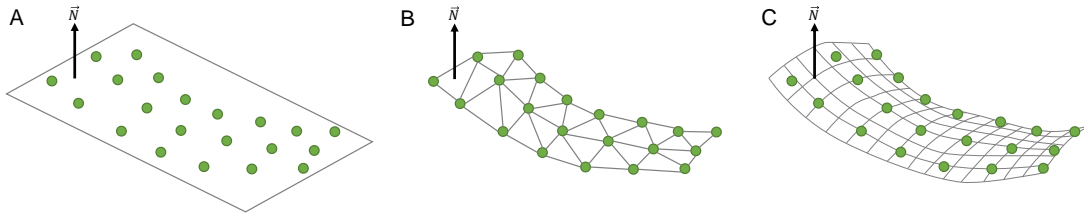


Figure 17: Concepts of local surface modelling for C2C. A: least square plane, B: Delaunay triangulation, C: quadric modelling

For the local modelling, either a number of neighbors or a spatial neighborhood (set by the radius around the point) is defined. The local modelling concepts provided by the C2C in CloudCompare are least square plane, a 2.5D Delaunay triangulation and a quadric function. The least square plane computes the locally best fitting plane (with the least square distance of all included points to the plane) for the reference point cloud and calculates the normal distance of the plane and the corresponding point of the comparing point cloud. The local model of the 2.5D Delaunay triangulation defines a local mesh of the reference point cloud using the points as vertices. For the measuring distance of the compared points and the created mesh, the normal direction of the least square plane is used. For a smoother surface, the third local surface modelling concept is defined by a quadric function. Also, the distance measurement direction is defined here by the surface normal calculated from the best fitting local plane model. Figure 17 shows the different local surface modelling concepts. The local modelling can be adapted to the given circumstances. 2.5D Delaunay triangulation is described to be the best model for representation of sharp edges, whereas the quadric function can represent smooth and curvy surfaces. As being the most versatile local model option, the quadric function is recommended by default. All different modelling approaches are based on an octree structure of the point cloud. (GIRARDEAU-MONTAUT ET AL 2005, CLOUDCOMPARE COMMUNITY 2018)

3.6.2 Cloud to cloud distance M3C2

LAGUE ET AL present in their 2013 article the cloud to cloud comparing multiscale model to model cloud comparison (M3C2) approach which adapts better to rough surfaces. The general concept is already described in Chapter 2.4.3, the change detection is hereafter specified more in detail. The following explanations are all gathered from LAGUE ET AL (2013). Figure 18 illustrates the concepts that are described.

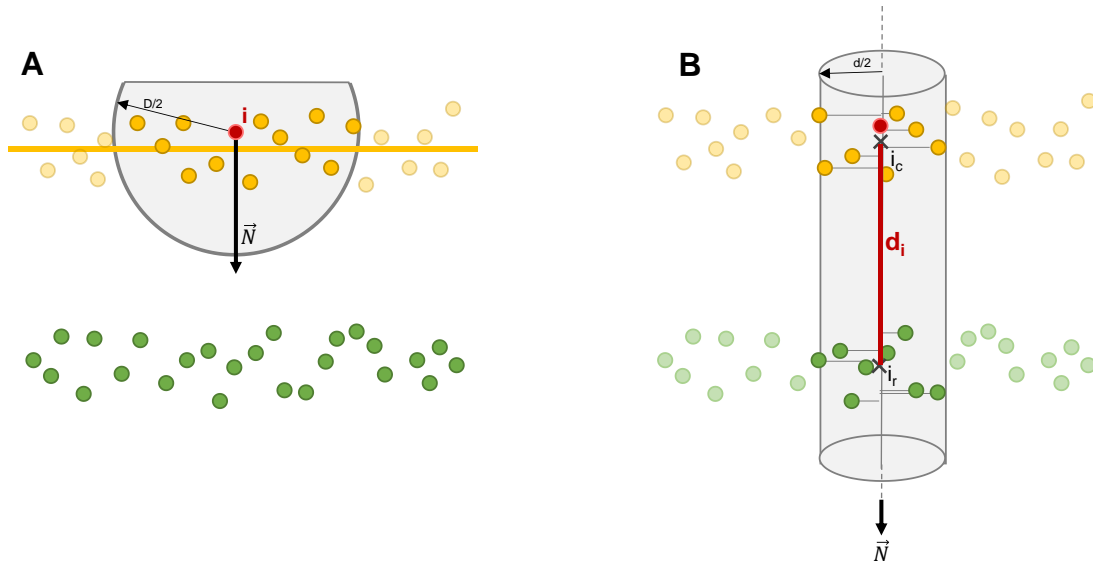


Figure 18: Illustration of the M3C2 change detection concept (after LAGUE ET AL 2013)

As for some applications, general trends of change are sufficient. For the M3C2, it is optional to define core points used for the following computing steps for a more efficient calculation. The core points are either defined by a minimum point spacing of the reference point cloud or other subsampling methods (see Chapter 3.5.2).

In a first step, for a given point i , a normal vector is defined. Therefore, using the points within a given radius $D/2$ are set as the used neighborhood. A best fitting plane, equivalent to local modelling of the least square plane in Chapter 3.6.1, is defined. Illustration A in Figure 18 visualizes the concept. When defining D , it has to be taken into account that D must be large enough to not being influenced by local roughness, but small enough to reflect general changes of surface orientation. Finding the optimal D is addressed as a key aspect of point cloud comparison. M3C2 provides an empirical approach of searching for the best plane fitting over different scale levels performing a PCA. The standard deviation of the distance of the neighboring points to the plane gives a measurement unit for the local roughness of the surface. The normal direction used for distance measurement can either be the estimated reference cloud normal, the estimated comparing cloud normal or an average of both normal directions.

In a next step, the projection scale d is defined for the observed point i of the comparing point cloud. Therefore, the chosen normal is placed through the point i and a cylinder with a radius $d/2$ using the normal as the central axis is defined. For estimating the position of the surface for both point clouds, the points within the

defined cylinder are projected on the central axis. The mean positions i_r and i_c of the projected points are estimated separately for both point clouds. The distance between these two averaged projected positions defines the distance of i to the reference point cloud. Illustration B in Figure 18 shows this methodical step. If there is no according point in the reference point cloud, the point is defined as not classified.

Besides the distance, also a spatially variable confidence interval is defined for each point. It reflects the local distance measurement accuracy and is used to distinguish if the detected change is statistically significant at the given confidence interval (usually 95%). As the confidence level boundary coincides with the minimum detection change, it is also called the Level of Detection at x% of confidence ($LOD_{x\%}$). For detailed specification of the calculation of the confidence intervals, the interested reader is referred to the original paper (LAGUE ET AL 2013).

3.6.3 Application and evaluation of chosen change detection approaches

For change detection and method evaluation within this thesis, different epochs and different point cloud sections are compared. The 2014 and 2017a point clouds are compared using the 2014 point cloud as the reference data, the 2016 and 2017a point clouds are compared using 2016 as the reference point cloud and 2017a and 2017b point clouds using 2017a as the reference point cloud.

Two different settings of the C2C approach are used: the Hausdorff distance as well as the quadric modelling approach. For the octree modelling, the default settings are used. Within the M3C2, the concept of core points addresses a lower resolution which is needed for results of change detection. As the change detection of this thesis aims high resolution results, all the points of the point clouds are used as core points. As LAGUE ET AL justify using the estimated reference point cloud normal for geomorphological applications, this setting is used for the cloud comparing within this thesis. Also, the automatically estimated parameter d and D are applied.

The results of the different approaches and settings are divided in classes of <0.01 m, 0.01 m – 0.1 m and >0.1 m detected change. The class from 0.01 m to 0.1 m is examined more in detail with a selection of areas of interest. The output of the change detection is a color-coded visualization of the point cloud. For the visualization of the distances, the points of the compared point clouds are used for the two C2C based approaches, the M3C2 algorithm creates new mean point positions for displaying the distances.

3. DATA AND METHODS

The comparison of the 2017a and 2017b point cloud is more extensive. Besides the comparison of the point clouds using a color-coded output, also histograms for the different approaches of the detected changes are generated and the data is examined by descriptive statistical analyses and statistical testing using the Wilcoxon rank sum test. In addition, the manipulated area is closer examined using the different change detection methods on different processing steps of the point cloud on two test areas to evaluate the methods. For M3C2, the parameters d and D are fixed to 0.05 m. Therefore, two sections of the 2017a and 2017b point clouds are taken. The first one covers only the area surrounding the installed objects, the second section is enlarged in order to cover areas with vegetation. The points are manually classified in areas with change and no change by selecting the visible structures and subsequently classified using the different algorithms at different processing steps of the point cloud. Therefore, two different levels of significance for change (0.1 m and 0.2 m) are used, and the points are divided in groups classified as change or no change by the algorithm-based change detection with respect to the chosen threshold.

4. Research Area

In the following chapter, the research area is described. The focus of the characterization is on the relevant physical environmental factors like geology, climate and hydrology and details of infrastructure as this is relevant for risk estimations.



Figure 19: Upper part of the Amtmann, a free-standing rock structure in the Ybbs Valley

The object of research is a 40 m (above street level) high, freestanding rock formation called Amtmann, shown in Figure 19, one of 321 geotopes in Lower Austria (WESSELY 2006). The rock structure shows an inhomogenous, rugged surface with overgrowing vegetation.

4.1 Location and infrastructure

The Amtmann is in the Ybbs valley orographically left of the Ybbs river in the village Kreilhof in the municipal district of Waidhofen an der Ybbs in the southwest of Lower Austria. The location is shown in Figure 20. The municipal district is part of the microregion Ybbstal-Eisenstraße for regional development and the province-crossing area Eisenwurzen, which also includes areas of the neighboring federal states Upper Austria and Styria and is characterized by former iron industry.

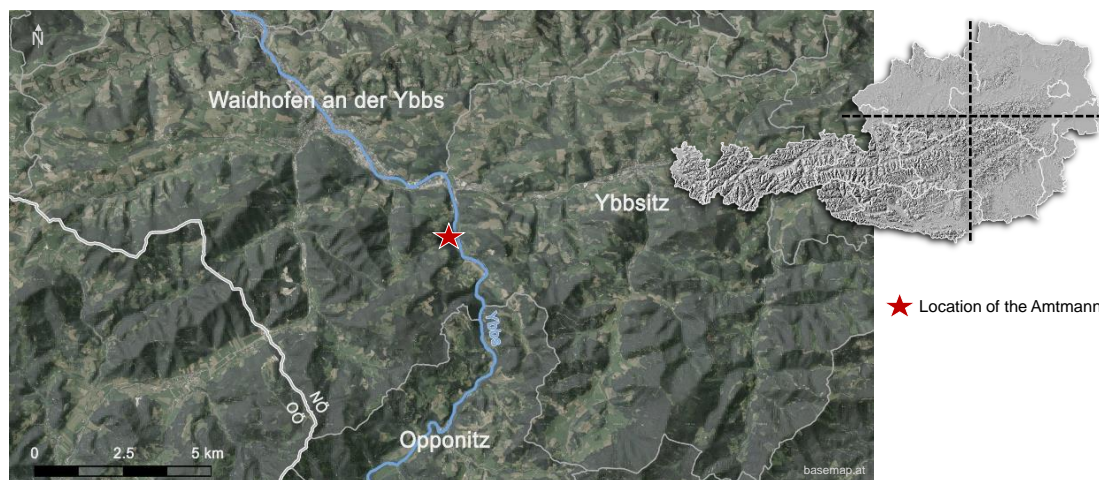


Figure 20: Location of the Amtmann in the Ybbs Valley, Lower Austria

Next to the Amtmann on the orographical left side of the Ybbs river, the Ybbstal highway (B31) passes which leads from Waidhofen an der Ybbs to Göstling an der Ybbs 44 km along the Ybbs valley. The Amtmann is located at km 6.0 to km 6.3 of the Ybbstal highway. Until 2010, the Ybbs Valley Railway, a narrow-gauge railway, connecting Waidhofen an der Ybbs and Kienberg-Gaming also passed the Amtmann on the orographical right side of the Ybbs river (STANFEL 2014). Today, the Ybbstal Cycle Trail, a major touristic project of the region costing 10 million Euro, which was inaugurated on June 17th 2017 (NÖN 2017), uses the former railway line. The public transport is covered by an hourly local bus from Waidhofen an der Ybbs to Lunz/See with the bus station Gaissulz Amtmann right next to the research object.

4.2 Environmental characteristics of the research area

Geologically, the Amtmann is located in the Northern Calcareous Alps at the transition zone of the Lunzer nappe and the Frankenfelder nappe with deposit of Jura and Tithon-Neokom with dominant rocks of limestone and marlstone and quaternary sediments in the valley floor (SCHNABEL 2002, WESSELY 2006). The material of the Amtmann is Rauhwacke, a porous calcite breccia with various accessory minerals (MÜLLER 1982). The area is tectonically undisturbed with a rare occurrence of earthquakes (WESSELY 2006).

Surrounding the Amtmann, the land cover is a managed mixed forest at a relatively steep slope up to 70% in the immediate vicinity of the Amtmann and more than 100% in a 100 m radius (AMT DER NIEDERÖSTERREICHISCHEN LANDESREGIERUNG 2017).

The valley in which the Amtmann is located is described as a V-shaped valley and is dominated by the Ybbs river, a 138 km long tributary of the Danube river which originates close to Mariazell and flows into the Danube at Ybbs an der Donau. In Opponitz, about 7 km upstream of the Amtmann, the Ybbs flow volume varies from a minimum of 10.8 m³/s in October to a maximum of 37.5 m³/s in April, according to a mean day flow volume, averaged from 1951 to 2014. (EHYD 2017)

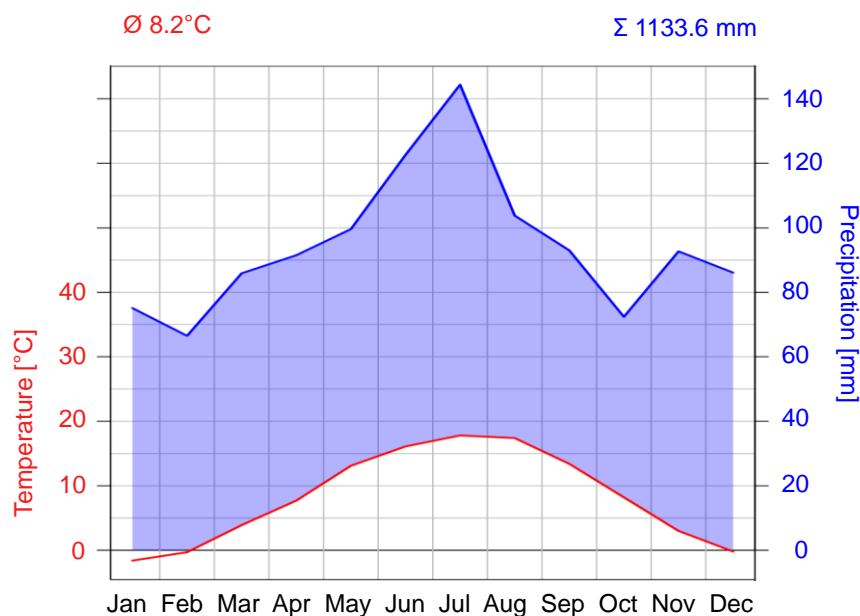


Figure 21: Climate diagramm Waidhofen an der Ybbs, 1971-2000 (data: ZAMG 2017)

Using the Köppen-Geiger-Classification (KOTTEK ET AL 2006, KÖPPEN 1918), the climate in the research area is described as warm temperature, fully humid climate with warm summers (Cfb). As shown in the climate diagram in Figure 21, the highest temperatures occur in July with a monthly average of 17.8 °C, the coldest month is January with an average of -1.6 °C. The precipitation reaches its maximum in July with average 144.4 mm, the lowest monthly precipitation is detected in February with average 66.5 mm. The annual precipitation rate is 1133.6 mm averaged from 1971 to 2000. There is an annual average of 100.5 days of frost (minimum daily temperature below 0 °C), 24.7 days of ice (all day temperature below 0°C), 43.4 summer days (maximum daily temperature over 25 °C) and 6.3 hot days (maximum temperature over 30 °V). (ZAMG 2017)

4.3 Rock falls and related investigations

Due to road construction, the slope in the Ybbstal valley is cut which lead to a loosened structure of the uncovered bedrock. The area from km 4.85 to km 9.18 of the Ybbstal highway, including the location of the Amtmann, is under constant monitoring (HOFMANN 2004, SCHWEIGL 2005a, SCHWEIGL 2005b, SCHOBER 2007, SCHWEIGL 2012). Potential rock fall areas are detected and investigations are made.

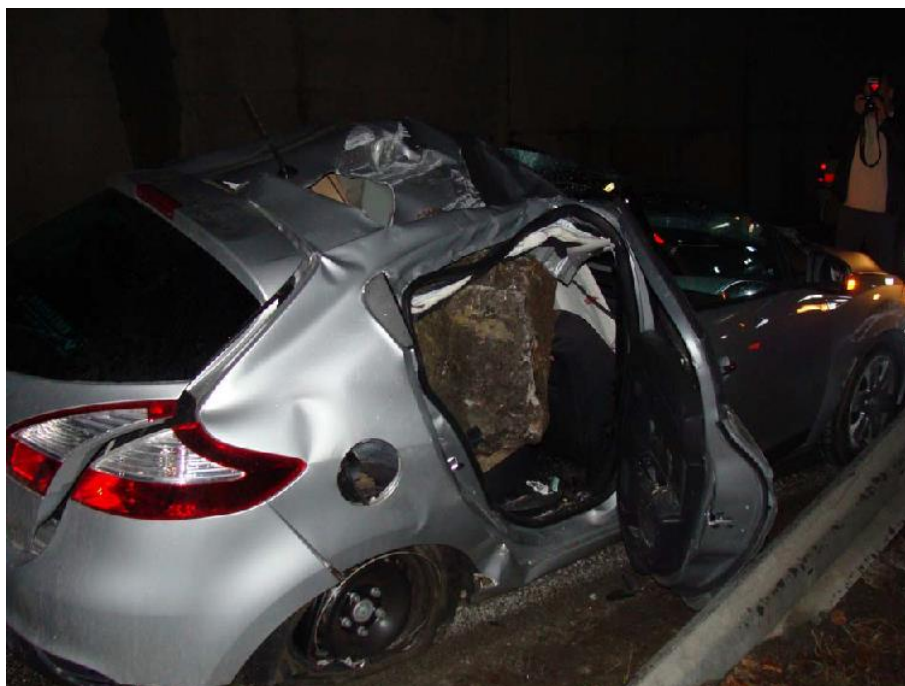


Figure 22: Car hit during a rock fall event in 2010 (photo: Freiwillige Feuerwehr Opponitz 2010)

Besides this, also natural rock faces with fissures and uphill situated stone pits are potential sources of rock falls. In the 1970, galleries were built along the street around km 9.0 to prevent the traffic from rock fall and snow avalanches. Since then, a lot of rock fall protection systems like wire mesh fences, anchored retaining walls or shotcrete seal are installed.

A documented harmful rock fall event occurred on the 21.03.2010 at km 9.15: a rock of 0.75 m³ hit a passing car (see Figure 22). The driver suffered from minor injuries, the car was totally damaged. Referring to the damage report, the initial area of the rock fall is 100 m upslope the street and triggering factors were the precipitation of the previous days, freeze-thaw cycles which led to expansion of fissure and the root pressure of a tree located in the initial area. (AMT DER NIEDERÖSTERREICHISCHEN LANDESREGIERUNG 2010)

5. Results

The following chapter shows the results achieved within this thesis. The chapter is separated in the different processing steps presenting results of different test settings and final data processing.

5.1 Field work

The field work took place on October 24th, 2016 and on October 5th, 2017. Before starting the campaigns, the scan positions are chosen. As the western side of the Amtmann is facing upslope a forest area, it is decided to skip this side and focus on the east side of the structure which is facing the street. The resulting scan positions in 2016 and 2017 are shown in Figure 13.

Within the field campaign 2016, 25 reflector patches are installed. For the scanning, the Riegl VZ 6000 scanner (see Chapter 2.3.2), is connected to the thoughbook and the scanning project is directly created in RiSCAN PRO. Several scanning attempts are necessary at SP03, as the scanning process aborted by the scanner due to the inclination of the instrument. Finally, fine scans from all three scan positions including high resolution images and fine scans of the extracted reflectors are taken.

The second field day is split into two scanning campaigns. The first campaign of the field day (2017a) is performed connecting the laptop to the scanner and performing scans from three different scan positions (see Figure 13). Fine scans from all three scan positions are taken. At SP03, the tie points are detected but due to software failure not fine-scanned. Subsequently, the eight objects for surface manipulations are installed in 8 m to 9 m down the top at the north-eastern face of the Amtmann. During the installation process, one object (the manipulated hemisphere 2) got lost. The second scanning campaign is performed directly on the scanner as the connection to the laptop failed. Two fine scans are performed including fine tie point scans. For all two campaigns of the field day, temperature and humidity are measured

and set as (optional) parameters within the scanning process day. Furthermore, due to software problems, no high-resolution images are taken.

5.2 Initial check of the raw data

As a first step of data analysis, the original scans are checked in RiSCAN PRO. For the scan positions of 2014, 2016 and 2017a, a project file is already available as the scanner was connected to the laptop and the scanning was performed using RiSCAN PRO. For 2017b data, a new project file is created, the single scans are exported from the instrument to a hard drive after the field work and imported to the new project file.

The data in general is detailed described in Chapter 3.2 and Appendix A. Therefore, only chosen noticeable details are described following. As also noticed in the field work, a first rough overview of the different scan position and epochs does not indicate any evident changes of the rock surface.

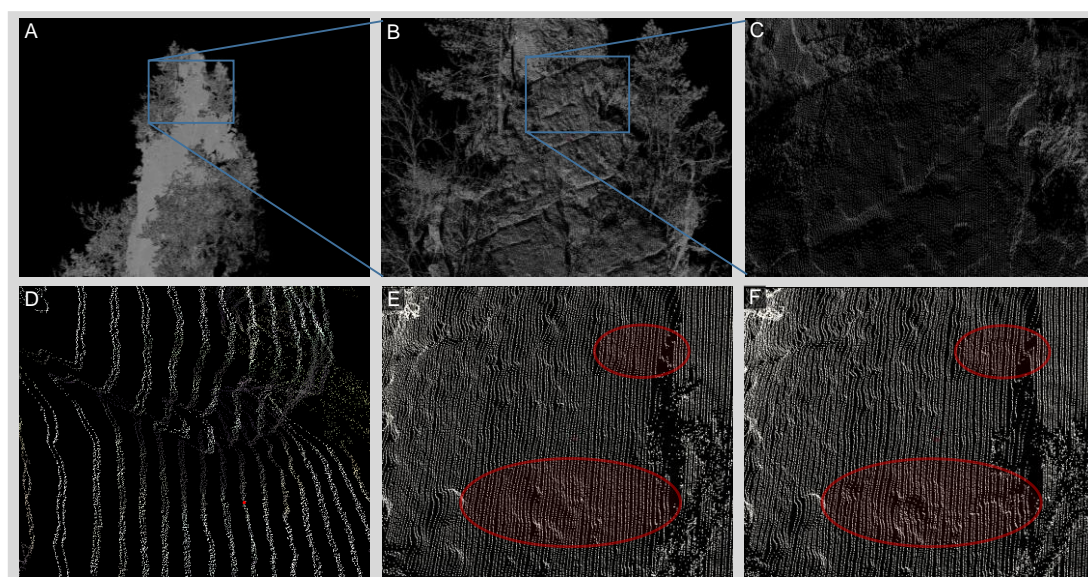


Figure 23: Selected views of the initial data check. A/B/C: Zooming in 2016 SP01 data. D. Close-up of the 2014 data. E/F: Same part of the 2017a (E) and 2017b (F) data – added structures visible on F within the red indications.

Figure 23 shows selected sections of the initial data review. The images A-C show zooming stages of SP01 of the 2016 data. The point cloud is greyscaled using the intensity values. Therefore, the reflector patches are clearly visible as white dots within the point cloud due to their high reflectivity values. B shows the structure of the

rock: several cleavages which are about 25° inclined to the horizontal plane are identifiable and the structure of the rock is better visible at this zooming level.

Besides the rock surface, individual trees and branches and leaves can be distinguished, as well as missing rock surface points due to shadowing effects. The third zoom level in C shows the structure of the point cloud. The single points with varying point density due to different surface structures are distinguishable. Also, the surface structure is visible more in detail. Image D shows a close-up of the 2014 data. Because of the different horizontal and vertical scanning resolution presented in Chapter 3.2, the points are arranged in pairwise vertical stripes of high density with gaps about double the size of a point-stripe pair. The distance between the double-stripes varies around 5 cm. E and F show the rock surface section before and after adding the polystyrene objects. Within the red indications, the two parts of the semitorus and two hemispheres are visible within the point cloud section in F. For further processing, the data of all four epochs are joined in one single project file.

5.3 Registration

Within a first sighting of the data, the raw point clouds are coarsely cropped to exclude obvious measurement errors and points that are clearly out of the area of interest. Following, different registration tests are performed which lead to a final registration of the point clouds of the different scanning campaigns.

5.3.1 Initial coarse registration: point pair picking and tie points

The initial coarse registration is performed using tie point registration in RiSCAN PRO for 2016, 2017a and 2017b (including initial co-registration of these two scanning campaigns) and manual registration by point pair picking in CloudCompare for the 2014 scans. Table 4 shows the accuracy of the initial coarse registration.

For the 2014 data, three distinctive points on the Amtmann (characteristic points at cleavages) which are identified in the three different scans are picked for the point pair registration. The registration using these points lead to a RMSD in the magnitude of 0.011 m for the registration of the first two scan positions, increasing to 0.036 m when adding the third scan position. In this calculation, only the identified points are included.

The tie point registration is performed using the automated tie point registration function in RiSCAN PRO. The accuracies from the tie point registration (the standard deviation of the differences from the data point cloud and the model point cloud) are

5. RESULTS

in a sub-cm magnitude for all registrations. For this calculation, only the tie points are considered. Adding the third scan position leads to accuracy improvement for the 2016 data and to a slight decreasing of accuracy in 2017a.

As the number of tie points with a maximum of 14 per registration process is a small sample and a normal distribution of the distances around 0 can't be assumed, the RMSD and the standard deviation can't be compared directly. Though, the differences in RMSD and standard deviation point to a better registration quality of tie point registration.

Table 4: Resulting errors of the initial coarse registration

| | 2014 point pair picking CloudCompare | | 2016 tie points RiSCAN PRO | | 2017a tie points RiSCAN PRO | | 2017b tie points RiSCAN PRO | |
|---------------------------------------|--|-------------|----------------------------------|------------------------------|-----------------------------------|------------------------------|-----------------------------------|------------------------------|
| | number of points | RMSD [m] | number of points | standard deviation [m] | number of points | standard deviation [m] | number of points | standard deviation [m] |
| SP01 (model) & SP02 (data) | 3 | 0.01068 | 14 | 0.0081 | 10 | 0.0028 | 12 | 0.0034 |
| SP01+SP02 (model) & SP03 (data) | 3 | 0.03594 | 10 | 0.0056 | 7 | 0.0032 | - | - |

5.3.2 Fine registration: testing different options

For the fine registration, different settings and approaches are tested for finding an optimal fine registration solution for the data. The first test deals with different settings using the MSA in RiSCAN PRO. Therefore, various polydata (objects created from the plane patch filter) from all scan positions for all epochs using the settings presented in Chapter 3.3.3 are produced. The various settings result in a different number of points used for the registration shown in Table 5.

Table 5: Number of data points resulting from the plane patch filter

| Used plane patch filter | 2014 | | | 2016 | | | 2017a | | | 2017b | |
|----------------------------------|---------|---------|---------|--------|---------|--------|--------|---------|---------|--------|---------|
| | SP01 | SP02 | SP03 | SP01 | SP02 | SP03 | SP01 | SP02 | SP03 | SP01 | SP02 |
| PPF1 | 28261 | 16520 | 17428 | 6416 | 7542 | 5561 | 5981 | 7796 | 7994 | 6299 | 8578 |
| PPF2 | 135724 | 73442 | 90816 | 39770 | 43692 | 32595 | 36176 | 48059 | 47140 | 37559 | 51401 |
| PPF3 | 784330 | 461236 | 561421 | 174243 | 263540 | 133334 | 161474 | 257570 | 287236 | 173682 | 309100 |
| PPF4 | 5308953 | 3152770 | 5308953 | 659542 | 1161000 | 510000 | 618731 | 1000467 | 1249129 | 677662 | 1296548 |

The number of points is increasing with lowering the maximum plane error, the minimum number of points and the minimum and maximum search radii. The points resulting from PPF4 are roughly 100 to 200 times the points resulting from PPF1. While for SP01 in 2016, 6416 points of PPF1 are 0.1% of the original 6,002,675 points of SP01, the proportion rises to about 11% of the original data using PPF4. It shall be emphasized, that the points resulting from the plane patch filter are no original raw data points but the center of gravity of the area of points used for the filtering (see Chapter 3.3.3).

Figure 24 shows where the polydata of the different plane patch filter are distributed over the point cloud. The increasing density is clearly visible from PPF1 to PPF4 with a domination of polydata on the vegetated areas and, considering PPF4, rock cleavages.

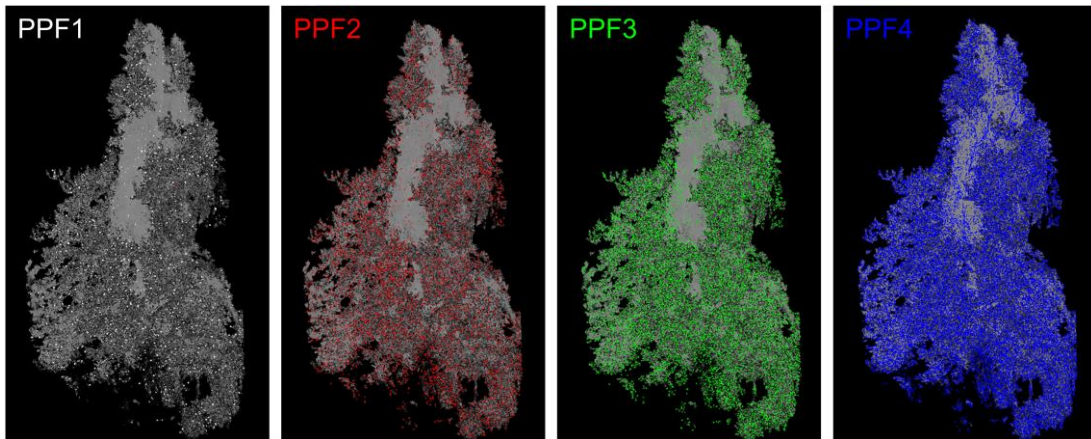


Figure 24: *Distribution of the polydata extracted by plane patch filter, exemplarily for SP01 of 2016 data*

Using this polydata and the tie points, the MSA is performed allowing for variable settings. One scan position is set as model point cloud and two (or one in 2017b) as data point cloud. The settings are refined within the testing process. Therefore, the test is an iterative process with primary a constant convergence of the point clouds. Following, the results for 2016 (see Table 6) are presented, the results of the other epochs and the histograms of the residues for all MSAs are attached in Appendix B and Appendix D.

5. RESULTS

Table 6: Example of the MSA registration test: test data 2016, SP01 as model point cloud, SP02 and SP03 as data point clouds, histograms of the residues added in Appendix D

| Epoch | Input Data | Parameters | | Statistics | | | Histogram of residues (see Appendix D) |
|-------------|-------------------------------|-----------------------------------|-----------------------------|-------------------------------|---|----------|--|
| | | Search radius [m] | Maximum tilt angle [degree] | Error: standard deviation [m] | Number of observations used for calculation | | |
| | | | | | Tie points | Polydata | |
| 2016 (3 SP) | Tiepoints | no changes with changing settings | | 0.0058 | 30 | 0 | 2016-TP |
| | Tie points & Polydata (PPF 1) | 0.5 | 15 | 0.0291 | 33 | 4010 | 2016-PPF1-01 |
| | | 0.2 | 15 | 0.0177 | 33 | 1670 | 2016-PPF1-02 |
| | | 0.1 | 15 | 0.0143 | 33 | 602 | 2016-PPF1-03 |
| | | 0.05 | 15 | 0.0103 | 33 | 175 | 2016-PPF1-04 |
| | | 0.5 | 10 | 0.0264 | 33 | 2573 | 2016-PPF1-05 |
| | | 0.2 | 10 | 0.016 | 33 | 1089 | 2016-PPF1-06 |
| | | 0.1 | 10 | 0.013 | 33 | 430 | 2016-PPF1-07 |
| | | 0.05 | 10 | 0.0095 | 33 | 132 | 2016-PPF1-08 |
| | | 0.5 | 5 | 0.0229 | 33 | 936 | 2016-PPF1-09 |
| | | 0.2 | 5 | 0.0143 | 33 | 423 | 2016-PPF1-10 |
| | | 0.1 | 5 | 0.0103 | 33 | 166 | 2016-PPF1-11 |
| | | 0.05 | 5 | 0.0079 | 33 | 55 | 2016-PPF1-12 |
| | Tie points & Polydata (PPF 2) | 0.5 | 15 | 0.0738 | 33 | 33421 | 2016-PPF2-01 |
| | | 0.2 | 15 | 0.0172 | 33 | 14266 | 2016-PPF2-02 |
| | | 0.1 | 15 | 0.0124 | 33 | 6225 | 2016-PPF2-03 |
| | | 0.05 | 15 | 0.0095 | 33 | 2102 | 2016-PPF2-04 |
| | | 0.5 | 10 | 0.0717 | 33 | 20384 | 2016-PPF2-05 |
| | | 0.2 | 10 | 0.0159 | 33 | 8296 | 2016-PPF2-06 |
| | | 0.1 | 10 | 0.0115 | 33 | 3654 | 2016-PPF2-07 |
| | | 0.05 | 10 | 0.0088 | 33 | 1270 | 2016-PPF2-08 |
| | | 0.5 | 5 | 0.068 | 33 | 6920 | 2016-PPF2-09 |
| | | 0.2 | 5 | 0.015 | 33 | 2668 | 2016-PPF2-10 |
| | | 0.1 | 5 | 0.0103 | 33 | 1245 | 2016-PPF2-11 |
| | | 0.05 | 5 | 0.0076 | 33 | 462 | 2016-PPF2-12 |
| | Tie points & Polydata (PPF 3) | 0.5 | 15 | 0.0913 | 33 | 330404 | 2016-PPF3-01 |
| | | 0.2 | 15 | 0.0397 | 33 | 126438 | 2016-PPF3-02 |
| | | 0.1 | 15 | 0.0169 | 33 | 48476 | 2016-PPF3-03 |
| | | 0.05 | 15 | 0.0099 | 33 | 16173 | 2016-PPF3-04 |
| | | 0.02 | 15 | 0.0059 | 33 | 2635 | 2016-PPF3-05 |
| | | 0.5 | 10 | 0.1127 | 33 | 236735 | 2016-PPF3-06 |
| | | 0.2 | 10 | 0.0394 | 33 | 69867 | 2016-PPF3-07 |
| | | 0.1 | 10 | 0.0159 | 33 | 25525 | 2016-PPF3-08 |
| | | 0.05 | 10 | 0.0091 | 33 | 8699 | 2016-PPF3-09 |
| | | 0.02 | 10 | 0.0055 | 33 | 1481 | 2016-PPF3-10 |
| | | 0.5 | 5 | 0.1319 | 33 | 95909 | 2016-PPF3-11 |
| | | 0.2 | 5 | 0.0383 | 33 | 20784 | 2016-PPF3-12 |
| | | 0.1 | 5 | 0.0146 | 33 | 7400 | 2016-PPF3-13 |
| | | 0.05 | 5 | 0.0082 | 33 | 2593 | 2016-PPF3-14 |
| | | 0.02 | 5 | 0.0052 | 33 | 502 | 2016-PPF3-15 |
| | Tie points & Polydata (PPF 4) | 0.5 | 15 | 0.0564 | 33 | 1856606 | 2016-PPF4-01 |
| | | 0.2 | 15 | 0.0392 | 33 | 1074177 | 2016-PPF4-02 |
| | | 0.1 | 15 | 0.0188 | 33 | 515352 | 2016-PPF4-03 |
| | | 0.05 | 15 | 0.0081 | 33 | 219192 | 2016-PPF4-04 |
| | | 0.02 | 15 | 0.0039 | 33 | 54233 | 2016-PPF4-05 |
| | | 0.5 | 10 | 0.0805 | 33 | 1596878 | 2016-PPF4-06 |
| | | 0.2 | 10 | 0.0427 | 33 | 721725 | 2016-PPF4-07 |
| | | 0.1 | 10 | 0.0183 | 33 | 300454 | 2016-PPF4-08 |
| | | 0.05 | 10 | 0.0075 | 33 | 117766 | 2016-PPF4-09 |
| | | 0.02 | 10 | 0.0036 | 33 | 29021 | 2016-PPF4-10 |
| | | 0.5 | 5 | 0.1181 | 33 | 984885 | 2016-PPF4-11 |
| | | 0.2 | 5 | 0.0435 | 33 | 282239 | 2016-PPF4-12 |
| | | 0.1 | 5 | 0.0172 | 33 | 96244 | 2016-PPF4-13 |
| | | 0.05 | 5 | 0.007 | 33 | 34902 | 2016-PPF4-14 |
| | | 0.02 | 5 | 0.0034 | 33 | 8679 | 2016-PPF4-15 |

With a maximum tilt angle of 15° , the best results considering the standard deviation (smaller than 0.01 m) are shown using PPF4, 3 and 2 and a low search radius of 0.02 m or 0.05 m. The used polydata varies from 2102 points with a maximum search radius of 0.05 m and PPF2 to 219192 points with a maximum search radius of 0.05 m and PPF4. Similar results considering the relations of PPF, search radius, number of points and standard deviation are shown with a maximum tilt angle of 10° and 5° . A lowering of the maximum tilt angle leads to a decreasing number of used polydata used errors. While the number of used polydata is roughly halved when using a maximum tilt angle of 10° instead of 15° , the decreasing of the standard deviation emerges only in the range of 10^{-4} m. With 10° maximum tilt angle, six test settings lead to a sub-centimeter standard deviation. Lowering the maximum tilt angle from 10° to 5° , the number of polydata used for the registration is lowered to less than 1/3, while the decreasing of the error is still in sub-millimeter range and still six settings show sub-centimeter standard deviations.

Taking the search radius in focus, it is shown that this setting is more sensitive using fine plane patch filter. A search radius of 0.5 m leads to standard deviation values of 0.056 m, increasing with PPF2, 3 and 4. The highest errors over 0.1 m correspond with PPF3 and 4 and maximum tilt angles of 5° and 10° . PPF1 leads to the lowest error values when using a 0.5 m search radius – all three maximum tilt angle settings are followed by standard deviations lower than 0.03 m. Lowering the search radius leads to lower error values and decreasing of the number of used polydata, but the results are not as proportional as for change of maximum tilt angle described above. While a search radius of 0.2 m or 0.1 m shows the smallest errors using polydata from PPF1 and 2, lowering the search radius to 0.05 m leads to the smallest error values using PPF4 corresponding with a higher number of polydata in comparison to PPF2 and PPF1. The search radius of 0.02 m is only tested on PPF3 and PPF4, as the number of polydata used on PPF1 and PPF2 is lower than 100 with these settings. Therefore too little improvement in number of points has been accomplished (considering the tie point registration).

The overall smallest standard deviation is reached using PPF4, a search radius of 0.02 m and a maximum tilt angle of 5° : the resulting error is 0.0034 m and 33 tie points and 8679 polydata points are used. Increasing the maximum tilt angle to 10° leads to more than triple polydata points (29021) with an error of 0.0036 m. All in all, 17 different settings lead to sub-centimeter errors with the largest number of polydata (219192) using PPF4, a 0.05 m search radius and 15° maximum tilt angle.

5. RESULTS

The visual interpretation of the histograms of the residues (Appendix D) shows that the residues are symmetrically distributed around 0 m.

For comparing the performance of MSA in RiSCAN PRO and ICP in CloudCompare, SP01 and SP02 from the 2016 data are used as test samples. As CloudCompare only allows to register one point cloud to another at a time, the tests for the MSA are performed again using only SP01 as model point cloud and SP02 as data point cloud. For the first test, the original point cloud data is used. For a second test run, the point clouds are cropped to the upper part of Amtmann decreasing the total number of points to 5.2% on SP01 (314,536 of 6,002,675) and to 3.3% on SP02 (385,323 of 11,765,226). The idea behind the second test run is, that the main interest is on a good registration of the point clouds for the focus area. If the results for the registration of the selected area are significantly better than for the whole point cloud, the transformation parameters for the main area of interest are applied to the rest of the data. For the MSA, PPF4 is used as it leads to the largest number of polydata. The tests are also performed using PPF3. The results are, next to the detailed results of PPF4, depicted in Appendix C, but not further discussed. The ICP in CloudCompare is also performed using a large number of points (the raw data) and it is intended that the results are on some level comparable. The settings for the MSA are the same as in the first test run, adding three test runs with 3 m search radius and 45° maximum tilt angle, 5 m search radius and 90° maximum tilt angle and 10 m search radius with 180° maximum tilt angle. These settings are chosen on purpose to lower and finally eliminate the effect of the surface normal within the polydata of the plane patch filter. Furthermore, after every MSA, the registration is set back to the results of tie point registration to prevent effects of convergence. The ICP in CloudCompare is performed with varying the chosen settings of the maximum number of points used as a random sampling limit ($5 \cdot 10^4$, $5 \cdot 10^5$ for both data sets and additionally $5 \cdot 10^6$ for the original data set) and different settings on final overlap of the point cloud of 100%, 75%, 50% and 25%. As in RiSCAN PRO, the original tie point registration was restored after every test.

Although both MSA and ICP are based on the ICP-algorithm, the customizing parameters vary between the two methods. While the ICP registration in CloudCompare uses a fixed maximum number of sample points (the number is lower if the maximum of the available points is lower than the defined level), the number of polydata RiSCAN PRO uses within the MSA arises from the settings of search radius and maximum tilt angle. Another difference is, that CloudCompare works with (a subset of) original data points, while the MSA uses the polydata objects which result from the plane patch filter and are defined by the gravity point of the extracted planes.

Concerning the error which represents the quality of registration, CloudCompare gives the RMSD of the related point pairs and RiSCAN PRO the standard deviation of the distance between the related point pairs. While the RMSD (see Equation 6) is simply based on the distance between the related points using the Euclidian metric (see Chapter 3.3.2), the standard deviation (see Equation 9) is based on the difference between two related points and the mean difference of all point pairs (see 3.3.4). As the MSA does not allow to export the residues of the registration numerically, the histograms are used for further considerations. As seen in the histograms of the residues in Appendix D and already described above within the first registration tests, the residues of the MSA are symmetrically distributed around 0 m. Therefore, it is assumed that the mean value of the MSA residues is 0 m, resulting in equating of RMSD and standard deviation as squaring leads to a positive value which eliminates the impact of the plus/minus sign depicted in Equation 11.

$$s = \sqrt{\frac{\sum_{i=1}^n (D_i - \bar{D})^2}{n}} \xrightarrow{\bar{D}=0} s = \sqrt{\frac{\sum_{i=1}^n (D_i)^2}{n}} = \sqrt{\frac{\sum_{i=1}^n (d_i)^2}{n}} = \text{RMSD}$$

s ... standard deviation of the point pair distances
D_i ... difference between the points of an associated point pair
 \bar{D} ... mean point pair difference
d_i ... difference between the points of an associated point pair
n ... number of associated point pairs
RMSD ... root – mean – square difference

(Equation 11)

Consequently, the two error values (standard deviation for MSA and RMSD for ICP) can be compared, as they are measuring the same. Furthermore, the points used for the registration within the ICP as well as the polydata (gravity points with normal vectors) used for MSA are treated equally.

After dealing with theoretical considerations on comparing the two registration approaches, the registration tests on the 2016 data are performed. The results of the two comparing registration tests are visually prepared in Figure 25 and Figure 26. The numerical results are listed in Appendix C. In both illustrations, the upper semicircle plotting area shows the results of the MSA, the lower semicircle plotting area the results of the ICP. The distance to the center point, which is marked with a small x in the center of the corresponding bubble, represents the registration quality using the equivalent standard deviation and RMSD on a logarithmic scale up to 1 m. The legends on the right side of the figure show the chosen settings, which differ between the registration methods. The customized MSA-settings are visualized in the color-coded search radius and the maximum tilt angle, which is indicated in the inclination

5. RESULTS

of the axis. The variable settings of the ICP are the number of points used for the calculation which is shown by the bubble area and derived from the random sample limit and the theoretical overlap in percentage, which is differentiated by the angle of the axis in the lower semicircle plotting area. For the MSA, the size of the circle is also a result of the registration process and is therefore also described within the plotting area. It is stressed that both bubble area legends within one figure use the same scale, the double implementation is just due to better clarity of the whole figure.

Regarding the MSA shown in Figure 25 with a focus on the maximum tilt angles of 5° , 10° and 15° , the search radius of 0.5 m leads to more accurate registration with increasing of the tilt angle. Hence, the number of observations used for the calculation rises. This also applies for the search radius of 0.2 m, but the decreasing of the standard deviation is smaller. Beginning with the search radius of 0.1 m and smaller, the standard deviation rises with increasing of the maximum tilt angle. The number of observations is still constantly increasing with higher maximum tilt angle values. For investigation of results using unusually large maximum tilt angles and search radii, the settings 45° maximum tilt angle with 3 m search radius, 90° maximum tilt angle with 5 m search radius and 180° maximum tilt angle with 10 m search radius are tested. Apart from long computational time (more than 6 hours for the $180^\circ/10$ m settings), the results according to standard deviation are, especially referring to the $180^\circ/10$ m settings with a standard deviation of 0.0066 m, in the range of the finer settings. Therefore, for 180° , the other used search radii are also tested. Comparing the results of low maximum tilt angle registration with complete exclusion of the maximum tilt angle by setting the value to 180° , the standard deviation values with a search radius of 0.5 m, 0.2 m and 0.1 m are smaller than with the tilt angles of 5° , 10° or 15° by a higher number of used polydata. Looking at the search radius of 0.05 m and 0.02 m, the standard deviation is slightly higher, but the number of polydata used for the calculation is 6.5 up to 53 times higher. It is furthermore noted, that the computational time drops down to 2 minutes and 3 seconds or less when using 0.5 m or less as search radius at a maximum tilt angle of 180° . Overall, 9 settings lead to a standard deviation smaller than 0.01 m. These are primary settings with a small search radius (the lowest 4 standard deviation values all go with 0.02 m search radius), but also the test setting of 10 m with 180° is with a standard deviation of 0.0066 m in this range. The number of used polydata varies from more than 1.1 million to 3620.

The registration results of the associated ICP are shown in the lower semicircle of Figure 25. For all test settings, except of 5 million points and 25% theoretical overlap (due to lack of more points, only 2.94 million points are used), the number of points

used for the calculation is equivalent to the chosen sample limit. Lowering the theoretical final overlap corresponds for all sample limits with decreasing of the final RMSD. A theoretical overlap of 100% corresponds with RMSD-values in the range of 0.37 m up to 0.55 m. For all other theoretical overlap settings, the RMSD drops (with one exception on 75% and 50,000 points) under 0.1 m. With more points used, the RMSD gets smaller within one theoretical overlap setting. The lowest RMSD, which is also the only one in sub-centimeter range, is 0.0079 m and comes with 2.94 million points and 25% theoretical overlap.

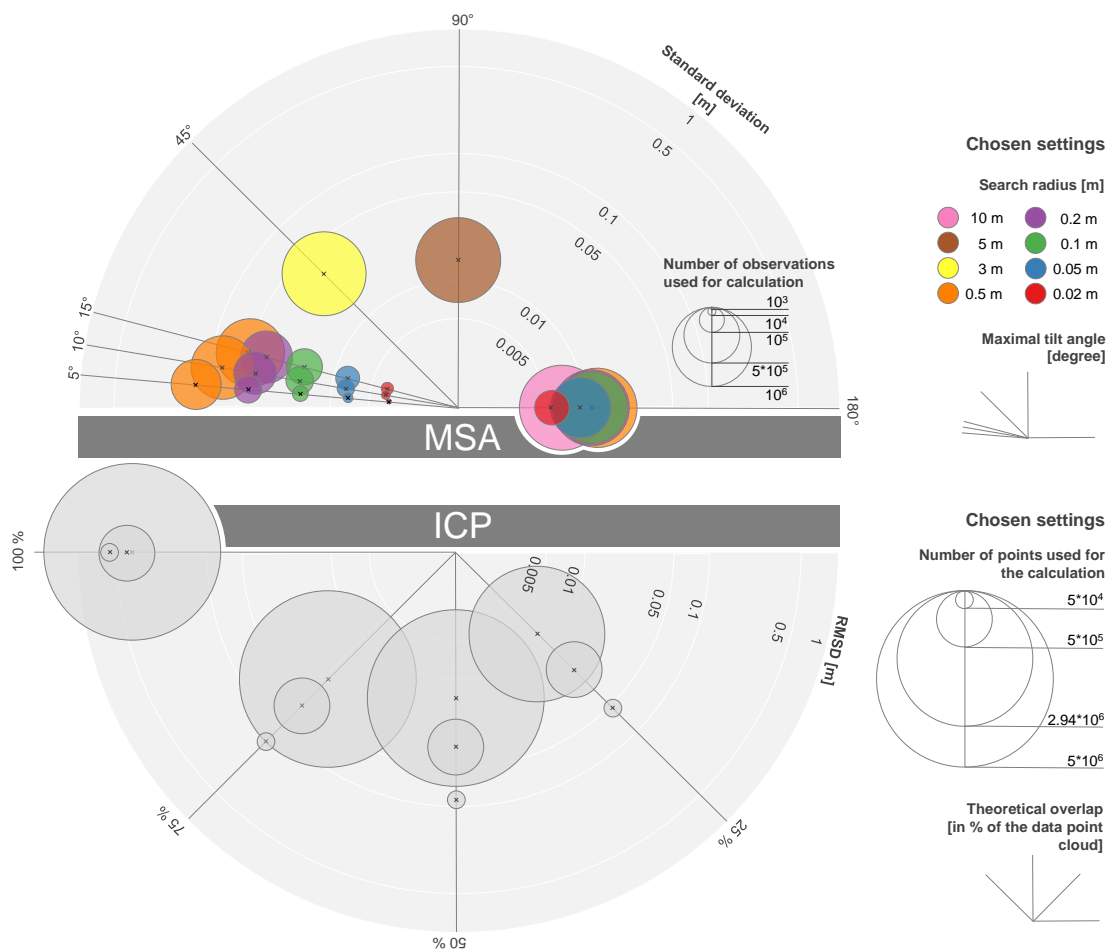


Figure 25: Output of MSA and ICP using different settings (test data: 2016, SP01 with 6,002,675 points and SP02 with 11,765,226 points)

Comparing the results of the MSA and the ICP shown in Figure 25, the first obvious difference is the number of points/observations used for the registration. While the number of observations used for the MSA registration results from the chosen settings

5. RESULTS

of maximum tilt angle and search radius and ranges from 3,629 to 1.15 million polydata, ICP registration uses the number of points as an (indirect) input parameter, and the numbers range from 50,000 to 5 million points. In contrary to the link of increasing number of points used for registration and decreasing RMSD in ICP registration, the greater number of polydata generally goes with a higher standard deviation when using MSA registration. While one registration test using ICP reaches a sub-centimeter error, 9 registration tests are linked with sub-centimeter standard deviation with the MSA. Although it is noted that the one sub-centimeter ICP registration is calculated on 2.5 times the number of points as the highest sub-centimeter registration with MSA. The upper end of all over error values is dominated by the three 100% final overlap settings of ICP.

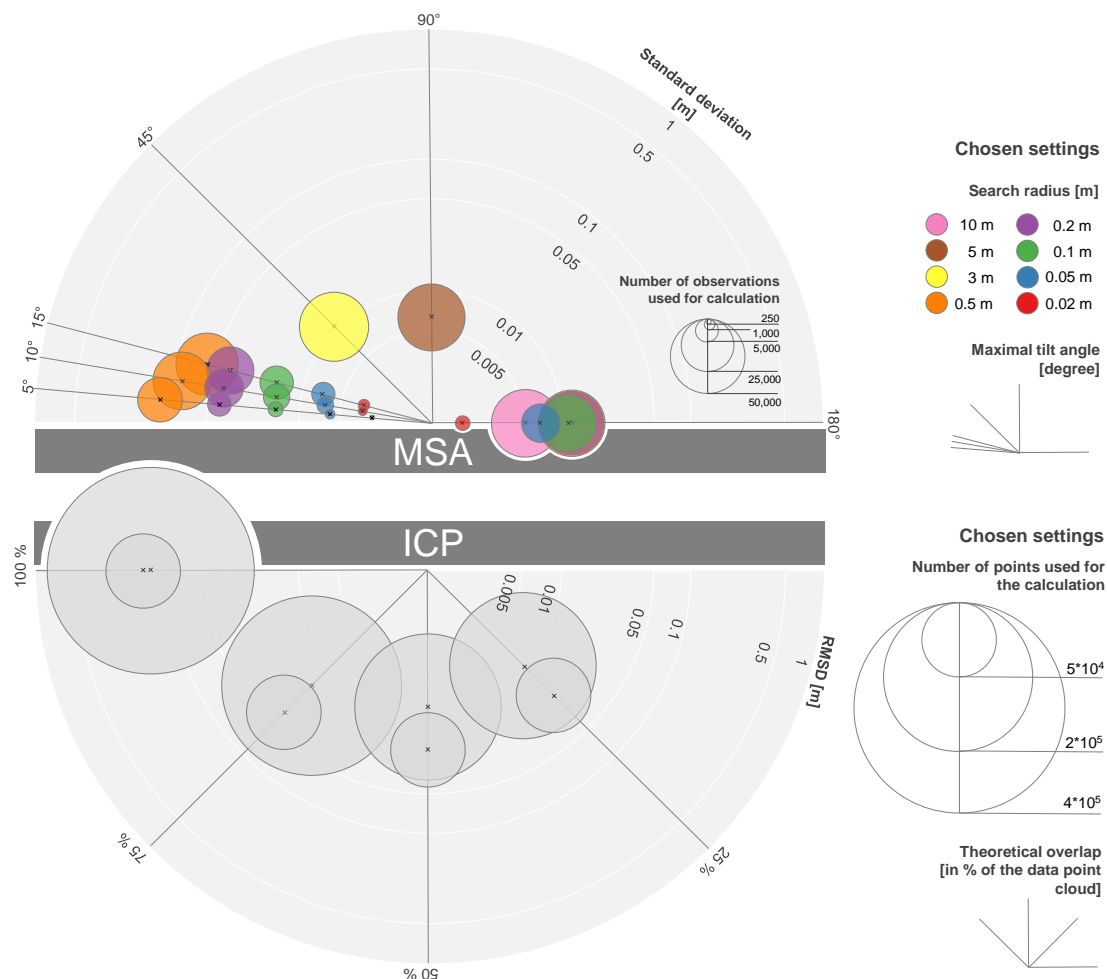


Figure 26: Output of MSA and ICP using different settings (test data: 2016, SP01 segmented using 314,536 points and SP02 segmented using 275,534 points)

For all the test settings chosen for the registration of the cropped point cloud, the computation time is 1 minute 7 seconds or lower. Referring to the results in Figure 26 (it is noted that the area legend is not equivalent to the area legend in Figure 25) and taking the maximum tilt angles from 5° to 15° in account, for the registration tests using the cropped point cloud, the same patterns as in Figure 25 are discovered: for 0.5 m and 0.2 m search radius, the standard deviation drops with higher maximum tilt angles, beginning from 0.1 m and smaller search radius and it rises slightly with a higher maximum tilt angle. Also, the number of observations is constantly rising with bigger search radii and greater maximum tilt angles. Furthermore, for the 180° maximum tilt angle, the search radii of 0.02 m, 0.05 m and 10 m show sub-centimeter standard deviation values which are higher than the values with the same search radii. From 0.1 m to 0.5 m search radius, the standard deviation values for 180° maximum tilt angle are all between 0.011 m and 0.012 m and therefore smaller than the corresponding results with lower maximum tilt angles by 1.1 up to 16.7 times the number of used polydata. The test leads to ten settings with a standard deviation smaller than 0.01 m. These are, like the results from Figure 25, settings with a small search radius (the lowest four standard deviation results with 0.02 m search radius and also all 0.05 m search radius settings are included), but also the test settings of 10 m with 180° and 5 m and 90° are sub-centimeter. The number of polydata of the sub-centimeter results varies from 190 to 40916.

The registration results of the performed ICP using the cropped point cloud are shown in the lower semicircle of Figure 26. As the chosen random sample limit of $5 \cdot 10^5$ is not reached for all different final overlap settings, the setting $5 \cdot 10^6$ is not tested for this data. As with the original data, lowering the theoretical final overlap leads to decreasing of the final RMSD for all sample limits. A theoretical overlap of 100% gives RMSD-values of 0.122 m to 0.139 m. The theoretical overlap settings of 75% and lower result in RMSD values of smaller than 0.035 m. The smallest and only sub-centimeter RMSD corresponds with 96,330 points for computation and 25% theoretical overlap.

The number of used polydata/observations for registration is, as seen in Figure 25, the most notable difference between ICP and MSA: all ICP registration tests work with more data points than the largest number of polydata. Also, the increasing number of points used for registration leads to a decreasing RMSD in ICP registration, and more used polydata leads mostly to a higher standard deviation when using MSA registration. From the eleven sub-centimeter error results, one (25% theoretical overlap and 96,330 used points) is a result of ICP registration. The two overall highest

5. RESULTS

error values with 0.122 m and 0.139 m are the ICP registrations with 100% final overlapping.

The same settings of the MSA used on the polydata extracted from the whole point cloud (Figure 25) and the polydata from the cropped sample (Figure 26) lead for the maximum tilt angles from 5° to 15° to differences from 0.0004 m to 0.0063 m. Considering the higher maximum tilt angles settings, 45° and 3 m lead to a difference of 0.0214 m, all other differences range from 0.0001 m to 0.0086 m. The number of observations for the same settings for the original data is 18 up to 98 times the number of observations of the cropped data. Comparing the results of the two ICP registration test data sets, the absolute differences of the RSDM range from 0.042 m to 0.41 m with same settings on random sampling limit and theoretical final. In perspective, the RMSD values of all data registration are 2.9 to 4 times the RMSD values of the cropped data registration by the same number of points for the $5 \cdot 10^4$ random sampling limit and 1.3 to 5.2 times the number of points for the $5 \cdot 10^5$ random sampling limit.

Figure 27 contrasts the errors and numbers of used data points of MSA and ICP in two scatter plots. For this illustration, also the results of the MSA from testing with PPF3 are used. Both plots show that ICP reaches a larger number of observations. On the contrary, MSA gives the lower registration error results.

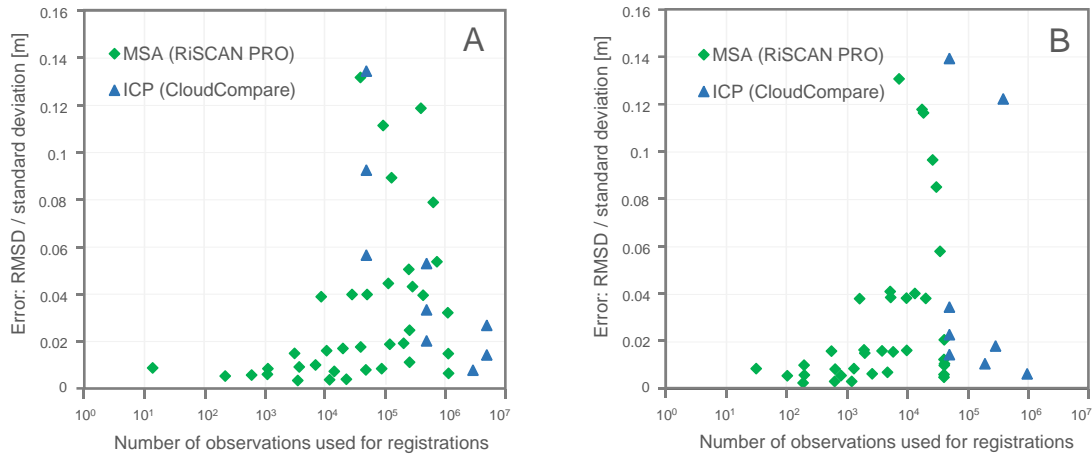


Figure 27: Comparing MSA and ICP - Error and numbers of observations used for registration. A: using all data, B: using cropped data

Concluding from the overall evaluation, the fine registration of the data for further processing is performed using the ICP in CloudCompare with a theoretical final overlap of 25%. (due to changing vegetation, especially considering the co-

registration, and smallest RMSD). In order to get overall acceptable results, all data are used and the maximum sample limit is set to of 5 million points. This decision is based on the comparable sub-centimeter ICP and MSA results within the registration test, the globally spread points used for the registration of ICP in comparison to the domination of vegetation based polydata for MSA and the preference of using open source software.

5.3.3 Fine registration: final registration

The parameters of the registration for all scan positions using ICP in CloudCompare are shown in Table 7. Within all fine registration steps, lowering the RMSD compared to the initial coarse registration is reached. While the final RMSD of 2016, 2017a and 2017b with all scan positions is in sub-centimeter range or just above (1.09 cm for 2017a), the 2014 data gives a final RMSD of 5.62 cm.

Table 7: Output of the final registration realized using ICP (CloudCompare). Settings: minimum change of RMS per iteration of 10^{-5} m, final overlap 25%, random sampling limit $5 \cdot 10^6$ points

| | 2014 | 2016 | 2017a | 2017b |
|---------------------------------------|--|----------------|----------------|----------------|
| | SP01 (model) & SP02 (data) | | | |
| Initial RMSD [m] | 0.02377 | 0.00802 | 0.00921 | 0.01203 |
| Number of points used for computation | 3,055,450 | 2,941,306 | 2,345,237 | 3,223,577 |
| Final RMSD [m] | 0.01387 | 0.00797 | 0.00852 | 0.00923 |
| | merge SP01 and SP02 SP01+SP02 (model) & SP03 (data) | | | - |
| Initial RMSD [m] | 0.06247 | 0.00811 | 0.01218 | |
| Number of points used for computation | 3,167,136 | 1,170,890 | 3,132,487 | |
| Final RMSD [m] | 0.05623 | 0.00777 | 0.01088 | |
| | merge and export | | | |
| Number of points | 43,756,493 | 22,451,461 | 27,614,924 | 19,269,988 |

Figure 28 shows the visual results of the registration. The big greyscale image illustrates the result colored by intensity. The red lines indicate the cross-sections (parallel to the x-y plane) shown below the point cloud image. On the right side, for all epochs, the different scan positions are shown in different colors with a last image combining all scan positions colored in the colors of the point clouds.

5. RESULTS

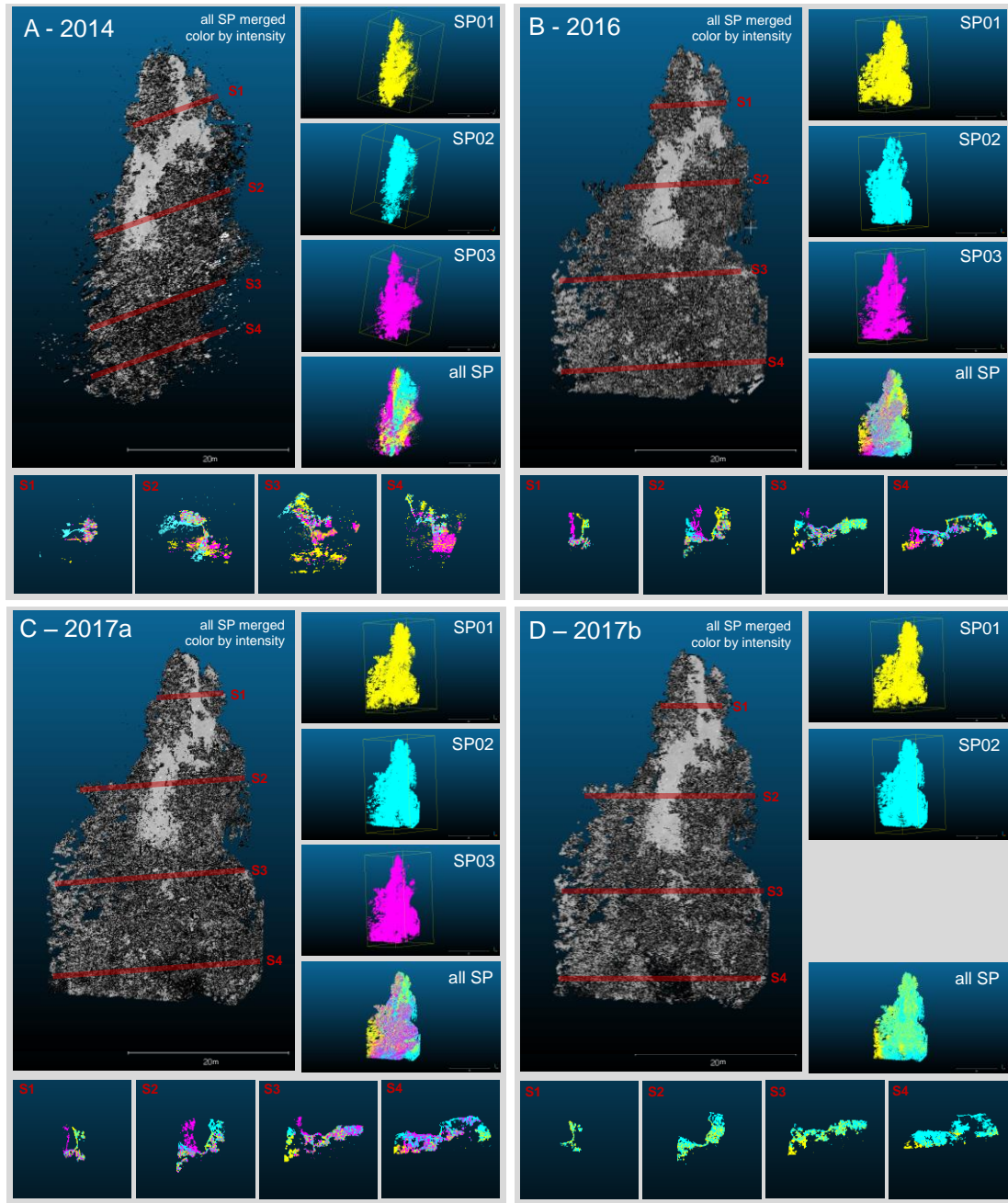


Figure 28: Visual presentation of the final registration for all four epochs

The cross-sections below the image are also colored using the point colors of the corresponding scan positions. Referring to all SP illustration in B, C and D, a mixture of the colors of the different scan positions is shown, whereas in the all SP illustration in A representing the 2014 data, the three colors representing the three different scan positions can clearly be distinguished. Concerning the different cross sections of

2016, 2017a and 2017b data, one rock surface can be identified drawn by a line of points representing the different scan positions. Considering the cross sections of the 2014 data, scattering of points does not allow to identify distinct surface borders.

5.4 Extraction and co-registration

The co-registration of the different epochs follows the same workflow as the registration of the different scan positions. Between the coarse and the fine registration, the point cloud of the different epochs is cropped to the final area of interest. The 2016 point cloud is chosen as the model point cloud for all co-registrations and defines therefore the final coordinate system for the data processing within this thesis.

For the coarse registration of the 2014 data, initially seven point pairs distributed along the upper part of the rock structure are identified (see Figure 29). The seven point pairs lead to an achievable RMSD of 0.2983 m. Different combinations of subsets of the point pairs are tested to lower the RMSD, and finally five point pairs with a RMSD of 0.0667 m are used for the manual coarse registration.

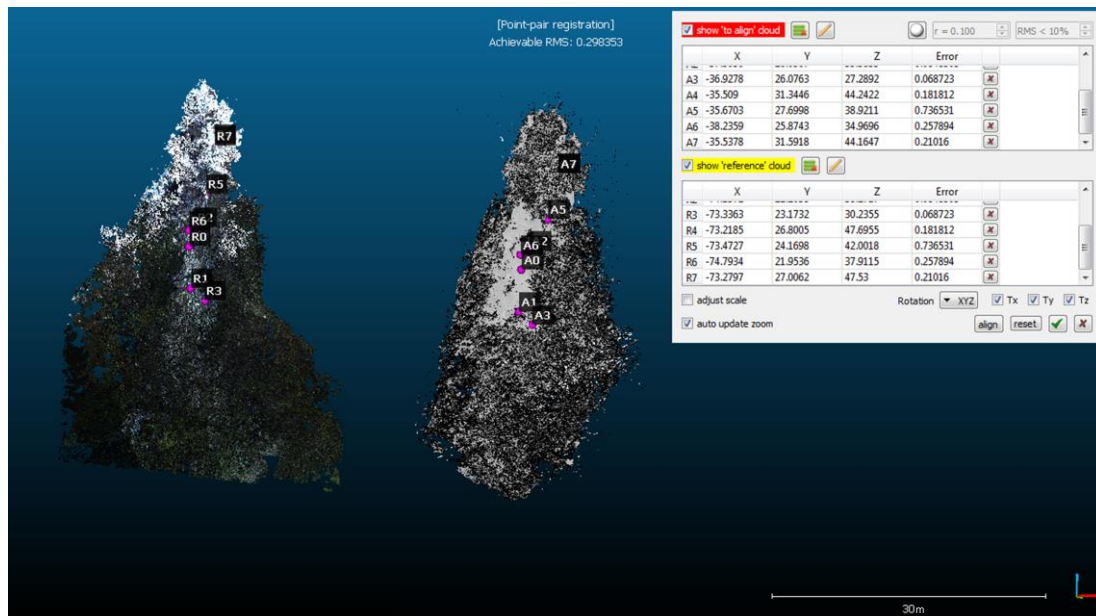


Figure 29: Screenshot: Coarse co-registration using manual point pair picking in CloudCompare

5. RESULTS

For the registration of 2017a and 2017b data, coarse registration, which was already performed during the scan position registration, is further used. Table 8 shows the errors (RMSD for the manual point picking registration performed in CloudCompare and the standard deviation for the tie point registration in RiSCAN PRO) of the coarse co-registration. While the standard deviation values from the tie point registration are below 0.005 m, the manual coarse registration is, as already described, with 0.067 m more than ten times higher. After the coarse registration, the point clouds are cropped to the final area of interest which is covered by the point clouds of all different epochs. Therefore, 35% - 36.5% of the points of each point cloud are removed.

Table 8: Co-registration of the point clouds from the different scanning campaigns

| | | | | |
|--|--|---------------------------|----------------------------|----------------------------|
| coarse registration | Model point cloud | 2016 – 22,451,461 points | | |
| | Data point clouds [SC / number of points] | 2014 59,107,864 | 2017a 27,614,942 | 2017b 19,269,998 |
| | Method | point pair picking | tie point registration | tie point registration |
| | Number of used point | 5 | 13 | 15 |
| | RMSD / standard deviation [m] | 0.0667 | 0.0038 | 0.0046 |
| cropping to the final area of interest | | | | |
| fine registration | Model point cloud | 2016 - 14,449,463 points | | |
| | Data point clouds | 2014 38,412,243 points | 2017a 17,787,617 points | 2017b 12,238,307 points |
| | Method | ICP (CloudCompare) | ICP (CloudCompare) | ICP (CloudCompare) |
| | Selected points for registration [number of points / percentages of the point cloud] | 17,628,563 (45%) | 13,976,446 (78%) | 9,667,165 (78%) |
| | Initial RMSD (calculated on the selected points) [m] | 0.0230 | 0.0086 | 0.0081 |
| | Number of points used for computation | 4,999,999 | 3,059,576 | 4,446,904 |
| | Final RMSD [m] | 0.0197 | 0.0077 | 0.0077 |
| | | | | |

The fine co-registration is performed on the cropped point clouds, using again 2016 as model data for fine co-registration of the other epochs. The different processing parameters and the results are shown in Table 8. Chosen a final theoretical overlap of 25%, 45% of the 2014 data points and 78% of the 2017a and 2017b data points are selected by the algorithm. The initial RMSD is calculated on these selected points. For the 2014 data, this value shows with 0.023 m a 0.044 m lower RMSD as calculated on the five manually picked point pairs. On the contrary, the initial RMSD calculated on the 2017a and 2017b is higher than the standard deviation from the tie point registration. It shall be emphasized, that, with a low sample of only 13 or 15 points for the tie point registration, the mean cannot be assumed as 0 and therefore

the standard deviation cannot be directly compared with the RMSD. The ICP fine registration results for all three to be registered epochs in decreasing of the initial RMSD. For 2014, with 0.0033 m the largest absolute reduction is reached, for 2017a, the RMSD is lowered 0.0009 m and for 2017b 0.0004 m. For 2017a and 2017b, with a final RMSD of 0.0077 m for both epochs, a sub-centimeter range is reached. For 2014, the final RMSD amounts 0.0197 m.

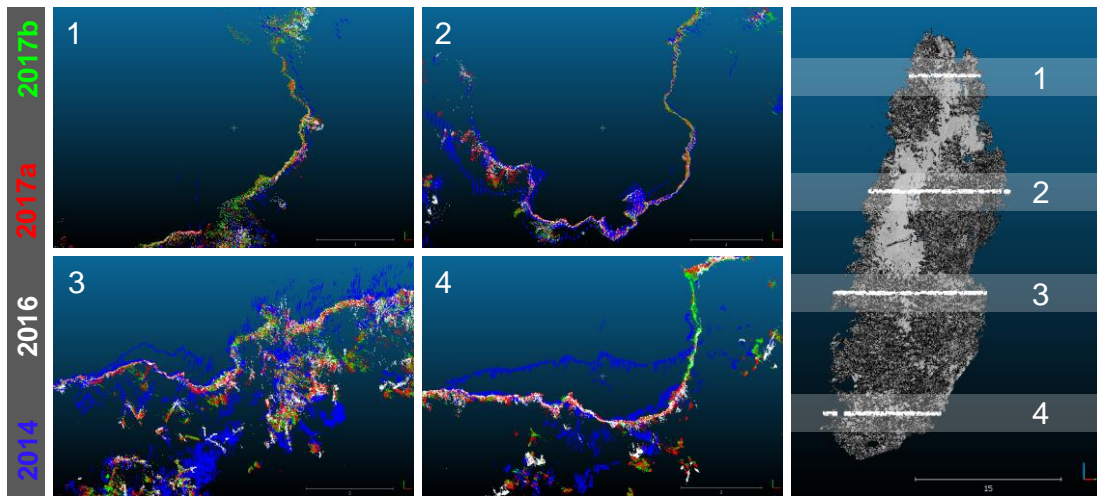


Figure 30: Cross-sections of the four co-registered point clouds revealing the co-registration quality

Figure 30 shows cross-sections of the co-registered point clouds. For all four sections, the white, red and green points representing the scanning campaigns of 2016, 2017a and 2017b overlap, the blue points, representing the scanning campaign 2014, are partly covering the other point data, as well as exhibit parts of clear distance to the points of the other three scanning campaigns.

5.5 Filtering

The filtering process is divided to the removal of the vegetation and homogenization of the point cloud. For the vegetation removal, a combination of classification based on the geometry of the point cloud and intensity values is used. The homogenization of the point cloud is based on statistical outlier removal and minimum point distance.

5.5.1 Removing the vegetation

The vegetation removal includes geometric and intensity based filtering. In a first step, the “rock” and “vegetation” areas for the training of the CANUPO filtering algorithm are defined and the training is performed. The results of the classification training are shown in Figure 31. Rock surfaces (1.2 million points) and different vegetation structures (6.5 million points) are extracted from the 2016 point cloud. The adapted PCA identifies the projection of the N dimension ($N = 100$ in this case, as 50 scale levels considering two different dimensions are chosen) which discriminates the two groups best using the LDA criteria on a plane. The discrimination line is left on the default value. The classification results in a balanced accuracy of 0.95, which indicates that 95% of the training data set points are correctly rated by the statistical classification. Looking to the sample classification, the classification of rock reaches 1.6 percentage points more truly classified points than vegetation. The Fisher Discriminant Ratio, describing the quality of the class discrimination, shows a value of 6.88.

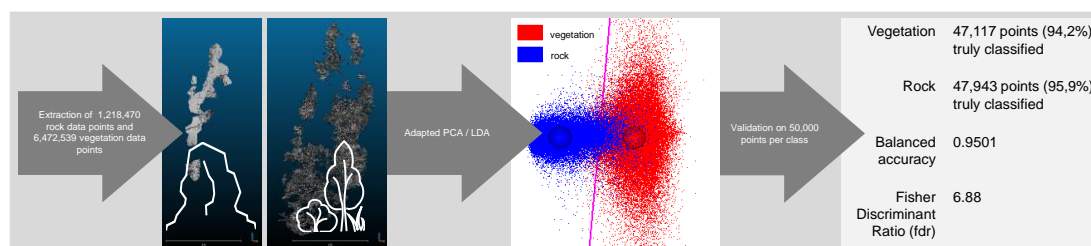


Figure 31: Training of the CANUPO classification using the 2016 point cloud data

The trained classifier is applied to the point cloud of the different epochs. Figure 32 shows the workflow of the vegetation filtering on the example of the 2014 data. All the mentioning of illustrations in the following paragraph refers to parts of Figure 32. In a first step, the data is split into nine sections, as the CANUPO plugin crashes with too large input point clouds. The sections are shown in the left illustration A. The CANUPO classification is applied separately on the different sections, and the results are merged again. The data classes rock, vegetation and separately vegetation with lower than 95% confidence of classification are exported to individual point clouds. The low-confidence classified vegetation point cloud is again filtered. Only points with intensity values higher than 26 dB are exported again to a new point cloud. As already announced in Chapter 3.5.1, the classification is problematic at the border of the point clouds – this is reflected in stripes of missing points in the merged rock class point

cloud. Therefore, these stripes are exported from the data classified as vegetation. Illustration B shows the single derivatives, which are merged (Illustration C) for the final manual classification. The results of the algorithm based filtering still include obvious vegetation point clouds. The final filtering is performed manually by selecting and deleting vegetation points. Therefore, the point cloud is sliced in sections of 2 m height along the z-axis for better visibility and orientation and merged again after the cleaning. The result of this process is shown in illustration D. Illustration E shows a close-up of the upper part of the final vegetation filtered point cloud. The “pinstripe” structure of the data, resulting from the different vertical and horizontal resolution, is clearly visible. Illustration F shows a cross-section of the point cloud. Different layers of points resulting from the registration of the different scan positions can be identified. Illustration G shows a close-up from the lower part of the point cloud: the point cloud surface is not consistent – a lot of point cloud gaps are visible.

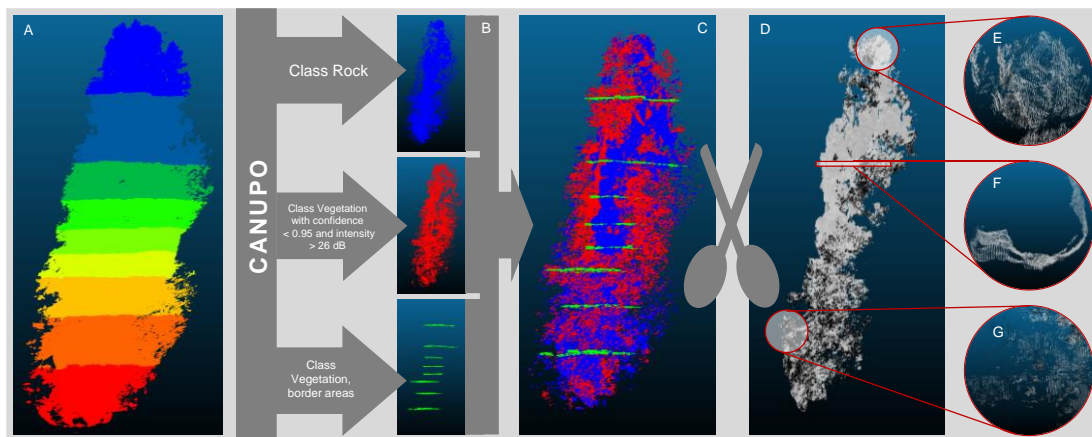


Figure 32: Workflow of vegetation filtering by the example of the 2014 data. A: Point cloud cut to 9 sections for filtering. B: Derivates from the filtering process. C: Merged combination of the selected derivatives. D: Final result of the filtering after manually filtering. E: Close-up from the upper part of the vegetation-filtered Amtmann. F: Cross-section of the point cloud. G: Close-up of a lower part of the point cloud.

The procedure for the vegetation filtering of the 2016, 2017a and 2017b data is equal to the 2014 vegetation filtering described in the last paragraph (except of only splitting the data to three sections). Therefore, the workflow for this data is not presented in detail. Figure 33 shows some chosen samples of the vegetation filtering process of these data sets. Illustration A and B demonstrate the effect of the CANUPO classification: A shows the original point cloud, B the points classified as rock after the CANUPO classification. Vegetation is clearly removed, but points scattered in the former vegetation area are still visible. Also, enlarging of the missing point data within

the region of cleavages is detected. Especially in the lower right corner of the illustration, missing rock surface points due to shadowing effects of the vegetation are noticed. Illustration C shows the cleavage-filling effect of the low-vegetation-confidence and high-intensity derivate (red data points) to the rock-classified data points (greyscale points) of the 2016 point cloud. A clear reduction of the missing data points in the cleavage areas is visible. Illustration D shows the final result of the vegetation filtering (including manual filtering) of the 2017b point cloud. The point cloud does not show a continuous surface, gaps on different scales are visible all over the point cloud. Four cross-sections of one m height with distances of 12 m, indicated by light-grey coloring of the points in the all over data view, are shown in the circles on the right side. For all cross-sections, only one surface layer is detected.

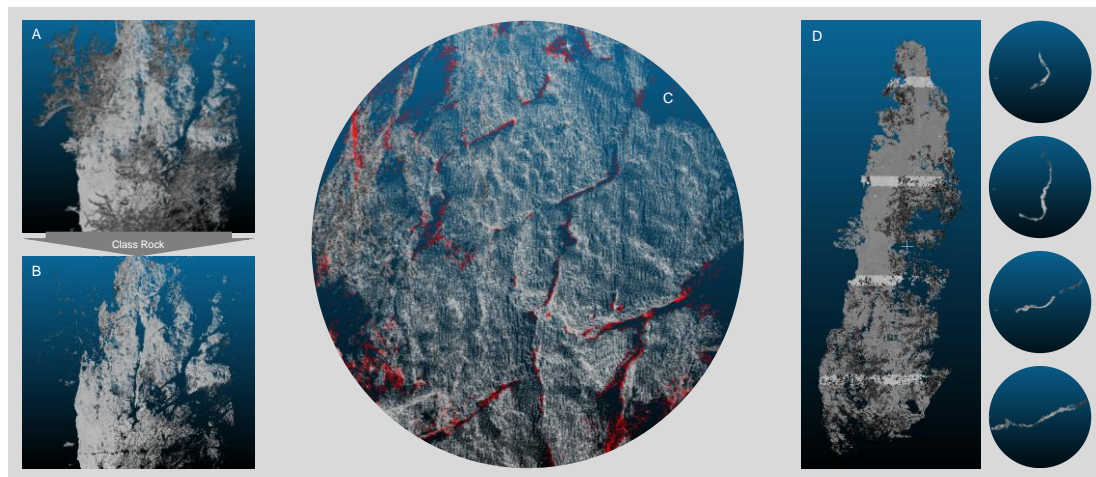


Figure 33: Examples of detailed results of the vegetation filtering. A: Original top part of the 2016 point cloud. B: Classified as "rock": detail section shown in A after applying the CANUPO filter. C: Close-up of 2017a data: points classified as rock and filling of the gaps using intensity filtered low confidence vegetation data. D: Results after the final manual vegetation filtering of the 2017b data with four cross-sections.

5.5.2 Further filtering

After the removal of the vegetation, further steps of processing of the point cloud are performed. For visualization of detailed changes, a close-up of the results of the two following filtering steps for all four point clouds is shown in Figure 34. The following description refers to single images within this figure. To exclude points, which are far away from the rest of the point cloud and are therefore no benefit in representing the rock surface, the SOR-filter is applied. For the calculation of the statistical outlier removal, 15 neighbor points are taken in account and two standard deviations define

the outlier distance. The sections of the point cloud shown in the second row are the results of this filtering. Looking at the 2014 data, it is visible, that scattering points in the upper right part of the section are removed with this filter. On the very spot, the 2016 data shown shrinking of a separated point cluster after applying the SOR-filter. Also, several single points are removed. On the lower left part of the section, an area with lower point density is more thinned out, which is resulting in a surface gap. The 2017a and 2017b data show similar effects of SOR-filtering: scattered points in the upper right part of the sections are removed with a few single remaining points in the area. The following subsampling adapts the point density – the differences between the single years and the variation of density within one point cloud due to overlapping of different scan positions are adjusted.

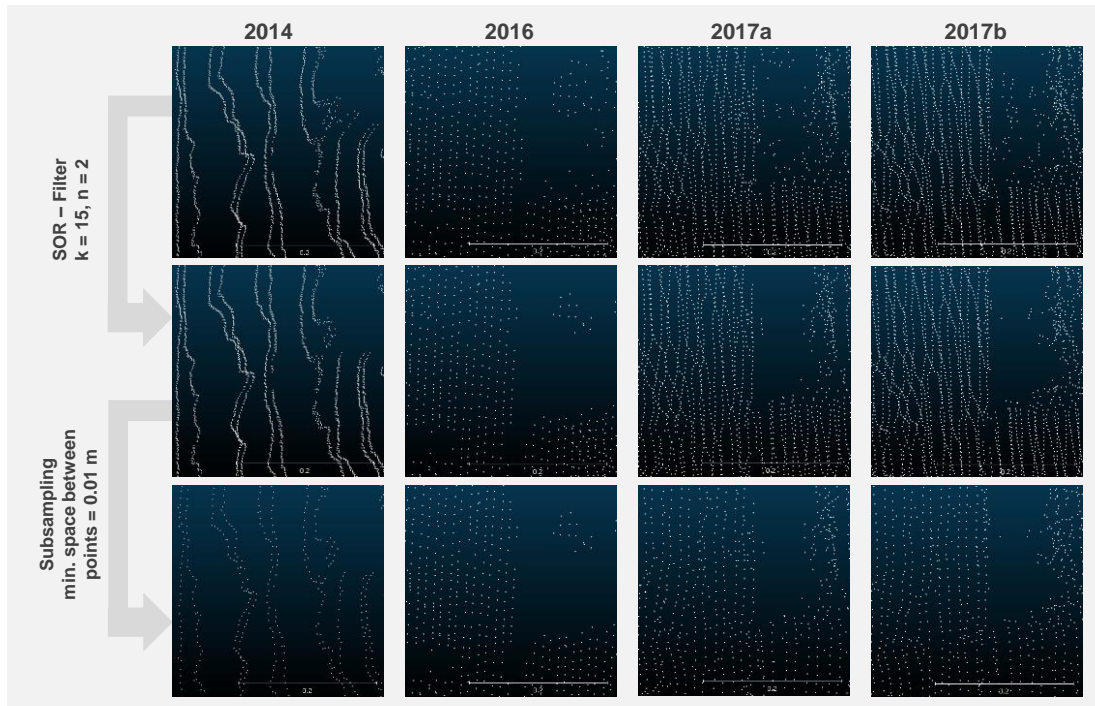


Figure 34: Close-up of the point clouds showing the different filtering steps (unit of the scale bar in m)

As the RMSD for registration and co-registration is, except for the 2014 data, below 0.01 m, a minimum distance of 0.01 m is chosen. The third row of images shows the results of the subsampling. For 2014, the vertical resolution of the point cloud is clearly thinned out. As the horizontal gaps of the vertical point lines are more than the chosen minimum distance of 0.01 m, no unification of the point cloud density in vertical and

5. RESULTS

horizontal direction is reached. In regions with overlapping scan positions, the gaps are not as dominant, but there is still a stripe structure visible and the point cloud does not have a consistent pattern. The higher point density of the SOR-filtered 2016 data in the lower right corner is thinned out by the subsampling. The 2017a and 2017b point clouds reveal again similar patterns: The points of the overlapping line structure caused by overlapping scan positions are reduced to a reasonably structured pattern with similar horizontal and vertical resolution. Only the points in the upper right corner appear still unstructured after the subsampling.

After the detailed results, the final processed point clouds are presented on a larger scale. The final representations of the rock surface after registration and filtering are shown in Figure 35. Due to final filtering, 53% to 83% of the points are excluded. The final number of points for all epochs ranges between 1.8 million and 2.5 million points.

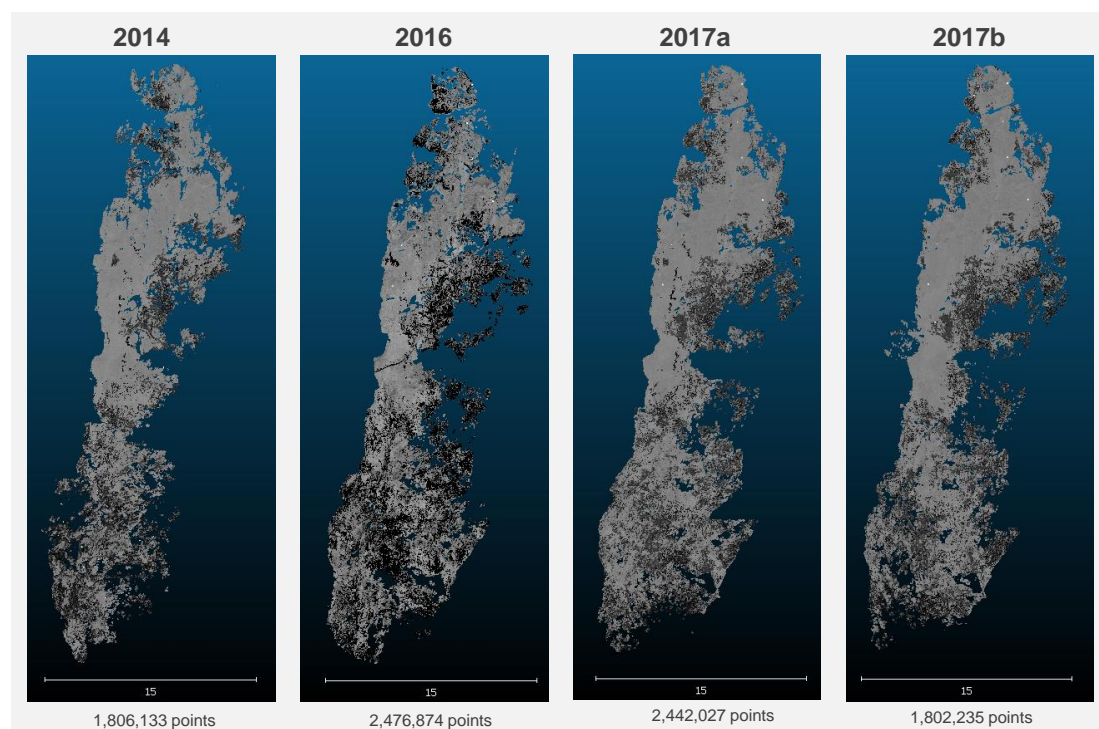


Figure 35: Final point clouds of the different epochs (colored by grey-scaled intensity values)

For all four epochs, the point clouds do not represent a continuous surface. Especially on the northern to north-eastern face of the Amtmann (represented by the right part of the illustrations in Figure 35), the surface can only be indicated by a few spotty clusters of points. The same applies to the south-eastern face, which is mapped at

the left side of the illustrations. Comparing these areas to the raw data, they come along with dense vegetation cover. From the upper right corner to the left center, a band of dense points represent, with a few gaps, a continuous part of the rock surface. The lower part of the illustrations of all epochs shows various intensity values and gaps of points scattered over the represented surface. Summarizing, for the four scanning epochs covered in this thesis, the collected TLS-data does not allow to extract a comprehensive point cloud representing the Amtmann's rock surface by using the presented registration and filtering methods.

5.6 Change detection

Change detection is performed using two different C2C and the M3C2 algorithm. Therefore, three different data combinations are used. Change detection is run combining 2014 and 2017a data, 2016 and 2017a data and 2017a and 2017b data. In all cases, the more recent data is used as the to-be-compared point cloud and the prior data as the reference point cloud. The results are presented visually with a focus on changes between 0.01 m and 0.1 m. Changes <0.01 m are precluded due to registration errors. Further, the distribution of the classes of distances <0.01 m, 0.01 m to 0.1 m and >0.1 m is discussed. Therefore, the focus is on the hot-spot-areas of the different classes. Chosen areas are extracted and presented separately. The 2017a-2017b change detection is examined more extensively.

5.6.1 Change detection comparing different epochs

Figure 36 shows the results of the 2014-2017a change detection. The C2C change detection with no local modelling classifies 9% of the 2.44 million compared points of the 2017a point cloud with a distance <0.01 m to the related 2014 point cloud. The majority of the points, 61.3%, have distances between 0.01 m and 0.1 m to the 2014 point cloud. About 30% of the points show distances >0.1 m. The mean distance is 0.1481 m with a standard deviation of 0.3132 m. View A reveals, that the point distances <0.01 m are located especially in the upper center region of the Amtmann, surrounded by areas of point distances between 0.01 m to 0.1 m. Point distances >0.1 m are most likely to be found in the lower part of the point cloud and on the border regions. Taking a closer look on the point distances from 0.01 m to 0.1 m (view B), the general trend of the distribution continues within this interval. The smaller distances are found in the center region, whereas larger distances up to 0.1 m are in the lower region of the point cloud. Adding the local quadric modelling to the C2C change detection algorithm leads to a higher percentage of point distances <0.01 m

5. RESULTS

(20.7%). The point distances between 0.01 m and 0.1 m represent also about 61% of all point distances, while the large distances >0.1 m are down to 18.3%.

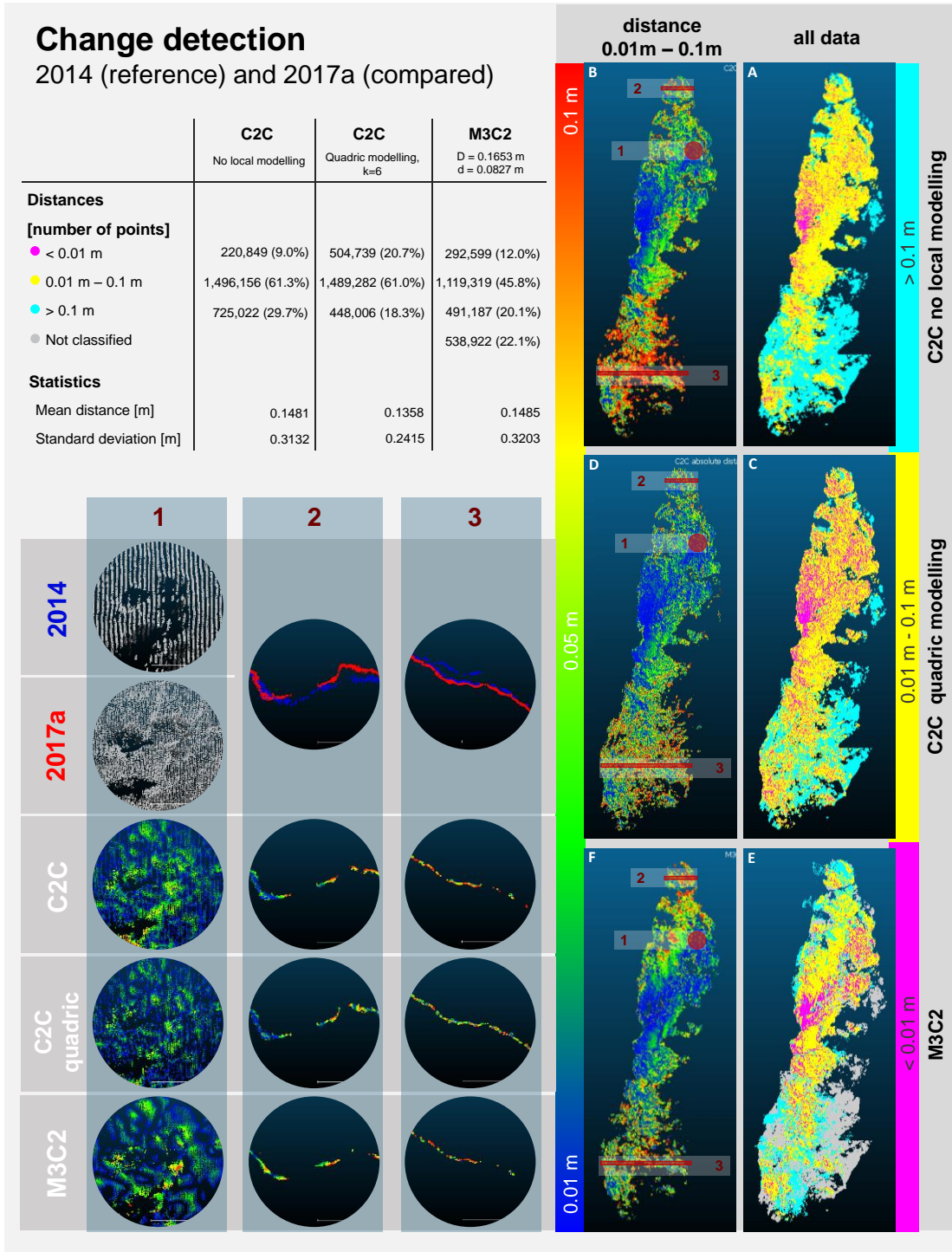


Figure 36: Results of the 2014-2017a change detection

View C reveals a distribution of the different classes similar to the distances of the C2C without local modelling. The occurrence of distances <0.01 m is more widespread within the yellow area, which represents the 0.01 m to 0.1 m distances. The mean of the distances is 0.1358 m with a standard deviation of 0.2415 m – therefore, both parameters are slightly lower than without local modelling. The differentiated look on the 0.01 m to 0.1 m distances (View D) exhibits a more inhomogeneous lower region with a mixture of distances between 0.01 m and 0.1 m. Generally, the visualization of the change interval of 0.01 m to 0.1 m is dominated by smaller distances which are displayed in blue color. The distribution of the three different distance classes using the M3C2 algorithm is illustrated in View E. The smallest distances up to 0.01 m (12% of the point distances) are again located in the center of the point cloud spreading to the upper right region of the view and to the lower parts of the point cloud. The distances from 0.01 m to 0.1 m (45.8% of the point distances) are located along the vertical center axis, while distances >0.1 m (20.1%) are found at the lower and at the very top part of the point cloud. The mean distance is 0.1485 m with a standard deviation of 0.3203 m. Both parameters are higher than the according C2C modelling results.

Further, 22.1% of the reference cloud points are not attributed with a distance to points of the 2014 point cloud and therefore displayed in grey color. These points are primary in the lower part of the Amtmann and on the borders of the point cloud. Comparing to the two C2C approaches, the point distances within the interval from 0.01 m to 0.1 m (view F) are less blended. The center region, colored in blue, is dominated by point distances close to 0.01 m. Adjoining, green areas point out an increased occurrence of distances around 0.05 m, where distances up to 0.1 m, indicated by red color, are found on the very top cloud and in the lower regions of the point cloud.

The red marks in views B, D and F indicate the location of the areas of interest shown in the left part of Figure 36. For the comparison of the areas of interest, only the point distances from 0.01 m to 0.1 m are considered. Area 1 shows a section with notable green spots within the surrounding blue area. While the C2C without local modelling shows large green to yellow areas, which indicate distances of 0.04 m to 0.07 m, the green areas with local quadric modelling are smaller. M3C2 points out a different pattern with fewer but larger greenish areas. Looking at the original point clouds from 2014 and 2017a, some of the spots with distances >0.05 m correspond with point cloud holes in the 2014 data which don't occur in the 2017a data. Area 2 and area 3 are 0.1 m high intersections of the point clouds. The combination of the 2014 and 2017a data shows the divergence of the surfaces of the two point clouds. In area 2, C2C without local modelling derives small distances on the left part of the intersection

5. RESULTS

and larger distances up to 0.1 m on the right part. C2C with quadric modelling shows similar patterns on the left part but smaller distances on the right part. Using M3C2, clearly less points are within the range from 0.01 m to 0.1 m, and the visible distances are mostly 0.03 m or larger. Area 3 shows mainly distances from 0.06 m to 0.1 m for the C2C without local modelling, smaller point distances but more values within the considered range for the quadric C2C and the least number of point distances, most likely 0.05 m or higher, for the M3C2 approach.

Figure 37 illustrates the results of the 2016-2017a change detection. C2C without local modelling derives for 56.8% of the 2.44 million 2017a data points distances <0.01 m. 40.8% of the points show distances between 0.01 m and 0.1 m, 2.3% distances >0.1 m. These results are illustrated in view A. The mean distance of the point clouds is 0.0188 m with a standard deviation of 0.0464 m. The distances <0.01 m, as visible in view A, are strongly present in the center areas of the point cloud and correspond with the originally vegetation-free parts of the Amtmann. Distances between 0.01 m and 0.1 m are mainly found in the lower part of the point cloud and in the top and left border regions. Distances >0.1 m are selectively visible on the margin of the point cloud. Focusing on the 0.01 m to 0.1 m range, most of the point distances are colored in blue which indicates distances close to 0.01 m. Green areas revealing distances around 0.05 m are primary at the lower region and at the margins, but also small green areas are within the blue area in the center region. Distances up from 0.07 m to 0.1 m are limited to the margins of the point cloud. C2C with local quadric modelling increases the class of <0.01 m distances up to 71.2%, 27.8% of the point distances are in the range from 0.01 m to 0.1 m and 1% of the points exhibit distances >0.1 m. Also, the mean distance with 0.0114 m and the standard deviation with 0.0303 m are smaller than the corresponding C2C without local modelling values. Contemplating view C, distances <0.01 m are spread all over the point cloud, with yellow points revealing the distances from 0.01 m to 0.1 m spread in the lower region, the upper left part of view C and at the margins. The general pattern is similar to view A but with lower point density. Distances >0.1 m are only visible in a few margin regions of view C. When taking a closer look to the 0.01 m to 0.1 m range, also the pattern of the corresponding view B is reflected. Points with distances close to 0.01 m are again widespread with spots of distances around 0.05 m up to 0.1 m in margin regions. The point cloud density is comparatively low, as the total number of points in this range is about 1/3 less than using C2C without local modelling. The M3C2 modelling goes along with further increasing of the amount of point distances <0.01 m to 75.8%. 17.8% of the points are in the range of 0.01 m to 0.1 m with this modelling approach. 1.5% show distances >0.1 m and with 4.9% of

the point cloud, about 118,000 points of the 2017a data are not attributed with distances to the 2016 point cloud.

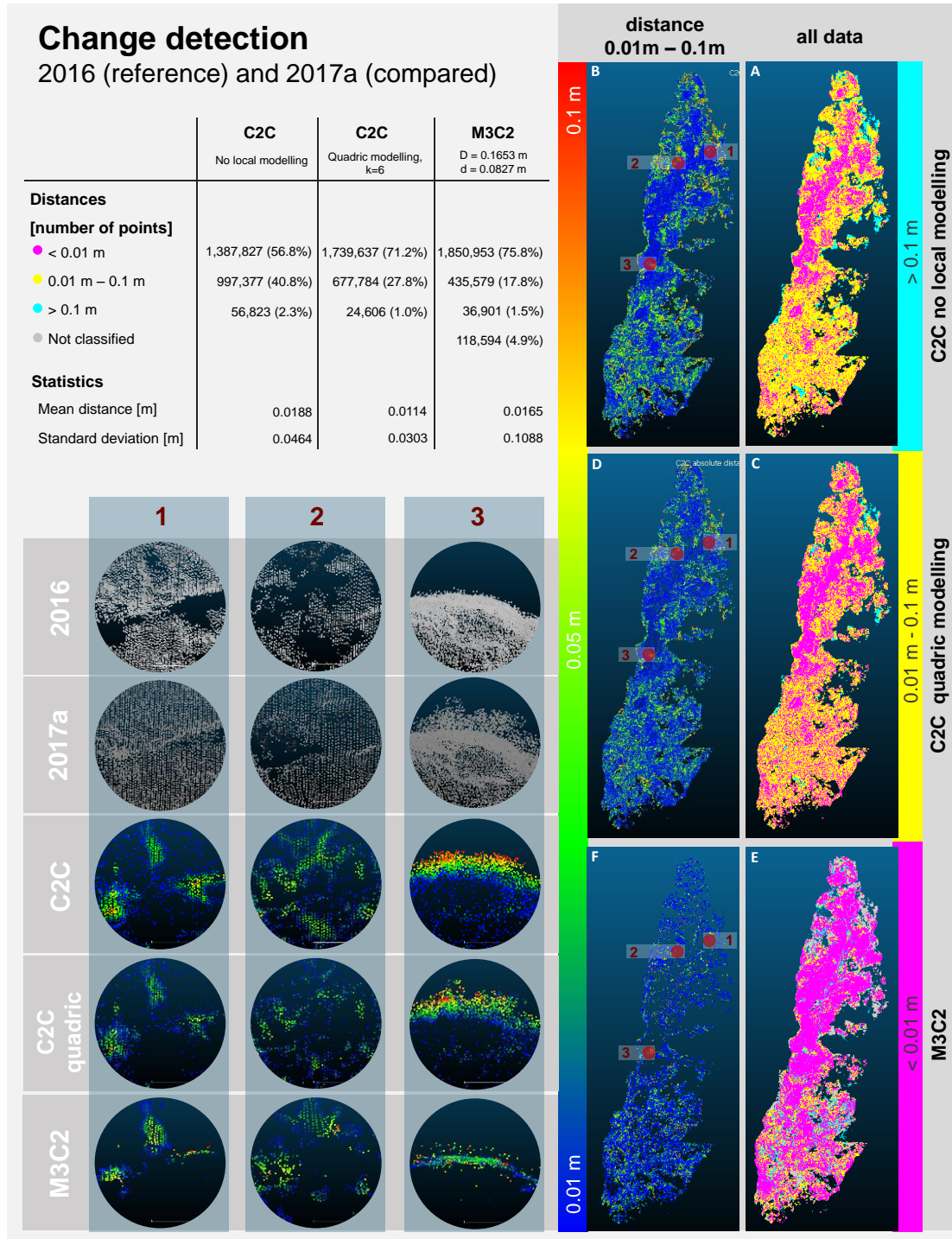


Figure 37: Results of the 2016-2017a change detection

5. RESULTS

The visualization of the distribution of the three classes shown in view E reveals the clear domination of the <0.01 m distances. Yellow points indicating the 0.01 m to 0.1 m range are located primary in the lower part of the point cloud with a few clusters in the center and upper part. The distances >0.1 m show similar patterns, but with less appearances. Non-classified points are clearly visible at some margin regions of the point cloud. Focusing on the range from 0.01 m to 0.1 m in view F, the density of the point cloud is in comparison to the views B and D quite low, as it consists of less than half of the points of view B and about $1/3$ less than view D. The visible points are dominated by distances close to 0.01 m with a more homogenous scattering of higher distance values up to 0.05 m. High values up to 0.1 m are confined to relatively few punctual areas.

Highlighted by three red circles in views B, C and D, noticeable areas of the 0.01 m to 0.1 m range are examined more in detail in the lower left illustrations in Figure 37. Area 1 shows a closeup of three triangularly arranged spots standing out with distances up to 0.75 m in the C2C with no local modelling. The point clouds from 2016 and 2017a show a small rock cleavage leading horizontally through the area. Moreover, the lower two spots are point cloud holes in 2016 but covered with points in 2017a. While the two lower identified spots are holes of the point cloud in 2016 and filled in 2017a, the spot on the upper part of the section shows lower point density in 2016 compared to 2017a data. This gives the impression of a protruding object in the 2016 data which is not present in 2017a. While the lower right spot is prominent in C2C without local modelling, the point distances are reduced in C2C with quadric modelling and nearly vanished with M3C2. Moreover, the prominence of the lower left spot decreases, although not as strong, with the different modelling approaches. In contrast, the upper spot shows slightly lower distance values using quadric C2C than no local modelling C2C, but gains on prominence and distance values with the M3C2 distance modelling. Area 2 reveals how the different algorithms handle point cloud holes. While the section of the point cloud is holey in 2016 data, only one point cloud gap in the center of the left region section is visible in 2017a data. The C2C without local modelling specifies distances up to 0.075 m at almost all areas without point data in 2016. With quadric modelling, the derived distances are smaller and less, but similarly distributed, while M3C2 shows different distance patterns with prominent focus on higher distances at the upper and the center left part of the section. Area 3 displays a section of the point cloud which shows a clean surface in 2016 data, but a surface with additional lower density points on top in 2017a. In C2C without local modelling, the different layers of distance to the surface are clearly visible up to 0.1 m and not representing the points furthest away from the surface. The change detection

results of C2C with quadric modelling are more inhomogeneous and are not represented by a continuous layer gradient but including more points. M3C2 projects calculated distances mainly on the surface layer with values from 0.01 m up to 0.05 m with individual points of different distances of the whole range from 0.01 m to 0.1 m above the surface.

5.6.2 Evaluation of change detection approaches

Figure 38 shows the results of the 2017a-2017b change detection. For this analysis, the 2017a is used as reference data and the 2017b data as compared data. Such as for the other change detection analyses, the detected distances are projected on the to-be-compared point cloud for the C2C approaches and on mean point positions of the to-be-compared point cloud for M3C2. Theoretically, only 346 points (0.0002% of the point cloud and therefore neglected for the following description) are affected by surface manipulation and should therefore show distances, as the data were collected on the same day without other change noticed. Therefore, this comparison presents an evaluation of the method.

C2C without local modelling calculates for 61.2% of the 1.8 million points distances <0.01 m. 36% of the points are in the range from 0.01 m to 0.1 m, 1.9% of the points are attributed with distances >0.1 m. The mean distance is 0.0207 m with a standard deviation of 0.1103 m. The distribution of the different classes is illustrated in view A. The distances up to 0.01 m are dominant in the left part of the center region and the right part of the upper section of the view. These areas overlap with the not vegetation-covered areas of the original point cloud. Yellow points representing distances from 0.01 m to 0.1 m are primary located in the lower part of the point cloud and on the margins of the view. Distances >0.1 m are clearly visible at distinct spots on the point cloud borders. Taking a closer look on the 0.01 m to 0.1 m range, small distances close to 0.01 m are clearly dominant. Areas with clear overlapping of green to red points which represent distances from 0.05 m up to 0.1 m are limited to the lower part, the margins and two hot spot areas in the center-right part of view B. Adding local quadric modelling to the C2C change detection approach leads to increasing of point distances <0.01 m to 77%. 21.9% of the point distances range between 0.01 m and 0.1 m within this modelling approach, 1.1% show distances >0.1 m. The mean distance decreases to 0.0118 m with a standard deviation of 0.0622 m. As visible in view C, the distribution of the three classes is in general similar to the C2C without local modelling with a clear thinning out of the yellow points representing the range of 0.01 m to 0.1 m. The cyan points revealing point cloud distances >0.1 m also correspond with the location of the points of the same class in view A and are therefore

located at single margin regions. The more precise breakdown of the range from 0.01 m to 0.1 m (View D) shows less point cloud density in the center region. Again, there is a clear domination of the distances around 0.01 m with, compared to view B, less appearance of points around 0.05 m and only few spots of point cloud distances up to 0.1 m at point cloud border regions. M3C2 modelling leads again to an increasing amount of point distances <0.01 m (83%), 12.5% of point distances between 0.01 m and 0.1 m and 1.2% of distances >0.1 m. 3.4% of the point distances are not classified. The mean distance with 0.0131 m and the standard deviation of 0.0949 are between the parameters of C2C without local modelling and C2C with quadric modelling. The visualization of the distribution in the three classes in view E is dominated by a base of distances <0.01 m with isolated yellow clusters in the middle and upper region of the view and scattered 0.01 m to 0.1 m distances in the lower part. Points indicating distances >0.1 m are scattered in the lower region, not classified areas partly overlap with the >0.1 m distances in C2C change detection. The data in view F, showing the range from 0.1 m to 0.01 m, hardly represent a surface due to many point cloud holes. It is still dominated by distances close to 0.01 m, but overall scattered point distances >0.05 m occur.

The three red circles in view B, D and F show the location of the areas of interest, closer examined in the illustrations on the lower left part of Figure 38. Area 1 displays the region, where the surface was manipulated between SC2017a and SC2017b by adding polystyrene objects. C2C without local modelling points out four of the seven objects by distances >0.025 m. Besides the objects, scattered distance points around 0.01 m and distances up to 0.08 m in the point cloud border region in the right part of the section are visible. C2C with local quadric modelling is characterized by decreasing of the scattered blue points around 0.01 m and revealing the objects and the point cloud border region similarly to C2C without local modelling. M3C2 results in only identifying distances related to four of the seven objects and a cluster of points on the right-hand point cloud border. Moreover, three single points occur within the section. For all approaches, the lower polystyrene objects (the original geometric forms) are better visible in the change detection point clouds. Area 2 shows the reaction of the different algorithms to point cloud holes. C2C without local modelling indicates the pointless area of 2017a with distances from 0.05 m up to single points showing distances around 0.1 m over a comprehensive occurrence of distances around 0.01 m in the center and upper part of the sections. With local quadric modelling, the 0.01 m values are thinning out, with hardly any change in the center region. M3C2 leads to increasing of the point density in the center region showing distances around 0.05 m, surrounded by blue points displaying distances around

0.01 m and no point cloud distances in the range from 0.01 m to 0.1 m in the border regions of the section.

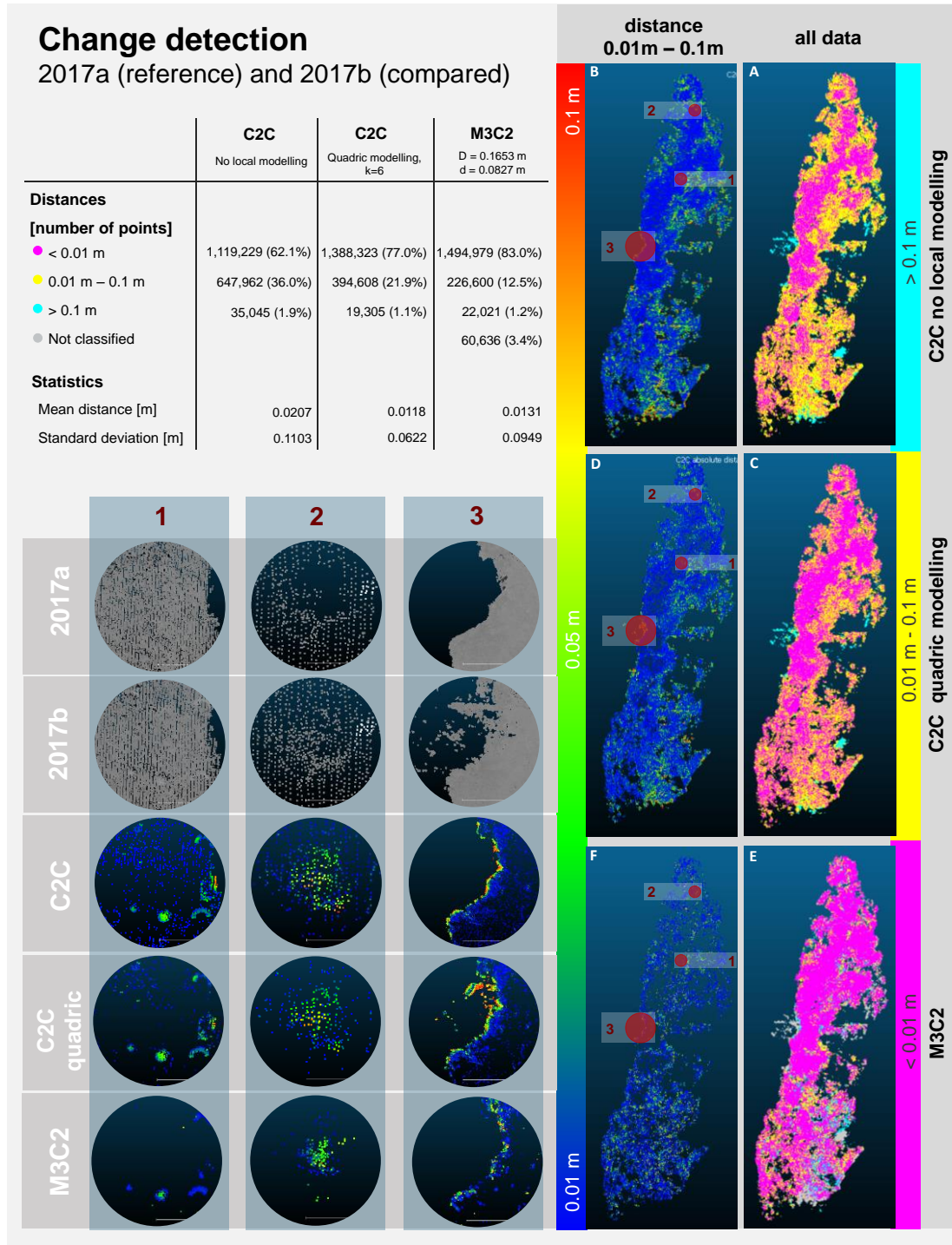


Figure 38: Results of the 2017a-2017b change detection

5. RESULTS

Area 3 shows a closeup of a point cloud border, where 2017a data is sharply cut and the 2017b data has a frayed border region. While C2C only shows point close to the 2017a point cloud border with a clear gradient within the 0.01 m to 0.1 m distance range, C2C with quadric modelling also includes points further away from the 2017a border. In comparison, M3C2 indicates less change and the location of the change detection points is, as in C2C without local modelling, limited to the 2017a border region.

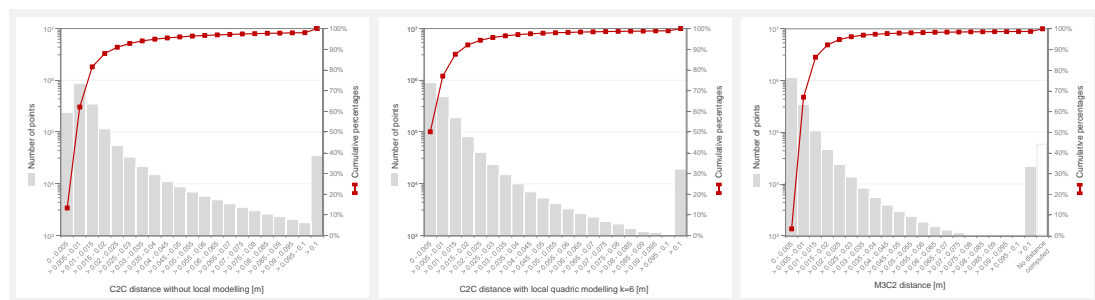


Figure 39: Histograms showing the results of the 2017a-2017b change detection

For the 2017a-2017b change detection, the distribution of the different distances is visualized in histograms illustrated in Figure 39. The number of points per class of 0.005 m is plotted on a logarithmic scale. All distributions are right-skewed indicating strong occurrence of smaller point distances, especially considering the logarithmic scale, for all change detection approaches. The cumulative percentages are shown on a secondary axis. Using C2C with quadric modelling and M3C2, the class of the smallest distances contains the most points: 50.1% of the points are <0.005 m using C2C with local quadric modelling, 65.8% of the classified points using M3C2. For C2C without local modelling, the smallest class is not the largest group. 13.3% of the point distances are <0.005 m using this approach. With no local modelling, the distances from 0.005 m to 0.01 m have the most frequent occurrence with 48.8% of all calculated point distances. Distances >0.1 m range between 1.07% (C2C quadric) and 1.94% (C2C without local modelling). M3C2 assigns 3.37% of the reference compared points undefined distances.

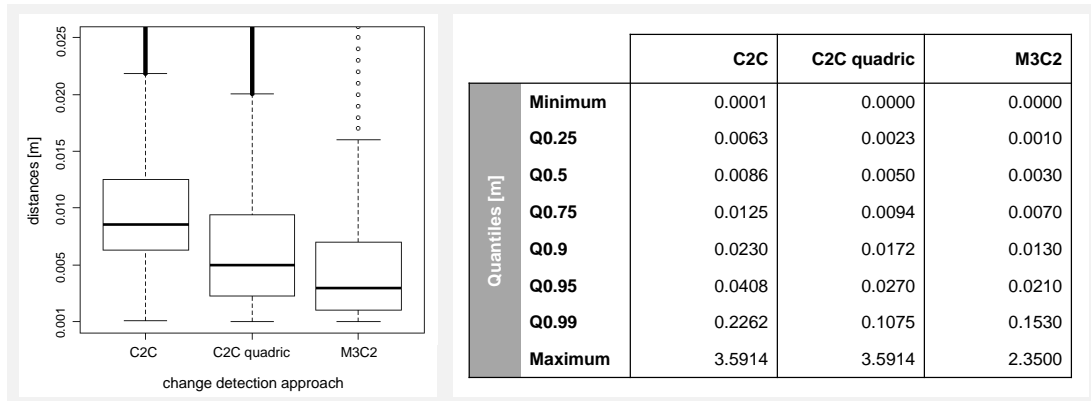


Figure 40: Boxplots and chosen quantiles from the analysis of the 2017a-2017b change detection results

The boxplots in Figure 40 make the difference of the distributions easier comparable. The y-axis is cut at a detected change of 0.025 m and excludes some outliers. The C2C without local modelling shows the median at 0.0086 m. With the use of local quadric modelling, the median decreases to 0.005 m with another reduction to 0.003 m using M3C2. The medians are, especially with C2C and M3C2 modelling, located in the lower part of the box, which indicates again the right skewed-distribution of the point distances. The interquartile range reaches from 0.006 m (M3C2) to 0.0071 m (C2C quadric). The 0.90 and the 0.95 quartile show a ranking similar to the medians with the highest values for C2C without local modelling, followed by C2C with quadric modelling and the lowest values for M3C2. With the 0.99 quartile, C2C with quadric modelling shows with 0.1075 m the lowest result.

To support the descriptive analyses, statistical tests are performed. As the data is not normally distributed, the Wilcoxon rank sum test is used. For testing of equal distribution of the data, a significance level of 0.01 is chosen. Statistical testing confirms the assumption taken from the descriptive analyses of the data, that M3C2 leads to the overall smallest detected changes between 2017a and 2017b data, followed by C2C with quadric modelling and C2C without local modelling: the Wilcoxon rank sum test, which is used pairwise on the data of the three different change detection results, gives p-values of $2.22 \cdot 10^{-16} < 0.01$ significance for all different combinations leading to reject the null hypothesis and accept the alternative hypothesis which indicates that the location shift is not equal to 0 and the samples are therefore from different distributions. As 60679 points (3.37%) are not classified in M3C2 change detection and it is presumed that these points have comparatively large distances to the nearest points in the reference point cloud, the tests are rerun excluding also the largest 3.37% of the distances of C2C without local modelling and

C2C with quadric modelling. The Wilcoxon rank sum test leads to the same results. Hence, it can be concluded, that M3C2 leads significantly to the smallest point cloud distances of the three considered approaches for the 2017a-2017b change detection, followed by C2C with quadric modelling and C2C without local modelling.

5.6.3 Detailed change detection evaluation for test areas

For a detailed evaluation of the surface manipulation between SC2017a and SC2017b, the point cloud is cropped to the area of the manipulated surface. Two areas of interest are defined: test area 1 containing only rock surface and a broader test area 2 including vegetation in the original point clouds.

The two test areas are shown in Figure 41. The three different change detection approaches C2C without local modelling, C2C with quadric modelling and M3C2 are applied on different point cloud processing levels: the different change detection algorithms are tested on the original point cloud, on the result of the CANUPO filtering, on the CANUPO filtering combined with the intensity based filtering and on the final filtered point cloud including the statistical outlier removal and the minimum distance filter. For the evaluation of the change detection, the manipulated objects are separated manually by visual interpretation from the rest of the surface for the point cloud of all different processing steps. From the seven installed objects, five are included in the analysis, as the two smallest objects are not clearly detectable in the point cloud. The classification in change of surface and no change of surface is shown in Figure 42.

Furtheron, the change detection approaches are applied on the whole data and the results are split up by the defined “objects” and “rest” classification. 829 points represent the objects point class in the unfiltered data. Test area 1 has 26,452 rest points, test area 2 128,580 rest points – also considering the unfiltered point cloud. For M3C2, only the points with calculated distances are included in the analyses. The amount of the compared data points with no calculated distances ranges from 0% to 1.5%. The data points are classified with threshold values of changes $>/\leq 0.01$ m and 0.02 m. Figure 43 and Figure 44 illustrate the results of the classification. The detailed numerical results are attached in Appendix E and Appendix F. For comparable results, the D and d values for the M3C2 (see Chapter 3.6.2) are fixed to 0.05 m.

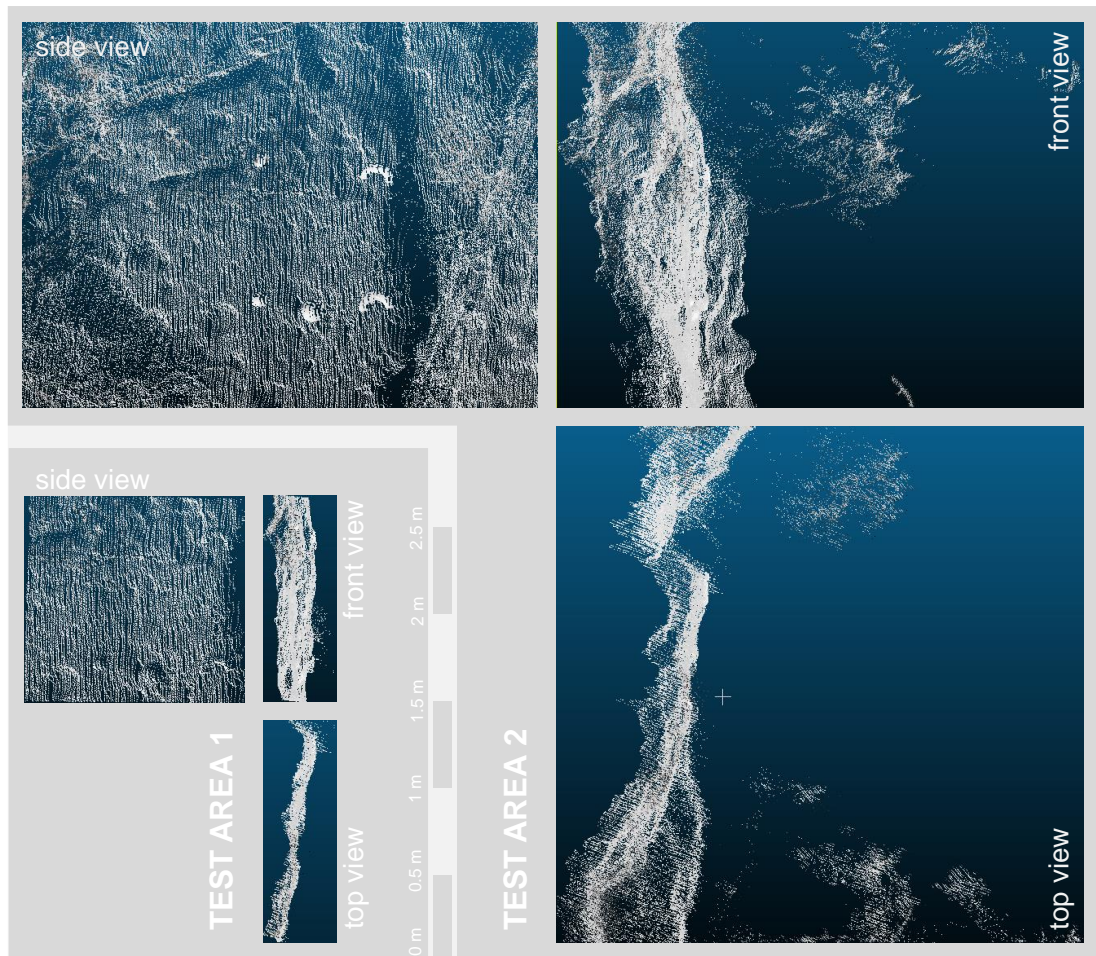


Figure 41: Test areas for the detailed change detection evaluation (unfiltered point cloud)

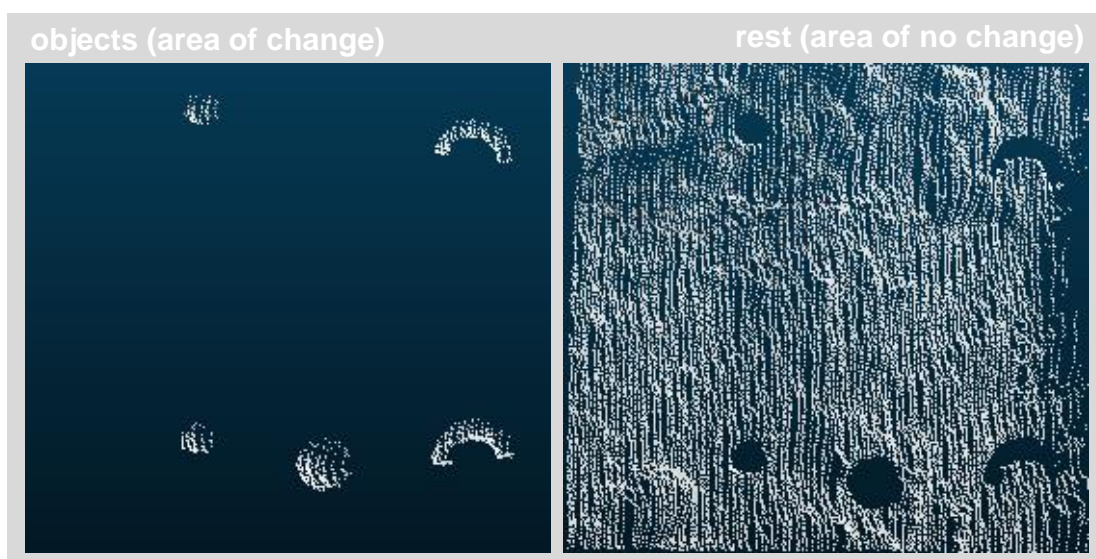


Figure 42: Area of changed surface (left) and area of no surface change (right) within test area 1

5. RESULTS

First, the graphs in Figure 43 using 0.01 m as a change detection threshold are discussed. For test area 1, which is limited to rock surface, using the original data, the CANUPO rock classification and the cleaned rock leads to similar results within the different change detection methods – the values vary up to 0.4%. C2C without local modelling identifies 80.2% to 80.5% of the object points of original, CANUPO and final filtered data with changes >0.01 m. For the same data varieties, the changes >0.01 m for C2C with quadric modelling range between 69.4% and 69.8%, M3C2 shows values from 81.0% to 81.4%. The rest representing the area without modification has change values >0.01 m for 4.4% to 4.8% of the C2C without local modelling, 2.2% to 2.5% for local quadric modelling and 0.6% to 1.0% for M3C2. After the final filtering, the pattern changes: while the object classification shows stable results in C2C without local modelling (increasing to 81.4%), the percentages of the rest classified as changes triples up to 14.7%. For C2C with quadric modelling, the percentages of the object points classified >0.01 m change increase with the final filtered data about 9 percentage points to 78.3%. For the rest, the proportion of the points >0.01 m change doubles to 4.9%. Such as C2C without local modelling, M3C2 shows similar results for the object classification using the final filtered data (80.9%), the percentages of the data >0.01 m change of the rest increase to 2.3%. Overall, for test area 1, the highest percentage of objects points attributed with changes >0.01 m is derived with M3C2 using the original data (81.4%) and the lowest percentages of rest points with changes >0.01 m also by M3C2 using the CANUPO classified data (0.6%).

Test area 2 includes vegetation in the original data section. The distinction between changes >0.01 m and ≤ 0.01 m is, as in area 1, for the object areas for all three change detection methods stable for the first three data processing steps. With exception of changes up to 0.2% with M3C2, the same values as in test area 1 are shown. The results using the final filtered point clouds deviate in similar patterns as in test area 1 with the same values including the same exception of 0.4 percentage points increasing to 81.3% with M3C2. Considering the not manipulated rest data points, the share of points with changes >0.01 m increases comparing to test area 1 and varies over the different data processing steps. For C2C without local modelling, 22.7% of the points show changes >0.01 m using the original data, decreasing to 13.8% using the CANUPO classification and 15.4% with the cleaned rock data and rises to a high of 30.9% with the final filtered data. Similar patterns occur for the other two change detection approaches. C2C with quadric modelling has 13.6% of changes >0.01 m for the rest points of the original data, 7.3% using the CANUPO classified data, 8.4% for the cleaned rock data and 15.1% for the final filtered data. M3C2 change detection results in 13.3% of detected changes >0.01 m for rest class using the original data,

5.8% for the CANUPO classified data, 7.1% for the cleaned rock and 13.6% for the final filtered data. For test area 2, M3C2 has the overall highest value of object points with detected changes >0.01 m with 81.6% using the original data and the overall lowest value for rest points with changes >0.01 m of 5.8% using the CANUPO classified data.

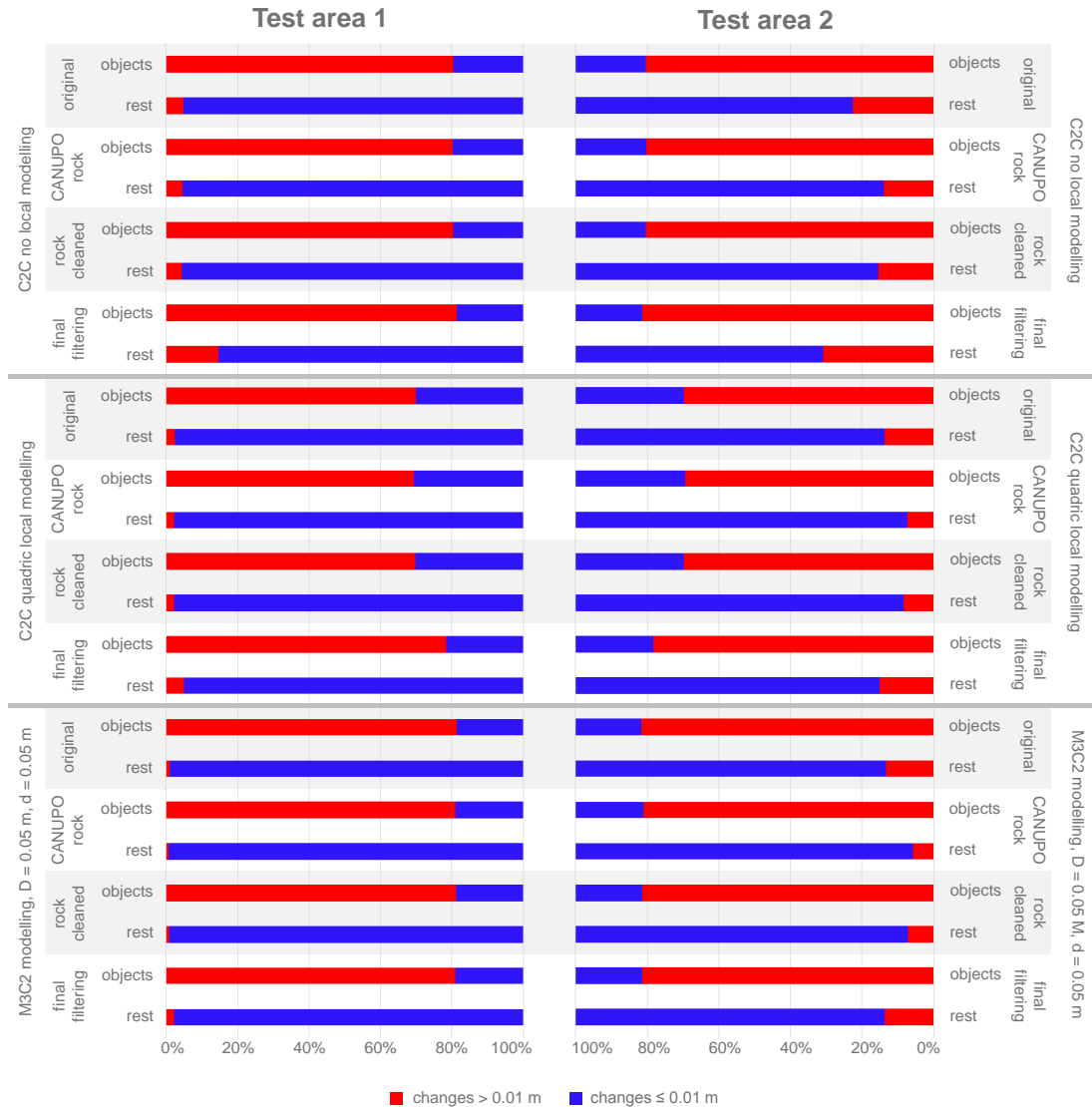


Figure 43: Results of the detailed change detection evaluation 2017a-2017b of the manipulated surface for the different processing steps of the point cloud, 0.01 m threshold for change

Figure 44 shows the results of change classification using a threshold value of 0.02 m. The results of the object classification are, as with the 0.01 m threshold in Figure 43,

5. RESULTS

constant for the first three data processing steps for test area 1 and test area 2. For C2C without local modelling, the amount ranges for both test areas between 45.2% and 45.5%. With this classification method, also the results using the final filtered data are within this range. Using C2C with local quadric modelling, the percentages of object distances >0.02 m are lower: 36.1% - 36.3% of the compared points of the first three processing steps show distances >0.02 m, 43.3% using the final filtered point cloud for both test areas. M3C2 leads to the highest shares from 48.9% to 49.6% of distances >0.02 m for the original, CANUPO classified and cleaned data and 45.4% to 45.5% for the final filtered data. The share of the rest data with distances >0.02 m varies for test area 1 for all change detection methods for the original, the CANUPO classified and the cleaned rock data set between 0.3% and 0.8%. The final filtered data leads to 1.0% of distances >0.02 m for M3C2 and C2C with quadric modelling and 1.9% for C2C without quadric modelling. Overall, M3C2 using the CANUPO classified data leads with 49.6% to the highest amount of object points with distances >0.02 m for test area 1, M3C2 using the CANUPO data and the cleaned rock data as well as C2C with local quadric modelling using the cleaned rock data lead to the lowest percentages (0.3%) of points of the rest data with distances >0.02 m.

For test area 2, the object data is already inspected in the paragraph above. While the object data is quite stable, the values for the rest data differ from test area 1. For all three change detection methods, the amount of points with distances >0.02 m using the original data and the final filtered data resemble as well as the values for the CANUPO classified data and the cleaned rock data. C2C without local modelling shows values of 5.9% respectively 5.5% for the original data and the final filtered data, 2.1% and 2.6% for the CANUPO filtered data and the cleaned rock data. Comparing to test area 1, the shares are up to 7 times higher using test area 2. The values for C2C with quadric modelling are 3.5% and 3.1% for original and final filtered data, 1.0% and 1.3% for CANUPO classified and cleaned rock data and up to 6.5 times higher with test area 1. M3C2 shows the highest increasing in comparison to test area 1: the amount of distances >0.02 m is 8.3% using the original data, 2.9% with the CANUPO classified data, 3.8% using the cleaned rock data and 7.2% for the final filtered data. This shows, regarding to the original data, an increase of 1820%. For the test area 2 and the distance threshold of 0.02 m, M3C2 using the CANUPO filtered data gives with 49.6% the largest amount of points with distances >0.02 m. The smallest share of rest points >0.02 m distance is given by the C2C with local quadric modelling: 1.0% of the points show distances >0.02 m.

Comparing the results of the object classification shown in Figure 43 and Figure 44, the percentages of distances higher than the chosen threshold decreases explicitly

with increasing of the threshold. For C2C without local modelling, the amount of the points with distances higher than the threshold is reduced about 44.5% with increasing the threshold from 0.01 m to 0.02 m. For C2C with quadric modelling, the distinction shows reductions of 48% for the first three data processing steps and 44.7% for the final cleaned data. M3C2 leads to the smallest change: 38.7% to 39.7% less points of the first three data processing steps and 44% for the final filtered data are classified higher than the threshold when increasing it from 0.01 m to 0.02 m.

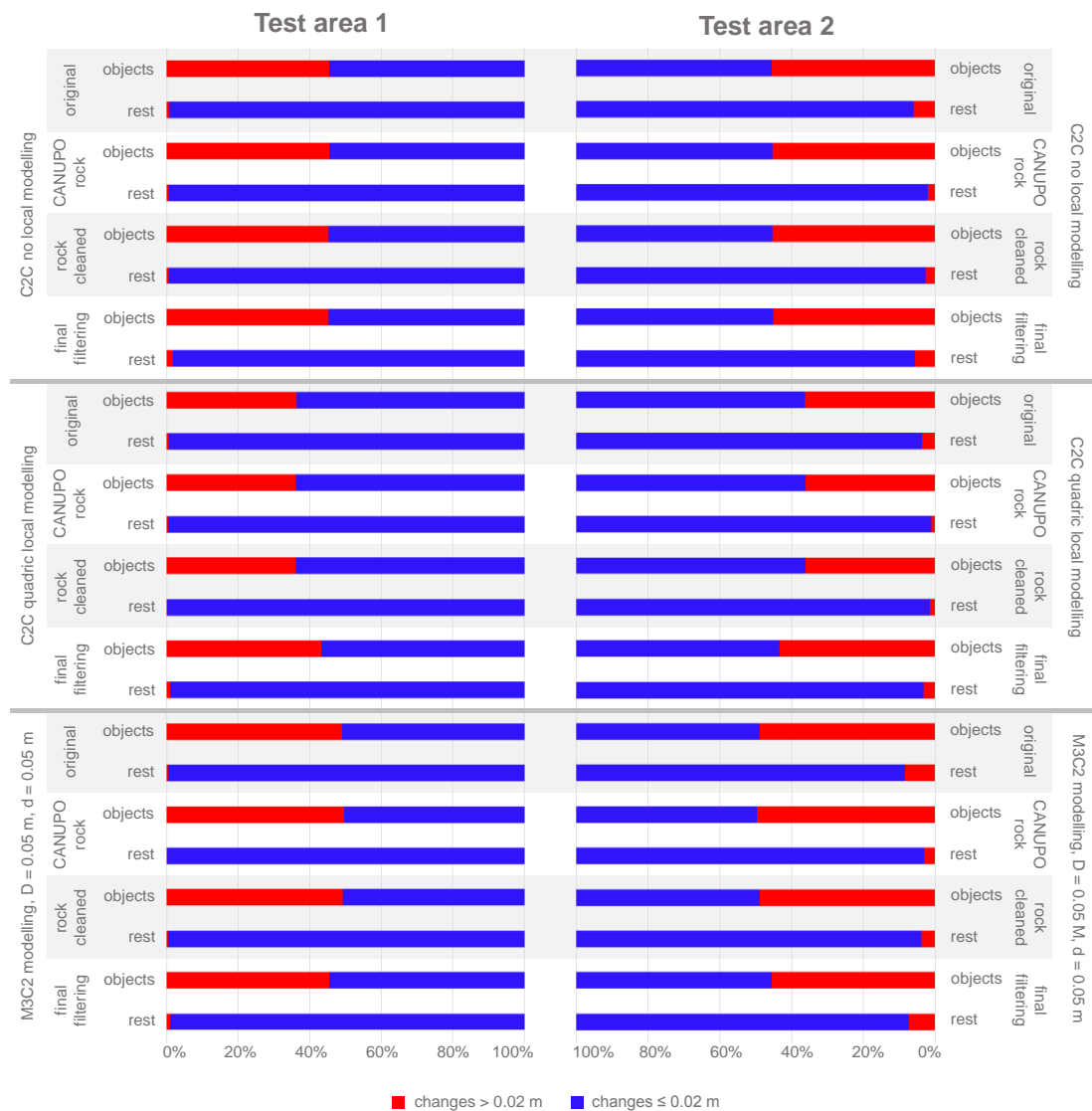


Figure 44: Results of the detailed change detection evaluation 2017a-2017b of the manipulated surface for the different processing steps of the point cloud, 0.02 m threshold for change

5. RESULTS

Considering the rest data for test area 1, increasing the threshold to 0.02 m leads to stronger decrement of the amount of points higher than the threshold value. For C2C without local modelling, the amount of points decreases 82.6% (original data) to 87.9% (cleaned rock data) when using 0.02 m as the threshold distance. C2C with quadric modelling exhibits reductions in the range from 78.2% to 87.5% from 0.01 m to 0.02 m threshold distance. M3C2 shows the relative smallest reductions in the range of 52.7% to 58.6%. The rest data for test area 2 shows less decreasing than test area 1 data when rising the threshold value from 0.01 m to 0.02 m. For C2C, 74.1% to 84.9% less distances are higher than the threshold value, for C2C with quadric modelling the range is 74.5% to 86.0%. For M3C2, the relative reduction values range from 37.8% to 49.7%.

Summarizing, M3C2 leads for all scenarios to the highest amounts of values larger than the chosen threshold value for the object data points. While for the data of test area 1 which just covers rock surface, the results mentioned above are reached using the original point cloud, the CANUPO filtered data gives the highest values for the broader defined test area 2 including vegetation. Considering the rest data which is not manipulated between the two scanning campaigns, M3C2 with the CANUPO filtered data results in the lowest amount of data >0.01 m for both test areas. Increasing the threshold to 0.02 m leads to three options of the lowest value of 0.3%: M3C2 with CANUPO data and the cleaned rock data as well as C2C with quadric modelling using the cleaned rock data. Test area 2 shows the lowest share of >0.02 m for the rest data using C2C with quadric modelling.

6. Discussion

In the first chapter, four research questions are defined to guide the research of this thesis. While the previous chapter gives a descriptive presentation of the results, in the following chapter, these results are discussed. The discussion is not limited to the research questions and includes challenges and limitations on data processing and impacts of the different processing steps along the workflow. Next to the discussion of the data processing within this thesis, relations to chosen publications are established, especially considering potential for optimization. Like the results, the discussion is structured in different sections of data processing, completed with a final section of drawing conclusions for the postulated research questions.

6.1 Data

As emphasized in the preface of HERITAGE AND LARGE (2009a), laser scanning provides a “*cost effective way to acquire massive amounts of high resolution 3D digital data*” (HERITAGE ET AL 2009a: ix). Especially under these circumstances, it is important to adjust parameters for data acquisition for the selected research area to gain the optimal spatial resolution for the defined research. Moreover, to achieve good comparability for multitemporal analyses, constant acquisition settings and scan positions are preferable.

The data used within this thesis is heterogenous concerning the resolution and scan positions. The 2014 data shows a vertical resolution of 0.001° , which is even out of the range defined by the manufacturer (see Chapter 2.3.2), up to 20 times higher than the horizontal resolution of 0.02° of 0.015° . Although not as high as in 2014, the two 2017 scanning campaigns also show differences of 2.5 to 3 times of horizontal and vertical resolution. Only the data of SC2016 has an equal vertical and horizontal resolution of 0.01° . Detailed information on the data is shown in Appendix A. Already with the first data inspection, following data processing challenges arise: the stripe-like structure of the 2014 data (see Figure 23) leads to concentration of the data in

vertical direction and comparatively large data gaps in horizontal direction resulting in challenges in data registration and limited scope for filtering and homogenization. The various scan positions of the different scanning campaigns are also a cause of varying point densities in registered point clouds. These issues already reflect that major impacts on point cloud processing are generated within the data acquisition process. The scanners' generated default settings do not necessarily reflect the optimal scanning parameters for the research area – different concepts of optimization of scanning resolutions are for example discussed in LICHTI (2004), LICHTI AND JAMTHSO (2006) and PESCI ET AL (2011).

6.2 Registration

Registration uncertainty represents a major cause of uncertainties in following data processing steps and point cloud comparing (LAGUE ET AL 2013, MUKUPA ET AL 2017). Hence, high registration accuracy is desirable for further point cloud processing. Within this thesis, the registration process is separated in a point based coarse registration and fine algorithm based registration. For the fine registration, two approaches (ICP and MSA, see Chapter 3.3) are tested.

For the coarse registration, two different methods are used. As the high reflective tie points are only installed during the SC2016, for the registration and co-registration of the 2014 data, the point pairs for coarse registration are manually picked. For the registration and co-registration of the other scanning campaigns, automated tie point registration implemented in RiSCAN PRO is applied for coarse registration. The results of the coarse registration are presented in Chapter 5.3.1. Strictly speaking, RMSD, the reference value for the 2014 data and standard deviation for the rest of the data can't be compared directly. Still, the differences of the registration errors are up to one order of magnitude: while tie point registration shows sub-centimeter error values using 7 to 14 tie points, the point pair picking RMSD values are up to 0.04 m using with three points only a third or a quarter of the number of points. The co-registration in Chapter 5.4 shows similar results. The lack of artificial structures complicates the manual identification of point pairs for registration. As natural rock surfaces do not show easily identifying straight structures, sharp edges or narrow planes, the extraction of distinct points in different point clouds, especially from different scanning perspectives, is difficult. Moreover, manual point pair picking is a highly time-consuming processing step. In comparison, artificial high reflective targets are clearly visible in the scans and are automatically detected and matched by the used software. Only a review of the detected point pairs is necessary. Considering

the error values and the work effort, it can be concluded that installing high reflective tie points and automatic tie point registration is the preferable method of coarse registration for the work within this thesis and can be recommended generally for scanning of natural surfaces.

Chapter 5.3.2 focusses on testing of different fine registration methods. Within the thesis, two different applications of ICP are examined: MSA, which is implemented in RiSCAN PRO, uses the ICP algorithm on data of the point cloud extracted by the plane patch filter, which also takes surface normals into account. Besides the parameters for the plane patch filter, the search radius and the maximum tilt angle can be varied within this fine registration method. The fine registration algorithm in CloudCompare uses the original ICP (further referred to as ICP). The modifiable parameters include the number of points used for the calculation and the theoretical overlap of the to-be-registered point clouds. The differences of the two software approaches are elaborated in detail in Chapter 5.3.2. Listing the adjustable parameters already gives a hint that finding optimal settings is a complex process.

Running the fine registration tests, it is tried to gain an overview of the outcome that results from varying different settings. Figure 25 and Figure 26 show an attempt of visualizing these results. Depending on the settings, the results range from sub-centimeter registration error values up to order of 0.1 m. This variety reflects the strong impact of the registration setting selection. For RiSCAN PRO, interesting conclusions considering software evaluation can be drawn: while the software intends to gain better results by iteratively lowering the maximum tilt angle differences of the surface normals, a total exclusion of the tilt angle by setting the possible range to 180° leads to preferable results. Comparable registration errors are reached with more data points used for the registration process. The MSA registration approach is, referring to the performance, not optimized for fine registration of natural surfaces without plane areas. Assuming patterns within the plots and disregarding other settings, the registration error increases with more data included using MSA for most settings, whereas more data points for registration lead to smaller registration errors using ICP. Only with 180° maximum tilt angle large search radii, MSA shows similar patterns to ICP. It is assumed that with these settings, conditions of the original ICP are simulated. All over, as fine registration based on ICP which counts for both approaches is an iterative process, for an optimal output, a decent coarse registration is necessary, which is given for the 2016 data used for the registration test. Summarizing, both MSA and ICP approach lead to sufficient registration accuracies with registration errors <0.01 m for several settings, as shown in Figure 27.

For all the registration tests, it must be stressed that the registration error calculation only includes points that are used for the registration and not all the data points. Moreover, the distributions of points used for registration vary between the different methods. Therefore, comparing different approaches is challenging and additionally, drawing conclusions for the point position certainty is difficult: as mentioned by BARBARELLA ET AL (2017), the true position of the point is unknown, and the evaluation of uncertainties in registration is hence not trivial. LAGUE ET AL (2013) suggest therefore quality assessment using independent control points with a known position. For this approach, registration of the point cloud is not sufficient – the data must be georeferenced for this evaluation.

For the registration of the scan positions of one scanning campaign and the co-registration of the different scanning campaigns within this thesis, ICP implemented in CloudCompare with 25% overlap, a maximum of 5 million points and the default termination condition of a minimum RMS difference of 10^{-5} m between two iterations is used. With closer examination, there is possibly potential of further optimization of the settings, but the reached values serve the accuracy striven for this thesis. The decision for the approach is based on various factors. ICP leads to a sufficient accuracy. Further, ICP uses points all over the point clouds and not only polydata resulted from plane patch filtering. The plane patch filter results are concentrated on vegetation areas for the point cloud data used for this thesis and therefore not on the surface area of interest. Another advantage is the implementation of ICP in open source software. Moreover, the algorithm is, relating to efficiency, more adapted to inhomogenous structures.

The registration results in a final RMSD of 0.056 m for the 2014 data, 0.008 m for 2016, 0.011 m for 2017a and 0.009 m for 2017b. The co-registration of the different epochs, using 2016 as model data, show 0.020 m for the 2014 data and 0.008 m for the 2017a and 2017b data. As already mentioned, the registration errors are calculated from the data used for registration. It is difficult to put the values in perspective as data of comparable studies is often scanned from various distances and under different circumstances and information on registration quality is often not provided. Moreover, if registration errors are presented, registration settings are not revealed within the publications. Still, values from chosen studies are mentioned at this point. OPPIKOFER ET AL (2009) reach registration errors of 0.027 m for scanning of a rock slide from 300 m to 400 m distance, CORSINI ET AL (2013) present final mean registration errors of 0.03 m to 0.04 m for scanning a rock slide in the northern Apennines with a scanning distance of 1.2 km and exact known GNSS position of the

scanner, STUNDEN ET AL (2015) reach registration errors from 0.16 m to 0.022 m for large scale rock wall monitoring in a deglaciated valley in Switzerland.

Putting the values reached within the point cloud processing into context, the registration of the 2016, 2017a and 2017b data leads comparatively to good results. The difference of the registration error to the 2014 data demonstrates the disadvantages of manual coarse registration. An approach for visual validation of the results is shown in Figure 28 for the registration and Figure 30 for the co-registration. The superimposed and color-coded registered point clouds in Figure 28 confirm by visual interpretation the registration error distribution: for the 2014 point cloud, the distinction of the different original point clouds is clearly noticeable, while the superimposed point clouds and the cross sections of the other years are blended and confirm the better registration quality. The same statements can be made for the co-registration illustrated in Figure 30.

6.3 Filtering

Although the process of filtering is not directly addressed in the research questions in Chapter 1.2, it turned out to be an important step during data processing and is discussed following. For optimal data analyses, the raw point cloud should be filtered by cutting out extraneous points and to extract the surface of interest (ABELLÁN ET AL 2014). Within this thesis, for removing the vegetation, a combination of an algorithm based on point cloud geometry (BRODU AND LAGUE 2012) and intensity-based filtering is used. For homogenization of the point cloud, the filtering process is finalized by statistical filtering.

The filtering process starts with training the CANUPO classification algorithm. The balanced accuracy of 95.01% comes close to the results in the original study by BRODU AND LAGUE (2012), where a balanced accuracy values from 95.7% to 97.0% for different dimensions and scales is reached. Therefore, the reached accuracy in this thesis is proposed as sufficient. The parameters for the registration (dimensions and scale level) estimated by the algorithm are used, adaptations are not further tested. Like for the registration, for optimization, further evaluation can be useful. Applying the trained CANUPO classification leads to partially good removal of the vegetated areas: while most of the trees and branches are removed, scattered points of leave areas are still present and cleavage areas of the rock surface are removed. Possible explanations for the misclassification of the algorithm are confusing leaves with small plane rock areas and interpreting the geometry of cleavages as branches. Also, as already proposed in BRODU AND LAGUE (2012), the algorithm struggles with edge

regions of the point cloud. Filling the filtered point cloud up with intensity-based filtered points partially solves the problem of missing cleavage areas but also adds again more not surface related points. The following manual filtering is time consuming and error-prone. Especially registration inaccuracies of the 2014 data lead to difficulties in visual interpretation: dividing the data for manual filtering reveals the various point surface layers of the different scan positions and complicates the extraction of the vegetation of originally individual scans. The statistical filtering leads, as shown in Figure 34, to homogenous structure of the 2016, 2017a and 2017b point cloud with approximately same horizontal and vertical resolution and continuous point spacing. For the 2014 data, this is not reached, as the adjusting the data to the coarse vertical resolution would result in massive data loss.

The process shows that filtering is a complex topic: besides different settings, also different filtering combinations of geometrical, intensity based and statistical filtering approaches can possibly lead to better results. Especially varying the order of different steps or repeating filters on different positions of the process could improve the automated approach and minimize the manual rework. Nevertheless, it can be concluded there is no standardized filtering approach and filtering must be adapted to the given circumstances. Moreover, filtering of the point cloud reveals the original incompleteness of the surface of interest: Figure 35 shows that the final surface model of the Amtmann is, for all scanning campaigns, not only incomplete due to missing scans from the western upslope area, but also the point cloud representing the surface of the scanned parts of the Amtmann is holey. As stressed by BRODU AND LAGUE (2012), this is a common issue when working with TLS data and a result of shadowing effects, missing data due to the position of the laser scanner and roughness characteristics of natural surfaces. Moreover, it is possible that suboptimal filtering increases the missing data within the filtering concept used in this thesis. For instance, not all rock surface data removed by the CANUPO algorithm is restored by the intensity-based filtering. Moreover, statistical filtering cleans the point cloud on the one hand, but removes points from point cloud borders and enlarges therefore data holes on the other hand. At this point of data processing it must be stressed that a comprehensive change detection for the research area on a sub-decimetric scale is not possible with the used data.

6.4 Change detection

After all the previous work, which can be referred to as data pre-processing, change detection represents the final data analysis. As this thesis aims analysis of small scale

change detection in a sub-decimetric range, high and accurate data density is desirable. Therefore, data reduction like deriving grids or meshes from the point cloud is renounced and the point cloud data is used for change detection. Three different approaches of change detection using point cloud data are chosen. The most basic concept is C2C without local modelling: the nearest neighbor in the comparing point cloud, the so-called Hausdorff-distance (see Figure 16), is calculated. By deriving surface normals, the enhanced C2C with local modelling adds a topological dimension to the point cloud. For this thesis, C2C with quadric surface modelling is used. Distances are therefore calculated with regard to the estimated object surface. M3C2 improves the local surface modelling by including the variation of the surface and averaging the point positions. (GIRARDEAU-MONTAUT ET AL 2005, LAGUE ET AL 2013, GIRARDEAU-MONTAUT 2017, CLOUDCOMPARE COMMUNITY 2018)

Before going into detailed discussion, it is mentioned that no obvious changes of the Amtmann's rock surface are detected by visual interpretation during the different scanning campaigns. Moreover, it is expected that the results improve with using the different approaches from C2C without local modelling to C2C with quadric modelling and M3C2.

As the deficient registration and co-registration quality of the 2014 data is known at this point, drawing conclusions from comparing the 2014 and the 2017a data is difficult. The mean point cloud distances are between 0.13 m and 0.15 m for all three change detection approaches with a clear global pattern for the whole point cloud. The lowest change values are shown condensed in the center area which is used for coarse co-registration, and largest distances or not classified points for M3C2 in the lower part and at the borders of the point cloud. Despite to these overall effects, local differences of change can be recognized. Visual verification of chosen areas identified as change by the algorithms with differences in change magnitude to the surrounding areas shows that these are results of various point cloud hole areas between the different years and differences in point cloud densities. Furthermore, cross-sections show, that changes can also be traced back to registration inaccuracies. Comparing the different change detection methods, no explicit differences or qualities can be concluded for the 2014 to 2017a change detection.

The change detection of the 2016 and 2017a data shows with means from 0.01 m to 0.02 m values with one magnitude lower than the 2014-2016 change detection data. The global pattern is quite similar, with a clear shift of the derived distances to smaller values. This can be explained by better registration accuracy, both in registration of the single point cloud within one scanning campaign for all used data and the more

6. DISCUSSION

precise co-registration. The overall distribution of the different distance classes shows again that the concentration of low calculated distances corresponds with the location of reflective tie points. For this comparison, a clear reduction of overall distances from C2C without local modelling to C2C with quadric modelling and M3C2 becomes clear. To eliminate overall effects, again areas with local change of distances are closer examined. Besides point cloud holes, carelessly filtered vegetation is identified as another reason of falsely indicated changes. The chosen examples show that C2C without and with quadric modelling react in a similar way to point holes or vegetation, with less susceptibility of the C2C with quadric modelling approach. One of the examined small scale changes of 2016-2017a change detection shown in Figure 45 cannot be clearly associated with data issues. The area, which is highlighted by all three change detection methods, but getting more prominent with M3C2, can't be explained by data holes or clearly identifiable vegetation. Also examining the original unfiltered point cloud and adding the 2017b data shows local surface changes between the 2016 and 2017 scanning campaigns. For clear validation, it would be necessary to examine the area in the field.

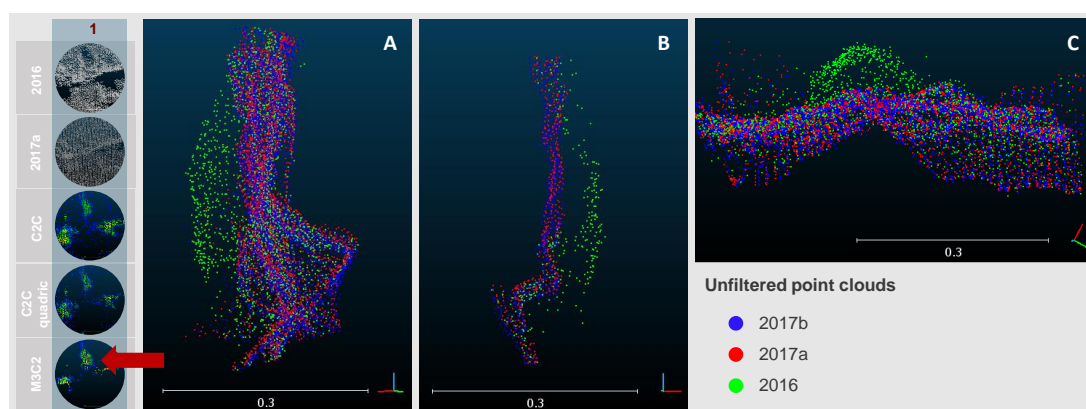


Figure 45: Small scale surface changes between 2016 and 2017 referring to the analyses in Figure 37. A/C: different views of the point cloud section. B: cross section revealing the different surfaces

Finally, it can be concluded that for the 2014 to 2016 change detection, data quality issues do not allow assure findings for surface changes. From 2016 to 2017a, surface changes, which are not related to the discussed issues, are detected, but data issues can't be completely excluded. It is not clear that the surface change is based on rock fall and evaluation in the field is necessary. Also, comprehensive photo documentary is useful for evaluation. Moreover, it cannot be excluded that there are more areas of

surface change within the point cloud, as only chosen examples are closer examined. Regarding the method, true surface changes are difficult to detect due to large amounts of indicated changes which are based on data holes or filtering issues. For the used methods, a visual check is necessary. For further research, it can be tested if a combination of the methods (differences of M3C2 and C2C quadric) provides better outcomes.

Further change detection of 2017a and 2017b serves as a general evaluation of the method, as the two compared epochs are scanned during one day, before and after applying the objects for surface manipulation. As already stressed in Chapter 5.6.2, the manipulated objects represent only 0.0002% of the whole point cloud and are therefore negligible for the overall interpretation. Mean distance values between 0.01 m and 0.02 m and considering the distribution of the defined distance classes, the data shows similar results to the 2016-2017a change detection. This is also an indication of the stable registration outcome using the automated tie point registration and the ICP algorithm. The detailed examination includes the section of the installed objects. Five installed objects are clearly visible in all three change detection approaches, the two smallest hemispheres with a height up to 0.02 m are not visible. This reveals already first ideas of the detectable changes.

The 2017a-2017b change detection is also statistically examined. From this, conclusions for the global change detection can be drawn. Plotting the distribution of the distances as histograms reveals the strong concentration of the distance values in small classes and therefore a strong right-skewness of the distribution. The amount of values in lower classes increases from C2C without local modelling to C2C with quadric modelling to M3C2 change detection. The drawn conclusion of smaller overall detected changes for the different approaches in this order is reinforced by the boxplot visualization and confirmed by the Wilcoxon rank test: using a significance of 0.01, the three data samples do not show the same distributions. M3C2 leads to the smallest detected changes, followed by C2C with quadric modelling, C2C without local modelling leads to the largest distances. M3C2 is therefore globally significantly the most precise of the tested algorithms for revealing stable surfaces of the data within this thesis.

For evaluation of local effects and small scale change detection, the area of the manipulated surface is examined in detail. The different approaches are tested on the different point clouds of the data processing. The statistical analyses are only descriptive but also reveal valuable results. The following discussion only considers the results using the 0.01 m threshold value. For the areas of no change, referred to

as “rest”, M3C2 shows the least false positive classifications (indicated change although no change occurred) for the bare rock surface area with values of $\leq 1\%$ for all tested data. Enlarging the test area and including vegetation leads to increasing of the false-positive classified changes up to 31%. M3C2 and C2C with quadric modelling lead to more similar results, with the lowest values (5.8% - 8.4%) for two vegetation free but not statistically filtered data sets. The false-negative respectively true-positive classification must be interpreted carefully as some changes within the object area smaller than the threshold value: as the hemispheres decrease in height towards the borders, the simulated changes are, at some point, smaller than the defined threshold value. Nevertheless, relative interpretations comparing the different approaches are possible. As the objects are not covered by vegetation, the results of the two different test areas are similar. Also, the results concerning different data only varies marginally: C2C without local modelling and M3C2 lead to 80.2% to 81.6% true-positive classified values, C2C with local modelling shows lower reliability with 69.4% to 69.8%. Summarizing, M3C2 leads to the best results for the combination of detecting small scale changes and revealing surfaces without change for this test areas.

Using the results of the CANUPO classification leads to the overall smallest false-positive classification values, but it must be considered that CANUPO also excludes surface points. The cleaned rock surface leads with 7.1% to the second smallest results for false-positive classification and shows small improvement considering the true-positive value comparing to CANUPO. Choosing one approach for the test area, applying the M3C2 on the vegetation-free, but not statistically filtered data provides the best all over outcome for detecting changes and identifying areas of no change. This raises the question of the necessity of statistical filtering – but the results only count for small point cloud areas, conclusions for using the whole point cloud can't be drawn from this point and require further testing.

6.5 Research questions

To extract the essence of the discussed results, in the following concluding discussion chapter, it is tried to summarize findings with regard to the postulated research questions.

RQ1 *What point cloud registration methods provide the most accurate and efficient approach (regarding usability and processing) for the research area?*

As discussed in Chapter 6.2, for the research area, the combination of automated tie point coarse registration using RiSCAN PRO and ICP-based fine registration implemented in CloudCompare yields the most preferable outcome of the tested approaches.

It is stressed that for co-registration of different epochs, the assumption is taken that the installed tie points and, considering the fine registration, the whole rock structure are stable between the different scanning campaigns. Therefore, this registration approach can only be used for local small scale change detection. Movements of the whole structure can't be detected as the points used for registration are in that case also exposed to the motion. For global change detection, tie points must be installed on stable locations around the Amtmann.

RQ2 What method of surface change detection using TLS data serves the requirements of the research area best?

While raster approaches are usable for plane areas, for change detection on structures like the Amtmann, 3D data is needed. After literature research it is presumed, that for small scale change detection, working with the original point cloud data leads to the best output. Therefore, three different change detection approaches using point clouds are tested.

Already before the development of M3C2, ABELLÁN ET AL (2009) performed tests of different TLS change detection scenarios with the conclusion, that averaging the point positions including the nearest neighbors leads to more accurate results than working with the raw data. LAGUE ET AL (2013) implemented averaging of positions in the M3C2 algorithm and got promoted for small scale TLS change detection of complex surfaces (BANHARD AND CROSBY 2013, ABELLÁN 2016, MARX ET AL 2017). The research within this thesis can confirm that M3C2 provides, comparing to the other two evaluated approaches, the best outcomes concerning overall and local disclosure of stable areas and detection of small scale changes for the explored rock surface of the Amtmann.

RQ 3 What magnitudes of change are detectable using the TLS under the given environmental conditions in the study area?

Studies focusing on small scale change detection in landslide monitoring conclude that 0.02 m to 0.07 m is the range of the minimal detectable change using M3C2 (BARNHART AND CROSBY 2013, MARX ET AL 2017). For the study within this thesis, the minimum detectable changes can therefore be ranged in the lower region of this proposed range, as objects from 0.025 m are detectable within the M3C2 point distance calculation. The range accuracy of 0.015 m and the precision of 0.01 m of the scanner given by the manufacturer (see Chapter 2.3.2) are also lower than this threshold range. The findings are based on visual interpretation and therefore imply subjective influence, for more statistical based evaluation, the examination of the certainty level for each point provided in M3C2 is recommended (LAGUE ET AL 2013).

In despite of the given results, the question can't be comprehensively answered, as several issues arose during the research process: unsatisfying vegetation filtering leads to false-positive indications of change and point cloud holes. Shadowing effects and unfavourable scan positions may also provide false information on change or lead to areas of missing data. Separation between real surface changes and point cloud data and getting comprehensive data are possible topics for further research.

RQ4 Which recommendations can be given for future scanning campaigns with regard to data analyses for the study site and comparable areas?

The answers to this research question, which are summarized in the following bullet points, are not directly derived from the results but a personal evaluation of the all over data processing. The list does not claim to be exhaustive and is rather seen as subjective advice for further research on this topic, especially within the project on this research area.

- Optimize the scan positions to be sure to cover the area of interest comprehensively. Also, positions are preferable where tilting the scanner is not required for the recording, as this leads to performance problems. Moreover, GNSS-measurement of the scan positions can further improve coarse registration. Also, keep the scan positions constant over different scanning campaigns.
- If possible, install high reflective tie points for registration – it usually increases the registration accuracy and minimizes the work effort. For large scale

change detection, tie points on ensured stable positions outside of the object of interest are necessary.

- Make sure to have consistent and optimized settings (e.g. resolution) for all scans within one campaign and for following campaigns.
- Add high resolution images during the scanning process as it simplifies visual interpretation of the point cloud.
- If possible, perform scans outside the vegetation period to reduce effects of vegetation like shadowing effects and following filtering issues.

7. Conclusion

In the introduction of this thesis it is already accented that TLS provides rapid and highly accurate surface recording and has revolutionized 3D data acquisition over the last 20 years in various fields of applied science. The gaining popularity of the method is accompanied by a raising number of publications. The first conclusion that can be drawn is that the enormous amount of research using TLS results in challenges of gaining an overview of the current state of the art, as new publications are arising up every day.

Thereby, also the amount of proposed data processing methods is extensive. Although many approaches are built on the same basic algorithms, there are a great variety and numerous different modifications of methods in registration, filtering and change detection. Hence, extracting the optimal combination of approaches and parameter settings is therefore difficult, especially considering individual requirements for a distinct research area. Moreover, not only the combination of methods, but also the order of processing steps results in different outputs and must therefore be considered. For an ensured choice of method, it is moreover necessary to perform and evaluate the point cloud processing iteratively over the various steps, which goes beyond the scope of this thesis.

The main emphases of this thesis are on the registration of point clouds and change detection, which are the opposite ends of the processing chain – implying a major issue of this thesis: clearing and filtering of the point cloud, situated inbetween the two steps chosen for closer examination, turned out to be the crux of the matter of data processing with a great influence on the outcome of the change detection. Moreover, filtering reveals the incompleteness of point clouds making it impossible to offer satisfactory reponses to the original problem statement of a comprehensive detection of small scale rock falls.

To improve the usability of the method for detecting small scale rock falls in the research area, optimizing the vegetation removal can lead to a major improvement in

7. CONCLUSION

change detection: falsely indicated changes can be minimized and therefore the extraction of real events simplified.

Nevertheless, shadowing effects by vegetation and the fact that there are no optimal scan positions to get a whole 3D model of the Amtmann will continue to be an issue. Furthermore, this leads to incomplete point cloud surfaces and therefore makes the detection of all the appearing rock falls impossible using TLS. Despite, it does not mean that using TLS as a method for small scale rock fall detection on the Amtmann is worthless – though it can't be used for comprehensive monitoring, with the use of TLS general dynamics can be identified and statements about the activity of small scale rock fall over time for the research area can be given.

8. Outlook

Concluding the findings gained within this thesis, both a more detailed look on the applied methods as well as a broader methodological framework are approaches for further research in the topic of small scale rock fall detection.

A lot of parameters influence the accuracy during the different steps of processing TLS data. These can be examined more in detail with a deeper look into the used algorithms combined with comprehensive statistical analyses of the different results. Adjustable parameters can be optimized, sound statistical threshold values for detectable change can be derived and therefore the output can possibly be improved.

Further, additional impacts like environmental effects on the scanning and systematic observational errors, which are not directly addressed within this thesis, can be considered in more detail.

Moreover, various approaches for the different processing steps have also the potential to optimize the point cloud processing. Although the output of the registration within this thesis is already satisfying, other concepts, e.g. implying geometry (HE ET AL 2017, TULADHAR ET AL 2017), could bypass the problems of coarse registration when installation of tie points is not possible. Numerous concepts of filtering and classifying are worth considering, like analyses of echoes and the returning waveforms and varying of footprint sizes (DANSON ET AL 2009, DI SALVO AND LO BRUTTO 2014), multispectral information, especially near infrared bands for extraction of vegetation (LAU ET AL 2015, EKHTARI ET AL 2017, LI ET AL 2018) or different geometric approaches (WILLIAMS ET AL 2018). Furthermore, for change detection, there are various approaches which could improve the output, e.g. modifications of the M3C2 (LEYLAND ET AL 2016, WILLIAMS ET AL 2018).

Besides the classical TLS, there are also other approaches of 3D surface generation are available. Mobile laser scanners have the advantage of no need for a static position (LEYLAND ET AL 2016) and even more flexibility and possibilities for comprehensive scanning when combining the laser scanner with an UAV (RIEGL

8. OUTLOOK

2018). Aside from high-end laser scanning devices, also tests with cheaper alternatives like Microsoft's Kinect lead to remarkable results for surface recording (LAHAMY ET AL 2016, HÄMMERLE ET AL 2014). Structure from motion – the use of images for 3D surface modelling – stands out with low acquisition costs, comparable results and more flexibility considering the use of UAVs for image acquisition (BEMIS ET AL 2014, SCAIONI ET AL 2015, SMITH ET AL 2015, ELTNER ET AL 2016, LONGCHAMP ET AL 2016, GUERIN ET AL 2017).

Summarizing, there is broad methodical potential for detection of small scale rock falls. With optimizing the data acquisition and the processing in consideration of the discussed limitations, further deployment of TLS for small scale rock fall detection on the Amtmann is useful, but other approaches can also be considered.

Bibliography

- ABELLÁN, A., CALVET, J., VILAPLANA, J. M. AND BLANCHARD, J. (2010): Detection and spatial prediction of rock falls by means of terrestrial laser scanner monitoring. – In: *Geomorphology* 100 (3-4), 162-171.
- ABELLÁN, A., DERRON, M.-H. AND JABOYEDOFF, M. (2016): “Use of 3D Point Clouds in Geohazards” Special Issue: Current Challenges and Future Trends. – In: *Remote Sensing* 8 (2), 130.
- ABELLÁN, A., JABOYEDOFF, M., OPPIKOFER, T. AND VILAPLANA, J. M. (2009): Detection of millimetric deformation using a terrestrial laser scanner: Experiment and application to a rock fall event. – In: *Natural Hazards and Earth System Science* 9 (2), 365-372.
- ABELLÁN, A., OPPIKOFER, T., JABOYEDOFF, M., ROSSER, N. J., LIM, M. AND LATO, M. J. (2014): Terrestrial laser scanning of rock slope instabilities. – In: *Earth Surface Processes and Landforms* 39, 80-97.
- ABELLÁN, A., VILAPLANA, J. M. AND MARTÍNEZ, J. (2006): Application of a long-range Terrestrial Laser Scanner to detailed rock fall study at the Vall de Núria (Eastern Pyrenees, Spain). – In: *Engineering Geology* 88 (3-4), 136-148.
- ABELLÁN, A., VILAPLANA, J. M., CALVET, J., GARCÍA-SELLÉS, D. AND ASENSIO, E. (2011): Rock fall monitoring by Terrestrial Laser Scanning – Case study of the basaltic rock face at Castellfollit de la Roca (Catalonia, Spain). – In: *Natural Hazards and Earth System Science* 11, 829–841.
- AKCA, D. (2007): Matching of 3D surfaces and their intensities. – In: *ISPRS Journal of Photogrammetry and Remote Sensing* 62 (2), 112–121.
- ALBA, M., FREGONESE, L., PRANDI, F., SCAIONI, M. AND VALGOI, P. (2006): Structural monitoring of a large dam by terrestrial laser scanning. – In: *International Archives of Photogrammetry, Remote Sensing and Spatial Information Science* 37 (B1), 133-139.

- ALBA, M., GIUSSANI, A., RONCORONI, F. AND SCAIONI, M. (2007): Review and comparison of techniques for terrestrial 3D-view georeferencing. – In: Proceedings of the 5th International Symposium on Mobile Mapping Technology 2007, Padua, Italy.
- AL-DURGHAM, K., HABIB, A. AND KWAK, E. (2013): RANSAC approach for automated registration of terrestrial laser scans using linear features. – In: ISPRS Annals of Photogrammetry, Remote Sensing and Spatial Information Sciences 2 (5/W2), 13–18.
- AL-MANASIR, K. AND FRASER, C. S. (2006): Registration of terrestrial laser scanner data using imagery. – In: The Photogrammetric Record 21 (115), 255–268.
- AMT DER NIEDERÖSTERREICHISCHEN LANDESREGIERUNG (2010): Schadensprotokoll Felssturz Ofenberg vom 21.03.2010. – St. Pölten.
- AMT DER NIEDERÖSTERREICHISCHEN LANDESREGIERUNG (2017): NÖ Atlas 4.0. - See online: atlas.noel.gv.at [Accessed on 21.11.2017]
- ASPERT, N., SANTA-CRUZ, D. AND EBRAHIMI, T. (2002): MESH: Measuring errors between surfaces using the Hausdorff Distance. – In: Proceedings of the IEEE International Conference in Multimedia and Expo 2002, Lausanne, Switzerland, 705-708.
- AVIAN, M., KELLERER-PIRKLBAUER, A. AND BAUER, A. (2009): LiDAR for monitoring mass movements in permafrost environments at the cirque Hinteres Langtal, Austria, between 2000 and 2008. – In: Natural Hazards and Earth System Science 9 (4), 1087-1094.
- BAE, K. H. AND LICHTI, D. D. (2004): Automated registration of unorganized point clouds from terrestrial laser scanners. – In: International Archives of Photogrammetry, Remote Sensing and Spatial Information Sciences 35 (B5), 222–227.
- BARBARELLA, M. AND FIANI, M. (2013a): Monitoring of large landslides by Terrestrial Laser Scanning techniques: field data collection and processing. – In: European Journal of Remote Sensing 46 (1), 126-151.
- BARBARELLA, M. AND FIANI, M. (2013b): Landslide monitoring using terrestrial laser scanner: Georeferencing and canopy filtering issues in a case study. – In: International Archives of Photogrammetry, Remote Sensing and Spatial Information Sciences 39, 157-162.

- BARBARELLA, M., DE BLASIIS, M. R. AND FIANI, M. (2017a): Terrestrial laser scanner for the analysis of airport pavement geometry. – In: *International Journal of Pavement Engineering*, 1-15.
- BARBARELLA, M., FIANI, M. AND LUGLI, A. (2017b): Uncertainty in terrestrial laser scanner surveys of landslides. – In: *Remote Sensing* 9 (2), 113.
- BARNHART, T. B. AND CROSBY, B. T. (2013): Comparing two methods of surface change detection on an evolving thermokarst using high-temporal-frequency terrestrial laser scanning, Selawik River, Alaska. – In: *Remote Sensing* 5 (6), 2813–2837.
- BEMIS, S. P., MICKLETHWAITE, S., TURNER, D. JAMES, M. R., AKCIZ, S., THIELE, S. AND BANGASH, H. A. (2014): Ground-based and UAV-based photogrammetry: A multi-scale, high-resolution mapping tool for structural geology and paleoseismology. – In: *Journal of Structural Geology* 69, 163–178.
- BERALDIN, J. A., BLAIS, F., BOULANGER, P., COURNOYER, L., DOMEY, J., EL-HAKIM, S. F., GODIN, G., RIOUX, M. AND TAYLOR, J. (2000): Real World modelling through high resolution digital 3D imaging of objects and structures. – In: *ISPRS Journal of Photogrammetry and Remote Sensing* 55, 230–250.
- BERALDIN, J.-A., BLAIS, F. AND LOHR, U. (2010): Laser Scanning Technology. – In: Vosselman, G., Maas, H.-G. (Ed.): *Airborne and Terrestrial Laser Scanning*. – Dunbeath, 1-44.
- BESL, P. AND MCKAY, N. D. (1992): A Method for Registration of 3-D Shapes. – In: *IEEE Transactions on pattern analysis and machine intelligence* 14 (2), 239-256.
- BITELLI, G., DUBBINI, M. AND ZANUTTA, A. (2004): Terrestrial Laser Scanning and Digital Photogrammetry Techniques to Monitor Landslide Bodies. – In: *Proceedings of the XXth ISPRS Congress 2004, Istanbul, Turkey*.
- BMLFUW IV/5 (2016): Das Ereignisportal des digitalen Wildbach- und Lawinenkatasters. – see online: <http://www.naturgefahren.at/karten/chronik/ereignisdoku/Ereignisportal.html> [Accessed on 26.02.2018]
- BOURRIER, F., DORREN, L. AND HUNGR, O. (2012): The use of ballistic trajectory and granular flow models in predicting rockfall propagation. – In: *Earth Surface Processes and Landforms* 38, 435-440.

- BRODU, N. AND LAGUE, D. (2012): 3D terrestrial lidar data classification of complex natural scenes using a multi-scale dimensionality criterion: Applications in geomorphology. – In: ISPRS Journal of Photogrammetry and Remote Sensing 68 (1), 121-134.
- BUREICK, J., NEUNER, H., HARMENNG, C. AND NEUMANN, I. (2016): Curve and Surface Approximation of 3D Point Clouds. – In: AVN Allgemeine Vermessungsnachrichten 123 (11-12), 315-327.
- BURTON, I., KATES, R. W. AND WHITE, G. F. (1978): The Environment as Hazard. – New York.
- CARREA, D., ABELLÁN, A., DERRON, M.-H., JABOYEDOFF, M. (2015): Automatic rockfalls volume estimation based on terrestrial laser scanning data. – In: Lollino, G., Giordan, G., Crosta, G. B., Corominas, J., Azzam, R., Wasowski, J. and Sciarra, N. (Ed.): Engineering Geology for Society and Territory – Volume 2: Landslide Processes. – Cham, Heidelberg, New York, Dordrecht, London, 425-428.
- CHARLTON, M. E., COVENEY, S. J. AND MCCARTHY, T. (2009): Issues in Laser Scanning. – In: Heritage, G.L. and Large, A.R.G. (Ed.): Laser Scanning for the Environmental Sciences. – Chinchester, 35-48.
- CHÁVEZ, A. AND KARSTOFT, H. (2012): Improvement of Kinect™ Sensor Capabilities by Fusion with Laser Sensing Data Using Octree. – In: Sensors 12 (4). 3868-3778.
- CHEN, Y. AND MEDIONI, G. (1991): Object modelling by registration of multiple range images. – In: Proceedings of the IEEE International Conference on Robotics and Automation 1991, Sacramento, California, 2724-2729.
- CHMELINA, K., JANSÁ, J., HESINA, G. AND TRAXLER, C. (2012): A 3-d laser scanning system and scan data processing method for the monitoring of tunnel deformations. – In: Journal of Applied Geodesy 6 (3-4), 177-185.
- CIGNONI, P., ROCCHINI, C. AND SCOPIGNO, R. (1998): Metro: Measuring Error on Simplified Surfaces. – In: Computer Graphics Forum 17 (2), 167-174.
- CLOUDCOMPARE COMMUNITY (2018): CloudCompare Version 2.6.1 User manual. – See online: <http://www.danielgm.net/cc/doc/qCC/CloudCompare%20v2.6.1%20-%20User%20manual.pdf> [Accessed on 17.02.2018]
- CLOUET, N., BERGER, F. AND LIÉVOIS, J. (2012): Rockfall modelling and risk zoning: a case study in the French alps usung [sic!] geomatics, airborne laser scanning,

- 2D and 3D runout models. – In: Proceedings of the 12th Congress INTERPRAEVENT 2012, Grenoble, France, 479-486.
- COROMINAS, J., VAN WESTEN, C., FRATTINI, P., CASCINI, L., MALET, J. P., FOTOPOULOU, S., CATANI, F., VAN DEN ECKHAUT, M., MAVROULI, O., AGLIARDI, F., PITILAKIS, K., WINTER, M. G., PASTOR, M., FERLISI, S., TOFANI, V., HERVÁS, J., AND SMITH, J. T (2014): Recommendations for the quantitative analysis of landslide risk. – In: Bulletin of Engineering Geology and the Environment 73 (2), 209-263.
- CORSINI, A., CASTAGNETTI, C., BERTACCHINI, E., RIVOLA, R., RONCHETTI, F. AND CAPRA, A. (2013): Integrating airborne and multi-temporal long-range terrestrial laser scanning with total station measurements for mapping and monitoring a compound slow moving rock slide. – In: Earth Surface Processes and Landforms 38 (11), 1330-1338.
- CROMMELINCK, S. AND HÖFLE, B. (2016): Simulating an autonomously operating low-cost static terrestrial LiDAR for multitemporal maize crop height measurements. – In: Remote Sensing 8 (3), 205.
- CROSTA, G. B., AGLIARDI, F., FRATTINI, P AND LARI, S. (2015): Key Issues in Rock Fall Modeling, Hazard and Risk Assessment for Rockfall Protection. – In: Lollino, G., Giordan, G., Crosta, G. B., Corominas, J., Azzam, R., Wasowski, J. and Sciarra, N. (Ed.): Engineering Geology for Society and Territory – Volume 2: Landslide Processes. – Cham, Heidelberg, New York, Dordrecht, London, 43-58.
- DANSON, F. M., MORSDORF, F. AND KOETZ, B. (2009): Airborne and Terrestrial Laser Scanning for Measuring Vegetation Canopy Structure. – In: Heritage, G.L. and Large, A.R.G. (Ed.): Laser Scanning for the Environmental Sciences. – Chinchester, 201-219.
- DEPARTMENT OF REGIONAL DEVELOPMENT AND ENVIRONMENT, EXECUTIVE SECRETARIAT FOR ECONOMIC AND SOCIAL AFFAIRS ORGANIZATION OF AMERICAN STATES (1990): Disaster, planning and development: managing natural hazards to reduce loss. – Washington, D.C.
- DI SALVO, F. AND LO BRUTTO, M. (2014): Full-waveform terrestrial laser scanning for extracting a high-resolution 3D topographic model: A case study on an area of archaeological significance. – In: European Journal of Remote Sensing 47 (1), 307-327.

- DOLD, C. AND BRENNER, C. (2006): Registration of terrestrial laser scanning data using planar patches and image data. – In: International Archives of Photogrammetry, Remote Sensing and Spatial Information Sciences 36 (5), 78–83.
- DONGES, A. AND NOLL, R. (2015): Laser Measurement Technology – Fundamentals and Applications. – Heidelberg, New York, Dordrecht, London.
- EHYD (2017): Bundesministerium für Land- und Forstwirtschaft, Umwelt und Wasserwirtschaft – Klimadaten. – See online: <http://ehyd.gv.at/> [Accessed on 21.08.2017]
- EINSTEIN, A. (1916): Zur Quantentheorie der Strahlung. – In: Mitteilungen der Physikalischen Gesellschaft Zürich 18, 47-62.
- EITEL, J. U. H., HÖFLE, B., VIERLING, L. A., ABELLÁN, A., ASNER, G. P., DEEMS, J. S., GLENNIE, C. L., JOERG, P. C., LEWINTER, A. L., MAGNEY, T. S., MANDLBURGER, G., MORTON, D. C., MÜLLER, J. AND VIERLING, K. T. (2016): Beyond 3-D: The new spectrum of lidar applications for earth and ecological sciences. – In: Remote Sensing of Environment 186, 372-392.
- EKHTARI, N., GLENNIE, C. AND FERNANDEZ-DIAZ, J.C. (2017): Classification of multispectral lidar point clouds. – In: Proceedings of the IEEE International Geoscience and Remote Sensing Symposium 2017, Fort Worth, USA, 2756-2759.
- ELING, D. (2009): Terrestrisches Laserscanning für die Bauwerksüberwachung. – Dissertation, Gottfried Wilhelm Leibnitz University Hannover, Munich.
- ELSEBERG, J., BORRMANN, D. AND NÜCHTER, A. (2011): Efficient processing of large 3D point clouds. – In: Proceedings of the XXIIIth International Symposium on Information, Communication and Automation Technologies 2011, Sarajevo, Bosnia, 6102102.
- ELSEBERG, J., BORRMANN, D. AND NÜCHTER, A. (2013): One billion points in the cloud - An octree for efficient processing of 3D laser scans. – In: ISPRS Journal of Photogrammetry and Remote Sensing 76, 76-88.
- ELTNER, A., KAISER, A., CASTILLO, C., ROCK, G., NEUGIRG, F. AND ABELLÁN, A. (2016): Image-based surface reconstruction in geomorphometry-merits, limits and developments. – In: Earth Surface Dynamics 4 (2), 359-389.

- ENGSTRÖM, T. AND JOHANSSON, M. (2009): The use of terrestrial laser scanning in archaeology. Evaluation of a Swedish project, with two examples. – In: Journal of Nordic Archaeological Science 16, 3-13.
- GIRARDEAU-MONTAUT D. (2017): CloudCompare plugins qM3C2 syntax - See online: <https://github.com/CloudCompare/CloudCompare/blob/master/plugins/qM3C2/qM3C2.cpp> [Accessed on 28.11.2017]
- GIRARDEAU-MONTAUT, D., ROUX, M., MARC, R. AND THIBAUT, G. (2005): Change Detection on Points Cloud Data acquired with a Ground Laser Scanner. – In: Proceedings of the ISPRS Workshop Laser Scanning 2005, Enschede, the Netherlands, 30-35.
- GLADE, T. AND RUDOLF-MIKLAU, F. (2015): Zusammenfassung - ÖROK-Schriftenreihe Nr. 193 – ÖREK-Partnerschaft „Risikomanagement für gravitative Naturgefahren in der Raumplanung. – In: ÖROK (ÖSTERREICHISCHE RAUMORDNUNGSKONFERENZ) (Ed.) (2015): Risikomanagement für gravitative Naturgefahren in der Raumplanung. – Wien, 13-22.
- GOEPFERT, J., SOERGEL, U., HEIPKE, C AND BRZANK, A. (2008): An approach for filtering lidar data in coastal vegetated areas using intensity information and multiple echoes. – In: The International Archives of the Photogrammetry, Remote Sensing and Spatial Information Sciences. 37 (B3), 219-225.
- GONZÁLEZ-AGUILERA, D., GÓMEZ-LAHOZ, J. AND SÁNCHEZ, J. (2008): A new approach for structural monitoring of large dams with a three-dimensional laser scanner. – In: Sensors 8 (9), 5866–5883.
- GORDON, G., LICHTI, D., FRANKE, J. AND STEWART, M. (2004): Measurement of structural deformation using terrestrial laser scanners. – In: Proceedings of the 1st FIG International Symposium on Engineering Surveys for Construction Works and Structural Engineering 2004, Nottingham, UK.
- GRACHEVA, R. AND GOLYEVA, A. (2009): Landslides in Mountain Regions: Hazards, Resources and Information – In: Beer, T. (Ed.) (2009): Geophysical Hazards. International Year of Planet Earth. – Dordrecht, 249-260.
- GRANT, D. G., BETHEL, J. S. AND CRAWFORD, M. C. (2012): Point-to-plane registration of terrestrial laser scans. – In: ISPRS Journal of Photogrammetry and Remote Sensing 72, 16-26.
- GRUEN, A. AND AKCA, D. (2005): Least squares 3D surface and curve matching. – In: ISPRS Journal of Photogrammetry and Remote Sensing 59 (3), 151–174.

- GUERIN, A., ABELLÁN, A., MATASCI, B., JABOYEDOFF, M., DERRON, M.-H. AND RAVANEL, L. (2017): Brief communication: 3D reconstruction of a collapsed rock pillar from web-retrieved images and terrestrial lidar data – the 2005 event of the West face of the Durs (Mont-Blanc massif). – In: *Natural Hazards and Earth System Sciences* 17, 1207-1220.
- HÄMMERLE, M., HÖFLE, B., FUCHS, J., SCHRÖDER-RITZRAU, A., VOLLWEILER, N. AND FRANK, N. (2014): Comparison of Kinect and terrestrial LiDAR capturing natural karst cave 3-D objects. – In: *IEEE Geoscience and Remote Sensing Letters* 11 (11), 1896-1900.
- HAN, J. Y. (2010): A noniterative approach for the quick alignment of multistation unregistered LIDAR point clouds. – In: *IEEE Geoscience and Remote Sensing Letters* 7 (4), 727–730.
- HANCOCK, J., LANGER, D., HEBERT, M., SULLIVAN, R., INGIMARSON, D., HOFFMANN, E., METTENLEITER, M. AND FRÖHLICH, C. (1998): Active laser radar for high-performance measurements. – In: *Proceedings of the IEEE International Conference on Robotics and Automation* 1998 (2), 1465–1470.
- HASHEMI, A., KALANTARI, M. AND KASSER, M. (2013): Direct Solution of the 7 parameters transformation problem. – In: *Applied Mathematics and Information Science* 7 (4), 1375-1382.
- HAUPT, M. AND PAFFENHOLZ, J.-A. (2016): 3D-Punktwolkenbasiertes Monitoring aus Sicht eines Ingenieurbüros – Chancen und Herausforderungen. – In: DVW – Gesellschaft für Geodäsie, Geoinformation und Landmanagement e.V. (Ed.): *Terrestrisches Laserscanning 2016*. DVW-Schriftenreihe 85. – Augsburg, 59-73.
- HE, L., LI, Z. AND CHEN, S. (2017): Aligning algorithm of 3D point cloud model based on dimensionality reduction. – In: *Proceedings of the 2nd International Conference on Multimedia and Image Processing 2017*, Wuhan, China, 281-285.
- HEJBUDZKA, K., LINDENBERGH, R., SOUDARISSANANE, S. AND HUMME, A. (2010): Influence of Atmospheric Conditions on the Range Distance and Number of Returned Points in Leica Scanstation 2 Point Clouds. – In: *International Archives of Photogrammetry, Remote Sensing and Spatial Information Sciences* 34 (5), 282–287.

- HERITAGE, G. L. AND LARGE, A. R. G. (Ed.) (2009a): Laser Scanning for the Environmental Sciences. – Chinchester.
- HERITAGE, G.L. AND LARGE, A.R.G. (2009b): Principles of 3D Laser Scanning. – In: Heritage, G.L. and Large, A.R.G. (Ed.): Laser Scanning for the Environmental Sciences. – Chinchester, 21-34.
- HOBBS, P. R. N., HUMPHREYS, B., REES, J. G., TRAGHEIM, D. G., JONES, L. D., GIBSON, A., ROWLANDS, K., HUNTER, G. AND AIREY, R. (2002): Monitoring the role of landslides in soft cliff coastal recession. – In: McInnes, R. G. and Jakeways, J. (Ed.): Instability. Planning and Management. – London, 589-600.
- HOFMANN, R. (2004): Bodenmechanischer Bericht über die Ankerungsarbeiten der Wandmauern im Herbst 2004 Ofenloch IV – Ybbstal – Bundesstraße B31 km 8,969 – km 9,180. – St. Pölten.
- HOLST, C. AND KUHLMANN, H. (2016): Challenges and Present Fields of Action at Laser Scanner Based Deformation Analyses. – In: Journal of Applied Geodesy 19 (1), 17-25.
- HOLST, C., NOTHNAGEL, A., BLOME, M., BECKER, P., EICHBORN, M., AND KUHLMANN, H. (2014): Improved area-based deformation analysis of a radio telescope's main reflector based on terrestrial laser scanning. - In: Journal of Applied Geodesy 9 (1), 1-13.
- HÜBL, J., KIENHOLZ, H. AND LOIPERSBERGER, A. (Ed.) (2002): DODODIS – Documentation of Mountain Disasters. – Hünibach.
- HUNGR, O., LEROUÉIL, S., PICARELI, L. (2014): The Varnes classification of landslide types, an update. – In: Landslides 11 (2), 167-194.
- HUNTER, G., PINKERTON, H., AIREY, R. AND CALVARI, S. (2003): The application of a long-range laser scanner for monitoring volcanic activity on Mount Etna. – In: Journal of Volcanology and Geothermal Research 123 (1-2), 203-210.
- JABOYEDOFF, M., METZGER, R., OPPIKOFE, T., COUTURE, R., DERRON, M.-H., LOCAT, J. AND TURMEL, D. (2007): New insight techniques to analyze rock-slope relief using DEM and 3D-imaging cloud points: COLTOP-3D software – In: Proceedings of the 1st Canada-US Rock Mechanics Symposium 2007, Vancouver, 61-68.

- JABOYEDOFF, M., OPPIKOFE, T., ABELLÁN, A., DERRON, M.-H., LOYE, A., METZGER, R., AND PEDRAZZINI, A. (2012): Use of LIDAR in landslide investigations: a review. – In: *Natural Hazards* 61, 5–28.
- JANERAS, M., NAVARRO, M., ARNÓ, G., RUIZ, A., KORNUS, W., TALAYA, J., BARBERÀ, M. AND LÓPEZ, F. (2004): LiDAR applications to rock fall hazard assessment in Vall de Núria. – In: *Proceedings of the 4th ICA Mountain Cartography Workshop 2004*, Vall de Nuria, Catalonia, Spain.
- KAHMEN, H. (2006²⁰): *Angewandte Geodäsie: Vermessungskunde*. – Berlin and New York.
- KÖPPEN W. (1918): Klassifikation der Klimate nach Temperatur, Niederschlag und Jahresablauf. – In: *Petermanns Geographische Mitteilungen* 64, 193-203.
- KOTTEK M., GRIESER J., BECK C., RUDOLF B. AND RUBEL F. (2006): World Map of the Köppen-Geiger climate classification updated. – In: *Meteorologische Zeitschrift* 15 (3), 259-263.
- KRAUS, K. (2004⁷): *Photogrammetrie. Geometrische Informationen aus Photographien und Laserscanneraufnahmen*. – Berlin and New York.
- KROMER, R. A., ABELLÁN, A., HUTCHINSON, D. J., LATO, M., CHANUT, M.-A., DUBOIS, L. AND JABOYEDOFF, M. (2017): Automated terrestrial laser scanning with near-real-time change detection - Monitoring of the Séchillienne landslide. – In: *Earth Surface Dynamics* 5 (2), 293-310.
- KROMER, R. A., ABELLÁN, A., HUTCHINSON, D. J., LATO, M., EDWARDS, T. AND JABOYEDOFF, M. (2015a): A 4D filtering and calibration technique for small-scale point cloud change detection with a terrestrial laser scanner. – In: *Remote Sensing* 7 (10), 13029-13052.
- KROMER, R. A., HUTCHINSON, D. J., LATO, M. J., GAUTHIER, D. AND EDWARDS, T. (2015b): Identifying rock slope failure precursors using LiDAR for transportation corridor hazard management. – In: *Engineering Geology* 195, 93-103.
- LAGUE, D., BRODU, N. AND LEROUX, J. (2013): Accurate 3D comparison of complex topography with terrestrial laser scanner: Application to the Rangitikei canyon (N-Z). – In: *ISPRS Journal of Photogrammetry and Remote Sensing* 82, 10-26.
- LAHAMY, H., LICHTI, D. D., STEWARD, J., EL-BADRY, M. AND MORAVVEJ, M. (2016): Measurement of Deflection in Concrete Beams during Fatigue Loading Test Using the Microsoft Kinect 2.0. – In: *Journal of Applied Geodesy* 10 (1), 71-77.

- LARGE, A.R.G. AND HERITAGE, G.L. (2009): Laser Scanning – Evolution of the Discipline. – In: Heritage, G.L. and Large, A.R.G. (Ed.): Laser Scanning for the Environmental Sciences. – Chinchester, 1-20.
- LAU, C.L., HALIM, S., ZULKEPLI, M., MOHD AZWAN, A., TANG, W.L. AND CHONG, A.K. (2015): Terrain extraction by integrating terrestrial laser scanner data and spectral information. – In: International Archives of the Photogrammetry, Remote Sensing and Spatial Information Sciences 40 (2W4), 45-51.
- LEICA (2017): Leica ScanStation P20 Data Sheet. – See online: http://w3.leica-geosystems.com/downloads123/hds/hds/ScanStation_P20/brochures-datasheet/Leica_ScanStation_P20_DAT_en.pdf [Accessed on 01.08.2017]
- LEYLAND, J., HACKNEY, C. R., DARBY, S. E., PARSONS, D. R., BEST, J. L., NICHOLAS, A. P., AALTO, R. AND LAGUE, D. (2016): Extreme flood-driven fluvial bank erosion and sediment loads: direct process measurements using integrated Mobile Laser Scanning (MLS) and hydro-acoustic techniques. – In: Earth Surface Processes and Landforms 42 (2), 334-346.
- LI, J., WAN, Y. AND GAO, X. (2012): A new approach for subway tunnel deformation monitoring: high-resolution terrestrial laser scanning. – In: International Archives of Photogrammetry, Remote Sensing and Spatial Information Sciences 39 (B5), 223–228.
- LI, Z., SCHAEFER, M., STRAHLER, A., SCHAAF, C., JUPP, D. (2018): On the utilization of novel spectral laser scanning for three-dimensional classification of vegetation elements. – In: Interface Focus 8 (2), 20170039.
- LICHTI, D. D. (2004): A resolution measure for terrestrial laser scanners. – In: Proceedings of the XXth ISPRS Congress 2004, Istanbul, Turkey, 216–221.
- LICHTI, D. D. AND JAMTSO, S. (2006): Angular resolution of terrestrial laser scanners. – In: Photogrammetric Record 21 (114), 141-160.
- LICHTI, D. D. AND SKALLOUD, J. (2010): Registration and Calibration. – In: Vosselman, G., Maas, H.-G. (Ed.): Airborne and Terrestrial Laser Scanning. – Dunbeath, 83-133.
- LIEBIG, J. P., GRÜNBERG, J., PAFFENHOLZ, J.-A. AND VENNEGEERTS, H. (2011): Taktile und laserbasierte Messverfahren für die messtechnische Überwachung einer Autobahnbrücke. – In: Bautechnik 88 (11), 749-756.

- LIM, M., MILLS, J. AND ROSSER, N. (2009): Laser Scanning Surveying of Linear Features: Considerations and Applications. – In: Heritage, G.L. and Large, A.R.G. (Ed.): Laser Scanning for the Environmental Sciences. – Chinchester, 245-261.
- LIM, M., PETLEY, D. N., ROSSER, N. J., ALLISON, R. J., AND LONG, A. J. (2005): Combined digital photogrammetry and time-of-flight laser scanning for monitoring cliff evolution. – In: The Photogrammetric Record 20 (110), 109–129.
- LINDENBERGH, R. AND PFEIFER, N. (2005): A statistical deformation analysis of two epochs of terrestrial laser data of a lock. – In: Proceedings of the 7th Conference on Optical 3D Measurement Techniques 2005 (2), Vienna, Austria, 61-70.
- LINDENBERGH, R. AND PIETRZYK, P. (2015): Change detection and deformation analysis using static and mobile laser scanning. – In: Applied Geomatics 7 (2), 65–74.
- LINDENBERGH, R., PFEIFER, N. AND RABBANI, T. (2005): Accuracy analysis of the Leica HDS3000 and feasibility of tunnel deformation monitoring. – In: Proceedings of ISPRS WG Workshop on Laser scanning 2005, Enschede, the Netherlands, 24-29.
- LONGCHAMP, C., ABELLÁN, A., JABOYEDOFF, M. AND MANZELLA, I. (2016): 3-D models and structural analysis of rock avalanches: The study of the deformation process to better understand the propagation mechanism. – In: Earth Surface Dynamics 4 (3), 743-755.
- LOVAS, T., BARSÍ, A., DETREKÓI, A., DUNAI, L., CSAK, Z., POLGAR, A., BERENYI, A., KIBEDY, Z. AND SZOCS, K. (2008): Terrestrial laser scanning in deformation measurements of structures. – In: International Archives of Photogrammetry, Remote Sensing and Spatial Information Sciences 37 (B5), 527–532.
- MAIMAN, T.H. (1960): Stimulated optical radiation in ruby. – In: Nature 187, 493-494.
- MARX, S., ANDERS, K., ANTONOVA, S., BECK, I., BOIKE, J., MARSH, P., LANGER, M. AND HÖFLE, B. (2017): Terrestrial laser scanning for quantifying small-scale vertical movements of the ground surface in Arctic permafrost regions. – In: Proceedings of the Arctic Change 2017, Québec, Canada, 268.

- MARX, S., HÄMMERLE, M., KLONNER, C. AND HÖFLE, B. (2016): 3D Participatory Sensing with Low-Cost Mobile Devices for Crop Height Assessment – A Comparison with Terrestrial Laser Scanning Data. – In: PLoS ONE 11 (4), e0152839.
- MAXWELL, J. C. (1864): A Dynamical Theory of the Electromagnetic Field. – In: Proceedings of the Royal Society of London Vol. XIII, 531-536.
- MEINERS-HAGEN, K. SCHÖDEL, R., POLLINGER, F. AND ABOU-ZEID, A. (2009): Multi-Wavelength Interferometry for Length Measurements Using Diode Lasers. – In: Measurement Science Review 9 (3/1), 16-26.
- MESCHEDE, D. (Ed.) (2015²⁵): Gerthsen Physik. – Bonn.
- METTERNICHT, G., HURNI, L., AND GOGU, R. (2005): Remote sensing of landslides: An analysis of the potential contribution to geo-spatial systems for hazard assessment in mountainous environments. – In: Remote Sensing of Environment 98 (2-3), 284–303.
- MILL, T. (2016): Simulation of terrestrial laser scanning errors occurring during deformation monitoring. – In: Proceedings of the 3rd Joint International Symposium on Deformation Monitoring 2016, Vienna, Austria.
- MONSERRAT, O. AND CROSETTO, M. (2008): Deformation measurement using terrestrial laser scanning data and least squares 3D surface matching. – In: ISPRS Journal of Photogrammetry and Remote Sensing 63 (1), 142-154.
- MUKUPA, W., ROBERTS, G. W., HANCOCK, C. M. AND AL-MANASIR, K. (2017): A review of the use of terrestrial laser scanning application for change detection and deformation monitoring of structures. – In: Survey Review 49 (353), 99-116.
- MÜLLER, W. H. (1982): Zur Entstehung der Rauhewacke. – In: Eclogae Geologicae Helvetiae 75 (3), 481-494.
- NEUNER, H., HOLST, C. AND KUHLMANN, H. (2016): Overview on Current Modelling Strategies of Point Clouds for Deformation Analysis. – In: AVN Allgemeine Vermessungs-Nachrichten 123 (11-12), 328-339.
- NÖN – NIEDERÖSTERREICHISCHE NACHRICHTEN (2017): Eröffnung des neuen Ybbstal-Radwegs. See online: <http://www.noen.at/ybbstal/ybbstal-eroeffnung-des-neuen-ybbstal-radweges/51.687.608> [Accessed on 29.08.2017]

- OHLMANN-LAUBER, J. AND SCHÄFER, T. (2011): Ansätze zur Ableitung von Deformationen aus TLS-Daten. – In: DVW – Gesellschaft für Geodäsie, Geoinformation und Landmanagement e.V. (Ed.): Terrestrisches Laserscanning 2016. DVW-Schriftenreihe 85. – Augsburg, 161-180.
- OLSEN, M. J., JOHNSTONE, E., KUESTER, F., DRISCOLL, N. AND ASHFORD, S. A. (2011): New automated point-cloud alignment for ground-based light detection and ranging data of long coastal sections. – In: Journal of Surveying Engineering 137 (1), 14-25.
- OLSEN, M. J., WARTMAN, J., MCALISTER, M., MAHMOUDABADI, H., O'BANION, M. S., DUNHAM, L. AND CUNNINGHAM, K. (2015): To fill or not to fill: Sensitivity analysis of the influence of resolution and hole filling on point cloud surface modeling and individual rock fall event detection. – In: Remote Sensing 7 (9), 12103-12134.
- OPPIKOFFER, T., JABOYEDOFF, M., BLIKRA, L., DERRON, M.-H., METZGER, R. (2009): Characterization and monitoring of the Åknes rockslide using terrestrial laser scanning. – In: Natural Hazards and Earth System Sciences 9, 1003-1019.
- OPPIKOFFER, T., JABOYEDOFF, M., KEUSEN, H.-R. (2008): Collapse at the eastern Eiger flank in the Swiss Alps. – In: Nature Geoscience 1 (8), 531-535.
- ORF (2017a): Toter bei Steinschlag auf Reschenstraße. – See online: <http://tirol.orf.at/news/stories/2853123/> [Accessed on 26.02.2018]
- ORF (2017b): Zwei Tote bei Alpinunfällen. – See online: <http://tirol.orf.at/news/stories/2857666/> [Accessed on 26.02.2018]
- ORF (2017c): Bundesstraße bis zu 20 Meter hoch verschüttet. – See online: <http://salzburg.orf.at/news/stories/2860220/> [Accessed on 26.02.2018]
- ORF (2017d): Frau nach Bergunfall gestorben. – See online: <http://ooe.orf.at/news/stories/2873813/> [Accessed on 26.02.2018]
- ORF (2017e): Riesiger Felssturz beim Wiesbachhorn. – See online: <http://salzburg.orf.at/news/stories/2874520/> [Accessed on 26.02.2018]
- ORF (2017f): Wochenlange Sperre nach Felssturz in Kufstein. – See online: <http://tirol.orf.at/news/stories/2877271/> [Accessed on 26.02.2018]
- ORF (2017g): Felsstürze blockierten mehrere Straßen. – See online: <http://tirol.orf.at/news/stories/2883411/> [Accessed on 26.02.2018]

- ORF (2017h): Weitere Gesteinsabbrüche im Valsertal. – See online: <http://tirol.orf.at/news/stories/2885906/> [Accessed on 26.02.2018]
- ORF (2018a): Zwei Felsstürze behindern Verkehr am Reschen. – See online: <http://tirol.orf.at/news/stories/2887932/> [Accessed on 26.02.2018]
- ORF (2018b): Felssturz in Partenen: Personen nicht gefährdet. – See online: <http://vorarlberg.orf.at/news/stories/2888117/> [Accessed on 26.02.2018]
- ORF (2018c): Felssturz blockierte alte Reschenstraße. – See online: <http://tirol.orf.at/news/stories/2889054/> [Accessed on 26.02.2018]
- ORF (2018d): Wieder Felssturz auf der Katschbergstraße. – See online: <http://salzburg.orf.at/news/stories/2889042/> [Accessed on 26.02.2018]
- ORF (2018e): Felssturz und Hangrutsch durch Schmelzwasser. – See online: <http://tirol.orf.at/news/stories/2891423/> [Accessed on 26.02.2018]
- ORF (2018f): Straßensperre nach Felssturz bei Umhausen. – See online: <http://tirol.orf.at/news/stories/2896816/> [Accessed on 26.02.2018]
- PAAR, G., NAUSCHNEGG, B. AND ULLRICH, A. (2000): Laser scanner monitoring - technical concepts, possibilities and limits. – In: Proceedings of the Workshop on Advanced Techniques for the Assessment of Natural Hazards in Mountain Areas 2000, Innsbruck, Austria, 101.
- PESCI, A., TEZA, G. AND BONALI, E. (2011): Terrestrial Laser Scanner Resolution: Numerical Simulations and Experiments on Spatial Sampling Optimization. – In: Remote Sensing 3 (1), 167–184.
- PESCI, A., TEZA, G. AND VENTURA, G. (2008): Remote sensing of volcanic terrains by terrestrial laser scanner: preliminary reflectance and RGB implications for studying Vesuvius crater (Italy). – In: Annals of Geophysics 51 (4), 633-653.
- PRICE, W.F. AND UREN, J. (1989): Laser Surveying. – London.
- PROMPER, C. AND RUDOLF-MIKLAU, F. (2015): Die ÖREK-Partnerschaft für “Risikomanagement für gravitative Naturgefahren”: Problemstellung und fachpolitische Ziele. – In: ÖROK (Österreichische Raumordnungskonferenz) (Ed.): Risikomanagement für gravitative Naturgefahren in der Raumplanung. – Wien, 33-42.
- RIEGL (2015): RiSCAN PRO manual 2.1.1. – Horn.

BIBLIOGRAPHY

- RIEGL (2017): Riegl VZ 6000 Data Sheet. – See online: http://www.riegl.com/uploads/tx_pxpriegldownloads/Datasheet_VZ-6000_2017-06-14.pdf [Accessed on 24.07.2017]
- RIEGL (2018): RiCOPTER Data Sheet. – See online: http://www.riegl.com/uploads/tx_pxpriegldownloads/RiCOPTER_sensor-platform_Infosheet_2017-09-12.pdf [Accessed on 11.05.2018]
- RIVEIRO, B., MORER, P., ARIAS, P. AND DE ARTEAGA, I. (2011): Terrestrial laser scanning and limit analysis of masonry arch bridges. – In: *Construction and Building Materials* 25 (4), 1726-1735.
- ROSSER, N. J., LIM, N., PETLEY, D. N., DUNNING, S. AND ALLISON, R. J. (2007): Patterns of precursory rock fall prior to slope failure. – In: *Journal of Geophysical Research: Earth Surface* 112 (F4), F04014.
- ROSSER, N. J., PETLEY, D. N., LIM, M., DUNNING, S. A. AND ALLISON, R. J. (2005): Terrestrial laser scanning for monitoring the process of hard rock coastal cliff erosion. – In: *Quarterly Journal of Engineering Geology and Hydrogeology* 38 (4), 363–375.
- ROWLANDS, K. A., JONES, L.D. AND WHITWORTH, M. (2003): Landslide laser scanning: a new look at an old problem. – In: *Quarterly Journal of Engineering Geology and Hydrogeology* 36 (2), 155–157.
- RUSINKIEWICZ, S. AND LEVOY, M. (2001): Efficient variants of the ICP algorithm. – In: *Proceedings of the 3rd International Conference on 3-D Digital Imaging and Modeling*, Québec City, Canada, 145-152.
- SANDERSON, D. AND SHARMA, A. (2016): *World Disaster Report 2016*. – Geneva.
- SARTI, P., VITTUARI, L. AND ABBONDANZA, C. (2009): Laser scanner and terrestrial surveying applied to gravitational deformation monitoring of large VLBI telescopes' primary reflector. In: *Journal of Surveying Engineering* 135 (4), 136-148.
- SCAIONI, M., FENG, T., BARAZZETTI, L., PREVITALI, M. AND RONCELLA, R. (2015): Image-based deformation measurement. – In: *Applied Geomatics* 7 (2), 75-90.

- SCHÄFER, T., WEBER, T., KYRINOVICH, P., AND ZÁMEČNIKOVÁ, M. (2004): Deformation Measurement using Terrestrial Laser Scanning at the Hydropower Station of Gabčíkovo. – In: Proceedings of the INGEO 2004 and FIG Regional Central and Eastern European Conference on Engineering Surveying 2004, Bratislava, Slovakia.
- SCHAWLOW A. L. AND TOWNES, C.H. (1958): Infrared and optical masers. – In: Physical Review 112, 1940-1949.
- SCHEIKL, M., POSCHER, G. AND GRAFINGER, H. (2000): Application of the new Automatic Laser Remote Monitoring System (ALARM) for the continuous observation of the mass movement at the Eiblschrofen rock fall area - Tyrol, Austria. – In: Proceedings of the Workshop on Advanced Techniques for the Assessment of Natural Hazards in Mountain Areas 2000, Innsbruck, Austria, 100.
- SCHNABEL, W. (Ed.) (2002): Geologische Karte von Niederösterreich 1:200 000. – Wien.
- SCHÖBER, C. (2007): B31 – Ybbstalstraße Abschnitt km 7,8 – 9,5 - Geologisch-geotechnisches Gutachten betreffend die Gesamtsanierung hinsichtlich Steinschlag- und Felssturzgefährdung. – Lochen.
- SCHÜRCH, P., DENSMORE, A.L., ROSSER, N. J., LIM, M. AND MCARDELL, B. W. (2011): Detection of surface change in complex topography using terrestrial laser scanning: application to the Illgraben debris-flow channel. – In: Earth Surface Processes and Landforms 36 (14), 1847 – 1859.
- SCHWEIGL, J. (2005a): Bauprotokoll der kurzfristigen Felssicherungsmaßnahmen an der B31 zwischen km 4,85 und km 9,85 (Ofenloch). – St. Pölten.
- SCHWEIGL, J. (2005b): 2. Bauprotokoll der kurzfristigen Felssicherungsmaßnahmen an der B31 zwischen km 4,85 und km 9,85 (Ofenloch). – St. Pölten.
- SCHWEIGL, J. (2012): Waidhofen/Y., Bundesstraße B31 - Ybbstal - Ofenloch, Steinschlaggefahr, Kontrollmessung beim Amtmann bei km 6,1 ca. – St. Pölten.
- SEQUEIRA, V. AND GONÇALVES, J.G.M. (2003): 3D Verification of Plant Design. – In: Proceedings of the 25th ESARDA Symposium on Safeguards and Nuclear Material Management, Stockholm, Sweden.
- SHAN, J. AND TOTH, C. K. (Ed.) (2009): Topographic laser ranging and scanning. Principles and Processing. – Boca Raton.

- SIMEONI, L. AND ZANEI, L. (2009): A method for estimating the accuracy of tunnel convergence measurements using tape distometers. – In: *International Journal of Rock Mechanics and Mining Sciences* 46 (4), 796–802.
- SINGH, S. AND WEST, J. (1991): Cyclone: A Laser Scanner For Mobile Robot Navigation. – In: Technical Report CMU-RI-TR-91-18 of the robotics Institute, Carnegie Mellon University, Pittsburg.
- SMITH, M. W., CARRIVICK, J. L. AND QUINCEY, D. J. (2015): Structure from motion photogrammetry in physical geography. – In: *Progress in Physical Geography* 40 (2), 247-275.
- SMULLIN, L. D. AND FIOCCO, G. (1962): Optical Echoes from the Moon. – In: *Nature* 194, 1267.
- STANFEL, D. (2014): Ybbstalbahn. – Wien.
- STRUNDEN, J., EHLERS, T. A., BREHM, D. AND NETTESHEIM, M. (2015): Spatial and temporal variations in rock fall determined from TLS measurements in a deglaciated valley, Switzerland. – In: *Journal of Geophysical Research: Earth Surface* 120 (7), 1251-1273.
- TAYLOR, J. R. (1997²): *An Introduction to Error Analysis*. – Sausalito, California.
- TELLING, J., LYDA, A., HARTZELL, P. AND GLENNIE, C. (2017): Review of Earth science using terrestrial laser scanning. – In: *Earth-Science Reviews* 169, 35-68.
- TEZA, G., GALGARO, A., ZALTRON, N. AND GENEVOIS, R. (2007): Terrestrial laser scanner to detect landslide displacement fields: a new approach. – In: *International Journal of Remote Sensing* 28 (16), 3425-3446.
- TOMÁS, R., ABELLÁN, A., CANO, M., RIQUELME, A., TENZA-ABRIL, A.J., BAEZA-BROTOS, F., SAVAL, J.M. AND JABOYEDOFF, M. (2017): A multidisciplinary approach for the investigation of a rock spreading on an urban slope. – In: *Landslides* 15 (2), 199-217.
- TONINI, M. AND ABELLÁN, A. (2014): Rock fall detection from terrestrial lidar point clouds: A clustering approach using R. – In: *Journal of Spatial Information Science* 8 (1), 95-110.
- TSAKIRI, M., LICHTI, D. AND PFEIFER, N. (2006): Terrestrial laser scanning for deformation monitoring. - In: *Proceedings of 12th FIG Symposium on Deformation Measurements 2006*, Baden, Austria.

- TULADHAR, U. M., LEE, G. M. AND AHN, S. (2017): A novel coarse-to-fine registration approach for aligning partially overlapped 3D scanned data. – In: International Journal of Computer Integrated Manufacturing, Article in Press.
- VAN GOSLIGA, R., LINDENBERGH, R. AND PFEIFER, N. (2006): Deformation analysis of a bored tunnel by means of terrestrial laser scanning. – In: International Archives of Photogrammetry, Remote Sensing and Spatial Information 36 (5).
- VARNES, D. J. (1978): Slope movement types and processes. – In: Schuster, R. L., Krizek, R. J. (Ed.): Landslides, Analysis and Control. Special Report 179. – Washington, D.C., 11-33.
- VEZOČNIK, R., AMBROŽIČ, T., STERLE, O., BILBAN, G., PFEIFER, N. AND STOPAR, B. (2009): Use of Terrestrial Laser Scanning Technology for Long Term High Precision Deformation Monitoring. – In: Sensors 9 (12), 9873-9895.
- VOSSelman, G. AND KLEIN, R. (2010): Visualisation and Structuring of Point Clouds. – In: Vosselman, G., Maas, H.-G. (Ed.): Airborne and Terrestrial Laser Scanning. – Dunbeath, 45-81.
- WALTON, G., DELALOYE, D. AND DIEDERICHs, M. S. (2014): Development of an elliptical fitting algorithm to improve change detection capabilities with applications for deformation monitoring in circular tunnels and shafts. – In: Tunnelling and Underground Space Technology 43, 336–349.
- WENIGHOFER, R., CHMELINA, K. AND GALLER, R. (2016): Erfassung von Tübbingverformungen bei TVM-Vortrieben. – In: DVW – Gesellschaft für Geodäsie, Geoinformation und Landmanagement e.V. (Ed.): Terrestrisches Laserscanning. DVW-Schriftenreihe 85. – Augsburg, 59-73.
- WESSELY, G. (2006): Geologie der österreichischen Bundesländer: Niederösterreich. – Wien.
- WESTOBY, M. J., DUNNING, S. A., WOODWARD, J., HEIN, A. S., MARRERO, S. M., WINTER, K. AND SUGDEN, D. E. (2016): Interannual surface evolution of an Antarctic blue-ice moraine using multi-temporal DEMs. – In: Earth Surface Dynamics 4 (2), 515-529.
- WHEATON, J. M., BRASINGTON, J., DARBY, S. E., AND SEAR, D. A. (2010): Accounting for uncertainty in DEMs from repeat topographic surveys: improved sediment budgets. – In: Earth Surface Processes and Landforms 35, 136-156.
- WHITTOW J. B. (2000²): The Penguin Dictionary of Physical Geography. – London.

BIBLIOGRAPHY

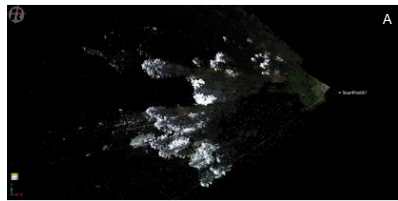
- WILLIAMS, J.G., ROSSER, N.J., HARDY, R.J., BRAIN, M.J. AND AFANA, A.A. (2018): Optimising 4-D surface change detection: An approach for capturing rockfall magnitude-frequency. – In: *Earth Surface Dynamics* 6 (1), 101-119.
- WUNDERLICH, T., NIEMEIER, W., WUJANZ, D., HOLST, C., NEITZEL, F. AND KUHLMANN, H. (2016): Areal Deformation Analysis from TLS Point Clouds – the Challenge. – In: *AVN Allgemeine Vermessungs-Nachrichten* 123 (11-12), 340-354.
- YANG, B. AND ZANG, Y. (2014): Automated registration of dense terrestrial laser scanning point clouds using curves. – In: *ISPRS Journal of Photogrammetry and Remote Sensing* 95, 109–121.
- ZAMG – ZENTRALANSTALT FÜR METEOROLOGIE UND GEODYNAMIK (2017): Klimadaten von Österreich 1971-2000. – See online: http://www.zamg.ac.at/fix/klima/oe71-00/klima2000/klimadaten_oesterreich_1971_frame1.htm [Accessed on 29.08.2017]
- ZHANG, Z. (1994): Iterative point matching for registration of freeform curves and surfaces. – In: *International Journal of Computer Vision* 13 (2), 119–152.

Appendix

Appendix A: Detailed presentation of the provided and collected scanning data of all scanning campaigns

<

APPENDIX



Amtmann, scanning campaign 2016, scan position 1

front view (A), top view (B) and left view (C) of the point cloud, colored using the true color channel (color from images).

Data: 570.5 MB



| Measurements | | |
|---|--|---------------|
| | vertical | horizontal |
| Covered range | 56.401° | 68.35° |
| Count | 5 823 rows | 6 836 columns |
| Given angular step width | 0.01° | 0.01° |
| Derived angular step width | 0.00969° | 0.01° |
| Total number of transmitted laser beams | 39 806 028 | |
| Laser Pulse Repetition Rate | 300 kHz (peak), effective measurement rate of 222 000 meas./s. | |
| Scanning time | 16 min 38 s | |



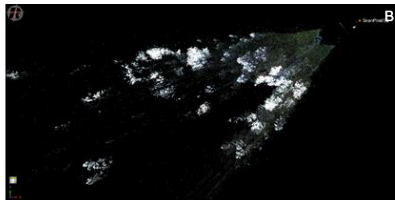
| Point cloud | | |
|----------------------------------|----------------------|--------------|
| Measurements | 31 458 885 | |
| Echo distribution | Targets per beam | Measurements |
| | 1 | 20 125 007 |
| | 2 | 6 022 505 |
| | 3 | 3 189 007 |
| | 4 | 102 |
| | 5 | 62 |
| | 6 | 12 |
| Total targets (number of points) | 50 226 845 | |
| Range (distance to scanner) | 0.247 m to 528.028 m | |
| Derived range of beam diameter | 15 mm to 63 mm | |



Amtmann, scanning campaign 2016, scan position 2

front view (A), top view (B) and left view (C) of the point cloud, colored using the true color channel (color from images).

Data: 314.4 MB



| Measurements | | |
|---|--|-------------|
| | vertical | horizontal |
| Covered range | 48.757° | 14.340° |
| Count | 5 034 rows | 957 columns |
| Given angular step width | 0.01° | 0.01° |
| Derived angular step width | 0.00969° | 0.01° |
| Total number of transmitted laser beams | 20 785 386 | |
| Laser Pulse Repetition Rate | 300 kHz (peak), effective measurement rate of 222 000 meas./s. | |
| Scanning time | 9 min 52 s | |



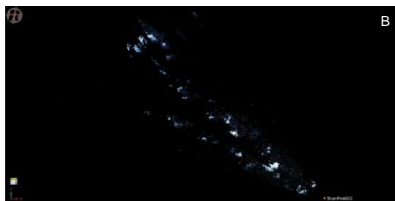
| Point cloud | | |
|----------------------------------|----------------------|--------------|
| Measurements | 15 642 501 | |
| Echo distribution | Targets per beam | Measurements |
| | 1 | 7 558 686 |
| | 2 | 4 668 200 |
| | 3 | 2 450 953 |
| | 4 | 964 662 |
| | 5 | - |
| | 6 | - |
| Total targets (number of points) | 28 106 593 | |
| Range (distance to scanner) | 0.248 m to 526.603 m | |
| Derived range of beam diameter | 15 mm to 63 mm | |



Amtmann, scanning campaign 2016, scan position 3

front view (A), top view (B) and left view (C) of the point cloud, colored using the true color channel (color from images).

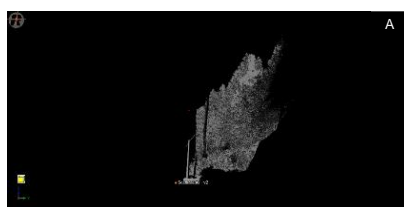

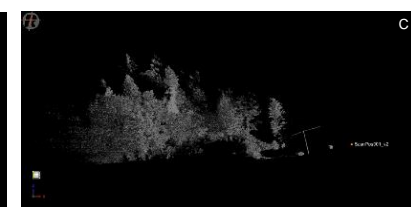
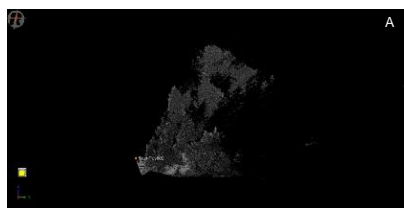
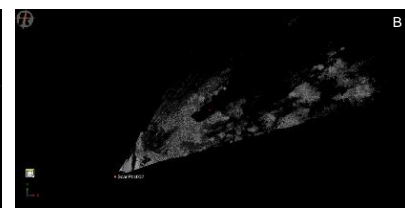
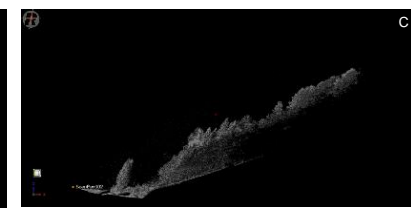
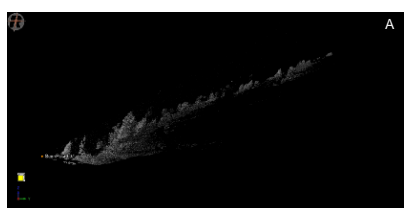
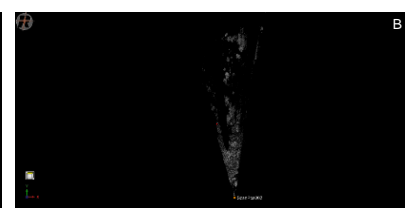
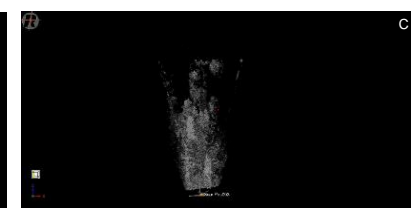
Data: 244 MB



| Measurements | | |
|---|--|---------------|
| | vertical | horizontal |
| Covered range | 38.886° | 35.170° |
| Count | 4 015 rows | 3 518 columns |
| Given angular step width | 0.01° | 0.01° |
| Derived angular step width | 0.00969° | 0.01° |
| Total number of transmitted laser beams | 51 357 376 | |
| Laser Pulse Repetition Rate | 300 kHz (peak), effective measurement rate of 222 000 meas./s. | |
| Scanning time | 8 min 12 s | |



| Point cloud | | |
|----------------------------------|----------------------|--------------|
| Measurements | 12 387 262 | |
| Echo distribution | Targets per beam | Measurements |
| | 1 | 6 028 232 |
| | 2 | 3 676 803 |
| | 3 | 1 867 886 |
| | 4 | 814 341 |
| | 5 | - |
| | 6 | - |
| Total targets (number of points) | 22 242 860 | |
| Range (distance to scanner) | 0.373 m to 524.584 m | |
| Derived range of beam diameter | 15 mm to 63 mm | |

|  |  |  | | | | | | | | | | | | | | | | | | | | | | | | | | | | | | | | | | | | | | | | | | | | | | | | | | | | | | | | | |
|--|---|--|----------|------------|---------------|---------|--------|-------|-------------|---------------|--------------------------|--------|-------|----------------------------|----------|-------|---|------------|--|-----------------------------|--|--|---------------|------------|--|---|--------------|------------|--|-------------------|------------------|--------------|--|---|------------|--|---|-----------|--|---|-----------|--|---|-----------|--|---|---|--|---|---|----------------------------------|------------|--|-----------------------------|----------------------|--|--------------------------------|----------------|--|
| Amtmann, scanning campaign 2017a, scan position 1 | Measurements | Point cloud | | | | | | | | | | | | | | | | | | | | | | | | | | | | | | | | | | | | | | | | | | | | | | | | | | | | | | | | | |
| front view (A), top view (B) and left view (C) of the point cloud, colored using the reflectance as intensity. Data: 379.1 MB | <table> <tr> <th></th><th>vertical</th><th>horizontal</th></tr> <tr> <td>Covered range</td><td>42.612°</td><td>25.55°</td></tr> <tr> <td>Count</td><td>10 490 rows</td><td>2 556 columns</td></tr> <tr> <td>Given angular step width</td><td>0.004°</td><td>0.01°</td></tr> <tr> <td>Derived angular step width</td><td>0.00406°</td><td>0.01°</td></tr> <tr> <td>Total number of transmitted laser beams</td><td colspan="2">26 812 440</td></tr> <tr> <td>Laser Pulse Repetition Rate</td><td colspan="2">300 kHz (peak), effective measurement rate of 222 000 meas./s.</td></tr> <tr> <td>Scanning time</td><td colspan="2">4 min 31 s</td></tr> </table> | | vertical | horizontal | Covered range | 42.612° | 25.55° | Count | 10 490 rows | 2 556 columns | Given angular step width | 0.004° | 0.01° | Derived angular step width | 0.00406° | 0.01° | Total number of transmitted laser beams | 26 812 440 | | Laser Pulse Repetition Rate | 300 kHz (peak), effective measurement rate of 222 000 meas./s. | | Scanning time | 4 min 31 s | | <table> <tr> <td>Measurements</td><td colspan="2">18 633 719</td></tr> <tr> <td>Echo distribution</td><td>Targets per beam</td><td>Measurements</td></tr> <tr> <td></td><td>1</td><td>10 296 336</td></tr> <tr> <td></td><td>2</td><td>4 377 271</td></tr> <tr> <td></td><td>3</td><td>2 857 216</td></tr> <tr> <td></td><td>4</td><td>1 102 896</td></tr> <tr> <td></td><td>5</td><td>-</td></tr> <tr> <td></td><td>6</td><td>-</td></tr> <tr> <td>Total targets (number of points)</td><td colspan="2">32 034 110</td></tr> <tr> <td>Range (distance to scanner)</td><td colspan="2">0.234 m to 358.98 m</td></tr> <tr> <td>Derived range of beam diameter</td><td colspan="2">15 mm to 43 mm</td></tr> </table> | Measurements | 18 633 719 | | Echo distribution | Targets per beam | Measurements | | 1 | 10 296 336 | | 2 | 4 377 271 | | 3 | 2 857 216 | | 4 | 1 102 896 | | 5 | - | | 6 | - | Total targets (number of points) | 32 034 110 | | Range (distance to scanner) | 0.234 m to 358.98 m | | Derived range of beam diameter | 15 mm to 43 mm | |
| | vertical | horizontal | | | | | | | | | | | | | | | | | | | | | | | | | | | | | | | | | | | | | | | | | | | | | | | | | | | | | | | | | |
| Covered range | 42.612° | 25.55° | | | | | | | | | | | | | | | | | | | | | | | | | | | | | | | | | | | | | | | | | | | | | | | | | | | | | | | | | |
| Count | 10 490 rows | 2 556 columns | | | | | | | | | | | | | | | | | | | | | | | | | | | | | | | | | | | | | | | | | | | | | | | | | | | | | | | | | |
| Given angular step width | 0.004° | 0.01° | | | | | | | | | | | | | | | | | | | | | | | | | | | | | | | | | | | | | | | | | | | | | | | | | | | | | | | | | |
| Derived angular step width | 0.00406° | 0.01° | | | | | | | | | | | | | | | | | | | | | | | | | | | | | | | | | | | | | | | | | | | | | | | | | | | | | | | | | |
| Total number of transmitted laser beams | 26 812 440 | | | | | | | | | | | | | | | | | | | | | | | | | | | | | | | | | | | | | | | | | | | | | | | | | | | | | | | | | | |
| Laser Pulse Repetition Rate | 300 kHz (peak), effective measurement rate of 222 000 meas./s. | | | | | | | | | | | | | | | | | | | | | | | | | | | | | | | | | | | | | | | | | | | | | | | | | | | | | | | | | | |
| Scanning time | 4 min 31 s | | | | | | | | | | | | | | | | | | | | | | | | | | | | | | | | | | | | | | | | | | | | | | | | | | | | | | | | | | |
| Measurements | 18 633 719 | | | | | | | | | | | | | | | | | | | | | | | | | | | | | | | | | | | | | | | | | | | | | | | | | | | | | | | | | | |
| Echo distribution | Targets per beam | Measurements | | | | | | | | | | | | | | | | | | | | | | | | | | | | | | | | | | | | | | | | | | | | | | | | | | | | | | | | | |
| | 1 | 10 296 336 | | | | | | | | | | | | | | | | | | | | | | | | | | | | | | | | | | | | | | | | | | | | | | | | | | | | | | | | | |
| | 2 | 4 377 271 | | | | | | | | | | | | | | | | | | | | | | | | | | | | | | | | | | | | | | | | | | | | | | | | | | | | | | | | | |
| | 3 | 2 857 216 | | | | | | | | | | | | | | | | | | | | | | | | | | | | | | | | | | | | | | | | | | | | | | | | | | | | | | | | | |
| | 4 | 1 102 896 | | | | | | | | | | | | | | | | | | | | | | | | | | | | | | | | | | | | | | | | | | | | | | | | | | | | | | | | | |
| | 5 | - | | | | | | | | | | | | | | | | | | | | | | | | | | | | | | | | | | | | | | | | | | | | | | | | | | | | | | | | | |
| | 6 | - | | | | | | | | | | | | | | | | | | | | | | | | | | | | | | | | | | | | | | | | | | | | | | | | | | | | | | | | | |
| Total targets (number of points) | 32 034 110 | | | | | | | | | | | | | | | | | | | | | | | | | | | | | | | | | | | | | | | | | | | | | | | | | | | | | | | | | | |
| Range (distance to scanner) | 0.234 m to 358.98 m | | | | | | | | | | | | | | | | | | | | | | | | | | | | | | | | | | | | | | | | | | | | | | | | | | | | | | | | | | |
| Derived range of beam diameter | 15 mm to 43 mm | | | | | | | | | | | | | | | | | | | | | | | | | | | | | | | | | | | | | | | | | | | | | | | | | | | | | | | | | | |
|  |  |  | | | | | | | | | | | | | | | | | | | | | | | | | | | | | | | | | | | | | | | | | | | | | | | | | | | | | | | | | |
| Amtmann, scanning campaign 2017a, scan position 2 | Measurements | Point cloud | | | | | | | | | | | | | | | | | | | | | | | | | | | | | | | | | | | | | | | | | | | | | | | | | | | | | | | | | |
| front view (A), top view (B) and left view (C) of the point cloud, colored using the reflectance as intensity. Data: 648.2 MB | <table> <tr> <th></th><th>vertical</th><th>horizontal</th></tr> <tr> <td>Covered range</td><td>50.934°</td><td>40.15°</td></tr> <tr> <td>Count</td><td>11 643 rows</td><td>4 016 columns</td></tr> <tr> <td>Given angular step width</td><td>0.004°</td><td>0.01°</td></tr> <tr> <td>Derived angular step width</td><td>0.00436°</td><td>0.01°</td></tr> <tr> <td>Total number of transmitted laser beams</td><td colspan="2">46 758 288</td></tr> <tr> <td>Laser Pulse Repetition Rate</td><td colspan="2">300 kHz (peak), effective measurement rate of 222 000 meas./s.</td></tr> <tr> <td>Scanning time</td><td colspan="2">7 min 33 s</td></tr> </table> | | vertical | horizontal | Covered range | 50.934° | 40.15° | Count | 11 643 rows | 4 016 columns | Given angular step width | 0.004° | 0.01° | Derived angular step width | 0.00436° | 0.01° | Total number of transmitted laser beams | 46 758 288 | | Laser Pulse Repetition Rate | 300 kHz (peak), effective measurement rate of 222 000 meas./s. | | Scanning time | 7 min 33 s | | <table> <tr> <td>Measurements</td><td colspan="2">33 764 774</td></tr> <tr> <td>Echo distribution</td><td>Targets per beam</td><td>Measurements</td></tr> <tr> <td></td><td>1</td><td>19 026 148</td></tr> <tr> <td></td><td>2</td><td>8 469 968</td></tr> <tr> <td></td><td>3</td><td>4 469 390</td></tr> <tr> <td></td><td>4</td><td>1 799 268</td></tr> <tr> <td></td><td>5</td><td>-</td></tr> <tr> <td></td><td>6</td><td>-</td></tr> <tr> <td>Total targets (number of points)</td><td colspan="2">56 571 328</td></tr> <tr> <td>Range (distance to scanner)</td><td colspan="2">0.235 m to 499.943 m</td></tr> <tr> <td>Derived range of beam diameter</td><td colspan="2">15 mm to 60 mm</td></tr> </table> | Measurements | 33 764 774 | | Echo distribution | Targets per beam | Measurements | | 1 | 19 026 148 | | 2 | 8 469 968 | | 3 | 4 469 390 | | 4 | 1 799 268 | | 5 | - | | 6 | - | Total targets (number of points) | 56 571 328 | | Range (distance to scanner) | 0.235 m to 499.943 m | | Derived range of beam diameter | 15 mm to 60 mm | |
| | vertical | horizontal | | | | | | | | | | | | | | | | | | | | | | | | | | | | | | | | | | | | | | | | | | | | | | | | | | | | | | | | | |
| Covered range | 50.934° | 40.15° | | | | | | | | | | | | | | | | | | | | | | | | | | | | | | | | | | | | | | | | | | | | | | | | | | | | | | | | | |
| Count | 11 643 rows | 4 016 columns | | | | | | | | | | | | | | | | | | | | | | | | | | | | | | | | | | | | | | | | | | | | | | | | | | | | | | | | | |
| Given angular step width | 0.004° | 0.01° | | | | | | | | | | | | | | | | | | | | | | | | | | | | | | | | | | | | | | | | | | | | | | | | | | | | | | | | | |
| Derived angular step width | 0.00436° | 0.01° | | | | | | | | | | | | | | | | | | | | | | | | | | | | | | | | | | | | | | | | | | | | | | | | | | | | | | | | | |
| Total number of transmitted laser beams | 46 758 288 | | | | | | | | | | | | | | | | | | | | | | | | | | | | | | | | | | | | | | | | | | | | | | | | | | | | | | | | | | |
| Laser Pulse Repetition Rate | 300 kHz (peak), effective measurement rate of 222 000 meas./s. | | | | | | | | | | | | | | | | | | | | | | | | | | | | | | | | | | | | | | | | | | | | | | | | | | | | | | | | | | |
| Scanning time | 7 min 33 s | | | | | | | | | | | | | | | | | | | | | | | | | | | | | | | | | | | | | | | | | | | | | | | | | | | | | | | | | | |
| Measurements | 33 764 774 | | | | | | | | | | | | | | | | | | | | | | | | | | | | | | | | | | | | | | | | | | | | | | | | | | | | | | | | | | |
| Echo distribution | Targets per beam | Measurements | | | | | | | | | | | | | | | | | | | | | | | | | | | | | | | | | | | | | | | | | | | | | | | | | | | | | | | | | |
| | 1 | 19 026 148 | | | | | | | | | | | | | | | | | | | | | | | | | | | | | | | | | | | | | | | | | | | | | | | | | | | | | | | | | |
| | 2 | 8 469 968 | | | | | | | | | | | | | | | | | | | | | | | | | | | | | | | | | | | | | | | | | | | | | | | | | | | | | | | | | |
| | 3 | 4 469 390 | | | | | | | | | | | | | | | | | | | | | | | | | | | | | | | | | | | | | | | | | | | | | | | | | | | | | | | | | |
| | 4 | 1 799 268 | | | | | | | | | | | | | | | | | | | | | | | | | | | | | | | | | | | | | | | | | | | | | | | | | | | | | | | | | |
| | 5 | - | | | | | | | | | | | | | | | | | | | | | | | | | | | | | | | | | | | | | | | | | | | | | | | | | | | | | | | | | |
| | 6 | - | | | | | | | | | | | | | | | | | | | | | | | | | | | | | | | | | | | | | | | | | | | | | | | | | | | | | | | | | |
| Total targets (number of points) | 56 571 328 | | | | | | | | | | | | | | | | | | | | | | | | | | | | | | | | | | | | | | | | | | | | | | | | | | | | | | | | | | |
| Range (distance to scanner) | 0.235 m to 499.943 m | | | | | | | | | | | | | | | | | | | | | | | | | | | | | | | | | | | | | | | | | | | | | | | | | | | | | | | | | | |
| Derived range of beam diameter | 15 mm to 60 mm | | | | | | | | | | | | | | | | | | | | | | | | | | | | | | | | | | | | | | | | | | | | | | | | | | | | | | | | | | |
|  |  |  | | | | | | | | | | | | | | | | | | | | | | | | | | | | | | | | | | | | | | | | | | | | | | | | | | | | | | | | | |
| Amtmann, scanning campaign 2017a, scan position 3 | Measurements | Point cloud | | | | | | | | | | | | | | | | | | | | | | | | | | | | | | | | | | | | | | | | | | | | | | | | | | | | | | | | | |
| front view (A), top view (B) and left view (C) of the point cloud, colored using the reflectance as intensity. Data: 400 MB | <table> <tr> <th></th><th>vertical</th><th>horizontal</th></tr> <tr> <td>Covered range</td><td>43.274°</td><td>23.56°</td></tr> <tr> <td>Count</td><td>10 653 rows</td><td>4 016 columns</td></tr> <tr> <td>Given angular step width</td><td>0.004°</td><td>0.01°</td></tr> <tr> <td>Derived angular step width</td><td>0.00406°</td><td>0.01°</td></tr> <tr> <td>Total number of transmitted laser beams</td><td colspan="2">25 109 121</td></tr> <tr> <td>Laser Pulse Repetition Rate</td><td colspan="2">300 kHz (peak), effective measurement rate of 222 000 meas./s.</td></tr> <tr> <td>Scanning time</td><td colspan="2">4 min 10 s</td></tr> </table> | | vertical | horizontal | Covered range | 43.274° | 23.56° | Count | 10 653 rows | 4 016 columns | Given angular step width | 0.004° | 0.01° | Derived angular step width | 0.00406° | 0.01° | Total number of transmitted laser beams | 25 109 121 | | Laser Pulse Repetition Rate | 300 kHz (peak), effective measurement rate of 222 000 meas./s. | | Scanning time | 4 min 10 s | | <table> <tr> <td>Measurements</td><td colspan="2">20 529 474</td></tr> <tr> <td>Echo distribution</td><td>Targets per beam</td><td>Measurements</td></tr> <tr> <td></td><td>1</td><td>10 321 105</td></tr> <tr> <td></td><td>2</td><td>5 316 880</td></tr> <tr> <td></td><td>3</td><td>3 015 758</td></tr> <tr> <td></td><td>4</td><td>1 575 731</td></tr> <tr> <td></td><td>5</td><td>-</td></tr> <tr> <td></td><td>6</td><td>-</td></tr> <tr> <td>Total targets (number of points)</td><td colspan="2">36 605 063</td></tr> <tr> <td>Range (distance to scanner)</td><td colspan="2">0.235 m to 442.172 m</td></tr> <tr> <td>Derived range of beam diameter</td><td colspan="2">15 mm to 53 mm</td></tr> </table> | Measurements | 20 529 474 | | Echo distribution | Targets per beam | Measurements | | 1 | 10 321 105 | | 2 | 5 316 880 | | 3 | 3 015 758 | | 4 | 1 575 731 | | 5 | - | | 6 | - | Total targets (number of points) | 36 605 063 | | Range (distance to scanner) | 0.235 m to 442.172 m | | Derived range of beam diameter | 15 mm to 53 mm | |
| | vertical | horizontal | | | | | | | | | | | | | | | | | | | | | | | | | | | | | | | | | | | | | | | | | | | | | | | | | | | | | | | | | |
| Covered range | 43.274° | 23.56° | | | | | | | | | | | | | | | | | | | | | | | | | | | | | | | | | | | | | | | | | | | | | | | | | | | | | | | | | |
| Count | 10 653 rows | 4 016 columns | | | | | | | | | | | | | | | | | | | | | | | | | | | | | | | | | | | | | | | | | | | | | | | | | | | | | | | | | |
| Given angular step width | 0.004° | 0.01° | | | | | | | | | | | | | | | | | | | | | | | | | | | | | | | | | | | | | | | | | | | | | | | | | | | | | | | | | |
| Derived angular step width | 0.00406° | 0.01° | | | | | | | | | | | | | | | | | | | | | | | | | | | | | | | | | | | | | | | | | | | | | | | | | | | | | | | | | |
| Total number of transmitted laser beams | 25 109 121 | | | | | | | | | | | | | | | | | | | | | | | | | | | | | | | | | | | | | | | | | | | | | | | | | | | | | | | | | | |
| Laser Pulse Repetition Rate | 300 kHz (peak), effective measurement rate of 222 000 meas./s. | | | | | | | | | | | | | | | | | | | | | | | | | | | | | | | | | | | | | | | | | | | | | | | | | | | | | | | | | | |
| Scanning time | 4 min 10 s | | | | | | | | | | | | | | | | | | | | | | | | | | | | | | | | | | | | | | | | | | | | | | | | | | | | | | | | | | |
| Measurements | 20 529 474 | | | | | | | | | | | | | | | | | | | | | | | | | | | | | | | | | | | | | | | | | | | | | | | | | | | | | | | | | | |
| Echo distribution | Targets per beam | Measurements | | | | | | | | | | | | | | | | | | | | | | | | | | | | | | | | | | | | | | | | | | | | | | | | | | | | | | | | | |
| | 1 | 10 321 105 | | | | | | | | | | | | | | | | | | | | | | | | | | | | | | | | | | | | | | | | | | | | | | | | | | | | | | | | | |
| | 2 | 5 316 880 | | | | | | | | | | | | | | | | | | | | | | | | | | | | | | | | | | | | | | | | | | | | | | | | | | | | | | | | | |
| | 3 | 3 015 758 | | | | | | | | | | | | | | | | | | | | | | | | | | | | | | | | | | | | | | | | | | | | | | | | | | | | | | | | | |
| | 4 | 1 575 731 | | | | | | | | | | | | | | | | | | | | | | | | | | | | | | | | | | | | | | | | | | | | | | | | | | | | | | | | | |
| | 5 | - | | | | | | | | | | | | | | | | | | | | | | | | | | | | | | | | | | | | | | | | | | | | | | | | | | | | | | | | | |
| | 6 | - | | | | | | | | | | | | | | | | | | | | | | | | | | | | | | | | | | | | | | | | | | | | | | | | | | | | | | | | | |
| Total targets (number of points) | 36 605 063 | | | | | | | | | | | | | | | | | | | | | | | | | | | | | | | | | | | | | | | | | | | | | | | | | | | | | | | | | | |
| Range (distance to scanner) | 0.235 m to 442.172 m | | | | | | | | | | | | | | | | | | | | | | | | | | | | | | | | | | | | | | | | | | | | | | | | | | | | | | | | | | |
| Derived range of beam diameter | 15 mm to 53 mm | | | | | | | | | | | | | | | | | | | | | | | | | | | | | | | | | | | | | | | | | | | | | | | | | | | | | | | | | | |

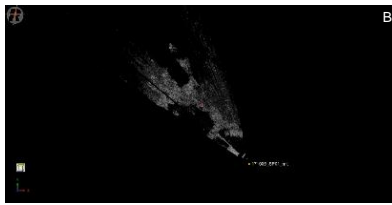
APPENDIX



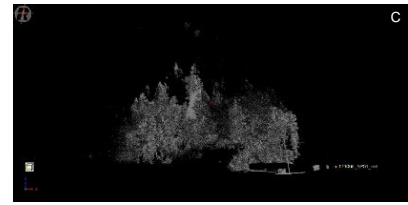
Amtmann, scanning campaign 2017b, scan position 1

front view (A), top view (B) and left view (C) of the point cloud, colored using the reflectance as intensity.

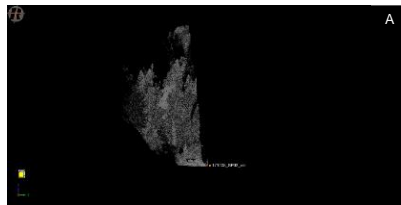
Data: 722.2 MB



| Measurements | | |
|---|--|---------------|
| | vertical | horizontal |
| Covered range | 46.155° | 41.45° |
| Count | 12 309 rows | 4 146 columns |
| Given angular step width | 0.004° | 0.01° |
| Derived angular step width | 0.00375° | 0.01° |
| Total number of transmitted laser beams | 51 033 114 | |
| Laser Pulse Repetition Rate | 300 kHz (peak), effective measurement rate of 222 000 meas./s. | |
| Scanning time | 7 min 30 s | |



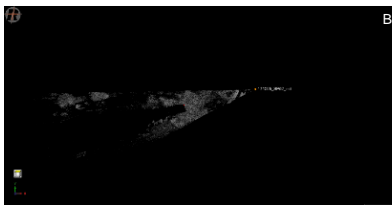
| Point cloud | | |
|----------------------------------|----------------------|------------|
| Measurements | 38 590 617 | |
| Echo distribution | Targets per beam | |
| | 1 | 22 996 345 |
| | 2 | 8 610 862 |
| | 3 | 4 738 819 |
| | 4 | 2 244 591 |
| | 5 | - |
| | 6 | - |
| Total targets (number of points) | 63 412 890 | |
| Range (distance to scanner) | 0.235 m to 522.485 m | |
| Derived range of beam diameter | 15 mm to 63 mm | |



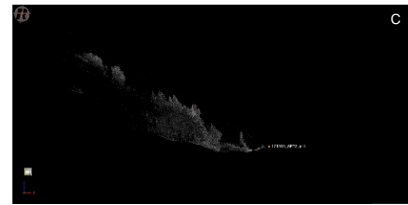
Amtmann, scanning campaign 2017b, scan position 2

front view (A), top view (B) and left view (C) of the point cloud, colored using the reflectance as intensity.

Data: 485.9 MB



| Measurements | | |
|---|--|---------------|
| | vertical | horizontal |
| Covered range | 40.769° | 24.15° |
| Count | 13 047 rows | 2 416 columns |
| Given angular step width | 0.003° | 0.01° |
| Derived angular step width | 0.00313° | 0.01° |
| Total number of transmitted laser beams | 31 521 552 | |
| Laser Pulse Repetition Rate | 300 kHz (peak), effective measurement rate of 222 000 meas./s. | |
| Scanning time | 4 min 13 s | |



| Point cloud | | |
|----------------------------------|---------------------|------------|
| Measurements | 25 949 575 | |
| Echo distribution | Targets per beam | |
| | 1 | 13 779 268 |
| | 2 | 7 259 220 |
| | 3 | 3 539 004 |
| | 4 | 1 372 083 |
| | 5 | - |
| | 6 | - |
| Total targets (number of points) | 44 403 052 | |
| Range (distance to scanner) | 0.24 m to 501.206 m | |
| Derived range of beam diameter | 15 mm to 60 mm | |

Appendix B: Detailed results of the MSA registration test for the 2014, 2017a and 2017b data

| Epoch | Input Data | Parameters | | Statistics | | | Histogram residues (see Appendix D) |
|----------------|------------------|-------------------|-----------------------------|-------------------------------|---|----------|-------------------------------------|
| | | Search radius [m] | Maximum tilt angle [degree] | Error: standard deviation [m] | Number of observations used for calculation | | |
| | | | | | Tie points | Polydata | |
| 2014 (3 SP) | Polydata (PPF 1) | 0.5 | 15 | 0.0842 | 0 | 2189 | 2014-PPF1-01 |
| | | 0.2 | 15 | 0.0318 | 0 | 756 | 2014-PPF1-02 |
| | | 0.1 | 15 | 0.024 | 0 | 230 | 2014-PPF1-03 |
| | | 0.05 | 15 | 0.0215 | 0 | 63 | 2014-PPF1-04 |
| | | 0.5 | 10 | 0.0703 | 0 | 1371 | 2014-PPF1-05 |
| | | 0.2 | 10 | 0.0279 | 0 | 467 | 2014-PPF1-06 |
| | | 0.1 | 10 | 0.0228 | 0 | 145 | 2014-PPF1-07 |
| | | 0.05 | 10 | 0.0271 | 0 | 44 | 2014-PPF1-08 |
| | | 0.5 | 5 | 0.0618 | 0 | 459 | 2014-PPF1-09 |
| | | 0.2 | 5 | 0.0228 | 0 | 160 | 2014-PPF1-10 |
| | | 0.1 | 5 | 0.0284 | 0 | 47 | 2014-PPF1-11 |
| | | 0.05 | 5 | 0.0138 | 0 | 20 | 2014-PPF1-12 |
| | Polydata (PPF 2) | 0.5 | 15 | 0.1287 | 0 | 28870 | 2014-PPF2-01 |
| | | 0.2 | 15 | 0.0362 | 0 | 7753 | 2014-PPF2-02 |
| | | 0.1 | 15 | 0.0213 | 0 | 2874 | 2014-PPF2-03 |
| | | 0.05 | 15 | 0.0143 | 0 | 830 | 2014-PPF2-04 |
| | | 0.5 | 10 | 0.1344 | 0 | 17927 | 2014-PPF2-05 |
| | | 0.2 | 10 | 0.0348 | 0 | 4499 | 2014-PPF2-06 |
| | | 0.1 | 10 | 0.0199 | 0 | 1680 | 2014-PPF2-07 |
| | | 0.05 | 10 | 0.0131 | 0 | 508 | 2014-PPF2-08 |
| | | 0.5 | 5 | 0.1327 | 0 | 5653 | 2014-PPF2-09 |
| | | 0.2 | 5 | 0.0332 | 0 | 1344 | 2014-PPF2-10 |
| | | 0.1 | 5 | 0.0173 | 0 | 507 | 2014-PPF2-11 |
| | | 0.05 | 5 | 0.0131 | 0 | 166 | 2014-PPF2-12 |
| | Polydata (PPF 3) | 0.5 | 15 | 0.0752 | 0 | 427272 | 2014-PPF3-01 |
| | | 0.2 | 15 | 0.0505 | 0 | 211115 | 2014-PPF3-02 |
| | | 0.1 | 15 | 0.0304 | 0 | 74038 | 2014-PPF3-03 |
| | | 0.05 | 15 | 0.0163 | 0 | 18061 | 2014-PPF3-04 |
| | | 0.02 | 15 | 0.0079 | 0 | 1908 | 2014-PPF3-05 |
| | | 0.5 | 10 | 0.0929 | 0 | 358859 | 2014-PPF3-06 |
| | | 0.2 | 10 | 0.0576 | 0 | 141804 | 2014-PPF3-07 |
| | | 0.1 | 10 | 0.0314 | 0 | 41254 | 2014-PPF3-08 |
| | | 0.05 | 10 | 0.0161 | 0 | 9362 | 2014-PPF3-09 |
| | | 0.02 | 10 | 0.0079 | 0 | 1048 | 2014-PPF3-10 |
| | | 0.5 | 5 | 0.132 | 0 | 205415 | 2014-PPF3-11 |
| | | 0.2 | 5 | 0.0661 | 0 | 50113 | 2014-PPF3-12 |
| | | 0.1 | 5 | 0.0322 | 0 | 11568 | 2014-PPF3-13 |
| | | 0.05 | 5 | 0.0159 | 0 | 2468 | 2014-PPF3-14 |
| | | 0.02 | 5 | 0.0081 | 0 | 297 | 2014-PPF3-15 |
| | Polydata (PPF 4) | 0.5 | 15 | 0.0568 | 0 | 2263079 | 2014-PPF4-01 |
| | | 0.2 | 15 | 0.0414 | 0 | 1238365 | 2014-PPF4-02 |
| | | 0.1 | 15 | 0.0288 | 0 | 552414 | 2014-PPF4-03 |
| | | 0.05 | 15 | 0.0184 | 0 | 168900 | 2014-PPF4-04 |
| | | 0.02 | 15 | 0.0084 | 0 | 17544 | 2014-PPF4-05 |
| | | 0.5 | 10 | 0.0646 | 0 | 2101334 | 2014-PPF4-06 |
| | | 0.2 | 10 | 0.0438 | 0 | 1110277 | 2014-PPF4-07 |
| | | 0.1 | 10 | 0.0298 | 0 | 480983 | 2014-PPF4-08 |
| | | 0.05 | 10 | 0.0187 | 0 | 139558 | 2014-PPF4-09 |
| | | 0.02 | 10 | 0.0084 | 0 | 17890 | 2014-PPF4-10 |
| | | 0.5 | 5 | 0.0961 | 0 | 1608215 | 2014-PPF4-11 |
| | | 0.2 | 5 | 0.0618 | 0 | 628033 | 2014-PPF4-12 |
| | | 0.1 | 5 | 0.0377 | 0 | 182912 | 2014-PPF4-13 |
| | | 0.05 | 5 | 0.0207 | 0 | 35351 | 2014-PPF4-14 |
| | | 0.02 | 5 | 0.0085 | 0 | 2768 | 2014-PPF4-15 |

APPENDIX

| Epoch | Input Data | Parameters | | Statistics | | | Histogram residues (see Appendix D) |
|-----------------|-------------------------------|--------------------------------------|-----------------------------|-------------------------------|---|---------------|-------------------------------------|
| | | Search radius [m] | Maximum tilt angle [degree] | Error: standard deviation [m] | Number of observations used for calculation | | |
| | | | | | Tie points | Polydata | |
| 2017a (3 SP) | Tie points | no changes with changing of settings | | 0.0039 | 22 | 0 | 2017a-TP |
| | Tie points & Polydata (PPF 1) | 0.5 | 15 | 0.0355 | 23 | 3908 | 2017a-PPF1-01 |
| | | 0.2 | 15 | 0.0191 | 23 | 1588 | 2017a-PPF1-02 |
| | | 0.1 | 15 | 0.0155 | 23 | 570 | 2017a-PPF1-03 |
| | | 0.05 | 15 | 0.0103 | 23 | 168 | 2017a-PPF1-04 |
| | | 0.5 | 10 | 0.0306 | 23 | 2322 | 2017a-PPF1-05 |
| | | 0.2 | 10 | 0.0163 | 23 | 972 | 2017a-PPF1-06 |
| | | 0.1 | 10 | 0.0134 | 23 | 379 | 2017a-PPF1-07 |
| | | 0.05 | 10 | 0.0091 | 23 | 109 | 2017a-PPF1-08 |
| | | 0.5 | 5 | 0.028 | 23 | 795 | 2017a-PPF1-09 |
| | | 0.2 | 5 | 0.0143 | 23 | 331 | 2017a-PPF1-10 |
| | | 0.1 | 5 | 0.095 | 23 | 126 | 2017a-PPF1-11 |
| | | 0.05 | 5 | 0.0058 | 23 | 40 | 2017a-PPF1-12 |
| | Tie points & Polydata (PPF 2) | 0.5 | 15 | 0.0873 | 23 | 38206 | 2017a-PPF2-01 |
| | | 0.2 | 15 | 0.0207 | 23 | 14188 | 2017a-PPF2-02 |
| | | 0.1 | 15 | 0.0144 | 23 | 6039 | 2017a-PPF2-03 |
| | | 0.05 | 15 | 0.0108 | 23 | 1987 | 2017a-PPF2-04 |
| | | 0.5 | 10 | 0.0867 | 23 | 22785 | 2017a-PPF2-05 |
| | | 0.2 | 10 | 0.0195 | 23 | 8129 | 2017a-PPF2-06 |
| | | 0.1 | 10 | 0.0133 | 23 | 3538 | 2017a-PPF2-07 |
| | | 0.05 | 10 | 0.0102 | 23 | 1231 | 2017a-PPF2-08 |
| | | 0.5 | 5 | 0.0845 | 23 | 7509 | 2017a-PPF2-09 |
| | | 0.2 | 5 | 0.0176 | 23 | 2580 | 2017a-PPF2-10 |
| | | 0.1 | 5 | 0.0121 | 23 | 1167 | 2017a-PPF2-11 |
| | | 0.05 | 5 | 0.0092 | 23 | 445 | 2017a-PPF2-12 |
| | Tie points & Polydata (PPF 3) | 0.5 | 15 | 0.095 | 23 | 421956 | 2017a-PPF3-01 |
| | | 0.2 | 15 | 0.0456 | 23 | 151690 | 2017a-PPF3-02 |
| | | 0.1 | 15 | 0.0203 | 23 | 52344 | 2017a-PPF3-03 |
| | | 0.05 | 15 | 0.0114 | 23 | 16067 | 2017a-PPF3-04 |
| | | 0.02 | 15 | 0.0064 | 23 | 2479 | 2017a-PPF3-05 |
| | | 0.5 | 10 | 0.1175 | 23 | 301896 | 2017a-PPF3-06 |
| | | 0.2 | 10 | 0.0459 | 23 | 81857 | 2017a-PPF3-07 |
| | | 0.1 | 10 | 0.0193 | 23 | 26751 | 2017a-PPF3-08 |
| | | 0.05 | 10 | 0.0108 | 23 | 8361 | 2017a-PPF3-09 |
| | | 0.02 | 10 | 0.006 | 23 | 1364 | 2017a-PPF3-10 |
| | | 0.5 | 5 | 0.1426 | 23 | 122372 | 2017a-PPF3-11 |
| | | 0.2 | 5 | 0.0445 | 23 | 23748 | 2017a-PPF3-12 |
| | | 0.1 | 5 | 0.0178 | 23 | 7631 | 2017a-PPF3-13 |
| | | 0.05 | 5 | 0.0101 | 23 | 2496 | 2017a-PPF3-14 |
| | | 0.02 | 5 | 0.0061 | 23 | 459 | 2017a-PPF3-15 |
| | Tiepoints & Polydata (PPF 4) | 0.5 | 15 | 0.0603 | 23 | 2203402 | 2017a-PPF4-01 |
| | | 0.2 | 15 | 0.0447 | 23 | 1210324 | 2017a-PPF4-02 |
| | | 0.1 | 15 | 0.0227 | 23 | 512814 | 2017a-PPF4-03 |
| | | 0.05 | 15 | 0.01 | 23 | 188933 | 2017a-PPF4-04 |
| | | 0.02 | 15 | 0.0045 | 23 | 40490 | 2017a-PPF4-05 |
| 0.5 | | 10 | 0.0864 | 23 | 1871435 | 2017a-PPF4-06 | |
| 0.2 | | 10 | 0.0489 | 23 | 774813 | 2017a-PPF4-07 | |
| 0.1 | | 10 | 0.022 | 23 | 283050 | 2017a-PPF4-08 | |
| 0.05 | | 10 | 0.0093 | 23 | 99149 | 2017a-PPF4-09 | |
| 0.02 | | 10 | 0.0042 | 8 | 21603 | 2017a-PPF4-10 | |
| 0.5 | | 5 | 0.1296 | 23 | 1117371 | 2017a-PPF4-11 | |
| 0.2 | | 5 | 0.0503 | 23 | 278568 | 2017a-PPF4-12 | |
| 0.1 | | 5 | 0.0207 | 23 | 85846 | 2017a-PPF4-13 | |
| 0.05 | | 5 | 0.0086 | 23 | 28756 | 2017a-PPF4-14 | |
| 0.02 | | 5 | 0.0038 | 6 | 6538 | 2017a-PPF4-15 | |

| Epoch | Input Data | Parameters | | Statistics | | | Histogram residues (see Appendix D) |
|-----------------|-------------------------------|--------------------------------------|-----------------------------|-------------------------------|---|----------|-------------------------------------|
| | | Search radius [m] | Maximum tilt angle [degree] | Error: standard deviation [m] | Number of observations used for calculation | | |
| | | | | | Tie points | Polydata | |
| 2017b (2 SP) | Tie points | no changes with changing of settings | | 0.0046 | 12 | 0 | 2017b-TP |
| | Tie points & Polydata (PPF 1) | 0.5 | 15 | 0.0349 | 12 | 1773 | 2017b-PPF1-01 |
| | | 0.2 | 15 | 0.0224 | 12 | 835 | 2017b-PPF1-02 |
| | | 0.1 | 15 | 0.018 | 12 | 320 | 2017b-PPF1-03 |
| | | 0.05 | 15 | 0.0119 | 12 | 94 | 2017b-PPF1-04 |
| | | 0.5 | 10 | 0.0304 | 12 | 1156 | 2017b-PPF1-05 |
| | | 0.2 | 10 | 0.0196 | 12 | 537 | 2017b-PPF1-06 |
| | | 0.1 | 10 | 0.0148 | 12 | 211 | 2017b-PPF1-07 |
| | | 0.05 | 10 | 0.0111 | 12 | 71 | 2017b-PPF1-08 |
| | | 0.5 | 5 | 0.026 | 12 | 388 | 2017b-PPF1-09 |
| | | 0.2 | 5 | 0.0186 | 12 | 200 | 2017b-PPF1-10 |
| | | 0.1 | 5 | 0.0114 | 12 | 77 | 2017b-PPF1-11 |
| | | 0.05 | 5 | 0.0095 | 12 | 26 | 2017b-PPF1-12 |
| | Tie points & Polydata (PPF 2) | 0.5 | 15 | 0.0835 | 12 | 15666 | 2017b-PPF2-01 |
| | | 0.2 | 15 | 0.0222 | 12 | 6441 | 2017b-PPF2-02 |
| | | 0.1 | 15 | 0.0159 | 12 | 2848 | 2017b-PPF2-03 |
| | | 0.05 | 15 | 0.0114 | 12 | 891 | 2017b-PPF2-04 |
| | | 0.5 | 10 | 0.084 | 12 | 9751 | 2017b-PPF2-05 |
| | | 0.2 | 10 | 0.0206 | 12 | 3838 | 2017b-PPF2-06 |
| | | 0.1 | 10 | 0.0143 | 12 | 1694 | 2017b-PPF2-07 |
| | | 0.05 | 10 | 0.0111 | 12 | 568 | 2017b-PPF2-08 |
| | | 0.5 | 5 | 0.0812 | 12 | 3360 | 2017b-PPF2-09 |
| | | 0.2 | 5 | 0.0191 | 12 | 1261 | 2017b-PPF2-10 |
| | | 0.1 | 5 | 0.0133 | 12 | 578 | 2017b-PPF2-11 |
| | | 0.05 | 5 | 0.0102 | 12 | 217 | 2017b-PPF2-12 |
| | Tie points & Polydata (PPF 3) | 0.5 | 15 | 0.0896 | 12 | 170527 | 2017b-PPF3-01 |
| | | 0.2 | 15 | 0.0453 | 12 | 68266 | 2017b-PPF3-02 |
| | | 0.1 | 15 | 0.0212 | 12 | 25476 | 2017b-PPF3-03 |
| | | 0.05 | 15 | 0.0122 | 12 | 8082 | 2017b-PPF3-04 |
| | | 0.02 | 15 | 0.0069 | 12 | 1226 | 2017b-PPF3-05 |
| | | 0.5 | 10 | 0.1129 | 12 | 125308 | 2017b-PPF3-06 |
| | | 0.2 | 10 | 0.0466 | 12 | 38303 | 2017b-PPF3-07 |
| | | 0.1 | 10 | 0.0206 | 12 | 13206 | 2017b-PPF3-08 |
| | | 0.05 | 10 | 0.0118 | 12 | 4247 | 2017b-PPF3-09 |
| | | 0.02 | 10 | 0.0071 | 12 | 649 | 2017b-PPF3-10 |
| | | 0.5 | 5 | 0.1389 | 12 | 53848 | 2017b-PPF3-11 |
| | | 0.2 | 5 | 0.0467 | 12 | 11673 | 2017b-PPF3-12 |
| | | 0.1 | 5 | 0.0195 | 12 | 3821 | 2017b-PPF3-13 |
| | | 0.05 | 5 | 0.0112 | 12 | 1236 | 2017b-PPF3-14 |
| | | 0.02 | 5 | 0.0075 | 12 | 203 | 2017b-PPF3-15 |
| | Tie points & Polydata (PPF 4) | 0.5 | 15 | 0.0584 | 12 | 839573 | 2017b-PPF4-01 |
| | | 0.2 | 15 | 0.043 | 12 | 485235 | 2017b-PPF4-02 |
| | | 0.1 | 15 | 0.0224 | 12 | 223785 | 2017b-PPF4-03 |
| | | 0.05 | 15 | 0.01 | 12 | 89927 | 2017b-PPF4-04 |
| | | 0.02 | 15 | 0.0043 | 0 | 21319 | 2017b-PPF4-05 |
| | | 0.5 | 10 | 0.084 | 12 | 723637 | 2017b-PPF4-06 |
| | | 0.2 | 10 | 0.0472 | 12 | 322217 | 2017b-PPF4-07 |
| | | 0.1 | 10 | 0.0218 | 12 | 129734 | 2017b-PPF4-08 |
| | | 0.05 | 10 | 0.0093 | 12 | 49190 | 2017b-PPF4-09 |
| | | 0.02 | 10 | 0.004 | 0 | 11681 | 2017b-PPF4-10 |
| | | 0.5 | 5 | 0.125 | 12 | 442276 | 2017b-PPF4-11 |
| | | 0.2 | 5 | 0.0489 | 12 | 124434 | 2017b-PPF4-12 |
| | | 0.1 | 5 | 0.0205 | 12 | 42361 | 2017b-PPF4-13 |
| | | 0.05 | 5 | 0.0086 | 12 | 15092 | 2017b-PPF4-14 |
| | | 0.02 | 5 | 0.0037 | 0 | 3586 | 2017b-PPF4-15 |

APPENDIX

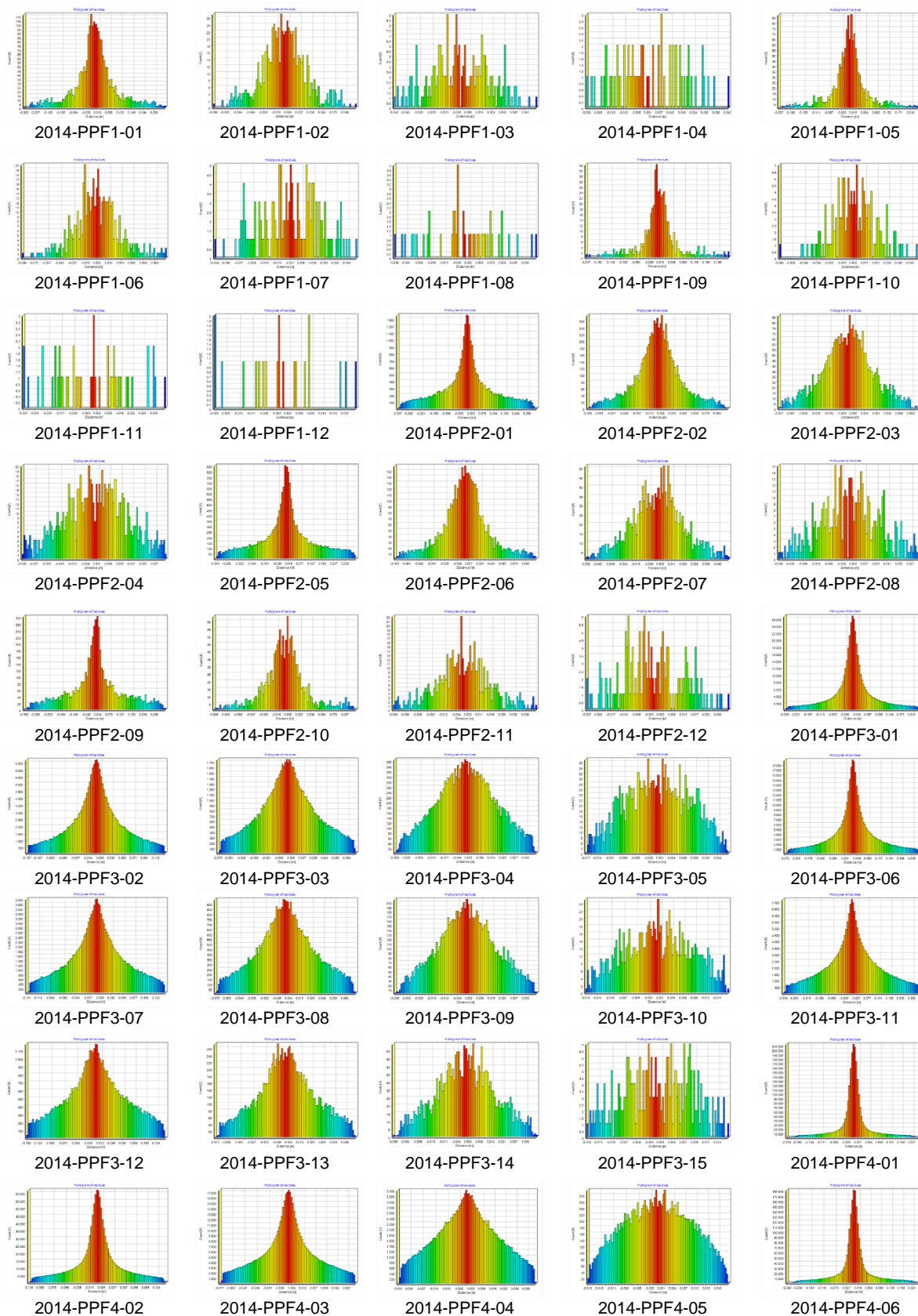
Appendix C: Detailed results of the comparison of the MSA registration test and the ICP registration test for 2016 data (SP01 as model point cloud, SP02 as data point cloud)

| Input Data: SP01 (6,002,675 points) and SP02 (11,765,226 points) 2016 | Parameters | | Statistics | | | Computational time | Histogram residues (see APPENDIX D) |
|---|-------------------------|--------------------------------|--|---|----------|--------------------|--|
| | Search radius [m] | Max. Tilt angle [degree] | Error: standard deviation [m] | Number of observations used for calculation | | | |
| | | | | Tie points | Polydata | | |
| Tie Points | | | 0.0088 | 14 | 0 | < 1 min | - |
| Tie points & Polydata (PPF 3) | 10 | 180 | 0.0112 | 14 | 259613 | 19 min 52 s | C2016-PPF3-17 |
| | 5 | 90 | 0.0248 | 14 | 259515 | 6 min 8 s | C2016-PPF3-16 |
| | 3 | 45 | 0.0506 | 14 | 252609 | 2 min | C2016-PPF3-18 |
| | 0.5 | 15 | 0.0894 | 14 | 130923 | < 1 min | C2016-PPF3-01 |
| | 0.2 | 15 | 0.0399 | 14 | 51298 | < 1 min | C2016-PPF3-02 |
| | 0.1 | 15 | 0.0171 | 14 | 20419 | < 1 min | C2016-PPF3-03 |
| | 0.05 | 15 | 0.0101 | 14 | 7092 | < 1 min | C2016-PPF3-04 |
| | 0.02 | 15 | 0.0061 | 11 | 1117 | < 1 min | C2016-PPF3-05 |
| | 0.5 | 10 | 0.1115 | 14 | 94874 | < 1 min | C2016-PPF3-06 |
| | 0.2 | 10 | 0.0399 | 14 | 28913 | < 1 min | C2016-PPF3-07 |
| | 0.1 | 10 | 0.0162 | 14 | 10921 | < 1 min | C2016-PPF3-08 |
| | 0.05 | 10 | 0.0093 | 14 | 3816 | < 1 min | C2016-PPF3-09 |
| | 0.02 | 10 | 0.0058 | 11 | 606 | < 1 min | C2016-PPF3-10 |
| | 0.5 | 5 | 0.1319 | 14 | 39804 | < 1 min | C2016-PPF3-11 |
| | 0.2 | 5 | 0.039 | 14 | 8838 | < 1 min | C2016-PPF3-12 |
| | 0.1 | 5 | 0.015 | 14 | 3196 | < 1 min | C2016-PPF3-13 |
| | 0.05 | 5 | 0.0085 | 14 | 1144 | < 1 min | C2016-PPF3-14 |
| | 0.02 | 5 | 0.0054 | 11 | 215 | < 1 min | C2016-PPF3-15 |
| Tiepoints & Polydata (PPF 4) | 10 | 180 | 0.0066 | 14 | 1154878 | 6 h 3 min 51 s | C2016-PPF4-17 |
| | 0.5 | 180 | 0.012 | 14 | 1004421 | 2 min 3 s | C2016-PPF4-19 |
| | 0.2 | 180 | 0.0108 | 14 | 922995 | 1 min 11 s | C2016-PPF4-20 |
| | 0.1 | 180 | 0.0109 | 14 | 814835 | < 1 min | C2016-PPF4-21 |
| | 0.05 | 180 | 0.009 | 14 | 581305 | < 1 min | C2016-PPF4-22 |
| | 0.02 | 180 | 0.0055 | 14 | 190758 | < 1 min | C2016-PPF4-23 |
| | 5 | 90 | 0.0149 | 14 | 1148333 | 1 h 44 min 52 s | C2016-PPF4-16 |
| | 3 | 45 | 0.0322 | 14 | 1123344 | 36 min 37 s | C2016-PPF4-18 |
| | 0.5 | 15 | 0.0538 | 14 | 744164 | 1 min 48 s | C2016-PPF4-01 |
| | 0.2 | 15 | 0.0396 | 14 | 435265 | < 1 min | C2016-PPF4-02 |
| | 0.1 | 15 | 0.0193 | 14 | 208080 | < 1 min | C2016-PPF4-03 |
| | 0.05 | 15 | 0.0085 | 14 | 89534 | < 1 min | C2016-PPF4-04 |
| | 0.02 | 15 | 0.004 | 10 | 23165 | < 1 min | C2016-PPF4-05 |
| | 0.5 | 10 | 0.079 | 14 | 645935 | < 1 min | C2016-PPF4-06 |
| | 0.2 | 10 | 0.0433 | 14 | 291950 | < 1 min | C2016-PPF4-07 |
| | 0.1 | 10 | 0.0189 | 14 | 121730 | < 1 min | C2016-PPF4-08 |
| | 0.05 | 10 | 0.008 | 14 | 48697 | < 1 min | C2016-PPF4-09 |
| | 0.02 | 10 | 0.0038 | 9 | 12214 | < 1 min | C2016-PPF4-10 |
| | 0.5 | 5 | 0.1188 | 14 | 402138 | 1 min 43 s | C2016-PPF4-11 |
| | 0.2 | 5 | 0.0446 | 14 | 115532 | < 1 min | C2016-PPF4-12 |
| | 0.1 | 5 | 0.0177 | 14 | 40140 | < 1 min | C2016-PPF4-13 |
| 0.05 | 5 | 0.0074 | 14 | 14603 | < 1 min | C2016-PPF4-14 | |
| 0.02 | 5 | 0.0035 | 9 | 3620 | < 1 min | C2016-PPF4-15 | |

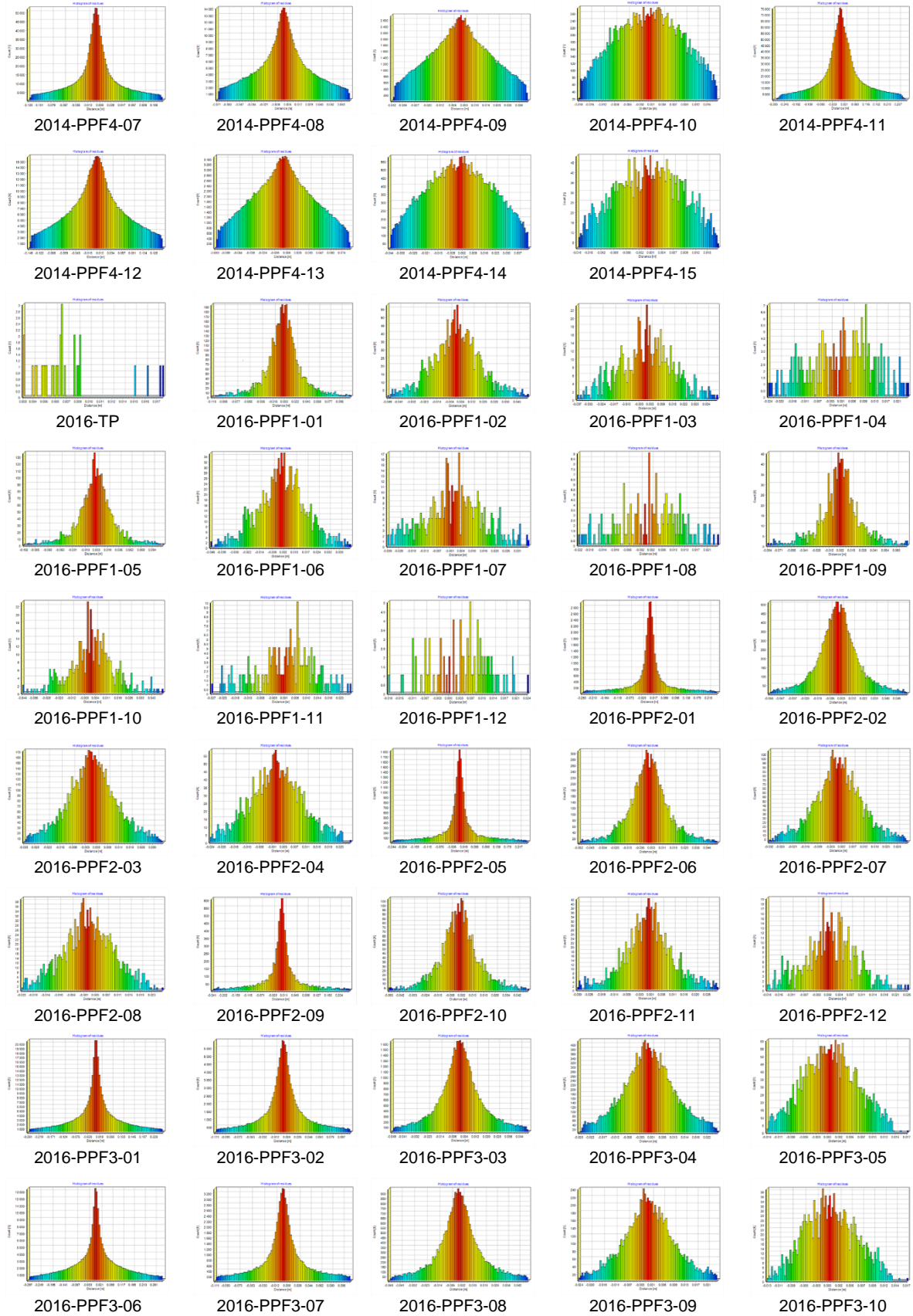
| Input Data: SP01 (314,536 points) and SP02 (385,323 points) 2016 selected | Parameters | | Statistics | | | Computational time | Histogram residues (see APPENDIX D) |
|--|-------------------------|--------------------------------|--|---|----------|--------------------|--|
| | Search radius [m] | Max. Tilt angle [degree] | Error: standard deviation [m] | Number of observations used for calculation | | | |
| | | | | Tie points | Polydata | | |
| Tie Points | - | | | | | | |
| Tie points & Polydata (PPF 3) | 10 | 180 | 0.0101 | 0 | 40896 | < 1 min | S2016-PPF3-17 |
| | 5 | 90 | 0.0126 | 0 | 40699 | < 1 min | S2016-PPF3-16 |
| | 3 | 45 | 0.0209 | 0 | 40859 | < 1 min | S2016-PPF3-18 |
| | 0.5 | 15 | 0.0967 | 0 | 26196 | < 1 min | S2016-PPF3-01 |
| | 0.2 | 15 | 0.0385 | 0 | 9743 | < 1 min | S2016-PPF3-02 |
| | 0.1 | 15 | 0.0162 | 0 | 3835 | < 1 min | S2016-PPF3-03 |
| | 0.05 | 15 | 0.0088 | 0 | 1318 | < 1 min | S2016-PPF3-04 |
| | 0.02 | 15 | 0.0061 | 0 | 199 | < 1 min | S2016-PPF3-05 |
| | 0.5 | 10 | 0.1165 | 0 | 18538 | < 1 min | S2016-PPF3-06 |
| | 0.2 | 10 | 0.0388 | 0 | 5343 | < 1 min | S2016-PPF3-07 |
| | 0.1 | 10 | 0.0167 | 0 | 1926 | < 1 min | S2016-PPF3-08 |
| | 0.05 | 10 | 0.0086 | 0 | 646 | < 1 min | S2016-PPF3-09 |
| | 0.02 | 10 | 0.0058 | 0 | 104 | < 1 min | S2016-PPF3-10 |
| | 0.5 | 5 | 0.1308 | 0 | 7318 | < 1 min | S2016-PPF3-11 |
| | 0.2 | 5 | 0.0382 | 0 | 1625 | < 1 min | S2016-PPF3-12 |
| | 0.1 | 5 | 0.0161 | 0 | 560 | < 1 min | S2016-PPF3-13 |
| | 0.05 | 5 | 0.0102 | 0 | 197 | < 1 min | S2016-PPF3-14 |
| | 0.02 | 5 | 0.0088 | 0 | 32 | < 1 min | S2016-PPF3-15 |
| Tiepoints & Polydata (PPF 4) | 10 | 180 | 0.0051 | 0 | 40916 | < 1 min | S2016-PPF4-17 |
| | 0.5 | 180 | 0.0115 | 0 | 39790 | < 1 min | S2016-PPF4-19 |
| | 0.2 | 180 | 0.0115 | 0 | 36397 | < 1 min | S2016-PPF4-20 |
| | 0.1 | 180 | 0.0108 | 0 | 29071 | < 1 min | S2016-PPF4-21 |
| | 0.05 | 180 | 0.0067 | 0 | 13408 | < 1 min | S2016-PPF4-22 |
| | 0.02 | 180 | 0.0017 | 0 | 1932 | < 1 min | S2016-PPF4-23 |
| | 5 | 90 | 0.0063 | 0 | 40428 | 1 min 7 s | S2016-PPF4-16 |
| | 3 | 45 | 0.0108 | 0 | 41342 | < 1 min | S2016-PPF4-18 |
| | 0.5 | 15 | 0.0582 | 0 | 34921 | < 1 min | S2016-PPF4-01 |
| | 0.2 | 15 | 0.0383 | 0 | 20137 | < 1 min | S2016-PPF4-02 |
| | 0.1 | 15 | 0.0165 | 0 | 9854 | < 1 min | S2016-PPF4-03 |
| | 0.05 | 15 | 0.0072 | 0 | 4738 | < 1 min | S2016-PPF4-04 |
| | 0.02 | 15 | 0.0034 | 0 | 1213 | < 1 min | S2016-PPF4-05 |
| | 0.5 | 10 | 0.0853 | 0 | 30230 | < 1 min | S2016-PPF4-06 |
| | 0.2 | 10 | 0.0404 | 0 | 13333 | < 1 min | S2016-PPF4-07 |
| | 0.1 | 10 | 0.0158 | 0 | 5836 | < 1 min | S2016-PPF4-08 |
| | 0.05 | 10 | 0.0066 | 0 | 2634 | < 1 min | S2016-PPF4-09 |
| | 0.02 | 10 | 0.0034 | 0 | 629 | < 1 min | S2016-PPF4-10 |
| | 0.5 | 5 | 0.1179 | 0 | 17512 | < 1 min | S2016-PPF4-11 |
| | 0.2 | 5 | 0.0413 | 0 | 5247 | < 1 min | S2016-PPF4-12 |
| | 0.1 | 5 | 0.0153 | 0 | 1980 | < 1 min | S2016-PPF4-13 |
| | 0.05 | 5 | 0.0059 | 0 | 804 | < 1 min | S2016-PPF4-14 |
| | 0.02 | 5 | 0.0028 | 0 | 190 | < 1 min | S2016-PPF4-15 |

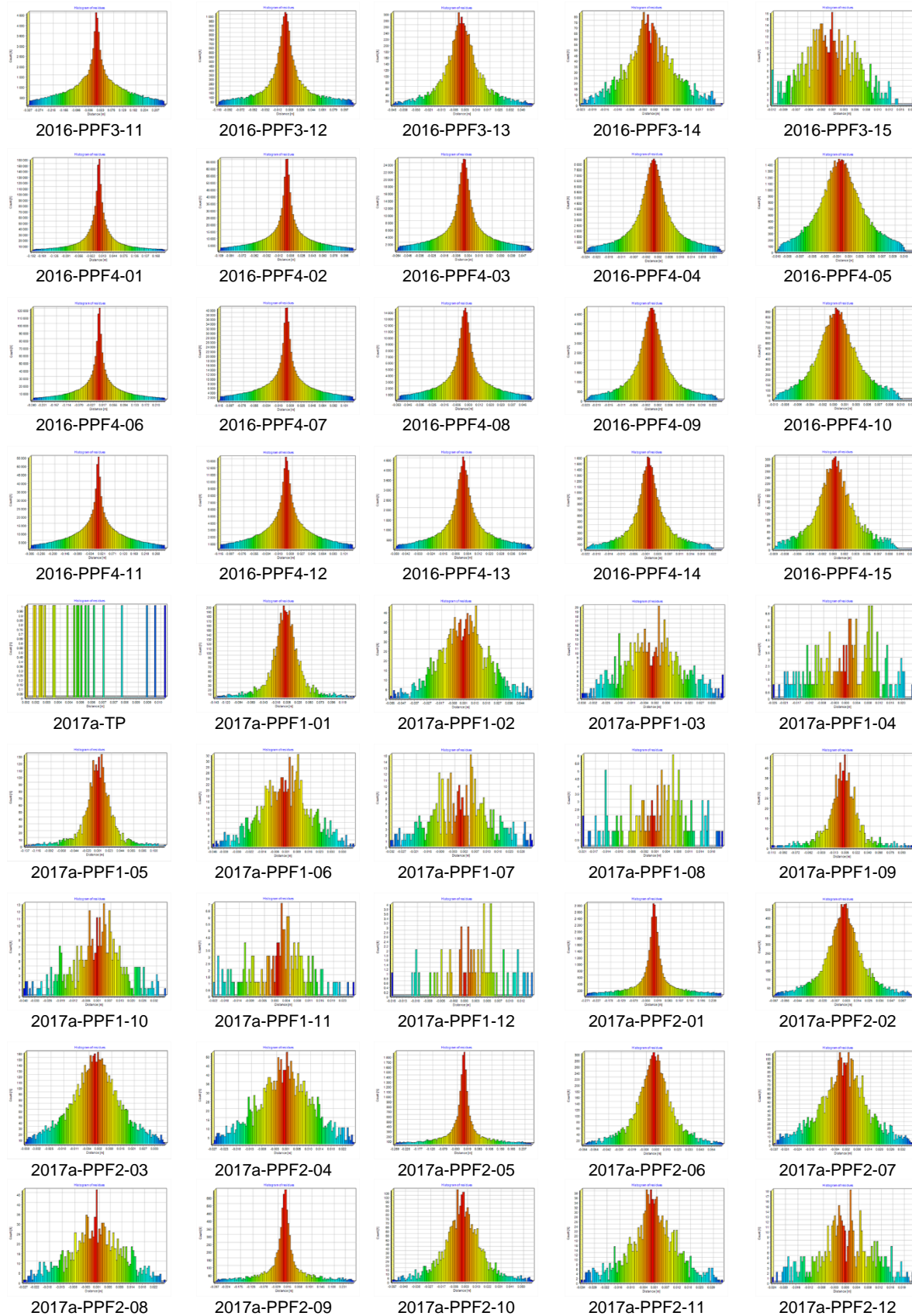
APPENDIX

| Input Data | Random sample limit | Number of points used for the calculation | theoretical overlap | Final RMS | Computational Time |
|--|---------------------|---|---------------------|------------|--------------------|
| SP01 (6,002,675 points) and SP02 (11,765,226 points) 2016 | $5 \cdot 10^4$ | 50,000 | 100 | 0.553216 | < 1 min |
| | | 50,000 | 75 | 0.134607 | < 1 min |
| | | 50,000 | 50 | 0.0926671 | < 1 min |
| | | 50,000 | 25 | 0.0566543 | < 1 min |
| | $5 \cdot 10^5$ | 500,000 | 100 | 0.40637 | < 1 min |
| | | 500,000 | 75 | 0.0531079 | < 1 min |
| | | 500,000 | 50 | 0.0334238 | < 1 min |
| | | 500,000 | 25 | 0.0203148 | < 1 min |
| | $5 \cdot 10^6$ | 5,000,000 | 100 | 0.368419 | 17 min 1 s |
| | | 5,000,000 | 75 | 0.0268709 | 4 min 37 s |
| | | 5,000,000 | 50 | 0.0143889 | 2 min 44 s |
| | | 2,941,306 | 25 | 0.00794865 | 4 min 8 s |
| SP01 (314,536 points) and SP02 (385,323 points) 2016 selected | $5 \cdot 10^4$ | 50,000 | 100 | 0.139379 | < 1 min |
| | | 50,000 | 75 | 0.0346795 | < 1 min |
| | | 50,000 | 50 | 0.0231414 | < 1 min |
| | | 50,000 | 25 | 0.0146627 | < 1 min |
| | $5 \cdot 10^5$ | 385,323 | 100 | 0.122446 | < 1 min |
| | | 288,992 | 75 | 0.0183232 | < 1 min |
| | | 192,611 | 50 | 0.0108526 | < 1 min |
| | | 96,330 | 25 | 0.0065997 | < 1 min |

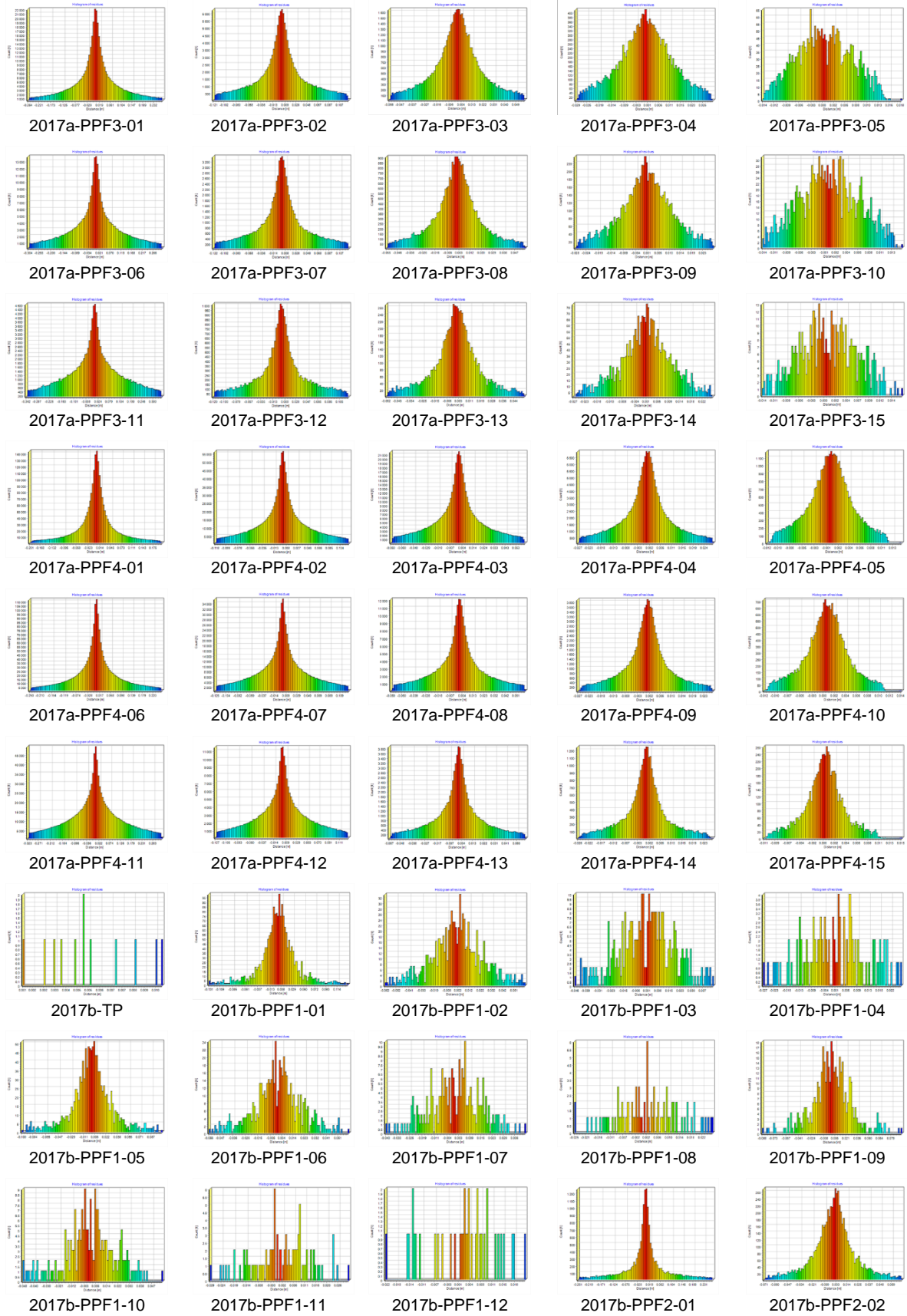
Appendix D: Histograms of the residues of the MSA registration tests

APPENDIX



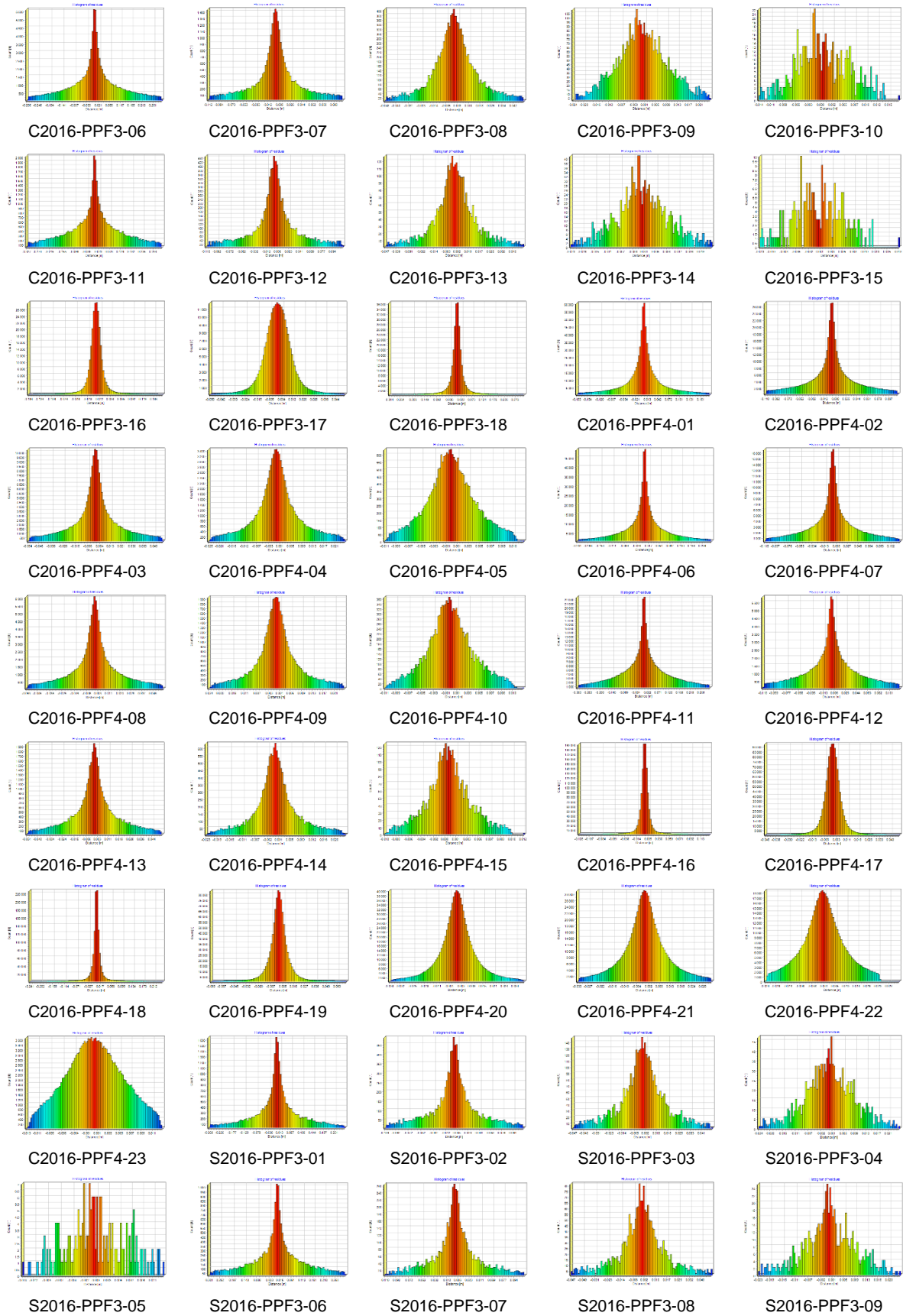


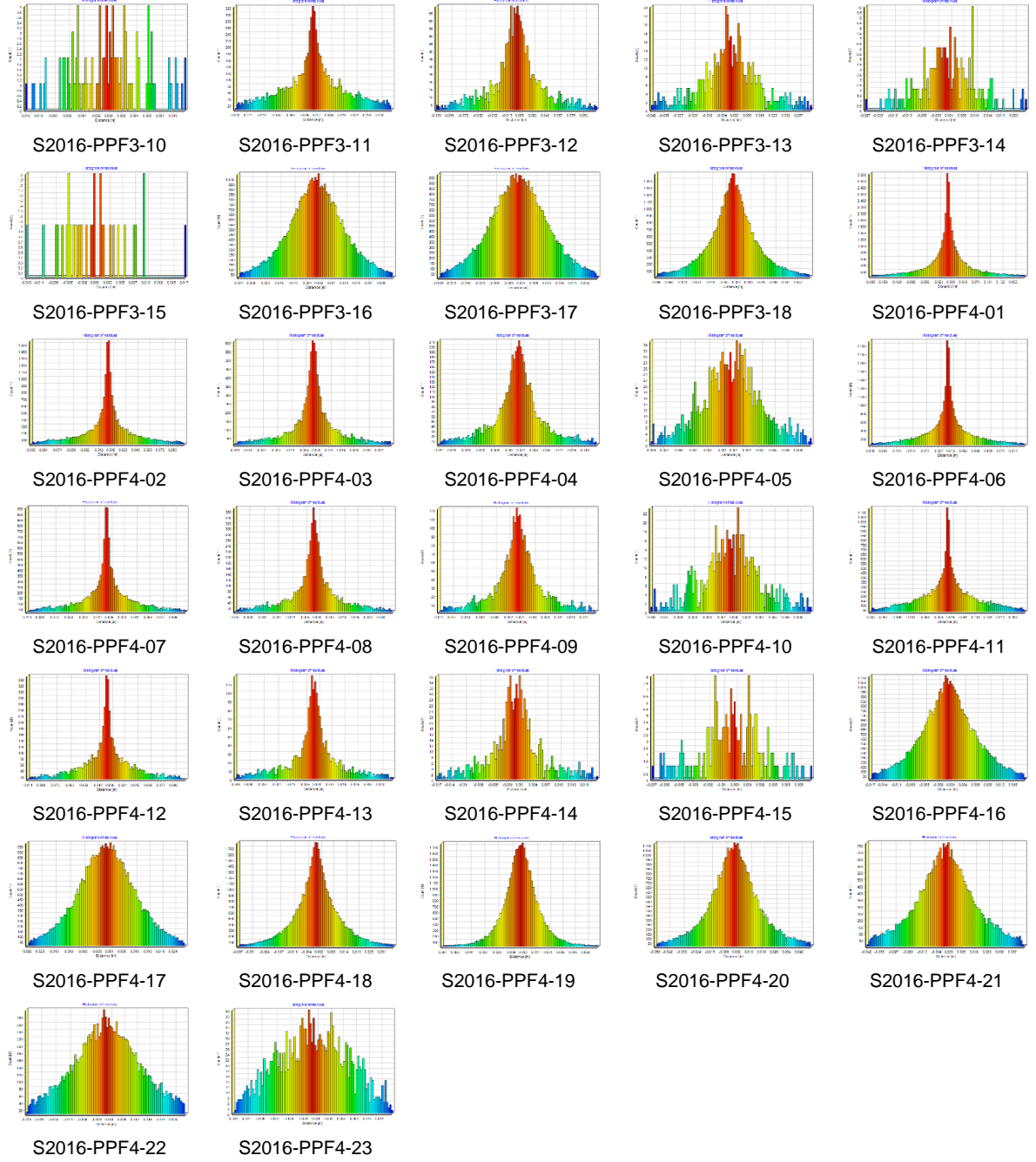
APPENDIX





APPENDIX





APPENDIX

Appendix E: Detailed results of change detection C2C

| | | | T1 original | T1 class_rock | T1 rock cleaned | T1 filtering final | T2 original | T2 class_rock | T2 rock cleaned | T2 filtering final |
|------------------------------|---------|--------|----------------|------------------|--------------------|-----------------------|----------------|------------------|--------------------|-----------------------|
| Total number of points | | | 27281 | 27101 | 27133 | 8674 | 129409 | 106152 | 110810 | 42442 |
| number of points - object | absolut | | 829 | 820 | 826 | 323 | 829 | 820 | 826 | 323 |
| | % | | 3.0% | 3.0% | 3.0% | 3.7% | 0.6% | 0.8% | 0.7% | 0.8% |
| number of points - rest | absolut | | 26452 | 26281 | 26307 | 8351 | 128580 | 105332 | 109984 | 42119 |
| | % | | 97.0% | 97.0% | 97.0% | 96.3% | 99.4% | 99.2% | 99.3% | 99.2% |
| C2C no local modelling | total | > 0.01 | 1931 | 1842 | 1831 | 1491 | 29794 | 15181 | 17642 | 13284 |
| | | % | 7.1% | 6.8% | 6.7% | 17.2% | 23.0% | 14.3% | 15.9% | 31.3% |
| | | < 0.01 | 25350 | 25259 | 25302 | 7183 | 99615 | 90971 | 93168 | 29158 |
| | | % | 92.9% | 93.2% | 93.3% | 82.8% | 77.0% | 85.7% | 84.1% | 68.7% |
| | | > 0.02 | 597 | 541 | 515 | 302 | 7934 | 2567 | 3186 | 2444 |
| | | % | 2.2% | 2.0% | 1.9% | 3.5% | 6.1% | 2.4% | 2.9% | 5.8% |
| | | < 0.02 | 26684 | 26560 | 26618 | 8372 | 121475 | 103585 | 107624 | 39998 |
| | | % | 97.8% | 98.0% | 98.1% | 96.5% | 93.9% | 97.6% | 97.1% | 94.2% |
| | objects | > 0.01 | 667 | 658 | 664 | 263 | 667 | 658 | 664 | 263 |
| | | % | 80.5% | 80.2% | 80.4% | 81.4% | 80.5% | 80.2% | 80.4% | 81.4% |
| | | < 0.01 | 162 | 162 | 162 | 60 | 162 | 162 | 162 | 60 |
| | | % | 19.5% | 19.8% | 19.6% | 18.6% | 19.5% | 19.8% | 19.6% | 18.6% |
| | | > 0.02 | 377 | 372 | 374 | 146 | 377 | 372 | 374 | 146 |
| | | % | 45.5% | 45.4% | 45.3% | 45.2% | 45.5% | 45.4% | 45.3% | 45.2% |
| | | < 0.02 | 452 | 448 | 452 | 177 | 452 | 448 | 452 | 177 |
| | | % | 54.5% | 54.6% | 54.7% | 54.8% | 54.5% | 54.6% | 54.7% | 54.8% |
| | rest | > 0.01 | 1264 | 1184 | 1167 | 1228 | 29127 | 14523 | 16978 | 13021 |
| | | % | 4.8% | 4.5% | 4.4% | 14.7% | 22.7% | 13.8% | 15.4% | 30.9% |
| | | < 0.01 | 25188 | 25097 | 25140 | 7123 | 99453 | 90809 | 93006 | 29098 |
| | | % | 95.2% | 95.5% | 95.6% | 85.3% | 77.3% | 86.2% | 84.6% | 69.1% |
| | | > 0.02 | 220 | 169 | 141 | 156 | 7557 | 2195 | 2812 | 2298 |
| | | % | 0.8% | 0.6% | 0.5% | 1.9% | 5.9% | 2.1% | 2.6% | 5.5% |
| | | < 0.02 | 26232 | 26112 | 26166 | 8195 | 121023 | 103137 | 107172 | 39821 |
| | | % | 99.2% | 99.4% | 99.5% | 98.1% | 94.1% | 97.9% | 97.4% | 94.5% |
| C2C local quadric modelling | total | > 0.01 | 1232 | 1151 | 1143 | 664 | 18080 | 8250 | 9829 | 6623 |
| | | % | 4.5% | 4.2% | 4.2% | 7.7% | 14.0% | 7.8% | 8.9% | 15.6% |
| | | < 0.01 | 26049 | 25950 | 25990 | 8010 | 111329 | 97902 | 100981 | 35819 |
| | | % | 95.5% | 95.8% | 95.8% | 92.3% | 86.0% | 92.2% | 91.1% | 84.4% |
| | | > 0.02 | 443 | 392 | 369 | 222 | 4775 | 1369 | 1758 | 1445 |
| | | % | 1.6% | 1.4% | 1.4% | 2.6% | 3.7% | 1.3% | 1.6% | 3.4% |
| | | < 0.02 | 26838 | 26709 | 26764 | 8452 | 124634 | 104783 | 109052 | 40997 |
| | | % | 98.4% | 98.6% | 98.6% | 97.4% | 96.3% | 98.7% | 98.4% | 96.6% |
| | objects | > 0.01 | 579 | 569 | 576 | 253 | 579 | 569 | 576 | 253 |
| | | % | 69.8% | 69.4% | 69.7% | 78.3% | 69.8% | 69.4% | 69.7% | 78.3% |
| | | < 0.01 | 250 | 251 | 250 | 70 | 250 | 251 | 250 | 70 |
| | | % | 30.2% | 30.6% | 30.3% | 21.7% | 30.2% | 30.6% | 30.3% | 21.7% |
| | | > 0.02 | 301 | 296 | 298 | 140 | 301 | 296 | 298 | 140 |
| | | % | 36.3% | 36.1% | 36.1% | 43.3% | 36.3% | 36.1% | 36.1% | 43.3% |
| | | < 0.02 | 528 | 524 | 528 | 183 | 528 | 524 | 528 | 183 |
| | | % | 63.7% | 63.9% | 63.9% | 56.7% | 63.7% | 63.9% | 63.9% | 56.7% |
| | rest | > 0.01 | 653 | 582 | 567 | 411 | 17501 | 7681 | 9253 | 6370 |
| | | % | 2.5% | 2.2% | 2.2% | 4.9% | 13.6% | 7.3% | 8.4% | 15.1% |
| | | < 0.01 | 25799 | 25699 | 25740 | 7940 | 111079 | 97651 | 100731 | 35749 |
| | | % | 97.5% | 97.8% | 97.8% | 95.1% | 86.4% | 92.7% | 91.6% | 84.9% |
| | | > 0.02 | 142 | 96 | 71 | 82 | 4474 | 1073 | 1460 | 1305 |
| | | % | 0.5% | 0.4% | 0.3% | 1.0% | 3.5% | 1.0% | 1.3% | 3.1% |
| | | < 0.02 | 26310 | 26185 | 26236 | 8269 | 124106 | 104259 | 108524 | 40814 |
| | | % | 99.5% | 99.6% | 99.7% | 99.0% | 96.5% | 99.0% | 98.7% | 96.9% |

Appendix F: Detailed results of change detection M3C2

| | | T1 original | T1 class_rock | T1 rock cleaned | T1 filtering final | T2 original | T2 class_rock | T2 rock cleaned | T2 filtering final |
|------------------------------------|--|------------------------|--------------------------|----------------------------|-----------------------------------|------------------------|--------------------------|----------------------------|-----------------------------------|
| Total number of points | no distance calculated | 79 | 89 | 38 | 60 | 1893 | 584 | 660 | 519 |
| | distance calculated | 27202 | 27012 | 27095 | 8625 | 127516 | 105568 | 110150 | 41923 |
| | significance does not comply with class | 13289 | 13168 | 13226 | 6189 | 61004 | 48815 | 51810 | 27553 |
| | significance does not comply with class | 13913 | 13844 | 13869 | 2436 | 66512 | 56753 | 58340 | 14370 |
| points class objects | no distance calculated | 2 | 1 | 0 | 0 | 1 | 0 | 0 | 0 |
| | distance calculated | 904 | 893 | 905 | 346 | 904 | 895 | 905 | 343 |
| | significance does not comply with class | 879 | 869 | 878 | 304 | 877 | 870 | 876 | 303 |
| | significance does not comply with class | 25 | 24 | 27 | 42 | 27 | 25 | 29 | 40 |
| points class rest | no distance calculated | 77 | 88 | 38 | 60 | 1892 | 584 | 660 | 519 |
| | distance calculated | 26298 | 26119 | 26190 | 8279 | 126612 | 104673 | 109245 | 41580 |
| | significance does not comply with class | 12410 | 12299 | 12348 | 5885 | 60127 | 47945 | 50934 | 27250 |
| | significance does not comply with class | 13888 | 13820 | 13842 | 2394 | 66485 | 56728 | 58311 | 14330 |
| total (classified points) | > 0.01 | 990 | 877 | 933 | 469 | 17630 | 6752 | 8476 | 5936 |
| | % | 3.6% | 3.2% | 3.4% | 5.4% | 13.8% | 6.4% | 7.7% | 14.2% |
| | < 0.01 | 26212 | 26135 | 26162 | 8156 | 109886 | 98816 | 101674 | 35987 |
| | % | 96.4% | 96.8% | 96.6% | 94.6% | 86.2% | 93.6% | 92.3% | 85.8% |
| | > 0.02 | 564 | 509 | 527 | 239 | 10957 | 3476 | 4614 | 3161 |
| | % | 2.1% | 1.9% | 1.9% | 2.8% | 8.6% | 3.3% | 4.2% | 7.5% |
| | < 0.02 | 26638 | 26503 | 26568 | 8386 | 116559 | 102092 | 105536 | 38762 |
| | % | 97.9% | 98.1% | 98.1% | 97.2% | 91.4% | 96.7% | 95.8% | 92.5% |
| objects (classified points) | > 0.01 | 736 | 723 | 735 | 280 | 738 | 725 | 736 | 279 |
| | % | 81.4% | 81.0% | 81.2% | 80.9% | 81.6% | 81.0% | 81.3% | 81.3% |
| | < 0.01 | 168 | 170 | 170 | 66 | 166 | 170 | 169 | 64 |
| | % | 18.6% | 19.0% | 18.8% | 19.1% | 18.4% | 19.0% | 18.7% | 18.7% |
| | > 0.02 | 444 | 443 | 445 | 157 | 442 | 444 | 443 | 156 |
| | % | 49.1% | 49.6% | 49.2% | 45.4% | 48.9% | 49.6% | 49.0% | 45.5% |
| | < 0.02 | 460 | 450 | 460 | 189 | 462 | 451 | 462 | 187 |
| | % | 50.9% | 50.4% | 50.8% | 54.6% | 51.1% | 50.4% | 51.0% | 54.5% |
| rest (classified points) | > 0.01 | 254 | 154 | 198 | 189 | 16892 | 6027 | 7740 | 5657 |
| | % | 1.0% | 0.6% | 0.8% | 2.3% | 13.3% | 5.8% | 7.1% | 13.6% |
| | < 0.01 | 26044 | 25965 | 25992 | 8090 | 109720 | 98646 | 101505 | 35923 |
| | % | 99.0% | 99.4% | 99.2% | 97.7% | 86.7% | 94.2% | 92.9% | 86.4% |
| | > 0.02 | 120 | 66 | 82 | 82 | 10515 | 3032 | 4171 | 3005 |
| | % | 0.5% | 0.3% | 0.3% | 1.0% | 8.3% | 2.9% | 3.8% | 7.2% |
| | < 0.02 | 26178 | 26053 | 26108 | 8197 | 116097 | 101641 | 105074 | 38575 |
| | % | 99.5% | 99.7% | 99.7% | 99.0% | 91.7% | 97.1% | 96.2% | 92.8% |